Ollscoil na hÉireann, Corcaigh

National University of Ireland, Cork

Ordered Macroporous Metal Oxides and Carbonaceous Composites for Li-ion and Beyond Li-ion Batteries

Thesis presented by

Aoife Carroll, B.Sc. (Hons)

for the degree of

Doctor of Philosophy

University College Cork

School of Chemistry

Thesis Supervisor: Prof. Colm O'Dwyer

December 2023

Declaration

This statement is to certify that the work presented in this thesis is my own research and that no part of this thesis has been submitted previously for consideration for another degree at University College Cork or any other research institute. All research was performed under the direction of Prof. Colm O'Dwyer and references are made to the contributions of other authors. I have read and understood the terms and conditions regarding plagiarism prior to submission, as outlined by University College Cork.

Signed

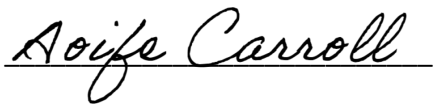

Aoife Carroll

Dedicated to
my amazing Mom and Dad,
Carmel and Kevin Carroll

Acknowledgements

First, I'd like to thank my supervisor, Prof. Colm O'Dwyer, who gave me the opportunity to do this PhD to begin with. Your unwavering support and guidance has been invaluable, steering me in the right direction with each project and advising me on when to persist (and when to stop). The enthusiasm and dedication you brought was truly inspiring and I can't thank you enough for your role in this work for the past 4 years.

To all the staff in School of Chemistry, who keep everything running smoothly. To everyone in our Applied Nano Group, Umair, Yan, Alex L (big Alex), Alex G (small Alex), and Matthew, I would also like to say thank you. I have had the pleasure to work with some of the best researchers who have always been there to help and answer any questions I had, all with incredible kindness. To Alex G, being stuck together nearly every day for the last 4 years, it's safe to say this PhD wouldn't have been the same without you, I'm truly grateful for everything you've done for me.

The group of friends I made outside our research group are friends I've made for life, while the group is always changing (as is the nature of doing a PhD), a special mention will go to Niall, Rachel, Paddy, Eadaoin, Will, Neil and Doireann. Lunch was my favourite time of the day, being able to chat about absolutely anything and laugh, even if everything was going wrong in the lab. Ye made this whole PhD process into something other than just work and I can't thank ye enough for that.

To the people outside of UCC that helped me, first of all Jason, you have always been there to support and encourage me and it has not gone unnoticed. From listening to me rehearse presentations to letting me vent if I couldn't work something out in the lab, I don't think I could have done this without you. To Nanny Mc, Nana and Granda, thank

you for always believing in me and supporting me, even if you're not 100 % sure what I've been doing in college for the last 8 years!

And last but definitely not least, to my wonderful Mom and Dad, your encouragement and belief in me is the reason I'm finishing this PhD. The work ethic and determination that you both have has always driven me to do my best. I appreciate everything ye have done for me in the past 26 years and as a way to say thank you, I dedicate this PhD thesis to you both. (Don't worry that doesn't mean you have to read it).

Publications

- **A. Carroll**, A. Grant, Y. Zhang, U. Gulzar, D. Douglas-Henry, V. Nicolosi, C. O'Dwyer, The Effect of TiO2 and GeO2 Composite Mixing on the Behavior of Macroporous Li-Ion Battery Anode Materials. *Journal of the Electrochemical Society,* **170**, 120521 (2023)

- **A. Carroll**, A. Grant, Y. Zhang, U. Gulzar, A. Ahad, H. Geaney, C. O'Dwyer, Three–Dimensionally Ordered Macroporous Amorphous C/TiO2 Composite Electrodes for Lithium-ion Batteries, *ECS Advances,* **170**, 010502 (2024)

- **A. Carroll**, A. Grant, Y. Zhang, A. Lonergan, A. Ahad, H. Geaney, C. O'Dwyer, Carbon Inverse Opals as Monolithic Structures for Sodium-ion and Potassium-ion Batteries. *Journal of The Electrochemical Society,* **171**, 030529 (2024)

- A. Grant, **A. Carroll**, Y. Zhang, U. Gulzar, S. A. Ahad, H. Geaney and C. O' Dwyer, Comparing cycling and rate response of SnO2 macroporous anodes in lithium-ion and sodium-ion batteries, *Journal of the Electrochemical Society*, **170**, 120505 (2023)

- Y. Zhang, A. Grant, **A. Carroll**, U. Gulzar, M. Ferguson, A. Roy, V. Nicolosi, C. O' Dwyer, Water-Soluble Binders That Improve Electrochemical Sodium-Ion Storage Properties in a NaTi2(PO4)3 Anode *Journal of The Electrochemical Society*, **170**, 050529 (2023).

- U. Gulzar, A. Lonergan, V. Egorov, Y. Zhang, A. Grant**, A. Carroll**, C. O'Dwyer, Methods—Ampero-Coulometry: A New Technique for Understanding Lithium-Sulfur Electrochemistry, *Journal of The Electrochemical Society*, **170**, 030503 (2023).

- Y. Zhang, A. Lonergan, A. Grant**, A. Carroll**, A. Roy, V. Nicolosi, T. Keene, C. O' Dwyer, Surface modification improves spinel LiCoO2 Li-ion battery cathode materials grown by low temperature solvothermal flow reaction, *Journal of The Electrochemical Society*. Manuscript Currently in Review.

Oral Presentations

- Composite TiO_2/GeO_2 for Higher Performance Inverse Opal Lithium-Ion Battery Electrodes, *242nd ECS Meeting, October 9-13, 2022, Atlanta, GA, USA.*

- Composite TiO_2/GeO_2 Inverse Opals for Higher Performance Lithium-Ion Battery Electrodes, *Early Career Researcher Regional Symposium on Electrochemistry, November 4, 2022, Queen's University Belfast, Ireland.*

- Nanocomposite Carbon/TiO_2 Inverse Opals for Lithium-Ion battery with High Capacity Retention, *E-MRS 2023 Spring Meeting, May 29 – June 2, 2023, Strasbourg, France.*
  Winner of Best Oral Presentation in Symposium

- Inverse Opal Materials for Improved Lithium-Ion Batteries, *74th Irish Universities Chemistry Research Colloquium, June 14-15, University of Galway, Ireland*
  Winner of Best Oral Presentation

Abstract

This thesis provides an in-depth investigation of three-dimensional ordered macroporous materials, specifically inverse opal materials, for electrochemical energy storage systems, particularly rechargeable batteries. Exploring the potential of composite structures, this research focuses on TiO_2/GeO_2 nanocomposites and C/TiO_2 inverse opal anodes in Li-ion batteries, and carbon inverse opal anodes in Na-ion and K-ion batteries. Employing comprehensive characterization techniques, this research studies intricate material properties and electrochemical responses inherent in these structures. The composite materials exhibit promising features such as enhanced electrolyte penetration, improved specific capacities and coulombic efficiency, and robust structural integrity during extended charge-discharge cycling. The study findings shed light on the unique advantages of inverse opal composites for application in next-generation battery technologies.

Highly ordered, macroporous inverse opal structures were fabricated as TiO_2/GeO_2 nanocomposites with varying GeO_2 content, showcasing coulombic efficiency and capacity retention. The overall capacity of these interconnected binder-free anodes was affected by the Ge content and its distribution at both slow and fast rates. Characterization techniques such as X-ray diffraction, high-resolution transmission electron microscopy (HRTEM), selected area electron diffraction, energy-dispersive X-ray spectroscopy, and electron energy loss spectroscopy were employed to analyse these anodes. The electrochemical response over 2000 cycles and at various rates elucidated the impact of the composite on key metric in battery cells. The results indicated that a composite of intercalation and alloying compounds yielded good specific capacity and excellent coulombic efficiency (>99%), even with low

quantities of the GeO_2. The cycling life reveals an increase in capacity with improved coulombic efficiency with suspicion that the GeO_2 material becomes electrochemically active within the composite matrix, undergoing modifications during cycling.

C/TiO_2 composite were synthesized from sucrose as the carbon precursor to form interconnected, porous inverse opal structures. Material characterization revealed amorphous TiO_2 and disordered carbon with a large pore size of ~400 nm. An atomic ratio of ~8:1 in favour of carbon yielded promising electrochemical responses with high specific capacity and capacity retention at 150 mA/g rate. Diffusion processes were shown to be the dominant contributor to current responses for all scan rates, with double-layer capacitance accounting for less than ~45 % even at the high scan rate of 1000 mV/s. When compared to individual carbon and TiO_2 inverse opals the composite demonstrated improved coulombic efficiency and high-rate performance attributed to the synergistic benefits of combining these two intercalation materials.

Carbon inverse opals were fabricated in a similar way from sucrose to study the effect of the macroporous structure on performance in sodium-ion and potassium-ion batteries. Composed of disordered carbon with short-range graphitic regions, the storage mechanism involved primarily diffusion processes at lower scan rate with capacitive behaviour governing the current response at faster scan rates. Structural integrity was maintained in all cells after 250 cycles showcasing impressive resistance to structural stresses. Comparing the inverse opal material to thin films of the same composition highlighted the improved capacity retention and cycling stability inherent to the three-dimensional ordered macroporous structure.

Table of Contents

Chapter 1

Thesis Overview

Chapter 2 of this thesis provides a comprehensive review of advanced materials and technologies crucial to the development and enhancement of energy storage systems, with a primary focus on lithium-ion batteries (LIBs). The chapter delves into the fundamental principles of LIB operation, elucidating the intricate electrochemical processes that govern their functionality. A particular emphasis is placed on the role of porous materials in electrode design, examining their unique properties that facilitate efficient ion transport and storage. Composite materials are discussed, highlighting the synergistic effects that arise from combining different components, with dedicated sections reviewing TiO_2-based and carbon-based materials. Finally, this introductory chapter explores emerging technologies contemplating the trajectory towards a 'beyond Li-ion' world, including the exploration of sodium-ion and potassium-ion batteries.

In Chapter 3, the experimental techniques employed throughout the research presented in this thesis are outlined. This chapter is structured into four distinct subsections: Sample Preparation, Structural Characterization Techniques, Electrochemical Characterization Methods, and Cell Assembly. The Sample Preparation section meticulously outlines the procedures used to fabricate each sample for the subsequent chapters. The Structural Characterization Techniques section delves into the theoretical underpinnings of the analytical tools utilized, shedding light on the rationale behind their selection. Likewise, the Electrochemical Characterization Techniques section offers a comprehensive overview of the chosen electrochemical methods, explaining their significance and relevance to the overall research objectives. Finally, the Cell Assembly section provides insights into the process of assembling cells for experimentation. Altogether, this chapter not only lays the groundwork for

the subsequent experimental work but also offers an in-depth understanding of the theory and rationale behind the chosen characterization techniques.

Chapter 4 is a results chapter which focuses on composite TiO_2/GeO_2 inverse opals for lithium-ion battery application. The materials, featuring varied GeO_2 content, are extensively characterized by SEM, TEM, XPS, XRD and Raman, revealing amorphous TiO_2 and GeO_2 at the atomic scale. Small amounts of GeO_2 significantly enhance specific capacity vs Li, and both materials display unique capacity retention between 200 and 900 cycles. This results chapter highlights the intricate balance in tailoring porous materials for optimized capacity and rate behaviour, showcasing the potential of composites integrating intercalation and alloying type materials.

Chapter 5 investigates TiO_2 and carbon composite inverse opals, this chapter delves into the fabrication and electrochemical performance of the nanocomposite electrode for lithium-ion systems. These C/TiO2 inverse opal electrodes exhibit remarkable initial discharge and charge capacities, surpassing theoretical limits for TiO_2 and carbon. Defects formed during calcination contribute to enhanced performance by providing additional charge compensation sites for lithium. The porous structure contributes to outstanding capacity retention and improved coulombic efficiency, outperforming individual carbon and TiO_2 materials.

Chapter 6 is the final results chapter and focuses on utilization of carbon inverse opals in Na-ion and K-ion batteries. Material characterization reveals a macroporous structure composed of disordered carbon with short range graphitic regions. The inverse opals exhibit incredible stability in sodium-ion batteries, while a degree of capacity fading is observed in potassium-ion cells. However, the macroporous structures demonstrate substantial advantages when tested against the

same material without the IO structure. The inverse opal architecture contributes to impressive resistance to volume expansion with SEM images showing the structure remains intact after cycling. These findings show the potential of three dimensional ordered macroporous structures for application in larger alkali-ion batteries.

In the conclusive Chapter 7, the findings from Chapters 4, 5, and 6 are summarised. Additionally, potential avenues for future research are delineated for each project, offering a guide for further investigations and development.

Chapter 2

Introduction

2.1 What Is a Battery and Why Do We Need It?

Today's world is dominated by electronics, where phones and laptops are part of everyday life, yet the issue of fossil fuel usage for energy and greenhouse gas emissions remains difficult to eradicate. With the population growing as fast as it is, the need for renewable energy sources is obvious. Fossil fuels and other non-renewable energy sources have been exploited to the detriment of our planet, it is clear that improvements to scientific and technological solutions are required to avoid an energy crisis. Renewable sources such as solar and wind are not always reliable in terms of sustained power, so for renewable sources to be properly utilized, high performance energy storage systems are needed to accommodate for supply and demand issues.

Electrochemical energy storage systems, such as batteries, can help alleviate our dependence on fossil fuels, with the development of electric vehicles (EVs), and grid-scale energy storage. Rechargeable batteries are not new technologies, yet the current standards are limited in terms of power and life cyclability, so need to be improved if countries want to reach a net zero carbon emission goal.[1] The first rechargeable battery was invented in 1859 by a French physicist, Gaston Planté. It was the lead-acid battery, it comprised of two spirally rolled lead electrodes immersed in sulfuric acid solution.[2] This was followed by the nickel-cadmium battery in 1899 by Waldemar Jungner and then nickel-iron systems by Thomas Edison in 1901.[3, 4] These inventions gave way to modern day batteries such as nickel-metal hydride (NiMH) batteries, which offered higher energy density and were more environmentally friendly than nickel-cadmium. However, the low operating voltage of lead-acid and nickel-based batteries as well as their size and weight, Fig. 2.1, were not suitable for the new

wave of portable electronics such as cordless phones or electric vehicles. The breakthrough in battery technology came in 1991 with Sony's introduction of the lithium-ion battery, lithium is the lightest (M = 6.94 g mol^{-1}) metal[5], with a specific gravity of 0.59 g cm^{-3},[6] and a theoretical capacity of 3860 mAh/g which allows for the possibility of lightweight batteries with high energy density. While lithium battery systems had been researched since the 1950s, safety issues such as thermal runaways halted them from being commercialised.[7, 8] Sony's Li-ion battery used a carbon host structure at the anode instead of lithium metal and by using $LiCoO_2$ as the cathode, intercalation of lithium ions at each electrode removed some of the safety issues and allowed for the development of the technology we have today.

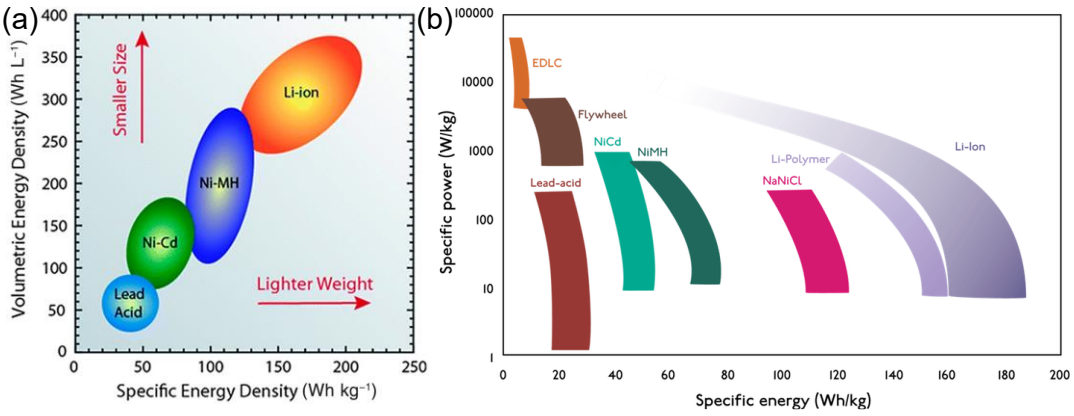

Figure 2.1. (a) Volumetric energy density vs specific energy density graph for various rechargeable batteries.[9] (b) Ragone plot comparing different electrochemical storage devices in terms of specific power and specific energy.[10]

Lithium-ion batteries are a type of rechargeable battery known as secondary batteries. They are comprised of an anode, a cathode, electrolyte, separator, and two current collectors. It operates based on the movement of lithium ions between two electrodes, the negative electrode is known as the anode and the positive electrode is known as the cathode. Both electrode materials are on current collectors which

facilitates the flow of current between the material and the external circuit. Between both electrodes is an organic salt known as the electrolyte, this carries the ions from one electrode to the other. A separator is placed in the electrolyte between the two electrodes, it should be sufficiently porous to allow the electrolyte to permeate it, however its main purpose is to prevent the flow of electrons directly between the anode and the cathode. This forces the electrons to find an alternative route to the opposite electrode, which comes in the form of an external circuit. The charge and discharge process determine the direction of electron flow, during the discharge Li^+ ions are driven electrochemically from the anode to the cathode. During the charge process, energy is supplied to drive the Li^+ ion back to the anode. The schematic for a state-of-the-art typical battery cell can be seen in Fig. 2.2.

The voltage at which the cell operates is determined by factors such as the anode, cathode, and electrolyte compatibility. Figure 2.2 (b) depicts the electrochemical window of the electrolyte and the relationship between electrochemical potentials of both electrodes. The working voltage, open circuit voltage (V_{oc}) is determined by the difference in electrochemical potentials between the anode (μ_A) and cathode (μ_c). However, this voltage is constrained by the electrolyte's "window".[11] The HOMO (highest occupied molecular orbital) and LUMO (lowest unoccupied molecular orbital) states of the electrolyte play a vital role. These states represent the energy levels of the electrons in the molecules of the electrolyte. The "window" of the electrolyte is the energy gap between the HOMO and LUMO states as shown in Fig 2.2 (b). If the anode's electrochemical potential exceeds the LUMO energy level of the electrolyte, it may lead to reduction of the electrolyte, unless mitigated by the solid electrolyte interface (SEI) layer.[12] Similarly, if the cathodes

electrochemical potential falls below the HOMO energy level of the electrolyte, it can lead to oxidation of the electrolyte unless mitigated by an SEI layer.

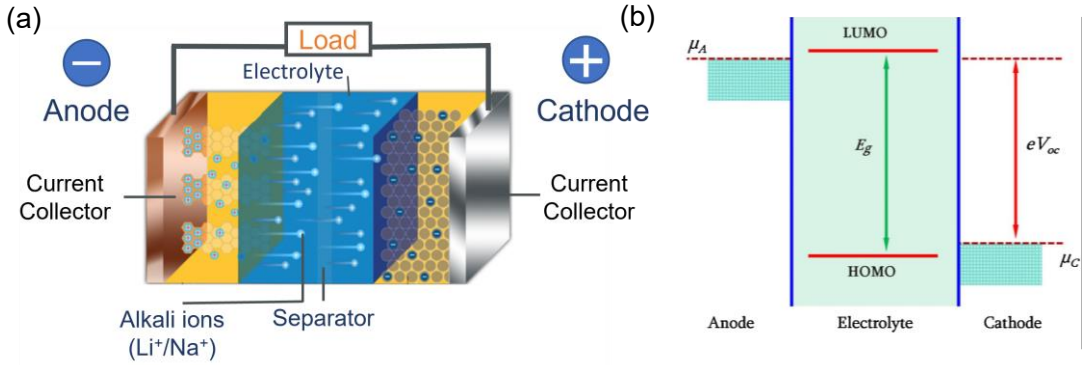

Figure 2.2. (a) Schematic of Li-ion battery consisting of positive electrode (cathode), negative electrode (anode) and electrolyte. The movement of lithium ions towards the cathode is typical of the discharging process. (b) The relative energies of the electrolyte window (Eg) and the correlation between the electrochemical potentials of electrodes and the HOMO or LUMO states of the electrolyte.[13]

Anode Development in Li-ion Batteries

Graphite is the currently used standard anode in most Li-ion batteries, it has a theoretical specific capacity of 372 mAh/g when LiC_6 is formed.[14] Graphite is composed of layers of carbon atoms arranged in a hexagonal lattice structure held together by relatively weak van der Waals forces, this creates interlayer spaces or gaps. Lithium ions are able to intercalate between these layers, Fig. 3.3, this causes the layers to expand slightly, however this expansion is reversible and so allows graphite to possess a good cycle lifetime. It is highly abundant, and the operating voltage (between 0.25 and 0.01V) is higher than that of lithium metal anodes so helps avoid dendrite formation. However, the operating potential still remains too low for organic carbonate-based electrolytes which commonly decompose at 0.8 V vs Li/Li^+.[14-16]

To overcome this issue, Dahn and collaborators[17] demonstrated that lithium ions can be reversibly intercalated into graphite when using electrolytes containing ethylene carbonate (EC) as a co-solvent rather than propylene carbonate (PC). In the case of PC, graphite exfoliation was observed due to the co-intercalation of Li^+ along with its solvation shell. The solvation shell that was present with PC electrolytes seemed to have a disruptive effect on the graphite layers causing them to separate and 'peel' off. However, in the case of EC electrolyte the formation of a solid layer of organic and inorganic decomposition products was observed on the graphite surface during the initial charge, this was known as the solid electrolyte interphase (SEI). This layer prevented direct electronic contact of graphite particles with the electrolyte which kinetically suppressed continuous electrolyte decomposition and inhibited solvent co-intercalation.[18]

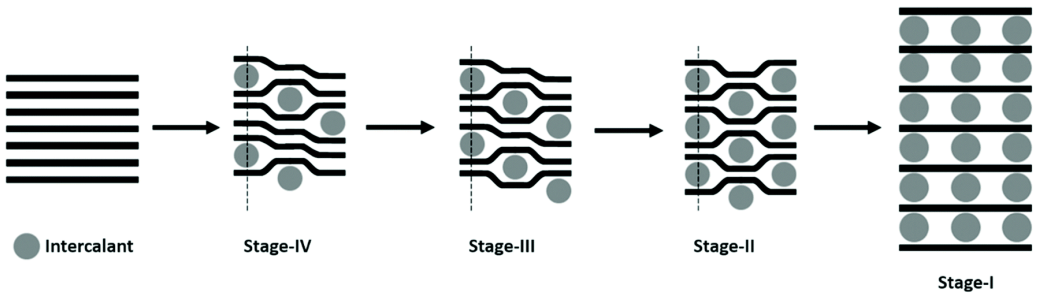

Figure 2.3. States of intercalation of Li in graphite using the Daumas-Hérold model. The grey balls represent lithium ions while the black lines represent the graphite layers.[19]

Cathode Evolution: Materials and Advancements

While graphite has been used almost exclusively as the anode for lithium-ion batteries, the positive electrode comes in a few variations. The cathode is the source of Li ions

and accepts the electrons (e^-) from the anode. Hence, the capacity of lithium-ion batteries is typically limited by the cathode. Investigations were initially centered around insertion mode materials, specifically chalcogenides.[20] TiS_2 garnered considerable amount of interest because of its stable layer structure and electronic conductivity. It was employed as the cathode material in the initial commercial lithium battery, alongside LiAl as the anode.[20] However, this proved to be unsafe due to the incompatibility with the electrolyte used. The voltage range at which TiS_2 operated (around 2.4 – 2.0 V) was not ideal for a non-aqueous carbonate-based electrolyte. As a result, alternative cathode materials such as oxides were studied.[21-24]

The first commercial cathode was $LiCoO_2$ (LCO) produced by Sony Corporation in 1991.[25] It offers good energy density but has some limitations such as thermal instability, it was developed for portable electronics and so has a relatively lower capacity compared to other materials. It has a theoretical capacity of 274 mAh/g when one mole of Li is deintercalated, however the reversible extraction of Li from $Li_{1-x}CoO_2$ is limited to $x = 0.5$, so only 140 mAh/g can be utilized. This limitation arises from the structural and chemical instabilities that occur if more than half a mole of lithium is removed, such as bulk phase transitions, surface degradation and inhomogeneous reactions.[13]

During high voltage operations, bulk phase transformation within $LiCoO_2$ cathodes involves structural changes and phase transitions as lithium ion deintercalated. These transitions, when $x = 0.5$, involve transitions between hexagonal, monoclinic, and hexagonal phases, with the monoclinic phase contributing to structural damage and capacity loss above 4.2 V.[26] Further lithium removal ($x < 0.45$) leads to phase transitions from O3 to H1-3 and then to O1 phase. The H1-3 structure combines features of O1 and O3 structures. As the structure shifts from O3 to H1-3,

internal stress generation and structural damage occur due to the rearrangement of lithium and O-Co-O layers.[27, 28] Surface structure and chemistry evolution also play a role in the degradation $LiCoO_2$.[11] At high voltages, the chemistry evolution of $LiCoO_2$ slows Li transportation and increases surface impedance.[29] With deep lithium deintercalation, cobalt (III) ion is oxidized to cobalt (IV) which is an unstable oxidation state. Higher voltage charging also causes the oxidation of O^{2-}, which results in formation of peroxide and O_2 release from the surface of the electrode.[30, 31] This promotes the irreversible phase transition to Li-poor Co_3O_4[32], which can lead to surface impedance and capacity decay. Additionally, partial oxidation of oxygen reduces the covalent bonding between cobalt and oxygen. The presence of Co^{+4} and peroxide aggravates the decomposition of the electrolyte and Co dissolution can lead to capacity fading.[33, 34] While LCO still dominates the market for small, portable electronics, it is not a practical choice for larger scale electronics.

A number of $LiMO_2$ oxides, where M = 3d transition metals, have been studied to improve safety and capacity since the discovery of LCO.[35] $LiFePO_4$ has emerged as the critical cathode material for applications such as EVs and other large scale applications where safety is a priority. It has a theoretical capacity of 170 mAh/g, a stable voltage plateau at 3.5 V vs Li/Li^+, thermal stability and good cycle stability.[36] $LiMnO_2$ has also been studied as an alternative cathode material, switching out cobalt for manganese offers higher capacity (285 mAh/g), and is also cheaper while being more environmentally friendly.[37, 38]

Mixed metal cathodes have received growing interest owing to their synergetic benefits, specifically $LiNi_{1-x-y}Al_xCo_yO_2$ (NCA)[39] and $LiNi_{1-x-y}Mn_xCo_yO_2$ (NMC)[40, 41]. NCA brought an increase in specific capacity (279 mAh/g) and cyclability compared to LCO while NMC improved lifetime and safety, albeit with a slightly lower energy

density. However, these mixed metal compounds can be altered to make them more Ni-rich which can increase their energy densities.[42] These mixed metal compounds are now widely used in modern battery cell offering a balance between energy density, stability, safety, and cost.

Electrolyte Materials and Their Importance

The electrolyte serves as the medium through which lithium ions shuttle or 'rock' between the cathode and the anode during cycling. It typically consists of a lithium salt dissolved in one or more solvents. Ideally the electrolyte would be an inert component in the battery, one that is stable at both electrode interfaces. However, with the ongoing pursuit of batteries with higher energy densities which involve more oxidizing cathodes and more reducing anode materials, there is a constant need for improved electrolyte stability.

Generally, an electrolyte should be electrochemically stable, i.e. possess a wide potential window encompassing the redox potentials of both electrode materials. Ideally the electrolyte should be a good ionic conductor to facilitate fast ion transport, while being electronically insulating to prevent self-discharging.[15, 43] The most commonly used electrolyte is $LiPF_6$, dissolved in solvents such as ethylene carbonate (EC)[44], dimethyl carbonate (DMC)[45], diethyl carbonate (DEC)[46] or ethyl methyl carbonate (EMC)[47]. These alkyl carbonates were chosen due to their desirable properties such as low toxicity, high dielectric constants, large temperature range, wide electrochemical stability window and allow for the formation of the stabilizing SEI layer.[15, 16, 46, 48] Additives are used in some carbonate electrolytes, such as vinylene

carbonate, which has been shown to reduce irreversible capacity and improve cyclability.[49]

The Separator: Safety Factors and Ion Transport

The separator is positioned between both electrodes, it functions as a barrier that prevents direct electrical contact between the cathode and the anode. This prevents short circuits which can lead to overheating and other safety hazards. Simultaneously, the separator allows for the continuous flow of lithium ions, and so should be sufficiently porous to allow lithium ions to penetrate. Additionally, the separator ensures the electrolyte stays in contact with both electrodes, enabling efficient ion transport.

Materials chosen as separators need to be chemically stable and mechanically robust. They are typically made from microporous polyolefin material with common choices including polyethylene (PE) and polypropylene (PP).[50] The separator's thickness can vary based on specific battery designs and applications, with thicker separators offering enhanced mechanical stability and thinner ones improving ion transport.

2.2 Inverse Opal Materials in Electrochemical Energy Storage Systems

In the pursuit of keeping pace with the rapid advancements in technology and electric vehicles, there has been a growing focus on nanostructuring as a means to

continuously enhance existing materials.[51-55] The majority of commercial batteries employ slurry-based electrodes, which consist of randomly arranged active material particles, binders and conductive additives. These components are densely packed, resulting in limited control over their structural characteristics.[56] To achieve better structural control beyond what conventional slurry-based electrodes provide, adopting ordered macroporous structures presents a promising option for enhancing both rate capability and cyclability, addressing limitations typically attributed to structural properties.

Inverted opal structures or inverse opals (IOs) are 3 dimensionally ordered macroporous structures (3DOM), which are generally formed by colloidal self-assembly. The structures arising from IOs consist of interconnected close-packed spherical spaces or holes of sub-micrometer diameters that are surrounded by nanometer thick walls, resembling honeycomb. This structure provides a continuous network of electrode material, a large interfacial area and open access for electrolyte and in principle, a limited material thickness for faster lithium insertion.[57] The general method of fabrication is outlined in Fig. 2.4(a). This method of fabrication starts with an initial sacrificial template, crafted using self-assembling colloidal crystals such as polystyrene spheres. The sphere's size and arrangement dictate the eventual pore size and periodicity within the inverse opal. There are various methods that have been established for the assembly of monodisperse spheres into ordered or semi-ordered lattices. The types of methods developed are differing in terms of forces used with the intention of impacting their assembly, including gravitational forces, surface tension or capillary forces, or else electric or magnetic fields.[58-60]

In the process of infiltration, the pores of the opal structure are filled, typically through capillary action, with a fluid, which can be in liquid or vapor form. This fluid

is then solidified through physical or chemical means, depending on the desired material and the specific fabrication method. For instance, if a monomeric precursor is used during infiltration, it may require chemical conversion through processes like heating or reactive deposition to form the target polymer or inorganic solid. The inversion process is determined by the initial opal template and can be either calcination[61], chemical etching[62] or solvent extraction[63].

Different variations of IOs have been researched previously for use as electrodes in batteries.[64-68] As mentioned, carbon leads the way for anode materials in most commercial LIBs. Although carbon boasts excellent electrical conductivity, its rate capabilities are known to be a limiting factor. The IO structure has been studied as an appealing architectural solution to enhance carbon's overall performance, primarily owing to its advantageous mass transport properties and facilitation of electrolyte infiltration. Carbon IOs synthesized from resorcinol-formaldehyde using a sol-gel method by Lee et al[69] showed significantly enhanced rate performance compared to non-templated carbon electrodes.

V_2O_5 inverse opal networks exhibit excellent capacity and cycling compared to non-templated V_2O_5 films.[64] These batteries show enhanced capacity retention due to improved mechanical stability and electrical contact with current collectors. Li^+ insertion occurs at different potentials compared to the non-templated electrode, as seen in Fig. 2.4(c) with phase changes more obvious. This is correlated with the IO network's exposure to the electrolyte. During the Li-uptake, V_2O_5 goes through several phase transitions resulting in the formation of α-, ε-, δ-, γ-, and ω-phase. The α-phase is observed at $x < 0.1$ in $Li_xV_2O_5$, ε-phase exists in the range of $0.35 < x < 0.7$, while the δ-phase appears at $0.9 < x < 1.0$ for $Li_xV_2O_5$. An irreversible transformation of δ-phase into γ-phase is observed when x is over 1. The γ-phase can

cycle reversibly in the range of $0 \leq x \leq 2.0$, preserving its γ-type structure. However, the irreversible formation of the ω-phase with a rocksalt-type structure occurs after the third lithium insertion into the V_2O_5 structure.[70] The oxidation state of vanadium in these electrodes during lithium uptake ranges from +5 in the pristine α-phase to a mixture of +5 and +4 oxidation states in the lithiated phases (ε, δ, γ, and ω). The V_2O_5 IO material demonstrated excellent accommodation to volume expansion and when prepared with excess electrolyte, showed impressive specific capacities and retention as seen in Fig 2.4 (d) & (e).

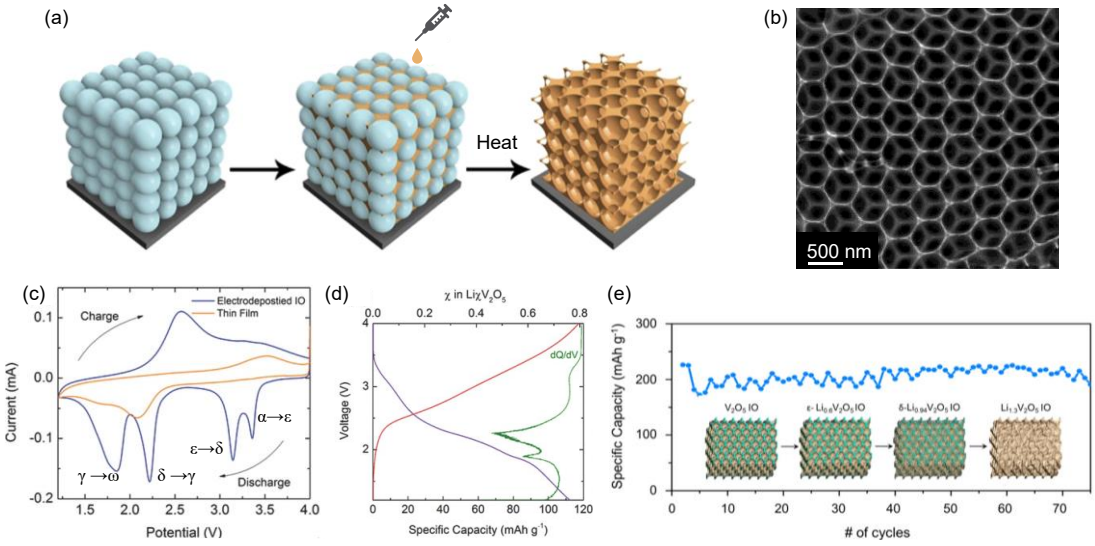

Figure 2.4. (a) Schematic detailing preparation of inverse opals. (b) SEM image of carbon IOs showing fcc sphere packing arrangement. (c) Cyclic voltammograms of V_2O_5 IO vs non templated V_2O_5 material. (d) Typical galvanostatic curves from V_2O_5 IO. (e) Specific capacity as a function of cycle number for V_2O_5 IO, the schematic indicates the phase changes that occur during discharge.[64, 71]

The macroporosity of the IO structure has also been suggested as a means to reduce structural stresses in materials that undergo significant volume changes during the insertion and removal of lithium ions. Additionally, the interconnectivity of the IOs offer the benefit of shorter diffusion lengths for lithium ions and can improve charge transfer rates because of a larger surface area. However, it's worth noting that

despite the relatively high specific energies associated with IO electrodes, their inherently high porosity (26% material, 74% porous) results in a lower volumetric energy density when compared to other electrode structures. Some efforts to enhance the volumetric energy density of IO electrodes have focused on applying additional material coatings onto the IO scaffold.[69, 72, 73]

2.3 Why Use Porosity in Electrochemical Systems?

Porous materials are widely used for applications such as chemical sensors, catalysis, energy conversion and biomedicine.[74-76] In recent years there has been a significant surge in interest in harnessing porous materials for energy storage applications.[77-80] Inverse opals represent a type of macroporous structures, macroporous meaning with pore sizes larger than 50 nm. However, a wide array of porous materials exists, each categorized based on either pore sizes (micropores < 2 nm, mesopores 2 - 50 nm, macroporous > 50 nm), morphologies and methods of synthesis. These materials have garnered significant attention due to their many advantages in electrochemical energy storage systems, including[81]:

- Providing more electrolyte access to the electrode surface.
- Facilitating faster charge transfer across the electrode/electrolyte interface.
- Reducing the diffusion distances for ions.
- Allowing for increased utilization of active materials, therefore elevating specific capacities.

- Providing bicontinuous transport pathways through the active phase (walls) and the electrolyte phase (pores).
- Constricting the growth of active materials during cycling within the void spaces.
- In certain instances, diminishing or eliminating the need for binders to secure the active material in place.

For non-storage applications, porous materials are generally attractive due to their high surface area, large accessible space, low density, various chemical compositions, and their tunable porosity which can facilitate light harvesting, electron and ion transport and drug delivery.

There are two main strategies for synthesizing porous materials, soft templating, and hard templating. These distinct approaches employ different techniques to guide the formation of porous structures, each offering unique advantages and applications. Soft templating typically utilizes surfactants as structure–directing agents and it commonly used for the synthesis of materials with dual mesoporous structures.[82, 83] The choice of surfactants, solvents and synthesis conditions enable control over the resulting pore structures, which can be ordered or disordered and exhibit different symmetries. These processes are typically conducted in aqueous environments but can be conducted in non-aqueous settings. They rely on the self-assembly of inorganic precursors in the presence of amphiphilic molecules known as surfactants, or around organized surfactant assemblies. This process results in the formation of mesoporous materials. The mesoporous material is ultimately obtained by removing the surfactant phase through solvent extraction or calcination.

Soft templating approaches have been applied to produce various mesoporous materials suitable for LIB electrodes, among other applications. By altering the surfactant, it becomes feasible to introduce flexibility in the synthesis conditions, mesopore dimensions, and the selection of precursor materials. The three major types of surfactants are cationic, anionic and non-ionic surfactants, characterized based on the charge (or lack thereof) carried by their head group in a neutral pH solution.[84] While cationic surfactants typically comprise of minimum one amine functional group as their hydrophilic head with one or more hydrophobic tails[85], there is more variation in anionic surfactants. These can include sulphates[86], sulfonates[87], carboxylates[88] and phosphates which are attached to a hydrophobic tail. Ionic surfactants primarily interact with precursors through electrostatic interactions. On the other hand, non-ionic surfactants typically function through van der Waals interactions and hydrogen bonding.

Hard templating is another approach which can be used when the temperature needed for crystallization is higher than the temperature used for template removal. If the template is removed before crystallization, the pore structure may collapse, so hard templates can be utilized instead. The materials used are typically preformed porous solids such as anodic aluminium oxide (AAO) membranes[89] and colloidal particles (e.g. silica or polymer based)[75, 90]. Two main methodologies involving colloidal particles in the hard templating approach include nanocasting and colloidal crystal templating (CCT). CCT, described in section 2.2, is a method used for fabricating inverse opals, typically used for synthesis of large mesopores or macropores. Figure 2.5 (a-c) show a report on the use of CCT in conjunction with electroplating, where polystyrene (PS) spheres were templated into the voids of a photoresist substrate.[91] The photoresist substrate had patterned holes of 1 cm in diameter while the diameter

of the PS spheres were 1 μm. The PS spheres self-assembled into an ordered lattice within the holes of the substrate before being infilled via electrodeposition with nickel and tin precursors. After solvent extraction of the PS spheres, cylindrical Ni-Sn alloys with an inverse opal structure were obtained. Electrochemical analysis showed impressive charge capacities of 747 mAh/g with a coulombic efficiency of 84 % for the first cycle. By controlling the state of charge in the Ni-Sn alloy, it was indicated that the macroporous structure was maintained during cycling, showing excellent cycle stability and a coulombic efficiency of over 99% for 200 cycles.

Alternatively, nanocasting is generally used for the formation of mesoporous materials that require high temperature treatment. The nanocasting process involves infiltrating thermally stable nanoporous molds, such as mesoporous silica[92] or mesoporous carbon[93], with the precursor material for the desired electrode. In 2008, Lim et al[94] synthesized $LiFePO_4$ nanowires and hollow $LiFePO_4$ by infilling SBA-15 and KIT-6 hard templates, respectively. Mesopores were obtained after forming a $SiO_2/LiFePO_4$ composite at 300 °C and removing the template, followed by annealing at 700 °C. Electrochemical cycling data showed the hollow cathodes displayed higher discharge capacities than the nanowire cathodes, attributed to enhanced electrolyte contact. Nevertheless, both nanostructured materials demonstrated higher power density at increased current densities than reported data for bulk $LiFePO_4$.

The use of anodic aluminium oxide membranes is another hard templating technique, commonly used for the synthesis of nanotubes[95, 96], which have been investigated as LIB electrodes[97, 98]. Figure 2.5 (d) and (e) shows SEM images of titania nanotubes with mesoporous walls that were grown within AAO membranes. Using a titanium alkoxide precursor and a co-polymer as a directing agent, hollow tubes were formed due to the attraction between the gel precursor and the hydrophilic alumina walls.[82]

This caused the gel to shrink perpendicular to the pore channels. Following the dissolution of alumina membranes, well-ordered, uniform nanotube arrays were obtained through a supercritical drying process. The hierarchical pore structure facilitated electrolyte distribution through the channels and mesopores as described in Fig 2.5 (f). This provided pathways for both electrons and lithium ions, leading to impressive high-rate performance (150 mAh/g at 240 C).

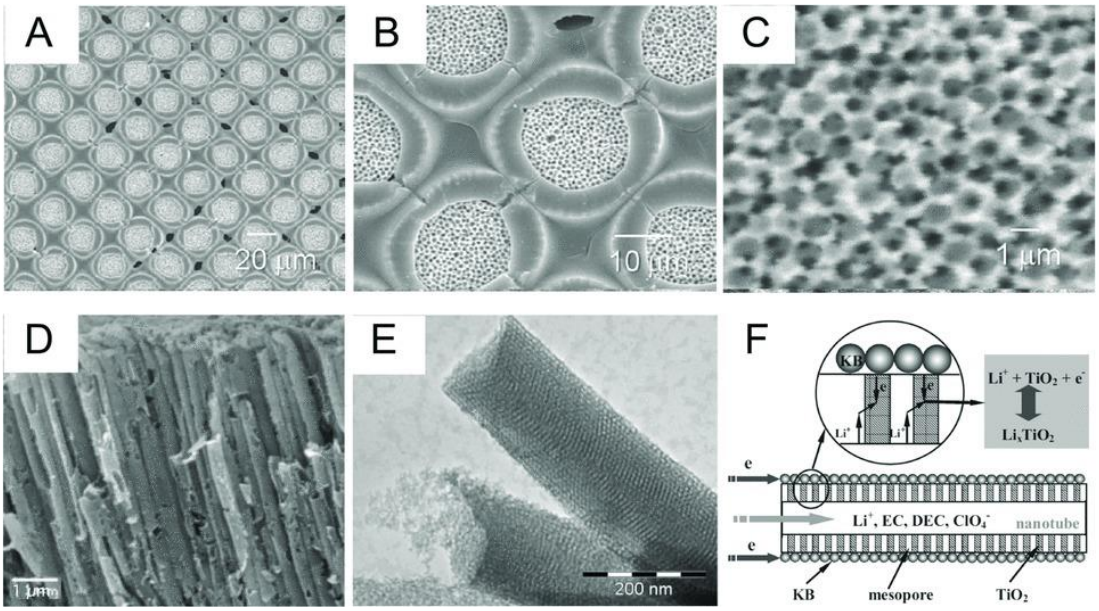

Figure 2.5. Electrode structures with hierarchical porosity. (A)–(C) SEM images of patterned 3DOM Sn-Ni alloy films at various magnifications, showing the lithographic patterns and the colloidal-crystal-templated macropores.[91] (D)–(F) Mesoporous titania nanotubes templated in an AAO membrane.[82] (D) SEM image of nanotube array. (E) TEM image showing the hexagonally ordered mesopore structure in the walls of the hollow nanotubes. (F) Schematic diagram of the transport path of lithium ions and electrons in the mesoporous titania nanotubes.

It has been demonstrated that porous materials possess significant promise for enhancing and advancing energy storage technologies. With the continued growth of EVs and hybrid electric vehicles (HEVs), the demand for electrodes capable of high-rate performance is rapidly increasing. The advantage of tunable porosity, enabling bicontinous paths for charge transport through the pores and walls of porous materials

make them a promising option for such applications. However, the loss of volumetric energy density is a crucial factor to consider, especially for applications where space constraints are more pronounced compared to transport applications. Nevertheless, research into porous materials remains a continuous effort, with various synthesis routes continuously improving current materials and investigating novel composites for integration into electrochemical energy systems.

2.4 TiO_2 -based Materials

Among the numerous materials studied as potential electrodes, titanium dioxide (TiO_2) has been researched extensively in recent years.[68, 99-101] TiO_2 is a semiconducting metal oxide with large application potential in many fields, such as photocatalysis, sensors, solar cells as well as energy storage systems. Titanium oxides are promising for use as an anode as they have a higher working potential than graphite and stable voltage insertion plateau. TiO_2 has been investigated at length as an intercalation mode material, showing little structural strain during the lithiation/delithiation process.[102-104] There are three main polymorphs of TiO_2, rutile, anatase, and brookite, all of which have been researched as potential electrodes[105-108], as well as metastable phases such as TiO_2(B). The following reaction equation explains the reversible lithium-ion insertion and removal from TiO_2.

$$xLi^+ + TiO_2 + xe^- \leftrightarrow Li_xTiO_2$$

where *x* is dependent on the polymorph of TiO_2, particle size, and morphology. Rutile is the thermodynamically stable crystal form, of which TiO_2 occurs naturally most often. It is a tetragonal crystal ($P4_2/mnm$) and the Li^+ insertion is anisotropic along the

tetragonal *c* direction. The diffusion is preferential along the *c* direction owing to the diffusion co-efficient in the *ab* plane being nine orders of magnitude smaller than that in the *c* direction.[109] The capacity for Li^+ increases in rutile TiO_2 with increasing temperature, leading to the implication that Li kinetics effects rutile TiO_2 electrochemical performance.[110, 111] In bulk form, rutile TiO_2 possesses a low theoretical capacity of 33.5 mAh/g. The anatase polymorph is also a tetragonal crystal with space group $I4_1/amd$ and in bulk form possesses a higher theoretical capacity than rutile with 167 mAh/g. Brookite is the orthorhombic form of TiO_2 and is a high-pressure form. It is rarer than both anatase and rutile and has a larger cell volume (8 TiO_2 groups in one unit cell). Brookite belongs to the point group *2/m* and the space group *Pcab.*[112, 113]

Although there are slight variations in properties among different TiO_2 polymorphs, TiO_2 generally exhibits a lower capacity (e.g., around 170 mAh/g for anatase) at a relatively higher potential than graphite at approximately 1.7 V vs. Li^+/Li. Numerous prior studies have shown that amorphous TiO_2 materials, characterized by their disordered atomic structures, can offer an increased number of active sites and faster ion diffusion pathways in comparison to crystalline phases.[114-116] This characteristic can result in greater capacity and improved rate performance for the storage of alkali metal ions. Moreover, its potential as an anode material becomes more evident when considering its ease of structural tailoring, minimal volume expansion during lithiation, good chemical and physical stability, and the absence of lithium plating issues.[51] These characteristics make it well-suited for charging and discharging at high current rates over extended cycles, a capability that is often challenging for other types of anodes. Nevertheless, TiO_2 does face significant challenges related to

its low electronic and ionic conductivities, which can be addressed through nanostructure engineering.[117]

Chen et al[118] constructed hierarchical spheres from anatase TiO_2 with nearly 100 % exposed (001) facets which are more reactive.[119] Usually TiO_2 single crystals with a high percentage of exposed (001) facets have low surface areas due to their relatively large thickness in the [001] direction. However, Chen et al developed ultrathin TiO_2 nanosheets with nearly 100 % exposed (001) facets, self-organized into hierarchical spheres. These hierarchical spheres exhibited a 3D nanoporous structure with a high specific surface area of about 170 m^2/g. Their distinctive structure (shown in Fig. 2.6 (a)), along with short transport paths within the nanosheets, was evaluated for its capability to reversibly insert and release lithium, making them ideal for high-power-density electrochemical energy storage in batteries. The results demonstrated high Coulombic efficiency for lithium extraction, excellent capacity retention, and superior rate performance.

Another variation of nanostructures includes nanowires or nanotubes. Particulate nanostructured materials tend to aggregate during cycling, which affects conduction and leads to connectivity issues. Additionally, long-range ion diffusion paths are still needed due to auxiliary additives like polymer binders and conductive agents. Tang et al[106] constructed a robust three-dimensional network with excellent cycling properties to overcome these issues. This was achieved by assembling continuous one-dimensional (1D) TiO_2(B) nanotubes, offering rapid ion/electron transport pathways, enhanced electrode-electrolyte contact, and shorter lithium-ion diffusion paths. The study employed a hydrothermal technique to grow elongated titanate nanotubes, as shown in Fig. 2.6(b). The electrode showed impressive rate capabilities when tested against a Li counter electrode, maintaining high capacity even

at ultra-high rates of 25 C, thanks to its lower resistance and faster lithium insertion kinetics when compared to shorter nanotubes.

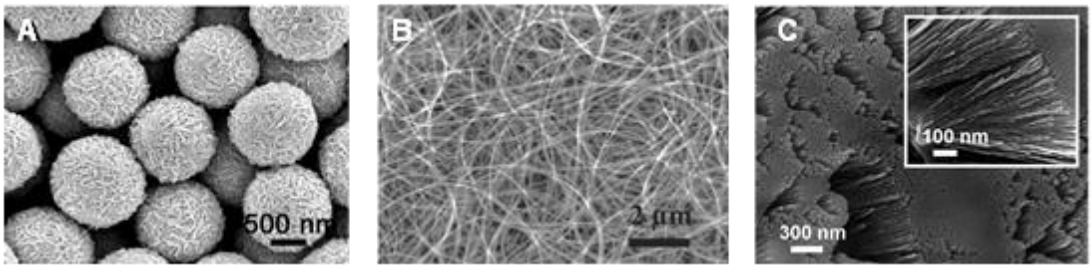

Figure 2.6. SEM image of (a) hierarchical spheres of TiO_2 nanosheets[118], (b) TiO_2-based nanotubular material[106], and (c) amorphous nanostructured TiO_2 film deposited at 80° incidence angle[116].

Nanostructuring amorphous TiO_2 has also been shown to improve lithium ion transfer kinetics. Lin et al[116] fabricated structured amorphous TiO_2 with nanopores directly onto a Cu current collector via reactive ballistic deposition (RBD). The films were deposited at normal incidence (dense) and at angles of 60°, 70°, and 80° (shown in Fig. 2.6 (c)) vs normal (nanoporous). The porous films significantly outperform dense (0°) bulk films in terms of charge/discharge rates and reversible capacities. The films deposited at 80° demonstrated high reversibility (285 mAh/g at 0.2 C), impressive rate capability (approximately 200 mAh/g at 5 C), and excellent cycling stability. These improved electrochemical properties of the RBD electrodes were attributed to their porous structure and substantial surface area.

Previously in our research group, rutile TiO_2 inverse opals were synthesized using a hard templating approach.[68] Material characterization showed pure rutile TiO_2 in the form of highly porous IO network with pore sizes of ~400 nm. Galvanostatic testing, at 75 mA/g current density, revealed impressive capacity retention of ~83 % from the 100^{th} to the 1000^{th} cycle. Moreover, SEM images shown in Fig. 2.7 present

the sustained IO structure after 100, 1000, and 5000 cycles, showcasing its resilience to volume expansion during fast charging. The average capacity at this fast current density of 450 mA/g, shown in Fig. 2.7 (e-g), remained at ~ 95 mAh/g, proving TiO_2 IOs as a highly promising anode material for long-cycle Li-ion batteries.

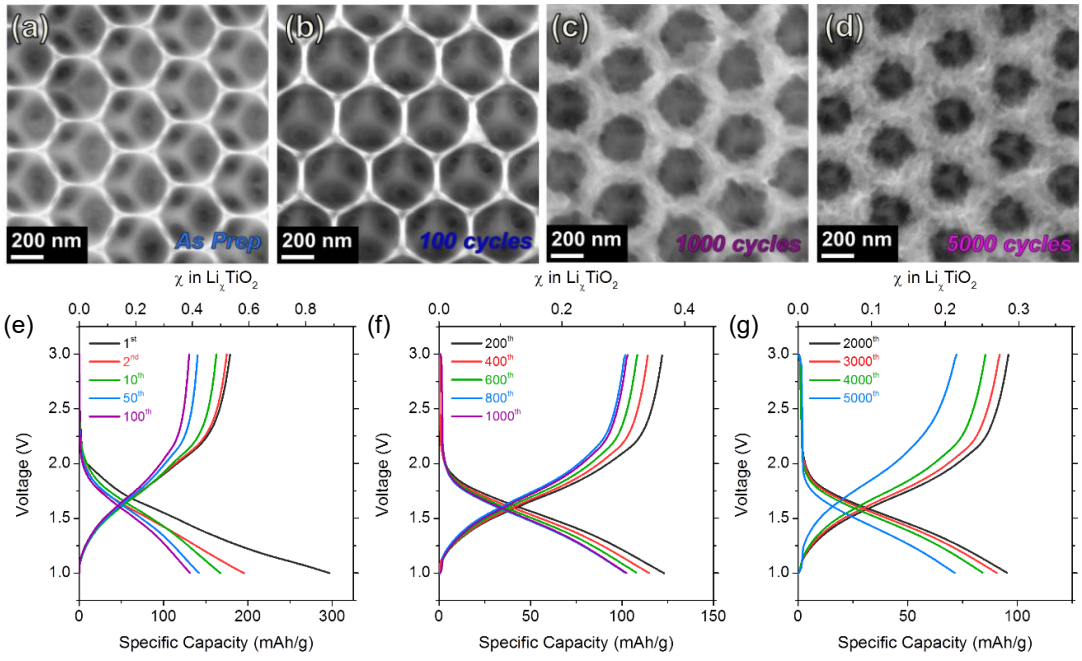

Figure 2.7. SEM images of rutile TiO_2 IO (a) before cycling, (b) after 100 cycles, (c) after 1000 cycles, and (d) after 5000 cycles demonstrating structural stability. GCPLs of TiO_2 inverse opals at 450 mA/g. (e) 1^{st} – 100^{th} cycle, (f) 200^{th} – 1000^{th} cycle, and (g) 2000^{th} – 5000^{th} cycle.[68]

TiO_2 has emerged as a promising candidate for the application of energy storage systems. While its different polymorphs, including rutile, anatase, and brookite, have varying properties, TiO_2 stands out as an anode material due to its low structural strain during the lithiation/delithiation process. Amorphous TiO_2 offers enhanced ion diffusion pathways and increased number of active sites, resulting in improved specific capacities. Moreover, the ability to tailor TiO_2's structure, coupled with its stability, makes it an excellent choice for high-power electrochemical energy

storage. Various nanostructured TiO_2 morphologies, hierarchical spheres, nanotubes, nanoporous films, and inverse opals, have shown significant promise in overcoming the material's intrinsic conductivity limitations and further enhancing its electrochemical performance. These advancements open new avenues for the development of high-performance energy storage devices using TiO_2 materials.

2.5 Carbon Materials and Their Versatility in Li-ion Batteries

Without a doubt, the intrinsic structures of electrode materials play a significant role in improving battery performance. Carbon materials serve as essential components that significantly influence the performance and efficiency of lithium-ion batteries, be it in the electrolyte or electrode. Graphite, a crystalline form of carbon is the common choice for anode material currently, however various other carbonaceous materials, such as carbon nanotubes, porous carbon, and graphene, have emerged as promising candidates for enhancing conductivity and capacity of electrodes. The unique structural and electronic properties of these carbon materials contribute to improved energy storage, faster charging rates and longer life cyclability, addressing key challenges in the quest for improved and more sustainable battery technologies.

Carbon materials can utilize different storage mechanisms when used as electrodes in batteries, such as faradaic and non-faradaic processes.[120] Faradaic processes involve charge transfer reactions that result in the storage of electrical energy within the electrode. In the context of carbon materials, this refers to the reversible intercalation/deintercalation of lithium during cycling. Faradaic processes are typically diffusion controlled and lead to changes in the oxidation state of the

carbon material, which results in the storage or release of charge. On the other hand, non-faradaic processes involve charge storage mechanisms that do not involve significant chemical changes within the electrode.[121, 122] These processes rely on surface reactions such as physical adsorption or desorption of ions on the surface of the electrode material. This occurs without substantial alteration to the structure or chemical composition of the electrode material. Faradaic processes often demonstrate higher energy density because they involve storing a greater amount of charge through chemical reactions. In contrast, non-Faradaic processes provide advantages like faster charge-discharge rates and longer cycle life due to their reversible nature.[123]

Carbon nanotubes (CNTs) appear as hopeful candidates for use in batteries, consisting of cylindrical structures composed of carbon atoms arranged in a hexagonal lattice.[124] These tubes can have a single layer of carbon atoms, known as single-walled carbon nanotubes (SWCNTs), or multiple layers, known as multi-walled CNTs (MWCNTs). One key feature of CNTs is their excellent electrical conductivity, which arises from the unique arrangement of carbon atoms, they also possess impressive mechanical strength and flexibility which favors them for the application of wearable electronics.[125] Figure 2.8 (b) shows an SEM image of SWCNTs while Fig. 2.8 (c) illustrates the flexibility of these materials by wrapping the material around a curved surface. SWCNTs can exhibit reversible capacities ranging from 300 to 600 mAh/g which surpasses the capacity of graphite (380 mAh/g).[126, 127] Additionally, subjecting SWCNTs to mechanical and chemical treatments can elevate their reversible capacities to as much as 1000 mAh/g.[128]

However, some challenges remain for CNTs, such as the absences of voltage plateaus which poses a challenge for their use in most electronic devices as these often require a stable voltage source. This means that the observed increase in specific

capacity does not necessarily translate to a corresponding increase in specific energy. Therefore, CNTs adorned with metal nanoparticles and composite anodes composed of CNTs and other materials have been studied which can display more stable profiles compared to CNTs alone.

In 2009 a study was done on coaxial MnO_2/CNTs to enhance lithium storage properties.[129] The nanotube structures were prepared by fabricating MnO_2 nanotubes inside AAO templates, followed by the growth of CNTs. These hybrid structures offered a combination of high porosity and low internal resistance, which enhances electronic conductivity and lithium storage capacity. The electrochemical performance of MnO_2/CNT coaxial nanotubes as cathodes for LIBs was evaluated, shown in Fig. 2.8 (d) and (e). A first discharge capacity of 2170 mAh/g and a reversible capacity of approximately 500 mAh/g after 15 cycles was observed, suggesting improved structural stability compared to MnO_2 nanotubes alone. This improved reversible capacity and cyclic stability was attributed to the two different lithium storage mechanisms which enhanced total capacity by facilitating fast ion diffusion through the MnO_2 shell and enabling efficient electron transport via the highly conductive CNT core.

Yang et al[126] reported on the modification of CNTs to improve their electrochemical performance as electrodes in LIBs. CNTs synthesized using conventional methods have limitations, such as low initial efficiency and high voltage hysteresis.

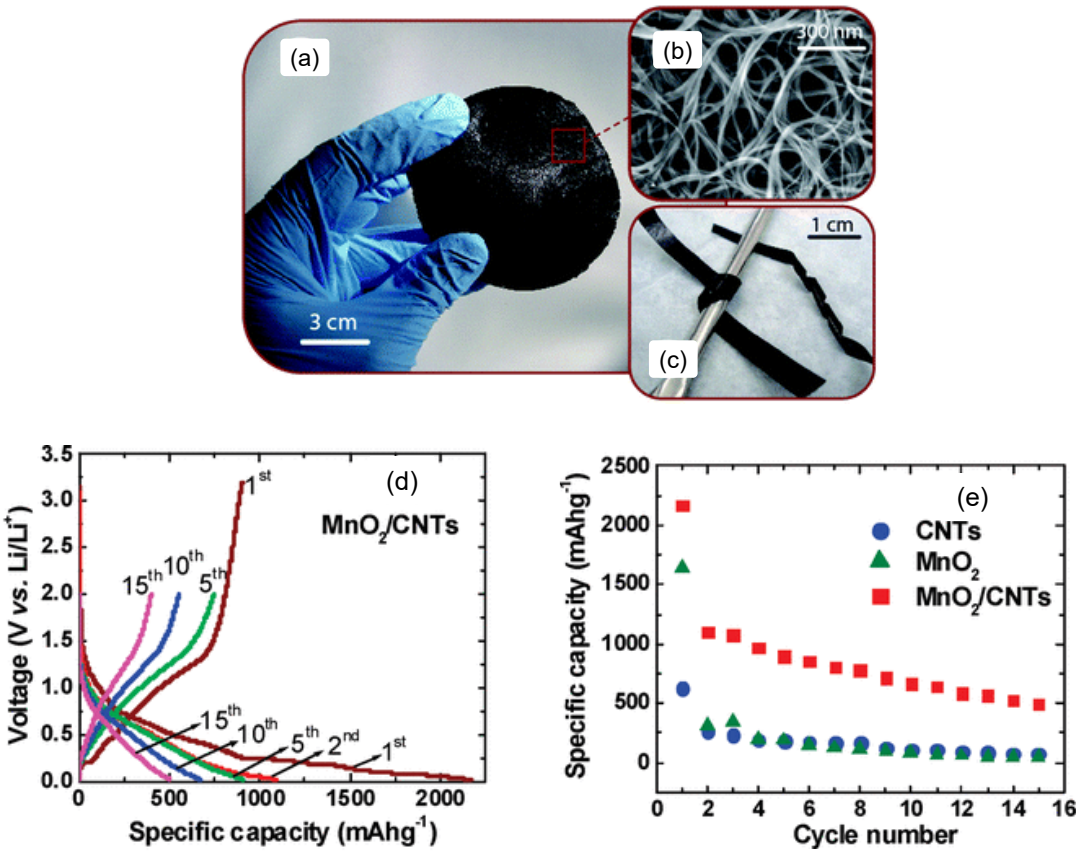

Figure 2.8. (a) Photograph of a free standing single walled carbon nanotube. (b) SEM of the SWCNT. (c) Photograph of the SWCNT wrapped around a curved surface to highlight flexible mechanical properties.[9] Charge and discharge curves showing (d) MnO_2/CNT nanotube electrodes cycled at a rate of 50 mA/g between 3.2 and 0.02 V vs Li/Li^+. (e) Variation in discharge capacity vs cycle number for MnO_2/CNT nanotubes, MnO_2 nanotubes, and carbon nanotubes.[129]

Various techniques, including chemical etching and ball milling, have been employed to address these issues, but they introduce structural defects.[127] This study introduced a new type of short CNTs with improved electrochemical properties, comparing them electrochemically with long CNTs produced by chemical vapor deposition (CVD) to understand the relationship between CNT structure and electrochemical performance. The results revealed that the shorter SNTs exhibited superior electrochemical performance, with nearly double the reversible capacity of the longer CNTs at various current densities. This improved performance was attributed to the lower surface resistance, better kinetic properties, and reduced

hindrance during lithium extraction in the shorter CNTs. Carbon materials, such as carbon blacks, graphene or CNTs, have been widely used as conductive additives owing to their high electrical conductivity and chemical inertness.[130-132] The addition of conductive additives to electrode materials has been shown to reduce the internal resistance, improving capacity and cyclability. Most conventional slurry-based electrodes contain a carbon-based conductive additive and binders along with the active materials in a paste-like mixture. Binders are polymers that are utilized to hold the electrode materials together and adhere them to the current collector. Common binders include polyvinylidene fluoride (PVDF) and carboxymethyl cellulose (CMC).[133] While slurry-based electrodes play an important role commercially, serving as medium for incorporating all the materials required and are relatively easy to fabricate, they also have many drawbacks. The high content of inactive materials (such as the binders and additives) as well as an inverse correlation between tortuosity and porosity, can lead to reduced power density and energy density.[134]

Exploring innovative methods for engineering electrode architectures has been a focus to tackle the issues with slurry-based electrodes. In this context, porous, free-standing carbons have garnered attention as a potential solution to eliminate the need for additives and binders. However, not all types of carbon are viable for use as electrodes. For example, activated carbon faces limitations such as low conductivity and low specific capacity while hard carbon suffers from low initial Coulombic efficiency and voltage hysteresis.[135, 136] The production of porous carbon with tunable pore size, high surface area and bicontinous transport paths appear promising in addressing concerns.[69, 137] Studies have reported carbon inverse opals fabrication using a facile method, and other carbon IOs have shown impressive electrochemical properties.[61, 138] To further enhance electrochemical performances and integrate novel

electrode material, researchers have studied porous carbon composites with other active materials. This allows for improved performance through enhanced electronic conductivity, high power capabilities, and increased electrode/electrolyte interface for superior energy storage and conversion.[139, 140] There are three main approaches for porous carbon composites, firstly creating porous carbon substrates with the desired pore structure and morphology and subsequently incorporating active materials or their precursors through nanocasting or grafting techniques; second approach involves generating porous active materials and applying a thin carbon layer to their surfaces; and third approach is forming active materials or their precursors in situ within porous carbon structures.

Previously, our research group investigated a mixed Ni, Mn, Co oxide inverse opal material and compared the material with a carbon coated version.[141] SEM images are shown in Fig. 2.9 (a) and (b) depicting the inverse opal structure with and without the carbon coating. Electrochemical tests are shown in Fig. 2.9 (c) – (e), and although there is not a significant difference in capacity between the Ni-Mn-Co-O IO samples with or without carbon coating, the carbon coating influences the electrochemical response. The charge and discharge profiles exhibit variations, with the C-coated IO showing a long flat plateau during the first charge cycle. The coulombic efficiency for the C-coated Ni-Mn-Co-O IO starts low but improves after the 10th cycle, remaining above 95 %. Carbon-coated Ni-Mn-Co-O IOs showed high-rate performance and capacity retention even after 50 cycles, outperforming the theoretical capacity. Paired with a V_2O_5 IO cathode, they formed a Li-ion full cell with specific capacities surpassing previous reports, improving round trip energy efficiency per cycle.

Lee et al[69] synthesized three-dimensional ordered macroporous (3DOM) monoliths of hard carbon and then coated tin oxide nanoparticles on to the surface.

The 3DOM carbon was also tested against non-templated carbon and spherical carbon electrodes mixed with binders, the 3DOM outperformed both with significantly higher discharge capacities at specific currents exceeding 12 mA/g and good cycling stability.

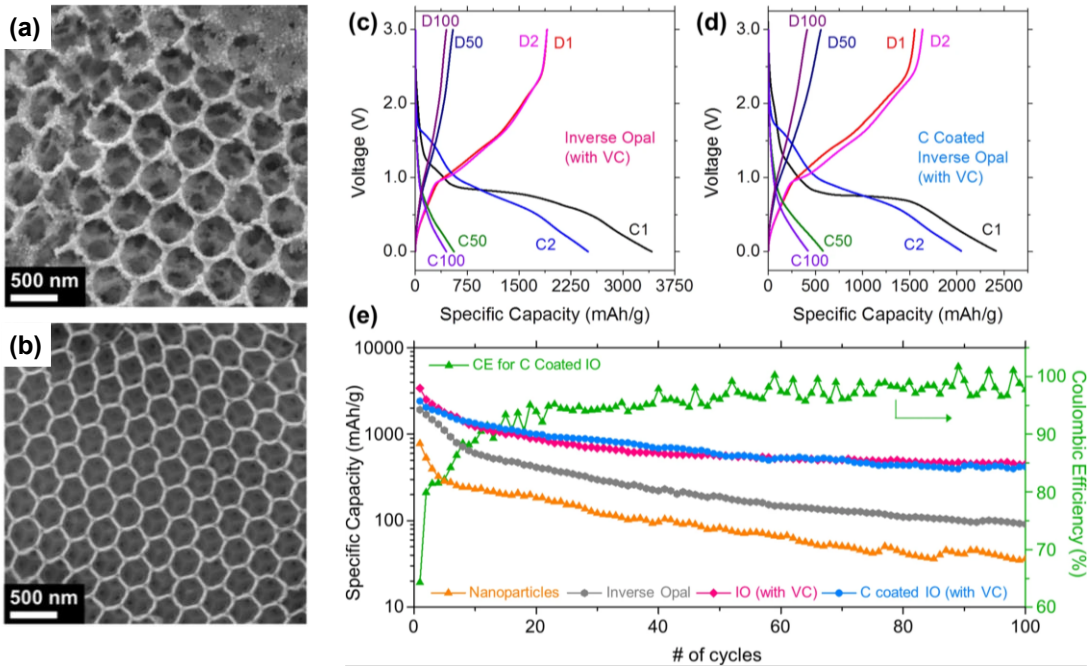

Figure 2.9. SEM images of (a) standard Ni-Mn-Co-O IO and (b) carbon coated Ni-Mn-Co-O IO. GCPLs for the 1st, 2nd, 50th, and 100th cycle for (c) Ni-Mn-Co-O IO and (d) carbon coated Ni-Mn-Co-O IO with electrolyte additive. (e) Comparison of specific capacities achieved for different Ni-Mn-Co-O variations with the CE recorded for the carbon coated Ni-Mn-Co-O IO.[141]

SnO_2 nanoparticles were coated onto the carbon inverse opal and initial discharge capacity was higher than 3DOM carbon at the specific current of 40 mA/g, however the SnO_2 coated samples experienced greater capacity fading and by the 30th cycle the capacity was the same as pure carbon. On the other hand, both samples were tested under various specific currents and the SnO_2 coated 3DOM carbon displayed higher capacities than 3DOM carbon at each rate, implying enhanced rate performance. This study indicates the potential for high-rate performance using the inverse opal geometry in carbon monoliths, which can be advantageous for battery applications. Clearly the choice of electrode material significantly influences LIB

performance, with various carbon–based materials holding promise for enhancement. Nanostructures such as nanotubes or nanowires boast unique properties such as electrical conductivity and tensile strength outperforming graphite in specific capacity, however CNTs face challenges such as voltage instability. Porous carbon and its composites have been shown to improve rate performance and capacity retention, with facile synthesis and ease of handling. Although graphite has been the primary choice for anode material, it is evident that alternative carbon-based materials hold great potential for battery research.

2.6 Composite Materials in Battery Electrodes

Composite materials, which combine multiple components with distinct properties, have been studied to harness synergistic benefits, addressing various challenges in energy storage.[142-144] This can enhance overall performance of LIBs, including higher energy density, improved rate capabilities and lengthen cycle life. Additionally, composites offer opportunities to replace or reduce the reliance on critical materials.[145] By making composites we can improve the conductivity of some materials, or enhance physical or chemical stability. Various oxide composites have been researched such as vanadium oxide composites with graphene oxide. Zhao et al[146] showed that by incorporating reduced graphene oxide (rGO) into nanostructured vanadium oxide, a higher specific capacity was achieved as well as enhanced cycling performance compared to pure V_2O_5 electrodes. Figures 2.10 (b) and (c) show the C-rate performance of V_2O_5 with and without the rGO coating, highlighting the improved reversible capacity obtained in the composite electrode.

Silicon has been researched extensively as an electrode material for lithium ion batteries due to its high theoretical capacity (~4200 mAh/g).[147] However, the large volume expansion observed during lithiation has hindered its application and use in LIBs. SiO_2 offers the potential of utilizing some of the theoretical capacity of silicon, while mitigating the issue of volume expansion. However, it is important to note that SiO_2 still undergoes volumetric changes during cycling, albeit to a lesser extent, with a 100% volume expansion compared to silicon's 300%.[148] Therefore, combining SiO_2 with a physical stable material with negligible volume changes like TiO_2 may suppress this volume expansion further and allow for a longer cycle life. Lee et al.[149] prepared SiO_2/TiO_2 composite film with micropores using plasma electrolytic oxidation, shown in Figs 2.10 (d-f). The films contained crystalline and amorphous TiO_2 and amorphous SiO_2, with the addition of SiO_2 influencing the micropore sizes within the anodic film, making them non-uniform as the SiO_2 content increases from 0% to 25% as seen in Figs 2.10 (d) and (e). The cycling performance was characterized by areal capacity and showed the porous SiO_2/TiO_2 composites exhibited higher capacity than other types of nanostructured TiO_2 electrodes (Fig. 2.10 (f)), because of the specific capacity arising from the addition of SiO_2. Post-mortem analysis confirmed that the film maintained its original structure after 200 cycles which was attributed to the addition of structurally stable TiO_2.

Zhu et al.[150] prepared a composite to tackle a similar issue with SnO_2. Tin oxide has a theoretical capacity of ~790 mAh/g, however it has the same volume expansion issues as Si.[151] In this report they combined manganese oxide with tin oxide in a 3D structure to minimize the volume expansion, MnO also has a high theoretical capacity similar to SnO_2 and can preserve the starting morphology of the composite. Figure 9 shows the SEM images of the as–prepared films of SnO_2-MnO (Fig. 2.10 (g)) and pure

SnO_2 (Fig. 2.10 (h)). Electrochemical tests performed in the potential window of 0.01 to 3.0 V at 0.5 C rate (Fig. 2.10 (i)), showed that the while the composite exhibited a lower initial discharge capacity (1188 mAh/g), its coulombic efficiency was higher and subsequent cycles showed a stable capacity when compared to pure SnO_2 material. Post – mortem analysis showed that MnO helped maintain the 3D structure and prevented Sn aggregation during cycling, improving cycle life.

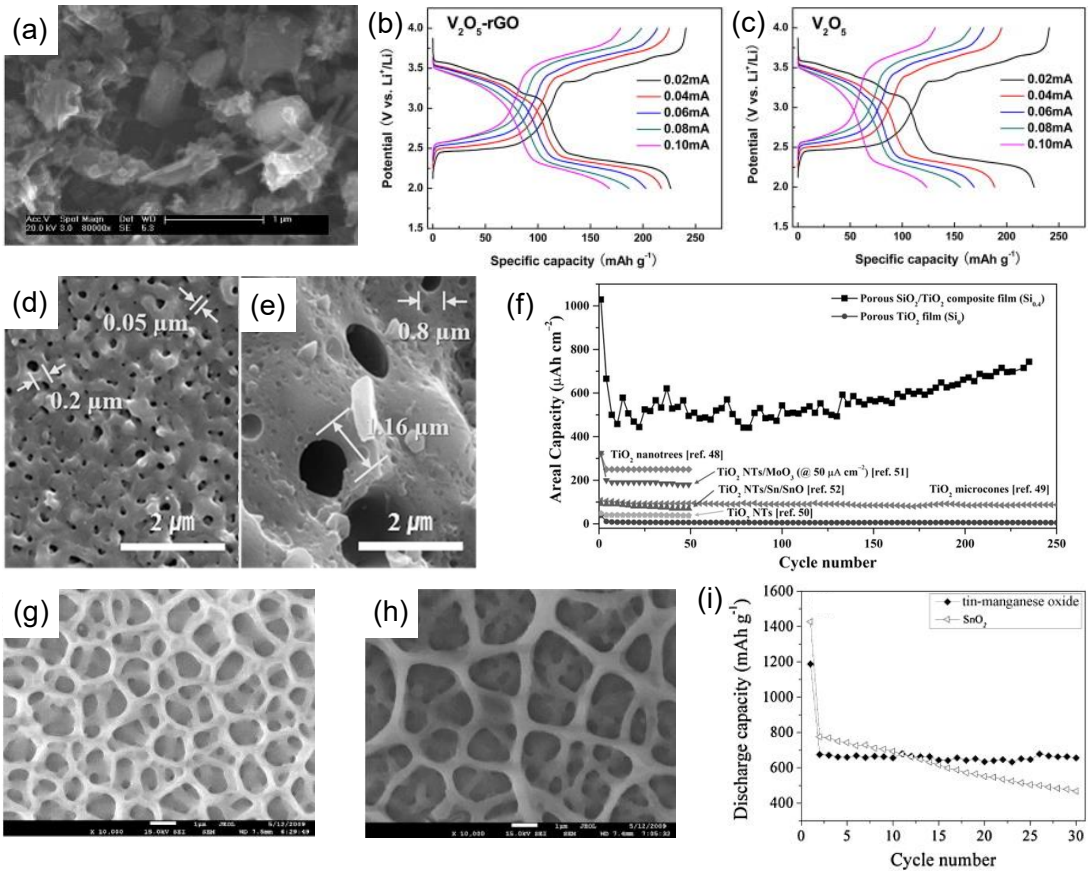

Figure 2.10. (a) SEM image of vanadium oxide- rGO composite material. Charge and discharge curves of (a) V_2O_5-rGO and (b) V_2O_5 as cathode materials at various current densities.[146] (d) & (e) SEM images of SiO_2/TiO_2 composite film with varying Si content, (d) Si_0 , (e) $Si_{0.4}$. (f) Cycle performance of the SiO_2/TiO_2 composite compared to other types of nanostructured TiO_2 and TiO_2 composite electrodes.[149] SEM images of (g) SnO_2-MnO_2 and (h) SnO_2. (i) Cycle performance of SnO_2-MnO_2 composite compared to SnO_2.[150]

While some additives or composites are centered around physical stability and cycle life, materials such as carbon composites aim to improve conductivity and rate

performance of materials with poor conductivity. Lithium- sulfur batteries have been researched as an alternative to lithium-ion due to sulfur's abundance and high theoretical capacity of 1675 mAh/g, however poor rate capability and electrical resistivity of sulfur as well as dissolution of intermediate products are obstacles that need to be addressed.[152, 153] Various sulfur-carbon composites have been developed to address these issues, Su et al.[154] developed a composite cathode consisting of sulfur and multi-wall carbon nanotubes (MWCNT) that demonstrated excellent cyclability at high discharge rates, Figs 2.11 (a – c). The MWCNTs maintained the structural integrity of the electrode and offers numerous electrical and ionic routes to enhance charge and discharge capabilities. The MWCNTS also trapped the soluble polysulfide intermediates preventing the irreversible depletion of active materials. The cathode achieved capacities of 1352 mAh/g at 1C discharge rate and 1012 mAh/g at 4C rate. The discharge capacity of the cell is able to recover and reach a capacity of over 1200 mAh/g after the C rate returns from 4 C back to 0.5 C, as shown in Fig. 2.11 (c), showing excellent cyclability and rate capabilities.

TiO_2 has been researched as an alternative anode material to graphite, having a similar theoretical capacity (~335 mAh/g) and stable voltage insertion plateau, however, TiO_2 possesses low conductivity which results in poor rate performances. Combining highly conductive materials such as carbon-based materials has been researched to enhance electronic conductivity for the application of TiO_2 in LIBs.[155-157] Liu et al.[158] synthesized mesoporous TiO_2 hollow spheres with a graphitic carbon coating, which showed improved electrochemical performance when compared to pure TiO_2 hollow spheres. The synthesis involved the preparation of SiO_2 nanospheres, which are then coated with mesoporous amorphous TiO_2 shells via a surfactant-free method. Subsequently, these SiO_2@TiO_2 core-shell spheres were

hydrothermally treated with glucose, followed by annealing to create TiO_2/graphitic carbon hybrid structures, and after etching, SiO_2 nanospheres were removed to obtain H-TiO_2/GC spheres. Figure 2.11 (d) &(e) show H-TiO_2/GC hollow spheres exhibited significantly better high-rate performance than H-TiO_2 spheres, delivering higher capacities across various current rates. Additionally, H-TiO_2/GC maintained excellent cycling stability with minimal capacity fading, even after 1000 cycles at a high current rate of 1 A g^{-1}.

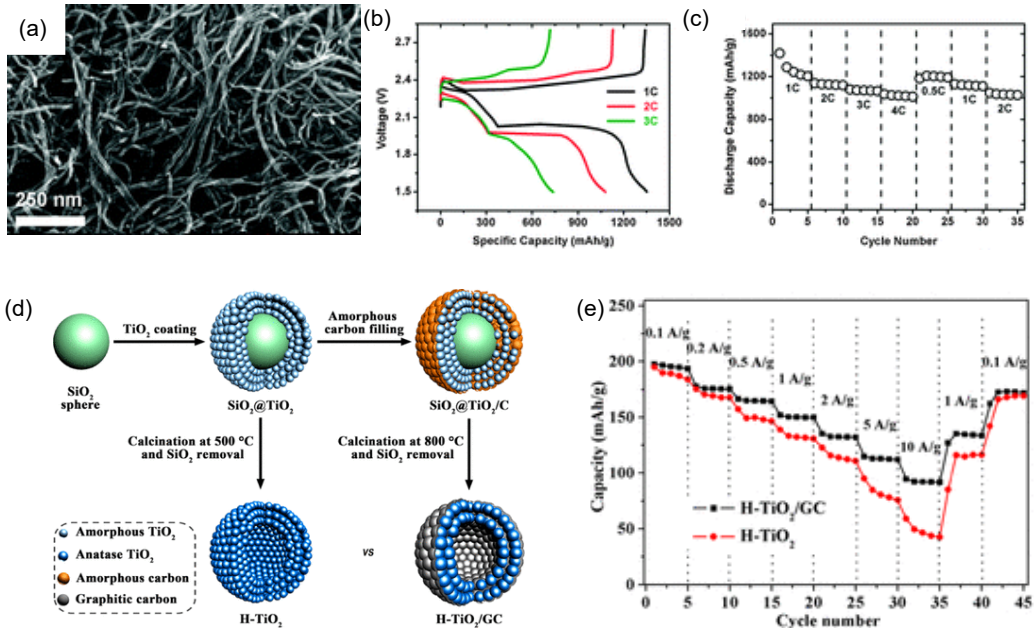

Figure 2.11. (a) SEM images of sulfur-CNT composite electrode. (b) Galvanostatic profiles for the first cycle for sulfur - MWCNT at 1 C, 2 C, and 3 C. (c) rate capability of the S–CNT cathode at various C rates. (d) Schematic illustration of the formation of conformal graphitic carbon coating of mesoporous TiO_2 hollow (H-TiO_2/GC) spheres and the preparation of mesoporous TiO_2 hollow spheres without the carbon coating. (e) Rate test performances of H-TiO_2/GC and H-TiO_2 spheres at various current densities.[158]

Composite materials structured into inverse opal (IO) configurations present an intriguing and innovative avenue in materials science, which combines the unique advantages of both composite materials and IO architectures, offering a potential solution to two critical challenges in battery materials technology. The IO structure

has shown its ability to minimize volumetric swelling effects and improve charge transfer at the expense of gravimetric energy density, making it a useful platform for investigating the relative influence of composition and material structure on electrode behavior. By integrating various materials within these IO structures, composites harness the potential synergy of two or more components, effectively merging their distinct benefits.

SnO_2 exhibits promising potential as an anode material for lithium-ion batteries (LIBs) due to its high theoretical capacity. However, as previously mentioned, SnO_2 is limited by significant volumetric swelling issues, intrinsically poor electrical conductivity, and capacity retention problems linked to the volume changes during lithiation and delithiation processes.[159] On a parallel note, research has extensively explored germanium-based nanostructures[160-162], mainly due to the remarkable high theoretical capacity of germanium (1384 mAh/g), which is comparable to that of SnO_2. Numerous studies have highlighted the impressive cycle life and capacity retention characteristics observed in Ge nanowires and GeO_2 nanoparticles.[163, 164] McNulty et al.[165] reported on the synthesis of SnO_2/GeO_2 inverse opals and compared them to pure SnO_2 IOs, emphasizing the effects of the addition of GeO_2 to the IO structure. The study evaluated the electrochemical performance of SnO_2 and SnO_2/GeO_2 IO electrodes and the results indicated that SnO_2/GeO_2 IOs offer higher specific capacities and improved capacity retention compared to pure SnO_2 IOs, despite both materials initially experiencing capacity fading over approximately 25 cycles, Fig. 2.12. SnO_2 IOs displayed a specific capacity of 498 mAh/g after 50 cycles, while SnO_2/GeO_2 IOs exhibited a significantly higher capacity of 881 mAh/g, with 89 % capacity retention after 100 cycles. Additionally, SnO_2/GeO_2 IOs demonstrated better Coulombic efficiency (CE) with an average CE of 99 %, compared to 97 % for

SnO_2 IOs. The introduction of GeO_2 nanoparticles contributed to increased specific capacities, enhancing overall performance. Furthermore, rate capability testing revealed that SnO_2/GeO_2 IOs outperformed SnO_2 IOs at higher specific currents, highlighting their potential for improved capacity retention during cycling.

Another IO composite study focused on Fe_3O_4 and improving rate capability and cyclic stability by adding copper and nanostructuring into a 3DOM structure. Tang et al.[166] synthesized a 3DOM Cu current collector using electrophoretic deposition before coating it with Fe_3O_4 nanoflakes. Cyclic voltammetry showed highly reversible processes while GCPLs showed improved specific capacities and capacity retention when compared to Fe_3O_4 film anodes, as shown in Figs 2.12 (e) and (f). The 3DOM Cu/Fe_3O_4 composite anode demonstrated excellent rate capability and cyclic stability. At various current densities, it achieves significantly higher discharge capacities compared to the Fe_3O_4 film anode, indicating that the 3D porous structure and the composition of the Cu/Fe_3O_4 anode enhances lithium-ion diffusion and reduces electrical resistances. Impedance measurements revealed that the 3DOM Cu/Fe_3O_4 anode had lower charge-transfer resistance compared to the Fe_3O_4 film anode, indicating better electron transference. The porous architecture also accommodated the volume changes during cycling, ensuring structural stability and preventing capacity decay, as observed in cycled electrodes.

The amalgamation of structural design and material composition has the potential to introduce a new era of batteries characterized by improved efficiency and extended lifespan.

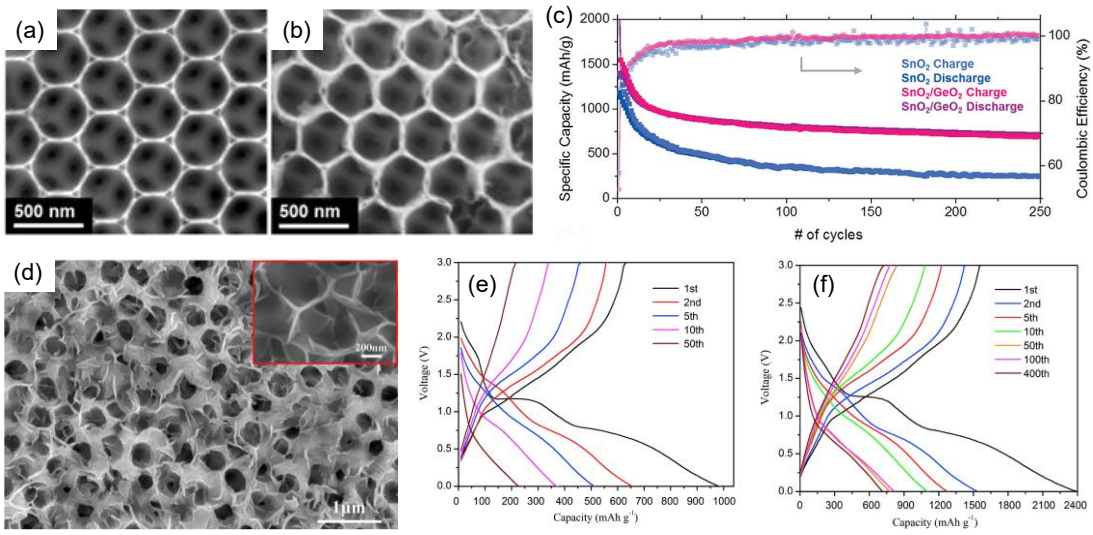

Figure 2.12. SEM images of (a) SnO_2 and (b) SnO_2/GeO_2 IOs. (c) Comparison of the specific capacity values and related Coulombic efficiencies obtained for an SnO_2 IO and an SnO_2/GeO_2 IO cycled using a specific current of 150 mA/g for 250 cycles.[165] SEM image of d) Fe_3O_4 on 3DOM Cu. Voltage profiles of (e) Fe_3O_4 film and (f) 3DOM Cu/Fe_3O_4 composite cycled at 500 mA/g.[166]

2.7 Beyond Lithium

The increasing global energy demand, driven by population growth, economic progress, and technological advancements, has prompted concerns about the sustainability of lithium-ion batteries (LIBs). Lithium supply constraints have raised questions about the long-term viability of these batteries in meeting the growing demand for electric vehicles and energy storage systems.[167] In response to this challenge, researchers and industry leaders are exploring alternative battery solutions, such as sodium-ion and potassium-ion batteries. While lithium has the highest gravimetric and volumetric energy density, sodium and potassium are more abundant and evenly distributed globally, making them attractive alternatives for battery development, as depicted in Fig. 2.13. These elements do not form electrochemically

limiting alloys with aluminium, allowing the use of aluminium foil as a current collector in both negative and positive electrodes for sodium-ion and potassium-ion batteries. Furthermore, the absence of expensive materials like lithium, copper, and cobalt in these battery systems suggests potential cost savings.[168]

The three alkali ion batteries work on a similar principle of ion movement, known as the 'rocking chair', however materials used, electrolytes and operating voltages may differ due to variations in ion size and properties. Table 2.1 outlines the difference in physical properties for the three metals. Lithium is the lightest of the three elements and possesses the smallest ionic radii, with potassium being the heaviest and possessing the largest ionic radii.[169] The energy density of batteries is a crucial factor determined by specific capacity and voltage plateau. Sodium-ion batteries (SIBs) typically have lower energy density compared to lithium-ion batteries because sodium has a higher standard redox potential than lithium, resulting in a lower voltage plateau. In contrast, potassium-ion batteries (PIBs) have a significant advantage in terms of low potassium plating voltage, making them suitable for high-energy applications. Although sodium and potassium ions have heavier atomic masses than lithium, which affects their theoretical capacities, various strategies can be employed to enhance the specific energy of SIBs and PIBs. These strategies include using specific electrode materials with higher voltage plateaus and carefully designed structures to accommodate more ions.

Another important aspect is power density, which depends on the time required to complete the charge process. The rate capability of batteries relies on ion diffusion in solids, the electrode/electrolyte interface, and in the electrolyte. Potassium has the largest atomic and ionic radius compared to Li and Na and this inhibits diffusion in solids, however the choice of electrode materials and their structure can enhance

charge/discharge rates. For instance, two-dimensional or three-dimensional electrode materials may provide more diffusion channels for ion migration.

Graphite is commonly employed as a negative electrode material in lithium-ion batteries (Li-ion) due to its high gravimetric and volumetric capacities and low working potential.[43] Comparing its performance in Li, Na, and K cells, graphite demonstrates its highest reversible capacity of ~370 mAh/g in the Li-ion cell, corresponding to LiC_6 formation. By electrochemical reduction, Li^+ ions are inserted between graphene layers and Li–graphite intercalation compounds (GIC) are formed with stage transformations.[170] However, in the Na-ion cell, the electrochemical insertion of sodium into graphite is minimal. On the other hand, in a K-ion cell, potassium is electrochemically and reversibly inserted into graphite, yielding a reversible capacity in the range of 240 – 260 mAh/g, with the theoretical capacity being 279 mAh/g, for KC_8 formation.[171]

$LiCoO_2$ was initially introduced as a cathode material for rechargeable lithium-ion batteries (LIBs) due to its high voltage and structural stability.[172] Following this success, similar electrochemical properties were found in $NaCoO_2$, leading to the use of $NaCoO_2$ as a cathode for rechargeable sodium-ion batteries (SIBs). However, the ionic radius of cobalt is relatively small compared to lithium and sodium ions. Layered materials containing both Li and Na can be easily prepared, but $LiCoO_2$ operates at a significantly higher voltage compared to $NaCoO_2$.[173] This voltage difference is more pronounced as the Na content increases, resulting in lower energy density for sodium systems. Recently, K_xCoO_2 with $x \leq 0.7$ has been reported as a cathode for rechargeable potassium-ion batteries (PIBs). The larger size and stronger repulsion of K^+ ions make their insertion into layered oxide materials even more challenging

compared to Li^+ and Na^+ ions.[174] Overcoming this energy density challenge requires different chemistry in sodium-ion and potassium-ion batteries.

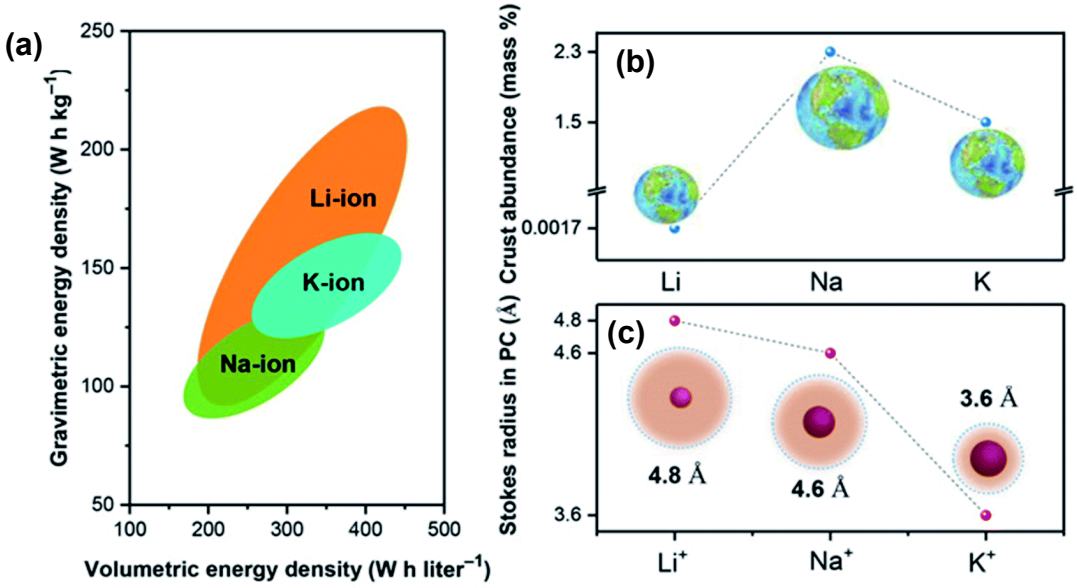

Figure 2.13. (a) Comparison of gravimetric vs volumetric energy densities for LIBs, SIBs, and PIBs. (b) Abundance (weight %) of lithium, sodium, and potassium metal in the Earth's crust. (c) Stokes radii of Li-, Na-, and K-ions in propylene carbonate (PC).

Prussian blue (PB) and its analogues, which are a type of metal organic framework, have been studied as possible cathode material for 'beyond Li-ion' batteries.[175-178] Prussian Blue Analogs (PBAs) possess a 3D open-framework structure where transition metals, typically Fe, are arranged in octahedral coordination with cyanides. This open framework structure features a generous channel size that is particularly well-suited for the diffusion of larger alkali-metal ions. Consequently, PBAs have garnered significant attention for their capacity to facilitate the insertion and extraction of larger alkali-metal ions, making them promising candidates as positive electrode materials in the context of sodium-ion and potassium-ion batteries.

Table 2.1. Comparison of physical properties for lithium, sodium, and potassium for use in secondary rechargeable batteries.

	Li	Na	K
Atomic weight (g mol^{-1})	6.94	22.990	39.098
Atomic radius (pm)	167	190	243
Shannon's ionic radius (pm)	76	102	138
E^0 vs SHE (V)	-3.04	-2.71	-2.94
Melting point (°C)	180.5	97.7	63.4
Abundance in the earth's crust (%)	0.002	2.8	2.6
Theoretical electrode capacity (mAh/g)	3860	1165	685

Clearly, a fresh perspective is essential when considering novel electrodes and their materials for Na-ion and K-ion batteries. Recent research indicates that macroporous structures, particularly inverse opal structures, show how porosity and the absence of additives are promising test electrode materials for sodium-ion batteries, and they have also demonstrated enhanced performance in various studies. Zhou et al[179] studied amorphous TiO_2 IOs to tackle solvent wettability challenges in SIBs. Surface ion availability, which is essential for high-rate performance, is determined by ion affinity and solvent wettability, with sodium ions having weaker affinity than lithium and requiring better solvent wettability for optimal performance. Inverse opal structures are considered favorable electrode architectures for improved solvent wettability due to their higher surface roughness and porosity. This study evaluated the IO electrode's battery performance against disordered porous amorphous TiO_2 and planar amorphous TiO_2. The results showed that the inverse opal amorphous TiO_2 had excellent SIB performance, with high capacities after long

cycling, notably outperforming the other two electrode architectures. Furthermore, the TiO_2 IO exhibited high-rate capabilities, even at a current density as high as 5000 mA/g. This improved performance was attributed to the structural properties of the inverse opal structure which allowed for enhanced electrolyte penetration.

Transition metal sulfides (TMs), like Co_9S_8, show promise for SIB anodes due to their high capacities, but drawbacks include low conductivity, volume changes, and unstable solid electrolyte interphases (SEI).[180] Hu et al.[181] investigated 3DOM structures as a way to tackle such issues, the structure contained small Co_9S_8 quantum dots (QDs) embedded within a highly graphitized, nitrogen-doped carbon framework. Electrochemical analysis of the material (Fig. 2.14 (b) and (c)) showed stable capacity retention and a CE of close to 100%. Additionally, the 3DOM Co_9S_8-QDs@NC material showed superior cycling performance and rate capability compared to bulk Co_9S_8-QDs@NC, electrochemical impedance spectroscopy (EIS) results indicated low charge-transfer resistance, favoring fast Na^+ insertion/desertion. The 3DOM material also displayed enhanced Na^+ diffusion due to its porous structure. Post-mortem analysis showed a stable 20 % change in thickness compared to the bulk Co_9S_8-QDs@NC electrodes 130 % change, showcasing structural stability attributed to the 3D ordered porous framework that acts as a "reservoir" for enhanced electrolyte contact, improved Na^+ accessibility, ultimately enhanced electrochemical performance.

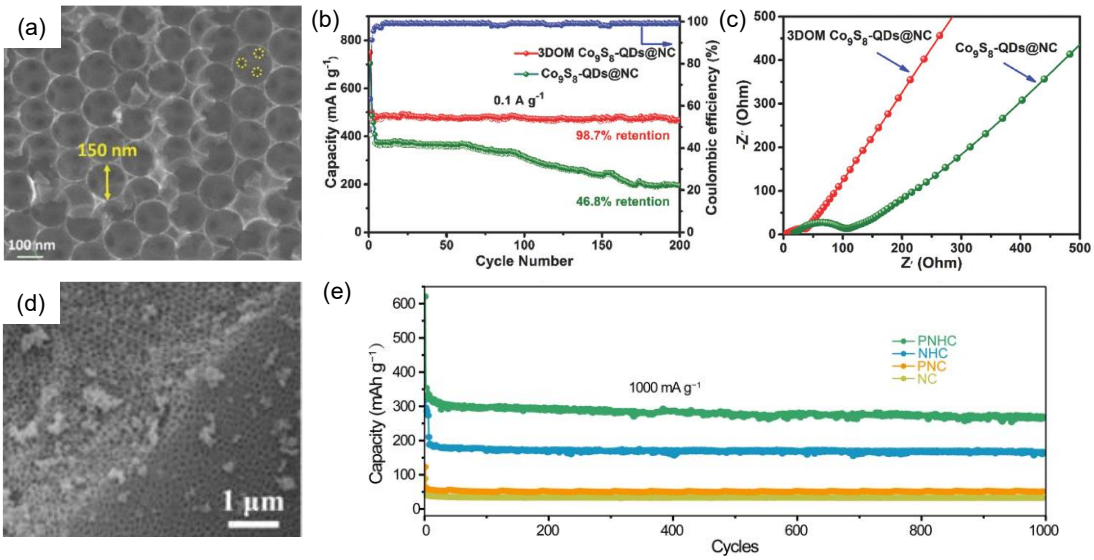

Figure 2.14. (a) FESEM image of inverse opal structured Co_9S_8 quantum dots imbedded in nitrogen doped carbon. (b) Comparison of cycling performance between 3DOM Co_9S_8-QDs@NC and bulk Co_9S_8-QDs@NC showing improved cycling stability and specific capacity. (c) Nyquist plots used for the impedance analysis of the 3DOM Co_9S_8-QDs@NC and bulk Co_9S_8-QDs@NC electrode obtained after 200 cycles at 0.1 A/g.[181] (d) SEM image of P-doped N-rich honeycomb-like carbon (PNHC). (e) Cycling performance of PNHC compared to N-rich honeycomb-like carbon (NHC), P-doped N-rich carbon (NPC) and N-rich carbon (NC) bulk electrodes at a current density of 1 A/g over 1000 cycles.[182]

While graphite exhibits a higher theoretical capacity for potassium-ion batteries than sodium ion batteries, its poor performance arises from volume expansion during potassiation/depotassiation. Amorphous carbon outperforms graphite due to a larger interlayer distance accommodating potassium ions and tolerance for volume expansion.[183] Recently, enhancements through atomic modulation, like nitrogen doping, and porous nanostructures have been researched to further improve anode materials for KIBs.[184, 185] In 2019, He et al[182] achieved a high level of pyridinic nitrogen (N) in carbon by creating a 3D honeycomb-like structure and introducing phosphorus doping. The 3D porous structure and phosphorus doping, which can be seen in Fig. 14 (d), enhanced the formation of pyridinic N by providing favorable conditions and open edge sites, thus improving the reactivity and K^+ adsorption

reactions in the carbon framework. Fig. 14 (e) shows the comparison of P-doped N-rich honeycomb-like carbon (PNHC) with N-rich honeycomb-like carbon (NHC), and non-templated P-doped N-rich carbon (PNC) and N-rich carbon (NC). The PNHC electrodes exhibited improved specific capacity and rate capability over the other samples. Both IO structured electrodes outperformed the bulk electrodes, implying that the 3D structure is an important factor in electrochemical performance while showing how heteroatom-doping can further improve a materials potential.

2.8 Conclusion and Outlook on the Role of Structure in Electrochemical Energy Storage

Electrochemical energy storage systems, particularly batteries, have played a vital role in reducing our reliance on fossil fuels, powering electric vehicles, consumer electronics, and medical devices. While rechargeable batteries are not a recent invention, current standards fall short in terms of power and lifespan. To reach net-zero carbon emission goals, improvements in battery technology are essential. In recent decades, significant advancements have been made in battery research, leading to a deeper comprehension of the fundamental relationships between the structure and properties of electrode materials. Inverse opals, 3D ordered macroporous structures, are gaining attention for their ability to enhance rate capability and cyclability. They offer better control for examining the influence of structural characteristics and mass transport properties. Whether through soft templating or hard templating, these porous materials can provide more electrolyte access, faster charge transfer, and shorter diffusion distances, improving specific capacities and electrode performance.

Porous electrodes offer distinct benefits for high-rate applications owing to shortened charge carrier diffusion paths, thereby enhancing rate capabilities. This is particularly beneficial for electric vehicles and other high-power applications. Be it for micro-, meso-, or macropores, methods of synthesis are largely facile in approach. Three-dimensional ordered macroporous electrode designs enable the use of novel materials with desirable properties but possess unfavorable drawbacks when used in bulk form, such as conversion type materials, which experience extensive volume changes during cycling.

TiO_2 based materials show promise as electrodes when nanostructured to increase specific capacity. Its different polymorphs, such as rutile, anatase, and brookite, offer varying properties, but amorphous TiO_2 can offer additional active sites for lithiation. Moreover, TiO_2 based materials can be tailored into various nanostructures, such as hierarchical spheres, nanotubes, nanoporous films and inverse opals, to overcome issues such as its intrinsic conductivity limitations and further enhance its electrochemical performance. These properties and tuneability make them hopeful candidates for high power battery applications.

While graphite is the dominant choice for anode material, various carbonaceous materials, such as carbon nanotubes, porous carbon, graphene as well as others, offer promising alternatives to enhance conductivity and capacity. CNTs can be combined with other high-capacity materials such as tin and silicon to address voltage instability issues. CNTs possess excellent electrical conductivity and mechanical strength while being lightweight and flexible and could provide low cost, light-weight Li-ion batteries. Porous carbon brings with it the benefit of better electrolyte integration and faster charge transfer while providing structural stability. Showing improved voltage stability for C-coated Ni-Mn-Co-O IO during lithiation

compared to the IO without carbon coating. As will be shown in this thesis, fully carbon IO structures provide a new way to integrate the carbon and the IO structure together, as a composite, so these electrode structuring benefits can be realized.

Integration of composite materials has shown to be a pivotal strategy to address challenges in energy storage, yielding synergistic benefits leading to improved performances such as enhanced energy density, superior rate capabilities and longer cycle life. Examining specific cases, vanadium oxide composites with graphene oxide, SiO_2/TiO_2, and SnO_2-MnO illustrate the effectiveness of composite strategies in overcoming limitations associated with volume expansion and stability. Moreover, the incorporation of conductive materials like multi-wall carbon nanotubes in sulfur composites showcases how composites can improve rate capabilities and cyclability in lithium-sulfur batteries. While composite IOs, like SnO_2/GeO_2 and Fe_3O_4 demonstrate the advantage of utilizing material composition with structural design. The diverse applications and success of composite strategies underscore their potential, positioning them as an important avenue for advancing energy storage technologies.

Nevertheless, while various electrodes are continuously being researched for lithium-ion batteries, the concerns about the long-term viability of LIBs need to be considered. While researchers are actively investigating alternative battery technology such as sodium-ion and potassium-ion batteries, they pose unique challenges. Differences in ion size and properties, voltage plateaus, and power density, require tailored approaches for materials design and structural considerations and it has been shown that the concepts and materials employed for LIBs may not be directly applicable. Innovative electrode materials, including macroporous structures like inverse opals, and strategies such as atomic modulation and heteroatom-doping,

exhibit promising potential in overcoming specific challenges associated with sodium-ion and potassium-ion batteries. The continued exploration of these alternative battery technologies highlights a dynamic shift towards more sustainable and cost-effective energy storage solutions to meet the evolving needs of our energy landscape.

2.9 References

(1) Fankhauser, S.; Smith, S. M.; Allen, M.; Axelsson, K.; Hale, T.; Hepburn, C.; Kendall, J. M.; Khosla, R.; Lezaun, J.; Mitchell-Larson, E.; et al. The meaning of net zero and how to get it right. *Nature Climate Change* **2022**, *12* (1), 15-21. DOI: 10.1038/s41558-021-01245-w.
(2) Jung, J.; Zhang, L.; Zhang, J. *Lead-acid battery technologies: fundamentals, materials, and applications*; Crc Press, 2015.
(3) Scrosati, B. History of lithium batteries. *Journal of Solid State Electrochemistry* **2011**, *15* (7), 1623-1630. DOI: 10.1007/s10008-011-1386-8.
(4) Thackeray, M. M.; Wolverton, C.; Isaacs, E. D. Electrical energy storage for transportation—approaching the limits of, and going beyond, lithium-ion batteries. *Energy & Environmental Science* **2012**, *5* (7), 7854-7863.
(5) Zhang, W.; Liu, Y.; Guo, Z. Approaching high-performance potassium-ion batteries via advanced design strategies and engineering. *Science Advances 5* (5), eaav7412. DOI: 10.1126/sciadv.aav7412 (acccessed 2023/09/06).
(6) Yoshio, M.; Brodd, R. J.; Kozawa, A. *Lithium-ion batteries*; Springer, 2009.
(7) Broussely, M.; Biensan, P.; Simon, B. Lithium insertion into host materials: the key to success for Li ion batteries. *Electrochimica Acta* **1999**, *45* (1-2), 3-22.
(8) Hughes, M.; Hampson, N. A.; Karunathilaka, S. A. G. R. A review of cells based on lithium negative electrodes (anodes). *Journal of Power Sources* **1984**, *12* (2), 83-144. DOI: https://doi.org/10.1016/0378-7753(84)80044-0.
(9) Landi, B. J.; Ganter, M. J.; Cress, C. D.; DiLeo, R. A.; Raffaelle, R. P. Carbon nanotubes for lithium ion batteries. *Energy & Environmental Science* **2009**, *2* (6), 638-654.
(10) Bernardini, A.; Barrero, R.; Macharis, C.; Van Mierlo, J. Technological solutions aiming at recovering metro braking energy: a multi-criteria analysis case study. *BDC - Bollettino del Centro Calza Bini - Università degli Studi di Napoli Federico II* **2015**, *14*, 301-325. DOI: 10.6092/2284-4732/2929.
(11) Goodenough, J. B.; Park, K.-S. The Li-Ion Rechargeable Battery: A Perspective. *Journal of the American Chemical Society* **2013**, *135* (4), 1167-1176. DOI: 10.1021/ja3091438.
(12) Nazri, G.-A.; Pistoia, G. *Lithium batteries: science and technology*; Springer Science & Business Media, 2008.
(13) Liu, C.; Neale, Z. G.; Cao, G. Understanding electrochemical potentials of cathode materials in rechargeable batteries. *Materials Today* **2016**, *19* (2), 109-123. DOI: https://doi.org/10.1016/j.mattod.2015.10.009.
(14) Asenbauer, J.; Eisenmann, T.; Kuenzel, M.; Kazzazi, A.; Chen, Z.; Bresser, D. The success story of graphite as a lithium-ion anode material–fundamentals, remaining challenges, and recent developments including silicon (oxide) composites. *Sustainable Energy & Fuels* **2020**, *4* (11), 5387-5416.
(15) Xu, K. Nonaqueous Liquid Electrolytes for Lithium-Based Rechargeable Batteries. *Chemical Reviews* **2004**, *104* (10), 4303-4418. DOI: 10.1021/cr030203g.
(16) Zhang, X.; Kostecki, R.; Richardson, T. J.; Pugh, J. K.; Ross, P. N. Electrochemical and Infrared Studies of the Reduction of Organic Carbonates. *Journal of The Electrochemical Society* **2001**, *148* (12), A1341. DOI: 10.1149/1.1415547.
(17) Fong, R.; von Sacken, U.; Dahn, J. R. Studies of Lithium Intercalation into Carbons Using Nonaqueous Electrochemical Cells. *Journal of The Electrochemical Society* **1990**, *137* (7), 2009. DOI: 10.1149/1.2086855.

(18) Peled, E. The Electrochemical Behavior of Alkali and Alkaline Earth Metals in Nonaqueous Battery Systems—The Solid Electrolyte Interphase Model. *Journal of The Electrochemical Society* **1979**, *126* (12), 2047. DOI: 10.1149/1.2128859.
(19) Sole, C.; Drewett, N. E.; Hardwick, L. J. In situ Raman study of lithium-ion intercalation into microcrystalline graphite. *Faraday Discussions* **2014**, *172* (0), 223-237, 10.1039/C4FD00079J. DOI: 10.1039/C4FD00079J.
(20) Whittingham, M. S. Electrical energy storage and intercalation chemistry. *Science* **1976**, *192* (4244), 1126-1127.
(21) Padhi, A. K.; Nanjundaswamy, K. S.; Goodenough, J. B. Phospho-olivines as positive-electrode materials for rechargeable lithium batteries. *Journal of the electrochemical society* **1997**, *144* (4), 1188.
(22) Mizushima, K.; Jones, P. C.; Wiseman, P. J.; Goodenough, J. B. LixCoO2 (0<x<-1): A new cathode material for batteries of high energy density. *Materials Research Bulletin* **1980**, *15* (6), 783-789. DOI: https://doi.org/10.1016/0025-5408(80)90012-4.
(23) Goodenough, J. B.; Mizushima, K.; Takeda, T. Solid-Solution Oxides for Storage-Battery Electrodes. *Japanese Journal of Applied Physics* **1980**, *19* (S3), 305. DOI: 10.7567/JJAPS.19S3.305.
(24) Pistoia, G.; Pasquali, M.; De Picciotto, L. A.; Thackeray, M. M. Behaviour of the spinel LiV2O4 as a positive electrode for secondary Li cells. *Solid State Ionics* **1988**, *28-30*, 879-885. DOI: https://doi.org/10.1016/S0167-2738(88)80163-2.
(25) Ozawa, K. Lithium-ion rechargeable batteries with LiCoO2 and carbon electrodes: the LiCoO2/C system. *Solid State Ionics* **1994**, *69* (3), 212-221. DOI: https://doi.org/10.1016/0167-2738(94)90411-1.
(26) Sun, L.; Zhang, Z.; Hu, X.; Tian, H.; Zhang, Y.; Yang, X. Realization of Ti doping by electrostatic assembly to improve the stability of LiCoO2 cycled to 4.5 V. *Journal of The Electrochemical Society* **2019**, *166* (10), A1793.
(27) Jiang, Y.; Qin, C.; Yan, P.; Sui, M. Origins of capacity and voltage fading of LiCoO 2 upon high voltage cycling. *Journal of materials chemistry A* **2019**, *7* (36), 20824-20831.
(28) Gu, R.; Ma, Z.; Cheng, T.; Lyu, Y.; Nie, A.; Guo, B. Improved electrochemical performances of LiCoO2 at elevated voltage and temperature with an in situ formed spinel coating layer. *ACS applied materials & interfaces* **2018**, *10* (37), 31271-31279.
(29) Chen, Z.; Dahn, J. Methods to obtain excellent capacity retention in LiCoO2 cycled to 4.5 V. *Electrochimica Acta* **2004**, *49* (7), 1079-1090.
(30) Long, X.-H.; Wu, Y.-R.; Zhang, N.; Yu, P.-F.; Feng, X.-F.; Zheng, S.; Fu, J.-M.; Liu, X.-S.; Liu, N.; Wang, M. Charge compensation and capacity fading in LiCoO2 at high voltage investigated by soft X-ray absorption spectroscopy. *Chinese Physics B* **2018**, *27* (10), 107802.
(31) Wang, H.; Rus, E.; Sakuraba, T.; Kikuchi, J.; Kiya, Y.; Abruña, H. D. CO2 and O2 evolution at high voltage cathode materials of Li-ion batteries: a differential electrochemical mass spectrometry study. *Analytical chemistry* **2014**, *86* (13), 6197-6201.
(32) Li, B.; Xia, D. Anionic redox in rechargeable lithium batteries. *Advanced Materials* **2017**, *29* (48), 1701054.
(33) Qian, J.; Liu, L.; Yang, J.; Li, S.; Wang, X.; Zhuang, H. L.; Lu, Y. Electrochemical surface passivation of LiCoO2 particles at ultrahigh voltage and its applications in lithium-based batteries. *Nature Communications* **2018**, *9* (1), 4918. DOI: 10.1038/s41467-018-07296-6.

(34) Reimers, J. N.; Dahn, J. Electrochemical and in situ X-ray diffraction studies of lithium intercalation in Li x CoO2. *Journal of the Electrochemical Society* **1992**, *139* (8), 2091.
(35) Thackeray, M. M. Manganese oxides for lithium batteries. *Progress in Solid State Chemistry* **1997**, *25* (1), 1-71. DOI: https://doi.org/10.1016/S0079-6786(97)81003-5.
(36) Zhang, W.-J. Structure and performance of LiFePO4 cathode materials: A review. *Journal of Power Sources* **2011**, *196* (6), 2962-2970.
(37) G. Bruce, P.; Robert Armstrong, A.; L. Gitzendanner, R. New intercalation compounds for lithium batteries: layered LiMnO2. *Journal of Materials Chemistry* **1999**, *9* (1), 193-198, 10.1039/A803938K. DOI: 10.1039/A803938K.
(38) Armstrong, A. R.; Bruce, P. G. Synthesis of layered LiMnO2 as an electrode for rechargeable lithium batteries. *Nature* **1996**, *381* (6582), 499-500. DOI: 10.1038/381499a0.
(39) Ryu, H.-H.; Park, N.-Y.; Seo, J. H.; Yu, Y.-S.; Sharma, M.; Mücke, R.; Kaghazchi, P.; Yoon, C. S.; Sun, Y.-K. A highly stabilized Ni-rich NCA cathode for high-energy lithium-ion batteries. *Materials today* **2020**, *36*, 73-82.
(40) Jung, R.; Metzger, M.; Maglia, F.; Stinner, C.; Gasteiger, H. A. Oxygen release and its effect on the cycling stability of LiNixMnyCozO2 (NMC) cathode materials for Li-ion batteries. *Journal of The Electrochemical Society* **2017**, *164* (7), A1361.
(41) Noh, H.-J.; Youn, S.; Yoon, C. S.; Sun, Y.-K. Comparison of the structural and electrochemical properties of layered Li [NixCoyMnz] O2 (x= 1/3, 0.5, 0.6, 0.7, 0.8 and 0.85) cathode material for lithium-ion batteries. *Journal of power sources* **2013**, *233*, 121-130.
(42) Robert, R.; Villevieille, C.; Novák, P. Enhancement of the high potential specific charge in layered electrode materials for lithium-ion batteries. *Journal of Materials Chemistry A* **2014**, *2* (23), 8589-8598.
(43) Tarascon, J. M.; Armand, M. Issues and challenges facing rechargeable lithium batteries. *Nature* **2001**, *414* (6861), 359-367, Review. DOI: 10.1038/35104644 Scopus.
(44) Pistoia, G. Nonaqueous batteries with LiClO4-ethylene carbonate as electrolyte. *Journal of The Electrochemical Society* **1971**, *118* (1), 153.
(45) Guyomard, D.; Tarascon, J. M. Rechargeable Li1 + x Mn2 O 4 / Carbon Cells with a New Electrolyte Composition: Potentiostatic Studies and Application to Practical Cells. *Journal of The Electrochemical Society* **1993**, *140* (11), 3071. DOI: 10.1149/1.2220987.
(46) Aurbach, D.; Ein-Eli, Y.; Markovsky, B.; Zaban, A.; Luski, S.; Carmeli, Y.; Yamin, H. The Study of Electrolyte Solutions Based on Ethylene and Diethyl Carbonates for Rechargeable Li Batteries: II . Graphite Electrodes. *Journal of The Electrochemical Society* **1995**, *142* (9), 2882. DOI: 10.1149/1.2048659.
(47) Ein-Eli, Y.; Thomas, S. R.; Koch, V.; Aurbach, D.; Markovsky, B.; Schechter, A. Ethylmethylcarbonate, a Promising Solvent for Li-Ion Rechargeable Batteries. *Journal of The Electrochemical Society* **1996**, *143* (12), L273.
(48) Xu, K. Electrolytes and Interphases in Li-Ion Batteries and Beyond. *Chemical Reviews* **2014**, *114* (23), 11503-11618. DOI: 10.1021/cr500003w.
(49) Aurbach, D.; Gamolsky, K.; Markovsky, B.; Gofer, Y.; Schmidt, M.; Heider, U. On the use of vinylene carbonate (VC) as an additive to electrolyte solutions for Li-ion batteries. *Electrochimica Acta* **2002**, *47* (9), 1423-1439, Article. DOI: 10.1016/S0013-4686(01)00858-1 Scopus.

(50) Arora, P.; Zhang, Z. Battery Separators. *Chemical Reviews* **2004**, *104* (10), 4419-4462. DOI: 10.1021/cr020738u.
(51) Wu, H. B.; Chen, J. S.; Hng, H. H.; Wen Lou, X. Nanostructured metal oxide-based materials as advanced anodes for lithium-ion batteries. *Nanoscale* **2012**, *4* (8), 2526-2542, 10.1039/C2NR11966H. DOI: 10.1039/C2NR11966H.
(52) Zhang, Y.; Tang, Y.; Li, W.; Chen, X. Nanostructured TiO2-Based Anode Materials for High-Performance Rechargeable Lithium-Ion Batteries. *ChemNanoMat* **2016**, *2* (8), 764-775. DOI: 10.1002/cnma.201600093 (acccessed 2020/02/11).
(53) Wei, Z.; Li, R.; Huang, T.; Yu, A. Fabrication and electrochemical properties of Si/TiO2 nanowire array composites as lithium ion battery anodes. *Journal of Power Sources* **2013**, *238*, 165-172. DOI: https://doi.org/10.1016/j.jpowsour.2013.03.080.
(54) Bao, S.-J.; Bao, Q.-L.; Li, C.-M.; Zhi-Li, D. Novel porous anatase TiO2 nanorods and their high lithium electroactivity. *Electrochemistry Communications* **2007**, *9* (5), 1233-1238. DOI: https://doi.org/10.1016/j.elecom.2007.01.028.
(55) Amine, K.; Belharouak, I.; Chen, Z.; Tran, T.; Yumoto, H.; Ota, N.; Myung, S. T.; Sun, Y. K. Nanostructured anode material for high-power battery system in electric vehicles. *Advanced materials* **2010**, *22* (28), 3052-3057.
(56) Moshtev, R.; Johnson, B. State of the art of commercial Li ion batteries. *Journal of Power Sources* **2000**, *91* (2), 86-91. DOI: https://doi.org/10.1016/S0378-7753(00)00458-4.
(57) Armstrong, E.; O'Dwyer, C. Artificial opal photonic crystals and inverse opal structures – fundamentals and applications from optics to energy storage. *Journal of Materials Chemistry C* **2015**, *3* (24), 6109-6143, 10.1039/C5TC01083G. DOI: 10.1039/C5TC01083G.
(58) von Freymann, G.; Kitaev, V.; Lotsch, B. V.; Ozin, G. A. Bottom-up assembly of photonic crystals. *Chemical Society Reviews* **2013**, *42* (7), 2528-2554, 10.1039/C2CS35309A. DOI: 10.1039/C2CS35309A.
(59) Li, F.; Josephson, D. P.; Stein, A. Colloidal Assembly: The Road from Particles to Colloidal Molecules and Crystals. *Angewandte Chemie International Edition* **2011**, *50* (2), 360-388. DOI: https://doi.org/10.1002/anie.201001451 (acccessed 2023/09/15).
(60) Galisteo-López, J. F.; Ibisate, M.; Sapienza, R.; Froufe-Pérez, L. S.; Blanco, Á.; López, C. Self-assembled photonic structures. *Advanced Materials* **2011**, *23* (1), 30-69.
(61) McNulty, D.; Landgraf, V.; Trabesinger, S. Simplifying the synthesis of carbon inverse opals. *RSC advances* **2020**, *10* (40), 24108-24114.
(62) Zhang, Y.; Sun, Y.; Liu, J.; Guo, P.; Cai, Z.; Wang, J.-J. Polymer-infiltrated SiO2 inverse opal photonic crystals for colorimetrically selective detection of xylene vapors. *Sensors and Actuators B: Chemical* **2019**, *291*, 67-73. DOI: https://doi.org/10.1016/j.snb.2019.04.036.
(63) Harreld, J. H.; Dong, W.; Dunn, B. Ambient Pressure Synthesis of Aerogel-Like Vanadium Oxide and Molybdenum Oxide. *Materials Research Bulletin* **1998**, *33* (4), 561-567. DOI: https://doi.org/10.1016/S0025-5408(98)00022-1.
(64) Armstrong, E.; McNulty, D.; Geaney, H.; O'Dwyer, C. Electrodeposited Structurally Stable V2O5 Inverse Opal Networks as High Performance Thin Film Lithium Batteries. *ACS Applied Materials & Interfaces* **2015**, *7* (48), 27006-27015. DOI: 10.1021/acsami.5b09511.
(65) Kim, D. Y.; Suk, J.; Kim, D. W.; Kang, Y.; Im, S. H.; Yang, Y.; Park, O. O. An electrochemically grown three-dimensional porous Si@Ni inverse opal structure for

high-performance Li ion battery anodes. *Journal of Materials Chemistry A* **2014**, *2* (18), 6396-6401, 10.1039/C4TA00147H. DOI: 10.1039/C4TA00147H.
(66) McNulty, D.; Geaney, H.; Carroll, E.; Garvey, S.; Lonergan, A.; O'Dwyer, C. The effect of particle size, morphology and C-rates on 3D structured Co3O4 inverse opal conversion mode anode materials. *Materials Research Express* **2017**, *4* (2), 025011. DOI: 10.1088/2053-1591/aa5a26.
(67) McNulty, D.; Geaney, H.; Buckley, D.; O'Dwyer, C. High capacity binder-free nanocrystalline GeO2 inverse opal anodes for Li-ion batteries with long cycle life and stable cell voltage. *Nano Energy* **2018**, *43*, 11-21. DOI: https://doi.org/10.1016/j.nanoen.2017.11.007.
(68) McNulty, D.; Carroll, E.; O'Dwyer, C. Rutile TiO2 Inverse Opal Anodes for Li-Ion Batteries with Long Cycle Life, High-Rate Capability, and High Structural Stability. *Advanced Energy Materials* **2017**, *7* (12), 1602291. DOI: 10.1002/aenm.201602291.
(69) Lee, K. T.; Lytle, J. C.; Ergang, N. S.; Oh, S. M.; Stein, A. Synthesis and Rate Performance of Monolithic Macroporous Carbon Electrodes for Lithium-Ion Secondary Batteries. *Advanced Functional Materials* **2005**, *15* (4), 547-556. DOI: https://doi.org/10.1002/adfm.200400186 (acccessed 2023/09/15).
(70) Ng, S.-H.; Patey, T. J.; Büchel, R.; Krumeich, F.; Wang, J.-Z.; Liu, H.-K.; Pratsinis, S. E.; Novák, P. Flame spray-pyrolyzed vanadium oxide nanoparticles for lithium battery cathodes. *Physical Chemistry Chemical Physics* **2009**, *11* (19), 3748-3755.
(71) O'Dwyer, C. Color-Coded Batteries – Electro-Photonic Inverse Opal Materials for Enhanced Electrochemical Energy Storage and Optically Encoded Diagnostics. *Advanced Materials* **2016**, *28* (27), 5681-5688. DOI: 10.1002/adma.201503973 (acccessed 2019/10/01).
(72) Zhu, X.; Ren, W.; Cheng, C.; Yang, Y. Three-Dimensional Carbon@Fe2O3@SnO2 Hierarchical Inverse Opals Arrays as Li–ion Battery Anode with Improved Cycling Life and Rate Capability. *ChemistrySelect* **2017**, *2* (11), 3223-3230. DOI: https://doi.org/10.1002/slct.201700144 (acccessed 2023/09/05).
(73) Liu, H.; Cho, H.-M.; Meng, Y. S.; Li, Q. Engineering Three-Dimensionally Electrodeposited Si-on-Ni Inverse Opal Structure for High Volumetric Capacity Li-Ion Microbattery Anode. *ACS Applied Materials & Interfaces* **2014**, *6* (12), 9842-9849. DOI: 10.1021/am502277f.
(74) Yang, X.-Y.; Léonard, A.; Lemaire, A.; Tian, G.; Su, B.-L. Self-formation phenomenon to hierarchically structured porous materials: design, synthesis, formation mechanism and applications. *Chemical Communications* **2011**, *47* (10), 2763-2786, 10.1039/C0CC03734F. DOI: 10.1039/C0CC03734F.
(75) Fang, B.; Kim, J. H.; Kim, M.-S.; Yu, J.-S. Hierarchical Nanostructured Carbons with Meso–Macroporosity: Design, Characterization, and Applications. *Accounts of Chemical Research* **2013**, *46* (7), 1397-1406. DOI: 10.1021/ar300253f.
(76) Wang, X.; Li, X.; Ito, A.; Sogo, Y. Synthesis and characterization of hierarchically macroporous and mesoporous CaO–MO–SiO2–P2O5 (M=Mg, Zn, Sr) bioactive glass scaffolds. *Acta Biomaterialia* **2011**, *7* (10), 3638-3644. DOI: https://doi.org/10.1016/j.actbio.2011.06.029.
(77) Linares, N.; Silvestre-Albero, A. M.; Serrano, E.; Silvestre-Albero, J.; García-Martínez, J. Mesoporous materials for clean energy technologies. *Chemical Society Reviews* **2014**, *43* (22), 7681-7717.
(78) Li, Y.; Fu, Z. Y.; Su, B. L. Hierarchically structured porous materials for energy conversion and storage. *Advanced Functional Materials* **2012**, *22* (22), 4634-4667.

(79) Zhang, H.; Yu, X.; Braun, P. V. Three-dimensional bicontinuous ultrafast-charge and -discharge bulk battery electrodes. *Nature Nanotechnology* **2011**, *6* (5), 277-281. DOI: 10.1038/nnano.2011.38.
(80) Lacey, S. D.; Kirsch, D. J.; Li, Y.; Morgenstern, J. T.; Zarket, B. C.; Yao, Y.; Dai, J.; Garcia, L. Q.; Liu, B.; Gao, T. Extrusion-based 3D printing of hierarchically porous advanced battery electrodes. *Advanced Materials* **2018**, *30* (12), 1705651.
(81) Vu, A.; Qian, Y.; Stein, A. Porous Electrode Materials for Lithium-Ion Batteries – How to Prepare Them and What Makes Them Special. *Advanced Energy Materials* **2012**, *2* (9), 1056-1085, https://doi.org/10.1002/aenm.201200320. DOI: https://doi.org/10.1002/aenm.201200320 (acccessed 2023/06/22).
(82) Wang, K.; Wei, M.; Morris, M. A.; Zhou, H.; Holmes, J. D. Mesoporous Titania Nanotubes: Their Preparation and Application as Electrode Materials for Rechargeable Lithium Batteries. *Advanced Materials* **2007**, *19* (19), 3016-3020. DOI: https://doi.org/10.1002/adma.200602189 (acccessed 2023/09/04).
(83) Blin, J.-L.; Léonard, A.; Yuan, Z.-Y.; Gigot, L.; Vantomme, A.; Cheetham, A. K.; Su, B.-L. Hierarchically Mesoporous/Macroporous Metal Oxides Templated from Polyethylene Oxide Surfactant Assemblies. *Angewandte Chemie International Edition* **2003**, *42* (25), 2872-2875. DOI: https://doi.org/10.1002/anie.200250816 (acccessed 2023/10/11).
(84) Petkovich, N. D.; Stein, A. Controlling macro- and mesostructures with hierarchical porosity through combined hard and soft templating. *Chemical Society Reviews* **2013**, *42* (9), 3721-3739, 10.1039/C2CS35308C. DOI: 10.1039/C2CS35308C.
(85) Rosen, M. J.; Kunjappu, J. T. *Surfactants and interfacial phenomena*; John Wiley & Sons, 2012.
(86) Evans, H. 117. Alkyl sulphates. Part I. Critical micelle concentrations of the sodium salts. *Journal of the Chemical Society (Resumed)* **1956**, 579-586.
(87) Wang, D.; Choi, D.; Yang, Z.; Viswanathan, V. V.; Nie, Z.; Wang, C.; Song, Y.; Zhang, J.-G.; Liu, J. Synthesis and Li-Ion Insertion Properties of Highly Crystalline Mesoporous Rutile TiO2. *Chemistry of Materials* **2008**, *20* (10), 3435-3442. DOI: 10.1021/cm8002589.
(88) Liu, X.; Cao, Q.; Xu, D.; Luo, S.; Guo, R. Carboxylate Surfactants as Efficient and Renewable Promoters for Methane Hydrate Formation. *Energy & Fuels* **2021**, *35* (6), 5153-5162. DOI: 10.1021/acs.energyfuels.0c03987.
(89) Yao, B.; Fleming, D.; Morris, M. A.; Lawrence, S. E. Structural Control of Mesoporous Silica Nanowire Arrays in Porous Alumina Membranes. *Chemistry of Materials* **2004**, *16* (24), 4851-4855. DOI: 10.1021/cm0487425.
(90) Yan, H.; Sokolov, S.; Lytle, J. C.; Stein, A.; Zhang, F.; Smyrl, W. H. Colloidal-crystal-templated synthesis of ordered macroporous electrode materials for lithium secondary batteries. *Journal of the Electrochemical Society* **2003**, *150* (8), A1102.
(91) Woo, S.-W.; Okada, N.; Kotobuki, M.; Sasajima, K.; Munakata, H.; Kajihara, K.; Kanamura, K. Highly patterned cylindrical Ni–Sn alloys with 3-dimensionally ordered macroporous structure as anodes for lithium batteries. *Electrochimica Acta* **2010**, *55* (27), 8030-8035. DOI: https://doi.org/10.1016/j.electacta.2010.02.002.
(92) Liu, H.; Du, X.; Xing, X.; Wang, G.; Qiao, S. Z. Highly ordered mesoporous Cr2O3 materials with enhanced performance for gas sensors and lithium ion batteries. *Chemical Communications* **2012**, *48* (6), 865-867, 10.1039/C1CC16341H. DOI: 10.1039/C1CC16341H.
(93) Cheng, M.-Y.; Hwang, B.-J. Mesoporous carbon-encapsulated NiO nanocomposite negative electrode materials for high-rate Li-ion battery. *Journal of*

Power Sources **2010**, *195* (15), 4977-4983. DOI: https://doi.org/10.1016/j.jpowsour.2010.02.059.
(94) Lim, S.; Yoon, C. S.; Cho, J. Synthesis of nanowire and hollow LiFePO4 cathodes for high-performance lithium batteries. *Chemistry of Materials* **2008**, *20* (14), 4560-4564.
(95) Fu, J.; Cherevko, S.; Chung, C. H. Electroplating of metal nanotubes and nanowires in a high aspect-ratio nanotemplate. *Electrochemistry Communications* **2008**, *10* (4), 514-518, Article. DOI: 10.1016/j.elecom.2008.01.015 Scopus.
(96) Martin, C. R. Nanomaterials: a membrane-based synthetic approach. *Science* **1994**, *266* (5193), 1961-1966.
(97) Zhu, Q.; Hu, H.; Li, G.; Zhu, C.; Yu, Y. TiO2 Nanotube Arrays Grafted with MnO2 Nanosheets as High-Performance Anode for Lithium Ion Battery. *Electrochimica Acta* **2015**, *156*, 252-260. DOI: https://doi.org/10.1016/j.electacta.2015.01.023.
(98) Xu, X.; Liu, J.; Liu, Z.; Wang, Z.; Hu, R.; Liu, J.; Ouyang, L.; Zhu, M. FeP@ C Nanotube Arrays Grown on Carbon Fabric as a Low Potential and Freestanding Anode for High-Performance Li-Ion Batteries. *Small* **2018**, *14* (30), 1800793.
(99) Chen, X.; Mao, S. S. Titanium Dioxide Nanomaterials: Synthesis, Properties, Modifications, and Applications. *Chemical Reviews* **2007**, *107* (7), 2891-2959. DOI: 10.1021/cr0500535.
(100) Chen, Z.; Belharouak, I.; Sun, Y. K.; Amine, K. Titanium-based anode materials for safe lithium-ion batteries. *Advanced Functional Materials* **2013**, *23* (8), 959-969.
(101) Armstrong, G.; Armstrong, A. R.; Bruce, P. G.; Reale, P.; Scrosati, B. TiO2 (B) nanowires as an improved anode material for lithium-ion batteries containing LiFePO4 or LiNi0. 5Mn1. 5O4 cathodes and a polymer electrolyte. *Advanced Materials* **2006**, *18* (19), 2597-2600.
(102) Zhang, Y.; Tang, Y.; Li, W.; Chen, X. Nanostructured TiO2-Based Anode Materials for High-Performance Rechargeable Lithium-Ion Batteries. *ChemNanoMat* **2016**, *2* (8), 764-775. DOI: 10.1002/cnma.201600093.
(103) King, J. S.; Graugnard, E.; Summers, C. J. TiO2 Inverse Opals Fabricated Using Low-Temperature Atomic Layer Deposition. *Advanced Materials* **2005**, *17* (8), 1010-1013. DOI: 10.1002/adma.200400648.
(104) Liao, J. Y.; Manthiram, A. Mesoporous TiO2-Sn/C Core-Shell Nanowire Arrays as High-Performance 3D Anodes for Li-Ion Batteries. *Advanced Energy Materials* **2014**, *4* (14), 1400403-n/a. DOI: 10.1002/aenm.201400403.
(105) Yu, X.-Y.; Wu, H. B.; Yu, L.; Ma, F.-X.; Lou, X. W. Rutile TiO2 Submicroboxes with Superior Lithium Storage Properties. *Angewandte Chemie International Edition* **2015**, *54* (13), 4001-4004. DOI: 10.1002/anie.201411353 (acccessed 2020/02/14).
(106) Tang, Y.; Zhang, Y.; Deng, J.; Wei, J.; Tam, H. L.; Chandran, B. K.; Dong, Z.; Chen, Z.; Chen, X. Mechanical Force-Driven Growth of Elongated Bending TiO2-based Nanotubular Materials for Ultrafast Rechargeable Lithium Ion Batteries. *Advanced Materials* **2014**, *26* (35), 6111-6118. DOI: https://doi.org/10.1002/adma.201402000 (acccessed 2023/11/06).
(107) Zheng, J.; Liu, L.; Ji, G. B.; Yang, Q. F.; Zheng, L. R.; Zhang, J. Hydrogenated Anatase TiO2 as Lithium-Ion Battery Anode: Size-Reactivity Correlation. *Acs Applied Materials & Interfaces* **2016**, *8* (31), 20074-20081. DOI: 10.1021/acsami.6b05993.

(108) Beuvier, T.; Richard-Plouet, M.; Mancini-Le Granvalet, M.; Brousse, T.; Crosnier, O.; Brohan, L. TiO2(B) Nanoribbons As Negative Electrode Material for Lithium Ion Batteries with High Rate Performance. *Inorganic Chemistry* **2010**, *49* (18), 8457-8464. DOI: 10.1021/ic1010192.
(109) Wang, Y.-Q.; Gu, L.; Guo, Y.-G.; Li, H.; He, X.-Q.; Tsukimoto, S.; Ikuhara, Y.; Wan, L.-J. Rutile-TiO2 nanocoating for a high-rate Li4Ti5O12 anode of a lithium-ion battery. *Journal of the American Chemical Society* **2012**, *134* (18), 7874-7879.
(110) Macklin, W. J.; Neat, R. J. Performance of titanium dioxide-based cathodes in a lithium polymer electrolyte cell. *Solid State Ionics* **1992**, *53-56*, 694-700. DOI: https://doi.org/10.1016/0167-2738(92)90449-Y.
(111) Zachau-Christiansen, B.; West, K.; Jacobsen, T.; Atlung, S. Lithium insertion in different TiO2 modifications. *Solid State Ionics* **1988**, *28-30*, 1176-1182. DOI: https://doi.org/10.1016/0167-2738(88)90352-9.
(112) Meagher, E. P.; Lager, G. A. POLYHEDRAL THERMAL EXPANSION IN THE TiO2 POLYMORPHS: REFINEMENT OF THE CRYSTAL STRUCTURES OF RUTILE AND BROOKITE AT HIGH TEMPERATURE. *CANADIAN MINERALOGIST* **1979**, *17*, 77-85.
(113) Di Paola, A.; Addamo, M.; Bellardita, M.; Cazzanelli, E.; Palmisano, L. Preparation of photocatalytic brookite thin films. *Thin Solid Films* **2007**, *515* (7), 3527-3529. DOI: https://doi.org/10.1016/j.tsf.2006.10.114.
(114) Ye, J.; Shea, P.; Baumgaertel, A. C.; Bonev, S. A.; Biener, M. M.; Bagge-Hansen, M.; Wang, Y. M.; Biener, J.; Wood, B. C. Amorphization as a pathway to fast charging kinetics in atomic layer deposition-derived titania films for lithium ion batteries. *Chemistry of Materials* **2018**, *30* (24), 8871-8882.
(115) Wen, S.; Gu, X.; Ding, X.; Dai, P.; Zhang, D.; Li, L.; Liu, D.; Zhao, X.; Yang, J. Boosting fast and stable alkali metal ion storage by synergistic engineering of oxygen vacancy and amorphous structure. *Advanced Functional Materials* **2022**, *32* (6), 2106751.
(116) Lin, Y.-M.; Abel, P. R.; Flaherty, D. W.; Wu, J.; Stevenson, K. J.; Heller, A.; Mullins, C. B. Morphology Dependence of the Lithium Storage Capability and Rate Performance of Amorphous TiO2 Electrodes. *The Journal of Physical Chemistry C* **2011**, *115* (5), 2585-2591. DOI: 10.1021/jp110474y.
(117) Berger, T.; Monllor-Satoca, D.; Jankulovska, M.; Lana-Villarreal, T.; Gómez, R. The Electrochemistry of Nanostructured Titanium Dioxide Electrodes. *ChemPhysChem* **2012**, *13* (12), 2824-2875. DOI: https://doi.org/10.1002/cphc.201200073 (acccessed 2023/11/06).
(118) Chen, J. S.; Tan, Y. L.; Li, C. M.; Cheah, Y. L.; Luan, D.; Madhavi, S.; Boey, F. Y. C.; Archer, L. A.; Lou, X. W. Constructing Hierarchical Spheres from Large Ultrathin Anatase TiO2 Nanosheets with Nearly 100% Exposed (001) Facets for Fast Reversible Lithium Storage. *Journal of the American Chemical Society* **2010**, *132* (17), 6124-6130. DOI: 10.1021/ja100102y.
(119) Yin, Y.; Alivisatos, A. P. Colloidal nanocrystal synthesis and the organic–inorganic interface. *Nature* **2005**, *437* (7059), 664-670.
(120) Yao, F.; Pham, D. T.; Lee, Y. H. Carbon-Based Materials for Lithium-Ion Batteries, Electrochemical Capacitors, and Their Hybrid Devices. *ChemSusChem* **2015**, *8* (14), 2284-2311. DOI: https://doi.org/10.1002/cssc.201403490 (acccessed 2024/04/03).
(121) Brousse, T.; Bélanger, D.; Long, J. W. To Be or Not To Be Pseudocapacitive? *Journal of The Electrochemical Society* **2015**, *162* (5), A5185. DOI: 10.1149/2.0201505jes.

(122) Guan, L.; Yu, L.; Chen, G. Z. Capacitive and non-capacitive faradaic charge storage. *Electrochimica Acta* **2016**, *206*, 464-478. DOI: https://doi.org/10.1016/j.electacta.2016.01.213.
(123) Augustyn, V.; Come, J.; Lowe, M. A.; Kim, J. W.; Taberna, P.-L.; Tolbert, S. H.; Abruña, H. D.; Simon, P.; Dunn, B. High-rate electrochemical energy storage through Li+ intercalation pseudocapacitance. *Nature Materials* **2013**, *12* (6), 518-522. DOI: 10.1038/nmat3601.
(124) de las Casas, C.; Li, W. A review of application of carbon nanotubes for lithium ion battery anode material. *Journal of Power Sources* **2012**, *208*, 74-85. DOI: https://doi.org/10.1016/j.jpowsour.2012.02.013.
(125) Di, J.; Zhang, X.; Yong, Z.; Zhang, Y.; Li, D.; Li, R.; Li, Q. Carbon-nanotube fibers for wearable devices and smart textiles. *Advanced materials* **2016**, *28* (47), 10529-10538.
(126) Yang, S.; Huo, J.; Song, H.; Chen, X. A comparative study of electrochemical properties of two kinds of carbon nanotubes as anode materials for lithium ion batteries. *Electrochimica acta* **2008**, *53* (5), 2238-2244. DOI: 10.1016/j.electacta.2007.09.040.
(127) Mi, C. H.; Cao, G. S.; Zhao, X. B. A non-GIC mechanism of lithium storage in chemical etched MWNTs. *Journal of Electroanalytical Chemistry* **2004**, *562* (2), 217-221. DOI: https://doi.org/10.1016/j.jelechem.2003.09.004.
(128) Gao, B.; Bower, C.; Lorentzen, J. D.; Fleming, L.; Kleinhammes, A.; Tang, X. P.; McNeil, L. E.; Wu, Y.; Zhou, O. Enhanced saturation lithium composition in ball-milled single-walled carbon nanotubes. *Chemical physics letters* **2000**, *327* (1), 69-75. DOI: 10.1016/S0009-2614(00)00851-4.
(129) Reddy, A. L. M.; Shaijumon, M. M.; Gowda, S. R.; Ajayan, P. M. Coaxial MnO2/Carbon Nanotube Array Electrodes for High-Performance Lithium Batteries. *Nano Letters* **2009**, *9* (3), 1002-1006. DOI: 10.1021/nl803081j.
(130) Hong, J. K.; Lee, J. H.; Oh, S. M. Effect of carbon additive on electrochemical performance of LiCoO2 composite cathodes. *Journal of Power Sources* **2002**, *111* (1), 90-96. DOI: https://doi.org/10.1016/S0378-7753(02)00264-1.
(131) Guoping, W.; Qingtang, Z.; Zuolong, Y.; MeiZheng, Q. The effect of different kinds of nano-carbon conductive additives in lithium ion batteries on the resistance and electrochemical behavior of the LiCoO2 composite cathodes. *Solid State Ionics* **2008**, *179* (7), 263-268. DOI: https://doi.org/10.1016/j.ssi.2008.01.015.
(132) Wang, H.; Umeno, T.; Mizuma, K.; Yoshio, M. Highly conductive bridges between graphite spheres to improve the cycle performance of a graphite anode in lithium-ion batteries. *Journal of Power Sources* **2008**, *175* (2), 886-890. DOI: https://doi.org/10.1016/j.jpowsour.2007.09.103.
(133) Chou, S.-L.; Pan, Y.; Wang, J.-Z.; Liu, H.-K.; Dou, S.-X. Small things make a big difference: binder effects on the performance of Li and Na batteries. *Physical Chemistry Chemical Physics* **2014**, *16* (38), 20347-20359.
(134) Narita, K.; Citrin, M. A.; Yang, H.; Xia, X.; Greer, J. R. 3D Architected Carbon Electrodes for Energy Storage. *Advanced Energy Materials* **2021**, *11* (5), 2002637. DOI: https://doi.org/10.1002/aenm.202002637 (acccessed 2023/11/21).
(135) Liu, H.; Liu, X.; Li, W.; Guo, X.; Wang, Y.; Wang, G.; Zhao, D. Porous Carbon Composites for Next Generation Rechargeable Lithium Batteries. *Advanced Energy Materials* **2017**, *7* (24), 1700283. DOI: https://doi.org/10.1002/aenm.201700283 (acccessed 2023/11/10).
(136) Xie, L.; Tang, C.; Bi, Z.; Song, M.; Fan, Y.; Yan, C.; Li, X.; Su, F.; Zhang, Q.; Chen, C. Hard Carbon Anodes for Next-Generation Li-Ion Batteries: Review and

Perspective. *Advanced Energy Materials* **2021**, *11* (38), 2101650. DOI: https://doi.org/10.1002/aenm.202101650 (acccessed 2023/11/14).
(137) Yang, J.; Zhou, X.-y.; Zou, Y.-l.; Tang, J.-j. A hierarchical porous carbon material for high power, lithium ion batteries. *Electrochimica Acta* **2011**, *56* (24), 8576-8581. DOI: https://doi.org/10.1016/j.electacta.2011.07.047.
(138) Kang, D.-Y.; Kim, S.-O.; Chae, Y. J.; Lee, J. K.; Moon, J. H. Particulate Inverse Opal Carbon Electrodes for Lithium-Ion Batteries. *Langmuir* **2013**, *29* (4), 1192-1198. DOI: 10.1021/la304556w.
(139) Jayaprakash, N.; Shen, J.; Moganty, S. S.; Corona, A.; Archer, L. A.; Energy Frontier Research Centers . Energy Materials Center at, C.; Cornell Univ, I. N. Y. Porous Hollow Carbon@Sulfur Composites for High-Power Lithium-Sulfur Batteries. *Angewandte Chemie (International ed.)* **2011**, *50* (26), 5904-5908. DOI: 10.1002/anie.201100637.
(140) Xu, Y.; Zhu, Y.; Liu, Y.; Wang, C. Electrochemical performance of porous carbon/tin composite anodes for sodium-ion and lithium-ion batteries. *Advanced Energy Materials* **2013**, *3* (1), 128-133.
(141) McNulty, D.; Geaney, H.; O'Dwyer, C. Carbon-Coated Honeycomb Ni-Mn-Co-O Inverse Opal: A High Capacity Ternary Transition Metal Oxide Anode for Li-ion Batteries. *Scientific Reports* **2017**, *7* (1), 42263. DOI: 10.1038/srep42263.
(142) Luo, F.; Liu, B.; Zheng, J.; Chu, G.; Zhong, K.; Li, H.; Huang, X.; Chen, L. Nano-silicon/carbon composite anode materials towards practical application for next generation Li-ion batteries. *Journal of The Electrochemical Society* **2015**, *162* (14), A2509.
(143) Ho, M.; Khiew, P.; Isa, D.; Tan, T.; Chiu, W.; Chia, C. A review of metal oxide composite electrode materials for electrochemical capacitors. *Nano* **2014**, *9* (06), 1430002.
(144) Wu, Z.-S.; Zhou, G.; Yin, L.-C.; Ren, W.; Li, F.; Cheng, H.-M. Graphene/metal oxide composite electrode materials for energy storage. *Nano Energy* **2012**, *1* (1), 107-131.
(145) Ryu, H.-H.; Sun, H. H.; Myung, S.-T.; Yoon, C. S.; Sun, Y.-K. Reducing cobalt from lithium-ion batteries for the electric vehicle era. *Energy & Environmental Science* **2021**, *14* (2), 844-852.
(146) Zhao, H.; Pan, L.; Xing, S.; Luo, J.; Xu, J. Vanadium oxides–reduced graphene oxide composite for lithium-ion batteries and supercapacitors with improved electrochemical performance. *Journal of Power Sources* **2013**, *222*, 21-31. DOI: https://doi.org/10.1016/j.jpowsour.2012.08.036.
(147) Kasavajjula, U.; Wang, C.; Appleby, A. J. Nano- and bulk-silicon-based insertion anodes for lithium-ion secondary cells. *Journal of Power Sources* **2007**, *163* (2), 1003-1039. DOI: https://doi.org/10.1016/j.jpowsour.2006.09.084.
(148) Al Ja'farawy, M. S.; Hikmah, D. N.; Riyadi, U.; Purwanto, A.; Widiyandari, H. A Review: The Development of SiO2/C Anode Materials for Lithium-Ion Batteries. *Journal of Electronic Materials* **2021**, *50* (12), 6667-6687. DOI: 10.1007/s11664-021-09187-x.
(149) Lee, G.; Kim, S.; Kim, S.; Choi, J. SiO2/TiO2 Composite Film for High Capacity and Excellent Cycling Stability in Lithium-Ion Battery Anodes. *Advanced Functional Materials* **2017**, *27* (39), 1703538. DOI: https://doi.org/10.1002/adfm.201703538 (acccessed 2023/09/04).
(150) Zhu, X. J.; Guo, Z. P.; Zhang, P.; Du, G. D.; Poh, C. K.; Chen, Z. X.; Li, S.; Liu, H. K. Three-dimensional reticular tin–manganese oxide composite anode

materials for lithium ion batteries. *Electrochimica Acta* **2010**, *55* (17), 4982-4986. DOI: https://doi.org/10.1016/j.electacta.2010.03.107.
(151) Chen, Y.-C.; Chen, J.-M.; Huang, Y.-H.; Lee, Y.-R.; Shih, H. C. Size effect of tin oxide nanoparticles on high capacity lithium battery anode materials. *Surface and Coatings Technology* **2007**, *202* (4-7), 1313-1318.
(152) Manthiram, A.; Fu, Y.; Su, Y.-S. Challenges and prospects of lithium–sulfur batteries. *Accounts of chemical research* **2013**, *46* (5), 1125-1134.
(153) Seh, Z. W.; Sun, Y.; Zhang, Q.; Cui, Y. Designing high-energy lithium–sulfur batteries. *Chemical society reviews* **2016**, *45* (20), 5605-5634.
(154) Su, Y.-S.; Fu, Y.; Manthiram, A. Self-weaving sulfur–carbon composite cathodes for high rate lithium–sulfur batteries. *Physical Chemistry Chemical Physics* **2012**, *14* (42), 14495-14499.
(155) Liu, J.; Feng, H.; Jiang, J.; Qian, D.; Li, J.; Peng, S.; Liu, Y. Anatase-TiO2/CNTs nanocomposite as a superior high-rate anode material for lithium-ion batteries. *Journal of Alloys and Compounds* **2014**, *603*, 144-148. DOI: https://doi.org/10.1016/j.jallcom.2014.03.089.
(156) Chen, J.; Wang, E.; Mu, J.; Ai, B.; Zhang, T.; Ge, W.; Zhang, L. CNTs–C@TiO2 composites with 3D networks as anode material for lithium/sodium ion batteries. *Journal of materials science* **2019**, *54* (1), 592-604. DOI: 10.1007/s10853-018-2814-2.
(157) Zhang, Y.; Zhang, N.; Chen, J.; Zhang, T.; Ge, W.; Zhang, W.; Xie, G.; Zhang, L.; He, Y. Preparation and lithium storage properties of C@TiO2/3D carbon hollow sphere skeleton composites. *Journal of Alloys and Compounds* **2020**, *815*, 152511. DOI: https://doi.org/10.1016/j.jallcom.2019.152511.
(158) Liu, H.; Li, W.; Shen, D.; Zhao, D.; Wang, G. Graphitic Carbon Conformal Coating of Mesoporous TiO2 Hollow Spheres for High-Performance Lithium Ion Battery Anodes. *Journal of the American Chemical Society* **2015**, *137* (40), 13161-13166. DOI: 10.1021/jacs.5b08743.
(159) Li, L.; Yin, X.; Liu, S.; Wang, Y.; Chen, L.; Wang, T. Electrospun porous SnO2 nanotubes as high capacity anode materials for lithium ion batteries. *Electrochemistry Communications* **2010**, *12* (10), 1383-1386. DOI: https://doi.org/10.1016/j.elecom.2010.07.026.
(160) Giri, P. K.; Dhara, S. Freestanding Ge/GeO2 Core-Shell Nanocrystals with Varying Sizes and Shell Thicknesses: Microstructure and Photoluminescence Studies. *Journal of nanomaterials* **2011**, *2012*. DOI: 10.1155/2012/905178.
(161) Yan, S.; Song, H.; Lin, S.; Wu, H.; Shi, Y.; Yao, J. GeO2 Encapsulated Ge Nanostructure with Enhanced Lithium-Storage Properties. *Advanced Functional Materials* **2019**, *29* (8), 1807946, https://doi.org/10.1002/adfm.201807946. DOI: https://doi.org/10.1002/adfm.201807946 (acccessed 2022/06/28).
(162) Yang, L. C.; Gao, Q. S.; Li, L.; Tang, Y.; Wu, Y. P. Mesoporous germanium as anode material of high capacity and good cycling prepared by a mechanochemical reaction. *Electrochemistry Communications* **2010**, *12* (3), 418-421. DOI: https://doi.org/10.1016/j.elecom.2010.01.008.
(163) Zeng, L.; Huang, X.; Chen, X.; Zheng, C.; Qian, Q.; Chen, Q.; Wei, M. Ge/GeO2-Ordered Mesoporous Carbon Nanocomposite for Rechargeable Lithium-Ion Batteries with a Long-Term Cycling Performance. *ACS Applied Materials & Interfaces* **2016**, *8* (1), 232-239. DOI: 10.1021/acsami.5b08470.
(164) Chan, C. K.; Zhang, X. F.; Cui, Y. High Capacity Li Ion Battery Anodes Using Ge Nanowires. *Nano Letters* **2008**, *8* (1), 307-309. DOI: 10.1021/nl0727157.

(165) McNulty, D.; Geaney, H.; Ramasse, Q.; O'Dwyer, C. Long Cycle Life, Highly Ordered SnO2/GeO2 Nanocomposite Inverse Opal Anode Materials for Li-Ion Batteries. *Advanced Functional Materials* **2020**, *30* (51), 2005073, https://doi.org/10.1002/adfm.202005073. DOI: https://doi.org/10.1002/adfm.202005073 (acccessed 2021/02/22).
(166) Tang, Y.; Zhang, H.; Li, J.; Hou, G.; Cao, H.; Wu, L.; Zheng, G.; Wu, Q. Three-dimensional ordered macroporous Cu/Fe3O4 composite as binder-free anode for lithium-ion batteries. *Journal of Alloys and Compounds* **2017**, *719*, 203-209. DOI: https://doi.org/10.1016/j.jallcom.2017.05.172.
(167) Grosjean, C.; Miranda, P. H.; Perrin, M.; Poggi, P. Assessment of world lithium resources and consequences of their geographic distribution on the expected development of the electric vehicle industry. *Renewable and Sustainable Energy Reviews* **2012**, *16* (3), 1735-1744. DOI: https://doi.org/10.1016/j.rser.2011.11.023.
(168) Kubota, K.; Dahbi, M.; Hosaka, T.; Kumakura, S.; Komaba, S. Towards K-Ion and Na-Ion Batteries as "Beyond Li-Ion". *The Chemical Record* **2018**, *18* (4), 459-479. DOI: https://doi.org/10.1002/tcr.201700057 (acccessed 2023/11/10).
(169) Shannon, R. D. Revised effective ionic radii and systematic studies of interatomic distances in halides and chalcogenides. *Acta crystallographica section A: crystal physics, diffraction, theoretical and general crystallography* **1976**, *32* (5), 751-767.
(170) Ohzuku, T.; Iwakoshi, Y.; Sawai, K. Formation of lithium-graphite intercalation compounds in nonaqueous electrolytes and their application as a negative electrode for a lithium ion (shuttlecock) cell. *Journal of The Electrochemical Society* **1993**, *140* (9), 2490.
(171) Komaba, S.; Hasegawa, T.; Dahbi, M.; Kubota, K. Potassium intercalation into graphite to realize high-voltage/high-power potassium-ion batteries and potassium-ion capacitors. *Electrochemistry Communications* **2015**, *60*, 172-175. DOI: https://doi.org/10.1016/j.elecom.2015.09.002.
(172) Manthiram, A. A reflection on lithium-ion battery cathode chemistry. *Nature Communications* **2020**, *11* (1), 1550. DOI: 10.1038/s41467-020-15355-0.
(173) Yabuuchi, N.; Kubota, K.; Dahbi, M.; Komaba, S. Research Development on Sodium-Ion Batteries. *Chemical Reviews* **2014**, *114* (23), 11636-11682. DOI: 10.1021/cr500192f.
(174) Liao, J.; Han, Y.; Zhang, Z.; Xu, J.; Li, J.; Zhou, X. Recent progress and prospects of layered cathode materials for potassium-ion batteries. *Energy & Environmental Materials* **2021**, *4* (2), 178-200.
(175) Zhang, C.; Xu, Y.; Zhou, M.; Liang, L.; Dong, H.; Wu, M.; Yang, Y.; Lei, Y. Potassium Prussian Blue Nanoparticles: A Low-Cost Cathode Material for Potassium-Ion Batteries. *Advanced Functional Materials* **2017**, *27* (4), 1604307. DOI: https://doi.org/10.1002/adfm.201604307 (acccessed 2023/11/11).
(176) Yang, Y.; Zhou, J.; Wang, L.; Jiao, Z.; Xiao, M.; Huang, Q.-a.; Liu, M.; Shao, Q.; Sun, X.; Zhang, J. Prussian blue and its analogues as cathode materials for Na-, K-, Mg-, Ca-, Zn- and Al-ion batteries. *Nano Energy* **2022**, *99*, 107424. DOI: https://doi.org/10.1016/j.nanoen.2022.107424.
(177) Xue, L.; Li, Y.; Gao, H.; Zhou, W.; Lü, X.; Kaveevivitchai, W.; Manthiram, A.; Goodenough, J. B. Low-Cost High-Energy Potassium Cathode. *Journal of the American Chemical Society* **2017**, *139* (6), 2164-2167. DOI: 10.1021/jacs.6b12598.
(178) Wang, L.; Lu, Y.; Liu, J.; Xu, M.; Cheng, J.; Zhang, D.; Goodenough, J. B. A Superior Low-Cost Cathode for a Na-Ion Battery. *Angewandte Chemie International*

Edition **2013**, *52* (7), 1964-1967. DOI: https://doi.org/10.1002/anie.201206854 (acccessed 2023/11/11).
(179) Zhou, M.; Xu, Y.; Wang, C.; Li, Q.; Xiang, J.; Liang, L.; Wu, M.; Zhao, H.; Lei, Y. Amorphous TiO2 inverse opal anode for high-rate sodium ion batteries. *Nano Energy* **2017**, *31*, 514-524. DOI: https://doi.org/10.1016/j.nanoen.2016.12.005.
(180) Wang, Y.; Kong, D.; Shi, W.; Liu, B.; Sim, G. J.; Ge, Q.; Yang, H. Y. Ice Templated Free-Standing Hierarchically WS2/CNT-rGO Aerogel for High-Performance Rechargeable Lithium and Sodium Ion Batteries. *Advanced Energy Materials* **2016**, *6* (21), 1601057. DOI: https://doi.org/10.1002/aenm.201601057 (acccessed 2023/11/12).
(181) Hu, X.; Jia, J.; Wang, G.; Chen, J.; Zhan, H.; Wen, Z. Reliable and General Route to Inverse Opal Structured Nanohybrids of Carbon-Confined Transition Metal Sulfides Quantum Dots for High-Performance Sodium Storage. *Advanced Energy Materials* **2018**, *8* (25), 1801452. DOI: https://doi.org/10.1002/aenm.201801452 (acccessed 2023/11/12).
(182) He, H.; Huang, D.; Tang, Y.; Wang, Q.; Ji, X.; Wang, H.; Guo, Z. Tuning nitrogen species in three-dimensional porous carbon via phosphorus doping for ultra-fast potassium storage. *Nano Energy* **2019**, *57*, 728-736. DOI: https://doi.org/10.1016/j.nanoen.2019.01.009.
(183) Wang, W.; Zhou, J.; Wang, Z.; Zhao, L.; Li, P.; Yang, Y.; Yang, C.; Huang, H.; Guo, S. Short-range order in mesoporous carbon boosts potassium-ion battery performance. *Advanced Energy Materials* **2018**, *8* (5), 1701648.
(184) Li, D.; Ren, X.; Ai, Q.; Sun, Q.; Zhu, L.; Liu, Y.; Liang, Z.; Peng, R.; Si, P.; Lou, J.; et al. Facile Fabrication of Nitrogen-Doped Porous Carbon as Superior Anode Material for Potassium-Ion Batteries. *Advanced Energy Materials* **2018**, *8* (34), 1802386. DOI: https://doi.org/10.1002/aenm.201802386 (acccessed 2023/11/12).
(185) Zhou, X.; Chen, L.; Zhang, W.; Wang, J.; Liu, Z.; Zeng, S.; Xu, R.; Wu, Y.; Ye, S.; Feng, Y.; et al. Three-Dimensional Ordered Macroporous Metal–Organic Framework Single Crystal-Derived Nitrogen-Doped Hierarchical Porous Carbon for High-Performance Potassium-Ion Batteries. *Nano Letters* **2019**, *19* (8), 4965-4973. DOI: 10.1021/acs.nanolett.9b01127.

Chapter 3

Experimental Methods

3.1 Introduction

This chapter serves as an introduction to the experimental procedures and techniques utilized during the research conducted for this thesis. The fabrication method for electrode materials and the techniques used for material characterisation, such as scanning electron microscopy (SEM), transmission electron microscopy (TEM), X-ray diffraction (XRD), X-ray photoelectron spectroscopy (XPS), energy-dispersive X-ray Spectroscopy (EDX), electron diffraction and ramen will be detailed. Cell preparation procedures will be outlined, namely electrolyte preparation for lithium-ion, sodium-ion, and potassium-ion batteries as well preparation of counter electrodes and cell assembly. The techniques used for electrochemical characterisation will also be discussed. For each characterisation technique, the background theory and concept will be explained, followed by specific application.

3.2 Sample Preparation

3.2.1 Substrate Preparation and Template Formation

The substrates used through this thesis were stainless-steel (grade 304) discs of 15.5 mm diameter and 0.2 mm thickness. Firstly, successive sonication was used to clean the substrates using acetone (reagent grade 99.5% from Sigma Aldrich), isopropyl alcohol (IPA) (reagent grade 99.5% from Sigma Aldrich), followed by sonication in deionised water, each for 5 minutes at a time. This was done to remove any dust particles or inorganic salts on the discs. The cleaned discs were placed in an oven at 55 °C until dry. The substrates then underwent a one-hour treatment in a Novascan PSD Pro Series digital UV-ozone system to eliminate residual organic material and

enhance the surface hydrophilicity before photonic crystal template formation. The starting mass was then taken of each disc before template deposition.

The colloidal crystal solution used as the template was prepared using aqueous polystyrene sphere (PS) suspensions (2.5 % wt.) from Polysciences Inc. with diameters of 500nm. These were mixed with deionised water to yield either a 0.1 % (Chapter 4) or 0.2 % (Chapter 5 and 6) solution. The cleaned and dry discs were then suspended using Kapton tape at an angle of ~30° to aid the self-assembly process and immersed in the solution of PS spheres and deionised water as seen in Fig 3.1. The vials were then kept in a convection oven at 60 °C overnight to evaporate the water and allow the PS to self-assemble onto the stainless steel substrates.

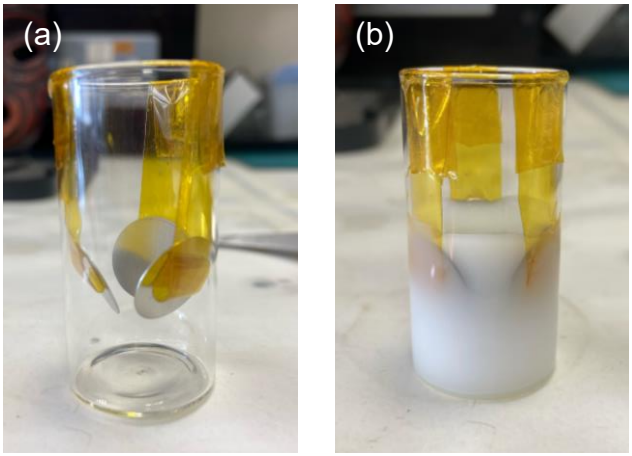

Figure 3.1 Photographs of (a) stainless steel discs suspended at angle in glass vial and (b) stainless steel discs submerged in polystyrene sphere solution before heating.

3.2.2 Inverse Opal Fabrication via Sol-Gel Deposition

Throughout this thesis, the sol-gel precursor deposition method was employed for infilling the opal templates. This method was chosen due to its cost-effectiveness and relatively rapid application compared to other deposition techniques, such as vapor phase processes. Another reason is the avoidance of very high temperatures, which

would be unsuitable for the polymer template used.[1, 2] Depending on the experiment, different precursors were prepared as detailed in the respective chapters. However, the process for infiltration was the same for all chapters, depicted in Fig 3.2. The precursor solution was infilled using a specific volume measured with a micropipette. The standard sol-gel process involves hydrolysis of a metal alkoxide species, followed by condensation of hydrolyzed molecules to form longer inorganic chains, which creates a gel. The gel consists of metal-oxo-metal or metal-hydroxy-metal bonds. Subsequent drying and calcination of the gel removes surface hydroxy groups and can crystallize amorphous metal oxide films. Calcination is also used to remove the opal template and therefore produce the inverse opal structure.

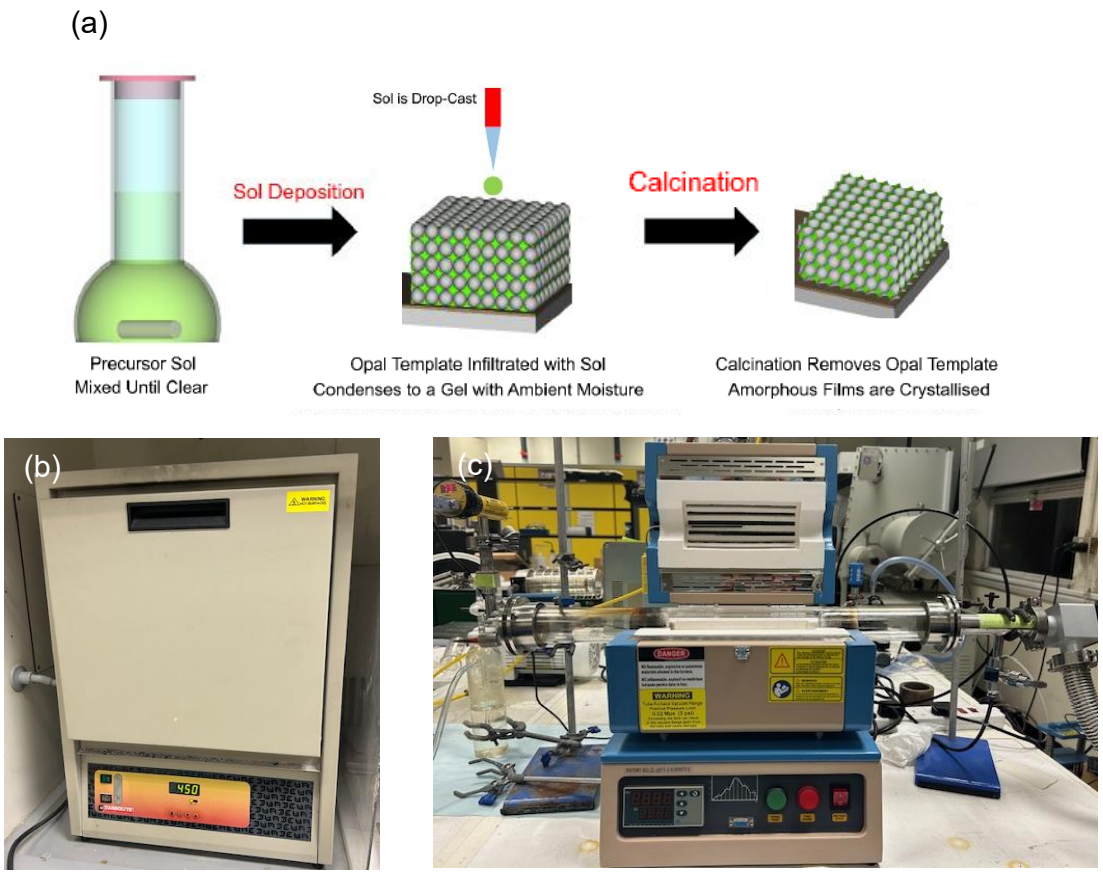

Figure 3.2. (a) Schematic diagram of sol-gel infilling technique, followed by calcination to produce inverse opal structure. Photographs of (b) convection oven to heat samples in air, and (c) tube furnace used to carbonize carbon samples.

Chapter 4 uses a titanium (IV) chloride tetrahydrofuran complex ($TiCl_4.2THF$) from Sigma Aldrich for the TiO_2 precursor and germanium ethoxide ($Ge(OC_2H_5)_4$) from Sigma Aldrich for the GeO_2 precursor. The $TiCl_4.2THF$ and $Ge(OC_2H_5)_4$ were mixed with IPA to a 0.1 M and 0.05 M concentration, respectively. These solutions were mixed individually until clear solutions were formed and then combined in a 1:1 v/v ratio. Subsequent calcination at 450 ℃ yielded the TiO_2/GeO_2 inverse opals.

Chapter 5 uses the same $TiCl_4.2THF$ precursor with a sucrose-based precursor for the carbon. The carbon precursor consists of sucrose, (EtOH), deionized water and sulphuric acid (18 M, Sigma Aldrich). The sucrose was weighed out at 0.2 g before being added to a solution of 9 mL EtOH, 1 mL of H_2O and 20 µL of H_2SO_4. This was mixed until the sucrose was dissolved. The $TiCl_4.2THF$ precursor was pipetted on to the template first before the same volume of the carbon precursor was pipetted on to the sample. The annealing process differs compared to Chapter 4, the C/TiO_2 samples were heated in air firstly, in a convection oven at 70 ℃ for 30 minutes to evaporate the H_2O and IPA, before being heated to 100 ℃ for 5 hours (in air). The samples were then transferred to a tube furnace and heated to 500 ℃ under argon at a ramp rate of 5 ℃ /min and held at this temperature for 2 hours.

Chapter 6 uses the same carbon precursor as Chapter 5, however the tube furnace was heated to 900 ℃ before being held for 2 hours.

3.2.3 Sample Preparation for Post-Mortem Analysis

For post-mortem SEM image acquisition, the electrodes used for electrochemical tested needed to be disassembled and washed in the glovebox to remove residual crystallized electrolyte. Additionally, incorporating a washing step proves beneficial

in mitigating sample corrosion. This is crucial because $LiPF_6$ reacts with both H_2O and O_2. Washing was done with the electrolyte solvent used during cycling, in Chapter 4 and 5 this was dimethyl carbonate (DMC). The cycled electrodes were immersed in DMC twice, firstly for 30 – 60 minutes followed by another 30 minutes in new DMC. The samples were then dried under vacuum using the glovebox antechamber for ~ 15 mins until dry.

3.3 Material Characterisation Techniques

3.3.1 Scanning Electron Microscopy

Scanning electron microscopy (SEM) is a useful imaging technique used to investigate the surface morphology and composition of different materials at high magnification. Using electrons rather than light to form an image, SEM scans the surface with a focused beam of electrons and detects the signals emitted as a result of interactions between the electron beam and the atoms in the specimen. The electron beam travels vertically through the microscope, which is held in a vacuum, and can possess energy of between 0.2 – 40 kV.

When the primary electron beam engages with the sample, it undergoes energy loss due to repeated random scattering and absorption within a region known as the interaction volume.[3] At specific accelerating voltages, the interaction volume takes on a "teardrop" shape for specimens with low atomic numbers and a hemisphere shape for specimens with high atomic numbers, shown in Fig.3.3. This volume extends from less than 100 nm to about 5 μm into the surface of the specimen. The expansion of volume and penetration depth occurs with increased beam energy but decreases with a rise in the atomic number of the specimen.[4] This is attributed to specimens with

higher atomic numbers having a greater number of particles that impede electron penetration. A notable impact of the interaction volume on signal acquisition is observed when utilizing a high accelerating voltage, as it leads to a deeper penetration length and a larger primary excitation region. This may potentially lead to the omission of detailed surface information in the samples. The interaction results in various phenomena, including the reflection of high-energy electrons through elastic scattering (backscattered electrons), the release of secondary electrons via inelastic scattering, and the emission of electromagnetic radiation. Secondary electron images are commonly obtained, providing surface details, but backscattered electron images also offer valuable information, varying with specimen composition, surface topography, crystallinity, and magnetism.

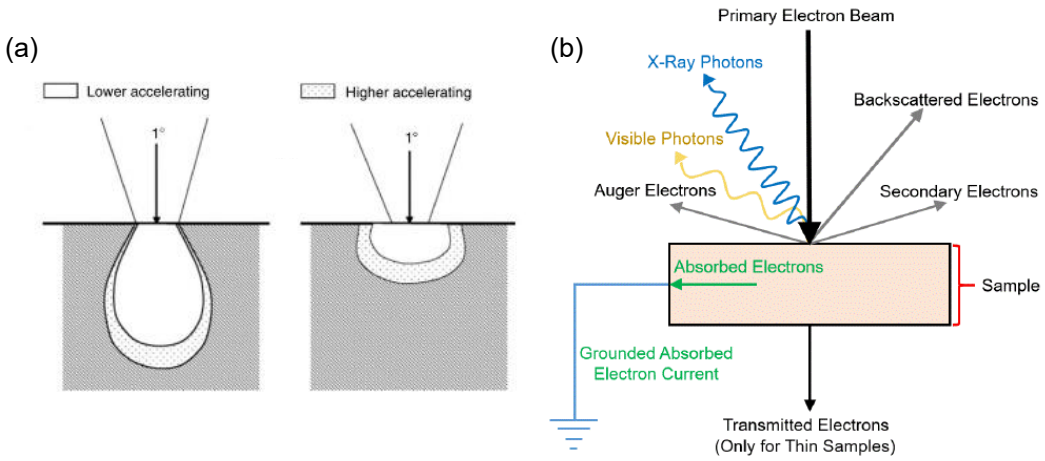

Figure 3.3. (a) Diagram showing injection volume for low atomic number (tear drop shape) and high atomic number (hemispherical shape).[4] (b) Illustration showing the various energy signals produces when a primary electron beam interacts with a sample surface in a standard SEM chamber.

SEM resolution relies on the size of the probe spot and the current density. The SEM process can induce charge buildup on low-conductivity samples, leading to image distortion. To optimize resolution, techniques such as sample tilting and adjusting probe current densities are employed. Sample tilting is also valuable for

assessing the thickness of the IO structure and ensuring uniformity across the structures. These methods enhance magnification and contrast while preserving high image quality. SEM analysis was performed using an FEI Quanta 650 SEM with accelerating voltages of 10 kV to 20 kV throughout Chapters 4-6.

3.3.2 Energy-Dispersive X-ray Spectroscopy

Energy dispersive X-ray spectroscopy (EDS or EDX) is an analytical technique used in conjunction with SEM to characterize elemental composition of materials. The fundamental principle behind EDS lies in the interaction between the high-energy electrons from the primary beam in SEM and the atoms within the sample. When the electrons strike the sample, X-ray photons are generated along with the secondary and backscattered electrons used for imaging in SEM. In the event of a collision with a primary electron, the displacement of an inner shell electron can prompt an outer shell electron to fall into the inner shell, restoring the appropriate charge balance within its orbitals after an ionization event.[5] The ionized atom returns to ground state, with the emission of an X-ray photon. Each element emits X-rays at specific energies, producing a spectral fingerprint which allows for identification and quantification of the elemental composition.

EDS was used in Chapter 4 and 5 and provide useful information on the atomic ratios of the composite electrodes. EDS analysis was performed using two instruments. An FEI Quanta 650 SEM with accelerating voltage of 20 kV was used for analysis and elemental mapping in Chapters 4. While a Zeiss Supra 40 high resolution SEM was used for Chapter 5 at an accelerating voltage of 20 kV.

3.3.3 Transmission Electron Microscopy

Transmission electron microscopy (TEM) is another microscopy technique used for imaging. Similar to SEM, TEM uses a beam of electrons to form an image, however in TEM rather than the electrons being reflected (like in SEM), they are transmitted through the sample. This is a similar working principle to optical microscopes, however since electrons in an electron microscope have shorter wavelengths compared to visible light, TEM offers significantly higher resolution.[6] The wavelength of electrons is inversely proportional to their momentum, making them ideal for imaging objects on the nanoscale. Acceleration voltages of the electron beams are usually in the range of 80 kV to 400 kV.[7]

The use of high-resolution TEM (HRTEM) images facilitates phase identification from atomic lattice fringes. When an image is generated using two waves, one transmitted from a crystal and the other diffracted from a set of lattice planes within the crystal, a pattern of bright and dark stripes emerge which correspond to the lattice spacing.[8] Another mode of TEM is called scanning transmission electron microscopy (STEM), combining the SEM and TEM techniques. STEM focuses the electron beam into a fine probe that scans across the sample in a raster pattern. The transmitted electrons are then collected and used to create an image.[9] STEM provides high-resolution images similar to TEM but offers additional capabilities, such as annular dark-field imaging, and the ability to acquire compositional and elemental information through techniques like EDS or electron energy loss spectroscopy (EELS). STEM also allows for the imaging of thicker specimens compared to TEM.

Regarding sample preparation, TEM requires ultra-thin specimens, often less than 150 nm thick to allow electrons to penetrate. TEM analysis was carried out in Chapter 4 - 6, using FEI Titan 80-300 ThermoFisher Scientific at 300 kV in Chapter 4

and JEOL JEM-2100F TEM operating at 200 kV in Chapter 5 and 6. The samples are prepared directly onto the current collector as outlined in section 3.2.2, however for TEM analysis the samples needed to be prepared on a specific TEM grid. Holey Carbon Films on 300 Mesh Copper were used from Agar Scientific Ltd. The samples were scraped on to B-2 sheets (from Sigma Aldrich), and lightly crushed with a spatula. The powder was poured into a clean vial before adding 0.2 mL deionized water to the vial. The vial was then sonicated for 5 minutes, if the solution was too dark or the samples hadn't dispersed more H_2O was added. The solution was sonicated again for a further 5 minutes before using a 1 mL syringe to drop 2 drops of the solution onto the TEM grid. An infrared light was used to dry the grids before another two drops were placed. The procedure for sample preparation was the same for both instruments.

3.3.4 Electron Diffraction

TEM utilizes controlled electron beams to conduct electron diffraction experiments which provide value information about lattice constants, symmetries, and crystal structures. The electron beam, manipulated by electron optics such as magnetic lenses, deflectors, and apertures, passes through a thin film of the material. Above and below the sample, optical elements control the incident beam, allowing for a wide range of beam manipulations. Different TEM modes, such as selected area electron diffraction (SAED), enable the collection of diffraction information from specific regions, although limitations arise with smaller regions due to the need for a focused probe.[10] TEM's diffraction patterns depend on factors like crystal orientation and the number of contributing crystallites, offering insights into material structures at the atomic and nanoscale. The method, however, has limitations, and distinguishing between small-

grain polycrystalline materials and truly random order amorphous substances can be challenging.[11]

This technique was employed in Chapters 4 and 5 to analyze crystallinity in TiO_2/GeO_2 IOs and C/TiO_2 IOs, respectively. In Chapter 6, this technique was employed to confirm graphitic regions in disordered carbon. It was performed using the transmission electron microscopes outlined in section 3.3.3.

3.3.5 Electron Energy Loss Spectroscopy

Electron energy loss spectroscopy (EELS) operates within TEM and enables characterization of the material's elemental composition and electronic structure with high spatial resolution. In EELS, a focused beam of electrons is transmitted through the sample, some of these electrons will undergo inelastic scattering due to interactions with the sample's inner-shell electrons.[12] These interactions cause the electrons to lose energy and have their paths altered or deflected, the energy lost corresponds to specific electronic transitions and excitations within the sample.[13]

The spectrum, known as an energy loss spectrum, contains peaks and edges corresponding to the energy losses associated with specific electronic transitions. The edges are formed when an inner-shell electron absorbs enough energy from a beam electron to be excited to a state above the Fermi level.[14] One of the notable applications of EELS is in mapping the distribution of elements within a sample. By acquiring EELS spectra at different locations, elemental maps can be generated revealing the spatial distribution of specific elements, offering detailed insights into the material's composition, similar to EDS. EELS is performed in Chapter 4 using a FEI Titan 80-

300 ThermoFisher Scientific TEM at 300 kV with a Tridium 863 spectrometer with the energy dispersion set to 0.1 eV/channel.

3.3.6 Raman Spectroscopy

Raman spectroscopy is an analytical technique that provides insights into molecular vibrations and structures. Raman spectroscopy operates by illuminating a sample with a monochromatic laser beam which causes scattering of photons when it interacts with molecular bonds in the sample. When a molecule scatters light, the oscillating electromagnetic field of a photon induces polarization in the molecular electron cloud.[15] This leaves the molecule in a higher energy state, with the photon's energy transferred to the molecule. This process can be conceptualized as the transient formation of a complex between the photon and the molecule, often referred to as the virtual state of the molecule. However, the virtual state is inherently unstable, and the photon is promptly reemitted as scattered light.

In most cases, the scattered photons maintain the same energy as the incident light (elastic scattering or Rayleigh scattering), but a small fraction undergoes inelastic scattering, resulting in either lower-energy (Stokes scattering) or higher-energy (Anti-Stokes scattering) photons.[16] The frequency difference between the incident and scattered photons, known as the Raman shift, provides information about the vibrational modes of the molecular bonds in the sample. Rayleigh scattering is filtered out by either a notch filter, edge pass filter, or a band pass filter in the case of this thesis, while the rest of the collected light is dispersed onto a detector.

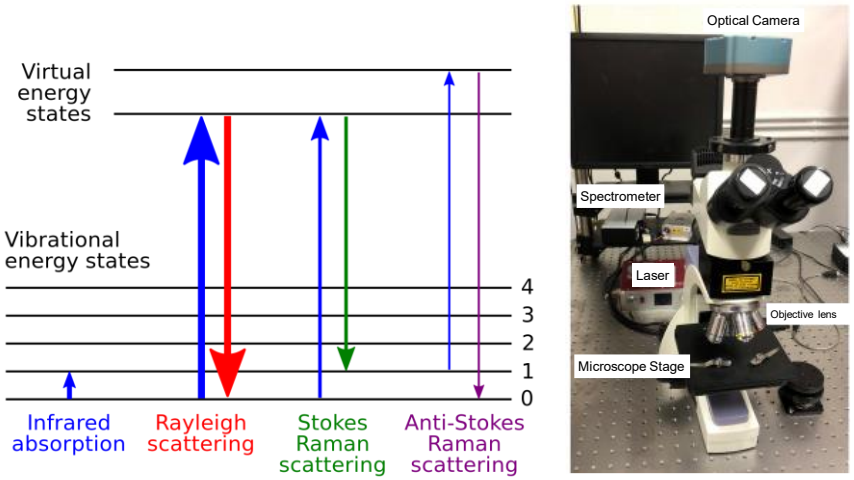

Figure 3.4 Energy-level diagram showing the states and excitations involved in Raman spectroscopy. Photograph of Raman microscope set-up used throughout this thesis.

The Raman spectrometer consists of a laser source, a monochromator to select desired wavelength, and a detector. An Ocean Optics QE65PRO Raman Spectrometer using a 20 mW Ar^+ laser at 532 nm laser served as the excitation source for all Raman spectra in Chapters 4-6, the power was adjusted depending on sample, as outlined in the respective chapters. Factors such as required scattering intensity, the photo-saturation limit of the detector, the materials susceptibility to fluorescence interference and potential sample degradation. The laser could be focused with a variety of microscope objective lenses, as shown in Fig. 3.4. An optical camera was fitted to the microscope to allow for image capturing of the area struck by the laser and focused by the objective lens. A RenCam charge-coupled device (CCD) was used in collection of the Raman signal. As stated, the power for the laser was adjusted based on material factors, in Chapter 4, 25 mW was used, while in Chapter 5 and 6, 40 mW was used. This was due to the fluorescence observed when analysing the TiO_2/GeO_2 which required the need for less power to reduce background noise/fluorescence. All measurements were taken over 4 scans to average with an integration time of 6 seconds.

3.3.7 X-ray Diffraction

X-ray crystallography or X-ray diffraction (XRD) is another material characterization technique used in this thesis work. XRD helps determine atomic and molecular structure of crystals by striking the sample with a beam of X-rays which diffract to specific directions. The interaction between X-rays and the crystal lattice gives rise to constructive interference, where X-rays are scattered in specific directions determined by the lattice spacings of the crystal sample. Bragg's Law (Eq. 3.1), a fundamental principle in XRD, mathematically describes this phenomenon, stating that for constructive interference to occur, the path difference between the scattered waves from adjacent crystal planes must be an integer multiple *n* of the X-ray wavelength λ for a given angle θ.[17] The reflections used in XRD are associated with evenly spaced sheets within a crystal. These sheets, which pass through the crystal lattice's atomic centers, are characterized by their Miller indices (h, k , l) and spacing (*d*).

$$2d \sin\theta = n\lambda \qquad \text{Eq. 3.1}$$

Indexed reflections provide information about the crystal lattice's unit-cell parameters and space group. However, amorphous materials, lacking a well-defined crystal structure, do not produce diffraction patterns suitable for analysis. It is worth noting that composite materials often consist of multiple phases with different crystal structures.[18] The diffraction patterns from different phases can often overlap which can lead to complex interpretations. In this context, the XRD preformed throughout this thesis is complemented with other characterization techniques to obtain a more comprehensive understanding of the structures. X-ray diffraction was conducted using a Philips X'pert Pro MPD, equipped with a Panalytical Empyrean Cu X-ray tube and a Philips X'celerator detector in Chapters 4 and 5.

3.3.8 X-Ray Photoelectron Spectroscopy

X-ray photoelectron spectroscopy (XPS) uses X-rays to determine elemental composition, chemical states (oxidation states), and electronic state of the atoms in a material. It differs from XRD in that the atoms of the samples surface absorb X-rays and emit electrons to be studied, whereas in XRD the atoms of the sample just reflect the X-rays. The incident X-rays that strike the sample, eject inner-shell electrons from the atoms near the surface of the material. The kinetic energies of the ejected electrons are measured by the detector, and are directly related to the energy of the incident X-ray and the binding energy of the electrons in the material.[19] The binding energy is the energy required to remove an electron from a specific atomic orbital, it depends not only on its atomic orbital but also on the chemical environment of that electron's atom.[20]

By collecting the emitted photoelectrons and analyzing them, a spectrum is generated that reveals the binding energy of electrons within the sample. Each element exhibits characteristic peaks in the XPS spectrum corresponding to its unique electronic structure. Furthermore, the intensity of the XPS peaks is proportional to the concentration of the corresponding elements, which allows for quantitative analysis.

Depth profiling uses an ion beam to etch layers of the surface, revealing subsurface information. Conducting a series of ion gun etch cycles in conjunction with XPS analyses offers both quantified information and layer thickness measurements. Initially, a spectrum or set of spectra is captured from the sample surface before any material removal. Subsequently, the surface undergoes etching as an ion beam is scanned across a square or rectangular area of the sample. Following the etch cycle, the ion beam is deactivated, and another set of spectra is acquired. The accuracy of the XPS depth profile outcome relies on the assumption that any damage caused by the

etching is confined to the very top surface of the remaining material. This assumption is supported by the relatively high probing depth of XPS, approximately 10 nm, ensuring that the signal predominantly originates from deeper, undamaged material.[21, 22] In Chapter 4, this is utilized to map concentrations of elemental Ge through the composite material. The spectra were acquired using a Kratos AXIS ULTRA spectrometer. Survey scans were recorded between 0 and 1486 eV with a step size of 1.0 eV, dwell time of 50 ms, and pass energy of 160 eV and 20 eV for narrow spectral regions. Core level scans were acquired with a step size of 0.05 eV, dwell time of 100 ms, and pass energy of 20 eV averaged over 10 scans with an analysis nominal area of ~220 μm^2. A non-monochromated Al Kα X-ray source at 300 W power was used for all scans. For depth profiling, Ar^+ sputtering was in GCIS mono mode, at an energy of 5 keV and a 1.5 mm raster.

3.4 Electrochemical Cell Preparation

3.4.1 Electrode Preparation

All inverse opal materials were grown and then infilled directly on the 15 mm stainless steel substrate as outlined in section 3.2. Once the material were calcinated they were ready to be assembled in the battery cell, so no additional preparation was needed before cell assembly. The mass of the active material was calculated by weighing the finalised sample and comparing it to the mass taken of the substrate before IO fabrication. The typical mass loadings were between 0.3 – 0.7 mg depending on the material.

3.4.2 Electrolyte Preparation

The electrolyte used for all lithium-ion cells was 1 M lithium hexafluorophosphate ($LiPF_6$) salt in a 1:1 (v/v) mixture of ethylene carbonate (EC) and dimethyl carbonate (DMC), this was purchased from Sigma-Aldrich as prepared.

A 1 M sodium perchlorate ($NaClO_4$) salt from Alfa Aesar was used in propylene carbonate (PC) with a 5 vol. % fluoroethylene carbonate (FEC) additive to stabilise the SEI layer. This was prepared in the glove box, under inert atmosphere.

The electrolyte used for the potassium-ion batteries, tested in Chapter 6, was 1 M potassium hexafluorophosphate (KPF_6) in a 1:1 (v/v) mixture of EC and DMC. The KPF_6 salt was purchased from Sigma Aldrich as well as the EC and DMC. The salt and solvent were anhydrous, so the electrolyte was prepared under argon, in a glovebox. To prepare 25 mL of electrolyte, 0.025 moles (4.60 g) of KPF_6 was added to a 25 mL volumetric flask. EC is a solid at room temperature, so this was heated on a hot plate in the glove box for 4 hours until melted. When the EC was melted, 12.5 mL was added to 12.5 mL of DMC. This solution was slowly added to the volumetric flask containing KPF_6, a magnetic stirrer was then added and left to stir until the salt had dissolved.

3.4.3 Cell Assembly

EL Cell PAT cells were used for all electrochemical testing, these cells consisted of stainless steel (grade 316L) upper and lower plungers, polypropylene insulation sleeve (ECC1-00-0210-D/X, EL Cell) and borosilicate glass fiber as separators (Grade GF/A, Whatman). The insulation sleeve can be separated into two parts (shown in Fig. 3.5) to comfortably fit the separator between the two electrodes. To assemble the cell, the

lower plunger is fitted to the outer clips ring and the working electrode is placed onto the plunger, the separator is placed on top of the electrode before being secured using the inner clips ring. 100 µL of electrolyte is measured using a micropipette and then the counter electrode is fitted to the cell. For lithium-ion cells, the lithium discs were pre-cut whereas the sodium and potassium metal were purchased in chunks from Sigma Aldrich. Hence, these had to be cut and rolled out to the desired thickness before being punched into discs of 15 mm diameters. Once the counter electrode is placed, the upper plunger is placed on stop and a sealing ring fitted to the PAT cell casing or 'housing'. The PAT cells were then clipped into a clamp or docking station.

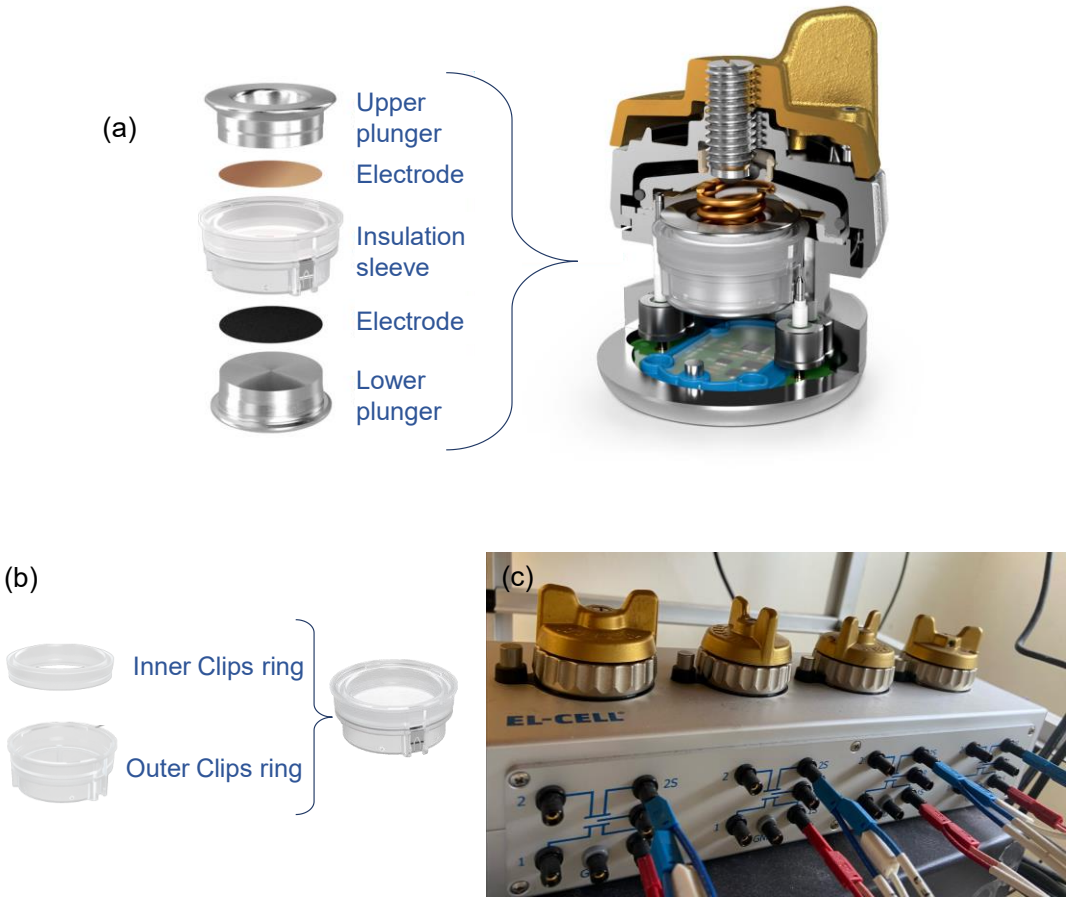

Figure 3.5. (a) Test cell equipment showing components such as upper plunger (conductor anode), and lower plunger (conductor cathode). (b) Insulation sleeve which can be disassembled to fit a separator (PAT-Cell by EL-CELL GmbH). (c) Photograph of docking station used to connect the PAT cells.

3.5 Electrochemical Characterisation Techniques

3.5.1 Cyclic Voltammetry

Cyclic voltammetry (CV) stands as a cornerstone technique in electrochemistry, employed to investigate the reduction and oxidation processes of chemical systems. CV measures the current response while cycling the potential of the working electrode. Fundamentally, CV involves sweeping the electrode potential linearly with time between two pre-defined potential limits. In contrast to linear sweep voltammetry, once the preset voltage is reached, the working electrode potential is reversed, returning to the initial potential, as can be seen in Fig. 3.6 (a). The potential sweep rate, known as the scan rate, is often denoted as v and dictates the speed at which the voltage is varied.[23] The generated voltammogram (Fig. 3.6 (b)), a plot of current vs voltage, reveals insights into the redox reactions taking place. The voltammogram's shape and features offer crucial details about the electrochemical systems being examined.

A complete CV scan comprises both negative and positive linear sweeps, known respectively as cathodic and anodic scans. The determination of peak potentials allows for the identification of the types of reactions occurring. Peak potentials play a crucial role in distinguishing the points at which each process unfolds. Quantitative information about the electrochemical system can also be extracted through analysis of the peak currents. The relationship between the current (i) and the sweep rate (v) is encapsulated by the Randles-Sevcik equation[24] for reversible redox processes. This equation provides a crucial link between the observed current and the concentration of electroactive species, aiding in the determination of diffusion coefficients and revealing information about mass transport limitations.

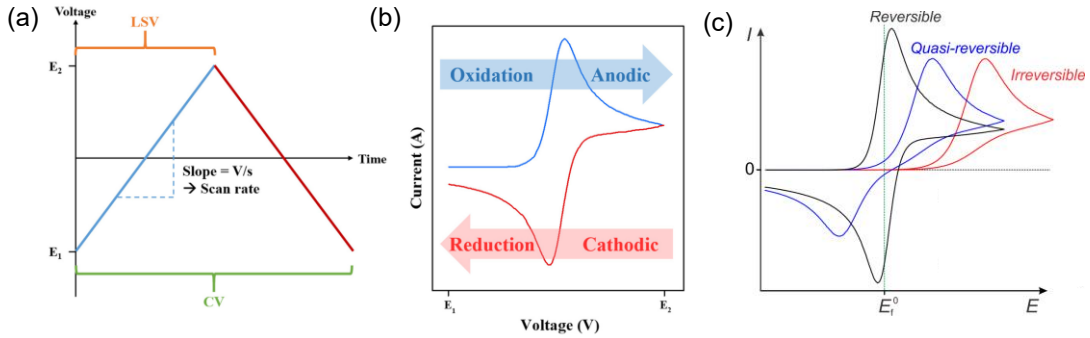

Figure 3.6 (a) Graph showing relationship between voltage and time during linear sweep voltammetry (LSV) and CV. (b)Typical CV graph generated, voltage vs current, showing reduction process (cathodic) direction and oxidation process (anodic) direction.[25] (c) Comparison of cyclic voltametric peaks and wave shapes for reversible, quasireversible and irreversible electron transfer processes.[26]

There are three main processes seen in cyclic voltammetry: reversible, quasireversible, and irreversible. In the context of reversible processes, the resulting voltammogram displays symmetric and well-defined peaks during both cathodic and anodic scans. For quasi-reversible processes, where the redox reaction involves a combination of reversible and irreversible components, CV provides a nuanced understanding of the electrochemical behavior. The voltammogram in such cases exhibits broadened and asymmetrical peaks, reflecting the influence of kinetic factors on the reaction.[27] In contrast, irreversible processes, marked by significant irreversibility and lack of backward reaction capability, are elucidated through CV by observing a single, distinct peak in the voltammogram. This is an important factor when studying electrode materials as alkali ions need to be inserted and extracted efficiently to provide long cycle life.

In Chapter 5 and 6, repeated cyclic voltammograms are taken at various scan rates to study diffusion (faradaic) and capacitive (non-faradaic) processes in the cell. By adjusting the scan rate, the contributions of these two fundamental mechanisms can be calculated. At lower scan rates, the electrochemical system has more time to

equilibrate or intercalate, emphasizing diffusion-controlled processes where the mass transport of ions to and from the electrode govern the current attained. In contrast, high scan rates promote capacitive processes, emphasizing the charging and discharging of the electrical double layer at the electrode interface. The formulas for calculating contributions are outlined in detail in Chapter 5 and 6, however in general the currents obey the power law[28],

$$i = av^b \qquad \text{Eq. 3.2}$$

where *I* is the current (mA), *v* is the scan rate (mV/s) and *a*, *b* are adjustable values. The *b*-values can be obtained by setting a log on both sides of equation 3.2 and finding the slope of the graph (Fig.3.7 (a)). The *b* value is the sum of the faradaic and non-faradaic currents, when the process is diffusion-controlled the *b* value is 0.5, whereas capacitive behavior is dominant when the *b* value approaches 1.[29]

To further dissect the contributions of diffusion-controlled and capacitive reactions, the total current (*i*) can be expressed at a specific voltage (V) in terms of the scan rate (*v)* as,

$$i(V,t) = k_1 v + k_2 v^{1/2} \qquad \text{Eq 3.3}$$

where $k_1 v$ and $k_2 v^{1/2}$ correspond to the current attributed to capacitive and diffusion-controlled process respectively. Rearranging this equation to yield the one displayed in Fig. 3.7 (b), a linear fit of of $\frac{i}{v^{1/2}}$ vs $v^{1/2}$ can be performed, allowing for the determination of k_1 and k_2. This analysis facilitates the differentiation between currents arising from Li^+ insertion (diffusion) and those stemming from capacitive processes. The outlined approach provides a comprehensive understanding of the

electrochemical processes occurring during the cyclic voltammetry experiment, offering valuable insights for optimizing battery performance.

Figure 3.7. (a) Log-scale plot of the power law showing relationship between peak current and scan rate. (b) Scan rate vs current/scan rate arising from equation 3.3 for analysing current contributions from CV data.[25]

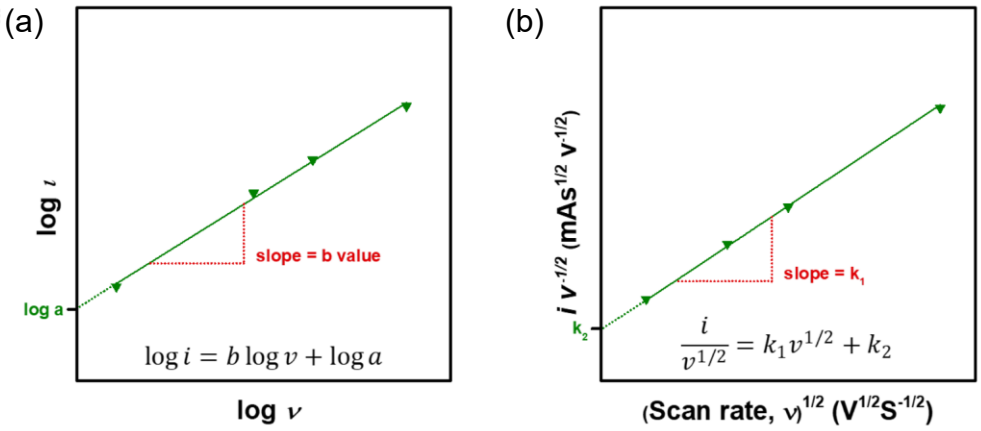

Cyclic voltammetry was conducted in Chapters 4-6, using a multichannel BioLogic VSP Potentiostat/Galvanostat. The experiment parameters, such as voltage window, scan rate, and number of cycles, were determined on a case-by-case basis as outlined in the experimental sections of each chapter.

3.5.2 Galvanostatic Cycling

Galvanostatic cycling is a fundamental technique for the testing and characterization of electrodes for alkali-ion batteries. Commonly referred to as GCPL (galvanostatic cycling with potential limitations) through this thesis, it involves applying a constant current to the cell and measuring the resulting voltage and capacity changes over time. All cells in this thesis were tested as half cells against a lithium (or sodium/potassium for Chapter 6) counter electrode. Technically, in this setup, the desired anode material

being tested functions as the initial cathode in the cell, undergoing alkali insertion during the first discharge. It is worth noting that employing this configuration is a common practice when examining various anode materials in half-cell arrangements as opposed to lithium metal. During the discharge cycle of a secondary battery, ions move from the anode to the cathode through the electrolyte, accompanied by the release of electrons from the anode. In a half-cell setup, only one electrode and its associated reactions are under investigation. Therefore, even though the material being tested is technically an anode, if it is undergoing reduction (i.e., accepting electrons), it is designated as the cathode for the purposes of that half-cell configuration.[30] In this context, the current is initially set to a discharge current and is referred to as the initial discharge, however this is the lithiation (sodiation/potassiation) of the tested material.

The key advantage of galvanostatic cycling relies in its ability to simulate real-world conditions by mimicking the continuous charge and discharge cycles a battery experiences during its operational life. By applying a constant current, the electrochemical performance of battery can be evaluated by observing changes in voltage plateaus and slopes. These changes can indicate phase transitions or reactions occurring with the electrode materials. Anomalies or deviations from expected voltage profiles may signal issues such as electrode degradation, electrolyte decomposition, or the formation of undesirable by-products.[31]

Performance indicators such as specific capacity, coulombic efficiency, and cycling stability can be gleaned from GCPLs. Specific capacity refers to the amount of charge a battery can store per unit mass or volume, denoted as mAh/g, and are shown in plots of capacity vs voltage, known as charge/discharge profiles.[32] Beyond conveying specific capacity information, charge-discharge curves offer insights into coulombic efficiency, which represents the ratio of charge inserted to charge extracted

and serving as an indicator of the effectiveness of specific capacity in discharge versus charge states. CE is crucial for assessing battery lifespan, particularly regarding charge sustainability, as the total amount of charge carriers is limited, and any loss is generally irrecoverable due to factors like electrolyte decomposition. Cycling stability can be examined by plotting specific capacity as a function of cycle number, similar to Fig. 3.8 (b). This provides a clear and quantitative assessment of how well the electrode material maintains its capacity over repeated charge and discharge cycles, offering valuable insights into its long-term durability and performance in secondary batteries.

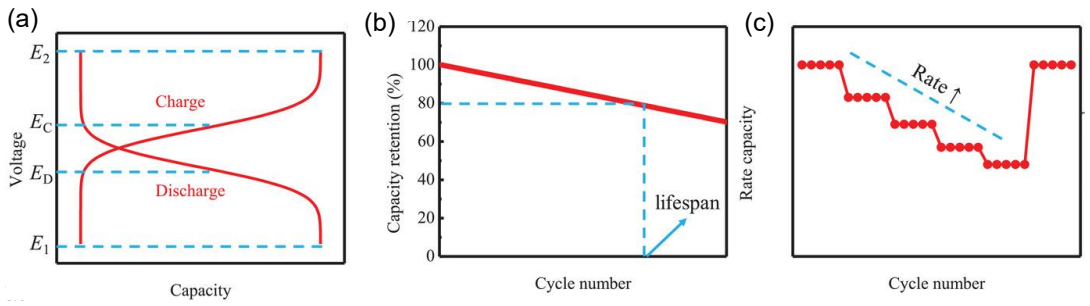

Figure 3.8 (a) Typical GCPL profile showing capacity as a function of voltage. (b) Plot depicting capacity (or capacity retention) as a function of cycle number, to show cycle stability. (c) Rate capability plot, showing relationship between specific capacity and applied current.[31]

Rate capability testing, or simply rate testing, is a galvanostatic cycling method using different current densities over a certain number of cycles. Used in Chapters 4 and 5, this testing assesses how well an electrode material can accommodate rapid changes in current, providing valuable information about its kinetics and electrochemical stability. The rate capability is often characterized by C-rates, where a C-rate of 1 corresponds to the current necessary to charge or discharge the entire capacity of the electrode in one hour. Higher C-rates represent faster charging or discharging. Through rate capability testing, we can gauge how effectively electrode materials maintain their specific capacity at different C-rates, revealing their suitability

for applications with diverse power demands. It is employed in this thesis to evaluate how well our electrode material regains original specific capacity when returned to lower C-rates.

Voltage windows for GCPLs are typically chosen in alignment with those employed for CVs. This selection is based on the potential range within which the active material interacts with the alkali ions. Specific voltage windows and current densities are detailed in the experimental sections of Chapters 4-6.

3.5.3 Differential Capacity Analysis

Differential capacity analysis, or incremental capacity analysis, is a secondary electrochemical technique employed to study the electrochemical behaviour of the electrode materials in response to changes in applied potential. In this context, , differential capacity plots (DCPs) often exhibit similarities in graphing to cyclic voltammograms. In both cases, the curves depict changes in current as the applied potential is swept over a certain range. The shape of the curves reflects the interplay of various electrochemical reactions, including redox processes, capacitive behavior, and other surface phenomena at the electrode-electrolyte interface. However, in CVs, the curve represents an overall view of the total current response as a function of the applied potential, showcasing the sum of capacitive and faradaic currents. In comparison, the differential capacity plots focus on the derivative of the current with respect to voltage (dQ/dV vs V) and is calculated by deriving the charge by the voltage measured during the GCPL. DCPs offer a more effective way to visualize the plateaus observed during the galvanostatic cycling, showing the plateaus as peaks as seen in Fig. 3.9. Alterations in cell electrochemistry during the lifespan of a battery can be

examined by studying the position, intensity, width, and overall magnitude of these peaks.[33]

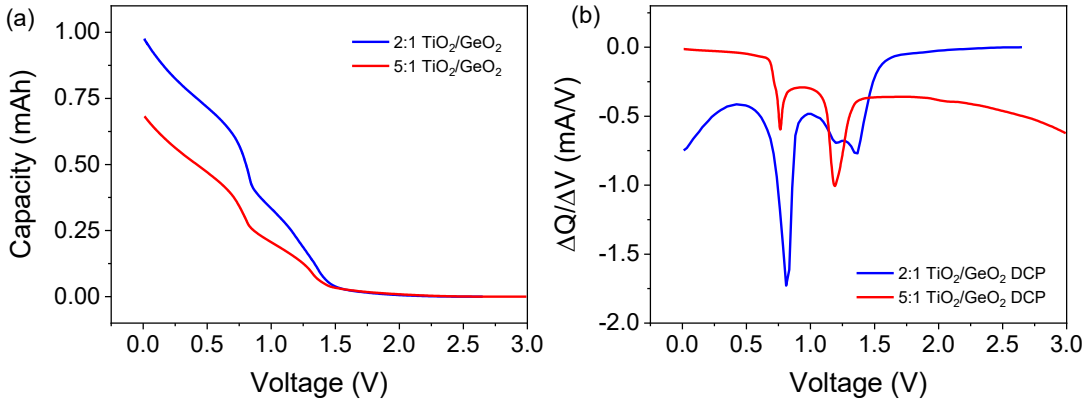

Figure 3.9. (a) Plot of voltage vs capacity for the 1st discharge of TiO_2/GeO_2 inverse opals (Chapter 4) showing distinct plateaus. (b) Resulting DCP, showing peaks instead of plateaus from (a).

DCP is utilized in Chapter 4, where heatmaps are employed to show the changes in differential capacity over 250 cycles.

3.6 References

(1) Hatton, B.; Mishchenko, L.; Davis, S.; Sandhage, K. H.; Aizenberg, J. Assembly of large-area, highly ordered, crack-free inverse opal films. *Proceedings of the National Academy of Sciences - PNAS* **2010**, *107* (23), 10354-10359. DOI: 10.1073/pnas.1000954107.
(2) Armstrong, E.; O'Dwyer, C. Artificial opal photonic crystals and inverse opal structures – fundamentals and applications from optics to energy storage. *Journal of Materials Chemistry C* **2015**, *3* (24), 6109-6143, 10.1039/C5TC01083G. DOI: 10.1039/C5TC01083G.
(3) Inkson, B. J. 2 - Scanning electron microscopy (SEM) and transmission electron microscopy (TEM) for materials characterization. In *Materials Characterization Using Nondestructive Evaluation (NDE) Methods*, Hübschen, G., Altpeter, I., Tschuncky, R., Herrmann, H.-G. Eds.; Woodhead Publishing, 2016; pp 17-43.
(4) Zhou, W.; Apkarian, R.; Wang, Z. L.; Joy, D. Fundamentals of scanning electron microscopy (SEM). *Scanning Microscopy for Nanotechnology: Techniques and Applications* **2007**, 1-40.
(5) Goldstein, J. *Scanning Electron Microscopy and X-Ray Microanalysis: Third Edition*; Springer US, 2003.
(6) Williams, D. B.; Carter, C. B. *The transmission electron microscope*; Springer, 1996.
(7) Malenica, M.; Vukomanović, M.; Kurtjak, M.; Masciotti, V.; Dal Zilio, S.; Greco, S.; Lazzarino, M.; Krušić, V.; Perčić, M.; Jelovica Badovinac, I. Perspectives of microscopy methods for morphology characterisation of extracellular vesicles from human biofluids. *Biomedicines* **2021**, *9* (6), 603.
(8) Fraundorf, P.; Qin, W.; Moeck, P.; Mandell, E. Making sense of nanocrystal lattice fringes. *Journal of Applied Physics* **2005**, *98* (11).
(9) Pennycook, S. J.; Nellist, P. D. *Scanning transmission electron microscopy: imaging and analysis*; Springer Science & Business Media, 2011.
(10) Kohli, R. Chapter 3 - Methods for Monitoring and Measuring Cleanliness of Surfaces. In *Developments in Surface Contamination and Cleaning*, Kohli, R., Mittal, K. L. Eds.; William Andrew Publishing, 2012; pp 107-178.
(11) Howie, A.; Krivanek, O. L.; Rudee, M. L. Interpretation of electron micrographs and diffraction patterns of amorphous materials. *The Philosophical Magazine: A Journal of Theoretical Experimental and Applied Physics* **1973**, *27* (1), 235-255. DOI: 10.1080/14786437308228927.
(12) Iakoubovskii, K.; Mitsuishi, K.; Nakayama, Y.; Furuya, K. Mean free path of inelastic electron scattering in elemental solids and oxides using transmission electron microscopy: Atomic number dependent oscillatory behavior. *Physical Review B* **2008**, *77* (10), 104102.
(13) Krivanek, O. L.; Lovejoy, T. C.; Dellby, N.; Aoki, T.; Carpenter, R. W.; Rez, P.; Soignard, E.; Zhu, J.; Batson, P. E.; Lagos, M. J.; et al. Vibrational spectroscopy in the electron microscope. *Nature* **2014**, *514* (7521), 209-212. DOI: 10.1038/nature13870.
(14) Hofer, F.; Schmidt, F.-P.; Grogger, W.; Kothleitner, G. Fundamentals of electron energy-loss spectroscopy. In *IOP conference series: Materials science and engineering*, 2016; IOP Publishing: Vol. 109, p 012007.
(15) Le Pevelen, D. D. NIR FT-Raman. In *Encyclopedia of Spectroscopy and Spectrometry (Third Edition)*, Lindon, J. C., Tranter, G. E., Koppenaal, D. W. Eds.; Academic Press, 2017; pp 98-109.

(16) Smith, E.; Dent, G. *Modern Raman spectroscopy: a practical approach*; John Wiley & Sons, 2019.
(17) Chauhan, A.; Chauhan, P. Powder XRD technique and its applications in science and technology. *J Anal Bioanal Tech* **2014**, *5* (5), 1-5.
(18) Holder, C. F.; Schaak, R. E. Tutorial on Powder X-ray Diffraction for Characterizing Nanoscale Materials. *ACS Nano* **2019**, *13* (7), 7359-7365. DOI: 10.1021/acsnano.9b05157.
(19) Hollander, J. M.; Jolly, W. L. X-ray photoelectron spectroscopy. *Accounts of chemical research* **1970**, *3* (6), 193-200.
(20) Chastain, J.; King Jr, R. C. Handbook of X-ray photoelectron spectroscopy. *Perkin-Elmer Corporation* **1992**, *40*, 221.
(21) Yancey, D. F.; Reinhardt, C. Damage and repair of organic and inorganic surfaces by Ar+ ion and gas cluster ion beam sputtering. *Journal of Electron Spectroscopy and Related Phenomena* **2019**, *231*, 104-108.
(22) Gilbert, J. B.; Rubner, M. F.; Cohen, R. E. Depth-profiling X-ray photoelectron spectroscopy (XPS) analysis of interlayer diffusion in polyelectrolyte multilayers. *Proceedings of the National Academy of Sciences - PNAS* **2013**, *110* (17), 6651-6656. DOI: 10.1073/pnas.1222325110.
(23) Elgrishi, N.; Rountree, K. J.; McCarthy, B. D.; Rountree, E. S.; Eisenhart, T. T.; Dempsey, J. L. A Practical Beginner's Guide to Cyclic Voltammetry. *Journal of Chemical Education* **2018**, *95* (2), 197-206. DOI: 10.1021/acs.jchemed.7b00361.
(24) Van Benschoten, J. J.; Lewis, J. Y.; Heineman, W. R.; Roston, D. A.; Kissinger, P. T. Cyclic voltammetry experiment. *Journal of Chemical Education* **1983**, *60* (9), 772.
(25) Kim, T.; Choi, W.; Shin, H.-C.; Choi, J.-Y.; Kim, J. M.; Park, M.-S.; Yoon, W.-S. Applications of Voltammetry in Lithium Ion Battery Research. *J. Electrochem. Sci. Technol* **2020**, *11* (1), 14-25. DOI: 10.33961/jecst.2019.00619.
(26) Lee, J. Electrochemical sensing of oxygen gas in ionic liquids on screen printed electrodes. Curtin University, 2014.
(27) Bard, A. J.; Faulkner, L. R. *Electrochemical methods: fundamentals and applications*; Wiley, 1980.
(28) Gosser, D. K. *Cyclic voltammetry: simulation and analysis of reaction mechanisms*; VCH New York, 1993.
(29) Liu, J.; Wang, J.; Xu, C.; Jiang, H.; Li, C.; Zhang, L.; Lin, J.; Shen, Z. X. Advanced energy storage devices: basic principles, analytical methods, and rational materials design. *Advanced science* **2018**, *5* (1), 1700322.
(30) Rowden, B.; Garcia-Araez, N. Estimating lithium-ion battery behavior from half-cell data. *Energy Reports* **2021**, *7*, 97-103. DOI: https://doi.org/10.1016/j.egyr.2021.02.048.
(31) Yang, X.; Rogach, A. L. Electrochemical Techniques in Battery Research: A Tutorial for Nonelectrochemists. *Advanced Energy Materials* **2019**, *9* (25), 1900747. DOI: https://doi.org/10.1002/aenm.201900747 (acccessed 2023/11/26).
(32) Borah, R.; Hughson, F. R.; Johnston, J.; Nann, T. On battery materials and methods. *Materials today advances* **2020**, *6*, 100046. DOI: 10.1016/j.mtadv.2019.100046.
(33) Dubarry, M.; Truchot, C.; Liaw, B. Y. Synthesize battery degradation modes via a diagnostic and prognostic model. *Journal of power sources* **2012**, *219*, 204-216.

Chapter 4

The Effect of TiO_2 and GeO_2 Composite Mixing on the Behaviour of Macroporous Li-ion Battery Anode Materials

Adapted from : The effect of TiO_2 and GeO_2 composite mixing on the behavior of macroporous Li-ion battery anode materials. *Journal of the Electrochemical Society.*

Journal of The Electrochemical Society **2023**, *170* (12), 120521. DOI: 10.1149/1945-7111/ad1371.

Abstract

Highly ordered, macroporous inverse opal structures can be made as TiO_2/GeO_2 nanocomposites with various GeO_2 content and provide Coulombic and voltage stable response where the Ge content and its distribution influence the overall capacity at both slow and fast rates. These interconnected binder-free anodes were characterised using X-ray diffraction, high resolution transmission electron microscopy, selected area electron diffraction, energy dispersive X-ray spectroscopy and electron energy loss spectroscopy. The electrochemical response in half cells over 2000 cycles and various rates showed how the mixture affected key metrics for the material in battery cells. The data shows that a composite of intercalation and alloying compounds can provide good capacity (between theatrical maxima for either material alone) and excellent coulombic efficiency (>99%), even with low quantities of the higher capacity alloying compound. Compositional gradients or spatial heterogeneities in the distribution on one material in the composite are shown to affect capacity during cycling life, where a coulombically efficient increasing capacity is found as the higher capacity material becomes electrochemically active within the composite matrix as the material is modified during cycling.

4.1 Introduction

Lithium-ion batteries (LIB) have revolutionized the electronics and automotive industries, giving us wireless mobility for devices and environmental friendly electric vehicles.[1] However, advancements in electronics and the need for long life and higher energy density EV batteries have led to a growing demand for more efficient, long-life lithium ion batteries (LIBs). While high energy density and fast charging times are beneficial, cost and safety also demand consideration. Subsequently, a lot of research has gone into developing novel battery materials capable of longer cycle life, materials that are scalable, cost effective, and with reduced dependence on critical raw materials. More recently, the focus on energy materials have involved significant efforts in nanostructured materials[2, 3], high entropy materials[4] and more sustainable compositions[5]. Looking at the anode side, intercalation mode materials such as graphite have been at the forefront of research and commercial batteries historically, with high quality graphite key to long lifetime cells based on NMC532 and NMC811 compounds.[6, 7] Alloying type materials such as Si, Sn and Ge give very high capacity and are being introduced into manufacturing in modern LIB cells.[8-17] Much of the development in alloying electrodes, particularly silicon, deals with mitigating or minimizing deleterious effects of cycle volume expansion and contraction[18], which requires specific material structures[19] and composites to form stable energy dense electrodes. However, for other alloying and intercalation materials, there are still some open questions related to their behavior and how composites of active materials can enhance overall anode response.

With this in mind, nano-structuring has been researched to accommodate this expansion as well as improve lithium diffusion in intercalation mode materials such

as TiO_2.[20, 21] In particular, 3D ordered macroporous materials (3DOM) such as inverse opal (IO) structures have gained considerably attraction due to their promising features. Inverse opals are composed of interconnected pores and wall structures, resembling honeycomb, with nanometer- thick walls.[15] This organized structure brings with it benefits for electrochemical energy storage such as improved mass transport of lithium ions and electrons, enhanced electrolyte contact, better mechanical stability (preventing pulverization and cracking of conversion type materials) and higher energy density. [22-24] They are formed by infilling the void spaces inside a sacrificial opal template compared of an FCC arrangement of polystyrene (PS) spheres. These voids can be filled with a variety of materials such as metal oxides, polymers and semiconducting materials depending on the desired physical properties. Many recent efforts to define their response has shown that they provide stable and long-life cycling behavior at quite high specific current in the absence of conductive additive or binders.[25-29]

As an inexpensive, nontoxic, and abundant material, TiO_2 has become an attractive anode material that is useful in non-aqueous chemistries such as current Li-ion batteries, but also in aqueous rechargeable cells.[30, 31] It limits cell performance and power due to a higher working potential compared to graphite, but it provides a similar working specific capacity and a structural integrity during battery cycling.[8] There are three main TiO_2 polymorphs that have been researched for use as anode materials: anatase, rutile and TiO_2-B, while amorphous TiO_2 has also been shown to be a promising candidate.[32, 33] Anatase TiO_2 has the highest theoretical capacity of the crystalline phases, with 167 mAh/g in bulk form which corresponds to $Li_{0.5}TiO_2$, however with nanostructuring this has been shown to improve to upwards of 300 mAh/g.[34] However all polymorphs of TiO_2 deal with poor electrical conductivity and

lower Li ion mobility, and to circumvent this issue composite materials have garnered significant interest in recent years.[8, 35, 36]

Compositing various anode materials is also useful for dual-stage intercalation or for modifying/mitigating behaviours of one or other material at certain voltages, and for tuning overall capacity, conductivity, and other parameters. Silicon/titanium composites[37-40] have been shown to be useful due to silicon's high theoretical capacity (4200 mAh/g), and compounds containing germanium, which has a higher electrical conductivity (100 times higher than silicon) as well as faster lithium diffusivity (400× faster than silicon) show stable response.[41, 42] It is still not clear how specifically the composites interact with alloying and how the ratio of composite materials improves overall electrode material behavior. With a theoretical specific capacity of 1623 mAh/g, germanium anodes also offer the potential of increased energy density.[43] Nevertheless, germanium is an alloying type anode and so deals with volume expansion issues, as well as this, pure Ge can be expensive to produce and so limits its scalability. However, previous reports have shown that by manufacturing GeO_2 (which is more cost effective) into an inverse opal structure, a high specific capacity can be obtained that is similar that of pure Ge.[44]

In this chapter, we describe the formation of highly ordered inverse opal nanocomposites of TiO_2 and GeO_2. We compare the effect of each oxide by investigating the electrochemical performance of two ratios of the material with higher volume fractions of GeO_2, a 2:1 TiO_2/GeO_2 inverse opal material and a 5:1 TiO_2/GeO_2. Structural characterisation in the form of X-ray diffraction (XRD) and Raman spectroscopy shows some crystalline content as anatase TiO_2 and hexagonal GeO_2, while localized atomic resolution analysis such as selected area electron diffraction (SAED) show the material is largely amorphous at the nanoscale. X-ray photoelectron

spectroscopy (XPS) indicates the material is composite of the individual oxides and depth profiling reveals elemental Ge within the structure. The electrochemical performances of both materials are analyzed by cyclic voltammetry (CV), galvanostatic cycling (GCPL) and rate testing. We demonstrate that the TiO_2/GeO_2 IOs offer significantly increased capacities and improved capacity retention compared to pure TiO_2 previously reported.[45] The dual-phase IO electrode will be shown to be coulombically efficient after the initial cycles and remains so for over 2000 cycles. Unlike pure TiO_2 and GeO_2 IO electrodes, these composites exhibit a specific capacity that increases with cycle life between the 150th and 1000th cycles due to changes in reversible reactions and is followed by a more severe fading of specific capacity up to 2000 cycles. These reactions are coulombically efficient (>99%) allowing Li-ions to access metalloid Ge deeper beneath the surface.

4.2 Experimental

4.2.1 Materials Preparation

The substrates used were stainless steel (SS) discs (grade 304) with a diameter of 15.5 mm. The opal template was fabricated using the evaporation induced self-assembly (EISA) method, which involved suspending the SS discs in a 0.1% solution of polystyrene spheres (500 nm diameter) and deionized water and placing in a convection oven at 60°C overnight.

A 0.1M solution of titanium(IV) chloride tetrahydrofuran ($TiCl_4$.2THF) was prepared in IPA and a solution of 0.05M germanium ethoxide ($Ge(OC_2H_5)_4$) was also prepared in IPA. These solutions were mixed in equal volumes to yield a molar ratio

of Ti:Ge of 2:1 and in a 2.5:1 v/v to yield a molar ratio of Ti:Ge of 5:1. The dried PS sphere templates were then infilled by drop casting a volume of ~30 μL of the mixed precursor. The samples were then calcined at 450°C for 1 hour.

4.2.2 Material Characterisation

SEM analysis was performed on FEI Quanta 650 FEG high resolution SEM at an accelerating voltage of 20 kV. EDS analysis of atomic composition was performed on FEI Quanta 650 FEG high resolution SEM at an accelerating voltage of 20 kV whilst EDS mapping was performed on Zeiss Supra 40 high resolution SEM at an accelerating voltage of 20 kV. Raman scattering was performed on an Ocean Optics QE65PRO Raman Spectrometer using a 20 mW Ar^+ laser at 532 nm excitation. The laser beam was focused onto the samples using a 40× objective lens and spectra were collected using a CCD camera. XPS spectra were acquired using a Kratos AXIS ULTRA spectrometer. Survey scans were recorded between 0 and 1486 eV with a step size of 1.0 eV, dwell time of 50 ms, and pass energy of 160 eV and 20 eV for narrow spectral regions. Core level scans were acquired with a step size of 0.05 eV, dwell time of 100 ms, and pass energy of 20 eV averaged over 10 scans with an analysis nominal area of ~220 μm^2. A non-monochromated Al Kα X-ray source at 300 W power was used for all scans. Data was processed using CasaXPS software where a Shirley background correction was employed, and peaks were fitted to Voigt profiles. For depth profiling, Ar^+ sputtering was in GCIS mono mode, at an energy of 5 keV and a 1.5 mm raster. X-ray diffraction (XRD) was conducted using a Philips X'pert Pro MPD, equipped with a Panalytical Empyrean Cu X-ray tube and a Philips X'celerator detector.

Transmission Electron Microscopy (TEM) was performed using a FEI Titan 80-300 ThermoFisher Scientific at 300 kV. Images were recorded using a Gatan UltraScan CCD camera. Selected Area Electron Diffraction (SAED) was done to evaluate crystallinity in the samples while elemental composition was determined by Energy Dispersive X-Ray Spectroscopy (EDS) using a Bruker XFlash 6-30 EDS detector. Mapped regions were imaged in Scanning Transmission Electron Microscopy (STEM) mode with an angle annular dark-field (HAADF) detector. EDS spectrum analysis was done using Bruker Esprit 2.0. Electron Energy Loss Spectroscopy (EELS) was performed using a Tridium 863 spectrometer with the energy dispersion set to 0.1 eV/channel.

4.2.3 Electrochemical Characterisation

All electrochemical characterisation was performed using a BioLogic VMP3 Potentiostat/Galvanostat. The TiO_2/GeO_2 IOs were investigated in a half-cell configuration against a pure Li counter electrode, using a stainless-steel PAT-cell from El-Cell in a two-electrode configuration. The electrolyte used was lithium hexafluorophosphate solution, in ethylene carbonate and diethyl carbonate, 1.0 M $LiPF_6$ in EC/DEC=50/50 (v/v), battery grade from Sigma Aldrich. The separator used was glass microfiber from Whatman Grade GF/A cut to size. The stainless-steel discs were used as the current collector. The typical mass loading of the electrodes was 0.4 – 0.7 mg. All electrochemical tests were investigated in a potential window of 3.0 V – 0.01 V. Cyclic voltammetry was performed at a scan rate of 0.1 mV/s for both ratios and galvanostatic cycling was preformed using various specific currents as mentioned in this report (75 mA/g – 450 mA/g).

4.3 Results and Discussion

4.3.1 Structure and Composition of TiO_2/GeO_2 Composite Inverse Opals

The TiO_2/GeO_2 inverse opal samples were prepared by evaporation induced self-assembly, then infilled with either the 2:1 ratio or the 5:1 ratio of the mixed precursor. The samples were annealed at 450°C which led to the formation of the inverse opal structure which can be seen in Figs. 4.1 (a) and (b) for the 2:1 ratio and Figs. 4.1 (c) and (d) the 5:1 ratio. A highly ordered macroporous structure was formed in both cases with data in Supplementary material, Fig. S4.1 showing average pores diameters of ~406 nm for the 2:1 ratio, and ~412 nm for the 5:1 ratio, consistent with the slightly smaller value compared to the parent PS sphere due to volume expansion of the liquid crystallizing into the final inorganic composite oxide. Alternating layers comprising the inverse structure of the (111)- face centered cubic (fcc) sphere packing arrangement of the colloidal crystal template are visible in the pores of the IO. This interconnected 3D macroporous structure has been shown to allow for faster overall lithiation into nanoscale walls of the active phase in binder-free electrodes, infilled throughout with the electrolyte phase, and the porosity allows for the walls of the IO to expand into the empty pores.[46]

EDS mapping was conducted to identify the atomic percentage and to establish the spatial distribution of Ti and Ge. Below are the EDS maps for each ratio with the corresponding picture shown without the mapping overlay, Figs 4.1 (e) and (f) display the 2:1 ratio and the 5:1 ratio, respectively, with related spectra in Supplementary material, Fig. S4.2. Both Ge and Ti appear to be distributed evenly within the material, not in isolated regions. XRD patterns for both composites prepared on stainless steel substrates were obtained (Fig. 4.1 (g)). The reflections observed in both ratios can be

readily indexed to both anatase TiO_2 (JCPDS No. 21-1272) and hexagonal GeO_2 (JCPDS No. 00-036-1463). The most predominant reflection observed for TiO_2 is the (004) reflection. For the 5:1 ratio, this is the most intense peak in relation to the other planes observed for anatase TiO_2, but show both forms of the composite have well crystallized phases.[47] For the 2:1 ratio, the other reflections (105), (101) and (303) are higher in intensity relative to the 5:1 ratio. The reflections observed for hexagonal GeO_2 which are (110), (200), (112) and (113) are seen with similar relative intensity in the 2:1 ratio. These reflections are diminished in appearance for the 5:1 ratio, as expected. The large peak for the (004) reflection from TiO_2 could possibly contain the (110) and (102) reflections from hexagonal GeO_2, however are difficult to detect due to the small deviance in reflectance angle.

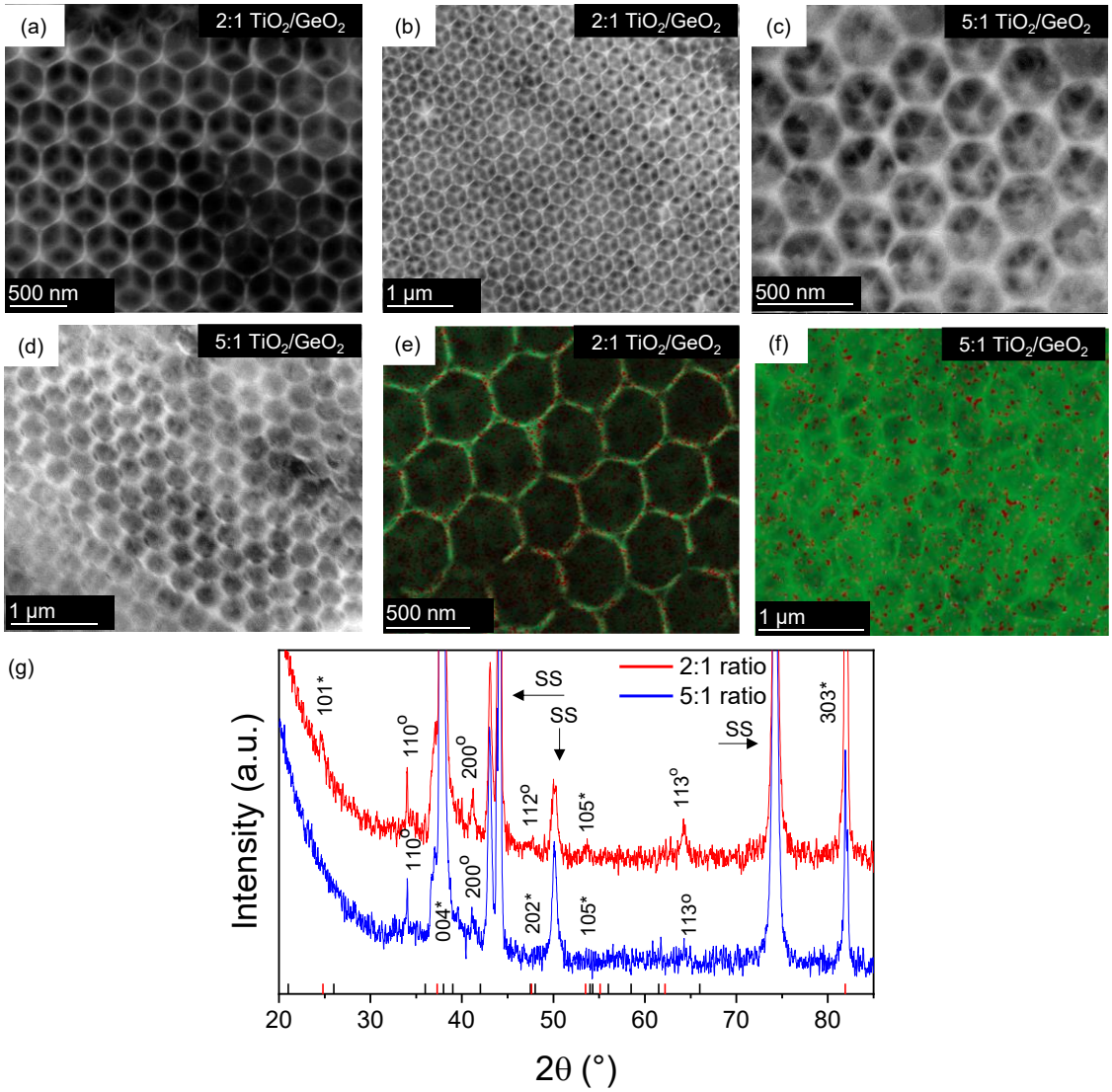

Figure 4.1. SEM images of TiO_2/GeO_2 inverse opals in (a,b) 2:1 ratio and (c,d) 5:1 ratio IOs. EDS elemental mapping of (e) 2:1 ratio and (f) 5:1 ratio with Ti depicted in green and Ge in red. (g) XRD patterns of both materials prepared on stainless steel. Reflections observed for stainless steel are denoted by SS while reflections labelled with * are from TiO_2 and reflections labelled with º are from GeO_2.

Raman spectroscopy was performed on both ratios and on anatase TiO_2 and hexagonal GeO_2 inverse opals individually to compare, shown in Fig. 4.2. There are six active fundamental modes in anatase TiO_2 (A_g^1, 2 B_g^1 and 3 E_g), and a further 12 Raman active modes in hexagonal GeO_2 (4 A_g^1 and 8 E_g).[48, 49] For the 2:1 TiO_2/GeO_2 material, Fig. 4.2(a), peaks are observed at 172.6 cm^{-1}, 232.9 cm^{-1} , 257.5 cm^{-1}, 306.4 cm^{-1}, 417.6 cm^{-1}, 503.4 cm^{-1}, 617.0 cm^{-1}, 669.0 cm^{-1}, and 823.4 cm^{-1}. The highest

intensity peak at 669.0 cm^{-1} matches well with the longitudinal optical (LO) E_g mode of hexagonal GeO_2. The peak beside this at 617.0 cm^{-1} is attributed to the E_g mode of anatase TiO_2, the proximity of these two peaks may be the cause of the high intensity when compared to the other peaks. The peaks recorded at 232.9 cm^{-1}, 257.5 cm^{-1} and 823.4 cm^{-1} are the three A_g^1 modes present in the 2:1 ratio which are consistent with the peaks observed for hexagonal GeO_2 only. The peaks observed at 172.6 cm^{-1} corresponds to the E_g mode of anatase TiO_2 and the peak at 503.4 cm^{-1} can be assigned to the characteristic split A_g^1 mode and B_g^1 mode of TiO_2. The peak at 417 cm^{-1} is difficult to assign due to the little variance in wavenumber of the A_g^1 mode of GeO_2 and the B_g^1 mode of TiO_2. The peak at 306.4 cm^{-1} can be attributed to the transverse optical (TO) phonon mode (E_g) of crystalline germanium, which indicates some metalloid of Ge is present throughout the structure.[44]

Figure 4.2(b) shows the Raman spectrum for the 5:1 TiO_2/GeO_2 IOs, compared to the phonon modes for single phase TiO_2 and GeO_2 in IO structure. The peaks observed are similar to that of the 2:1 spectrum, although some are slightly shifted. Nine peaks are initially recorded at 166.4 cm^{-1} , 237.4 cm^{-1}, 313.3 cm^{-1}, 375.4 cm^{-1}, 417.6 cm^{-1}, 497.3 cm^{-1}, 675.7 cm^{-1}, 698.8 cm^{-1} and 828.3 cm^{-1}. The peak at 237.4 cm^{-1} is attributed to the A_g^1 mode of hexagonal GeO_2 and can be deconvoluted to yield a second peak at 257.5 cm^{-1} also attributed to the A_g^1 mode. The 3rd A_g^1 mode for hexagonal GeO_2 is found at 828.3 cm^{-1}, slightly blue shifted from the peak observed for the 2:1 ratio. The largest peak centered at 692 cm^{-1} contains the doubly degenerate E_g mode for anatase TiO_2 (675.7 cm^{-1}) and hexagonal GeO_2 (698.8 cm^{-1}) both are observed at a longer wavenumber than recorded for the individual oxides and for the 2:1 ratio, this may indicate compression or shortened chemical bond lengths.[50] The peak assigned to the TO phonon mode (E_g) of crystalline germanium is observed at

313.3 cm^{-1} for the 5:1 ratio. The sharp peak at 417.6 cm^{-1} remains unchanged as seen for the 2:1 ratio however an additional peak is recorded at 375.4 cm^{-1} which is likely to be the B_g^1 mode of TiO_2, so the peak at 417.6 cm^{-1} may correspond to the A_g^1 mode of hexagonal GeO_2. The peak at 497.3 cm^{-1} can be assigned to the characteristic split A_g^1 mode and B_g^1 mode of TiO_2, red shifted from the peak observed for 2:1, which often indicates tensile strain within the crystal structure.

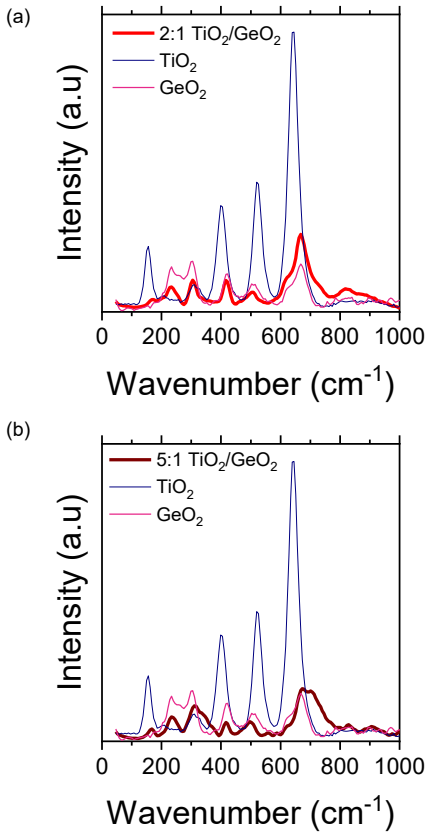

Figure 4.2. Raman spectra of (a) 2:1 ratio and (b) 5:1 ratio TiO_2/GeO_2 IOs overlayed with Raman spectra of anatase TiO_2 inverse opals (blue) and hexagonal GeO_2 inverse opals (pink).

XPS was used to study the chemical states and electronic structure of the TiO_2/GeO_2 IOs, an initial scan was performed first and then depth profiling was carried out to analysis subsurface chemistry. The XPS spectra of the Ti 2p and 3p, Ge 2p and 3d and the O 1s core levels for the TiO_2/GeO_2 2:1 ratio and 5:1 ratio IO samples are presented in Fig. 4.3. The C 1s core level emission is shown in Supplementary

materials, Fig. S4.3. The Ti 2p core-level photoemission for both ratios are very similar, consisting of two hyperfine split photoemission peaks at ~ 458.6, 464.3 eV for Ti $2p_{3/2}$ and Ti $2p_{1/2}$ with corresponding satellite peaks at 471.6 and 477.3 eV. The binding energies of these levels confirm that the Ti present in the IO samples correspond to Ti^{4+}.[51] The Ge 2p core-level spectra for both ratios are also similar , reading at 1219.7 eV for the 2:1 ratio and 1219.9 eV for the 5:1 ratio, and indicates Ge is present as Ge^{4+} in the form of GeO_2.[52] The Ge 3d spectra contain the Ge 3d and Ti 3p core level photoemission, and we see a noticeable difference between the two composite ratios. The Ge 3d peak is seen at 32.0 eV and can be readily assigned to GeO_2 and the Ti 3p peak has a binding energy of 37.1 eV which corresponds to TiO_2. No other oxidation state other than +4 is observed for Ge or Ti and so the material primarily consists of a complex of both GeO_2 and TiO_2 nanoparticles arranged in an ordered interconnected macroporous lattice. For the 2:1 ratio the Ge 3d core-level has a higher relative intensity compared to the Ti 3p peak, however, this relative intensity switches to the Ti 3p peak for the 5:1 ratio, indicating more Ti 3p electrons in the 5:1 ratio than in the 2:1 ratio when compared to Ge 3d electrons. This is expected for the 5:1 ratio as the likelihood of the XPS beam probing a Ti-rich area is higher. The O 1s core levels for both ratios can be deconvoluted into two peaks and appear at the same binding energy values, one at 530.1 eV and the other at 531.5 eV. The peak at 530.1 eV is attributed to the Ti-O bond in TiO_2, while the peak at 531.5 eV corresponds to the O 1s for GeO_2, again indicating that the TiO_2/GeO_2 IO samples are a composite of TiO_2 and GeO_2, and from the overall XPS analysis, are stoichiometric +4 oxidation states of both Ti and Ge.[53]

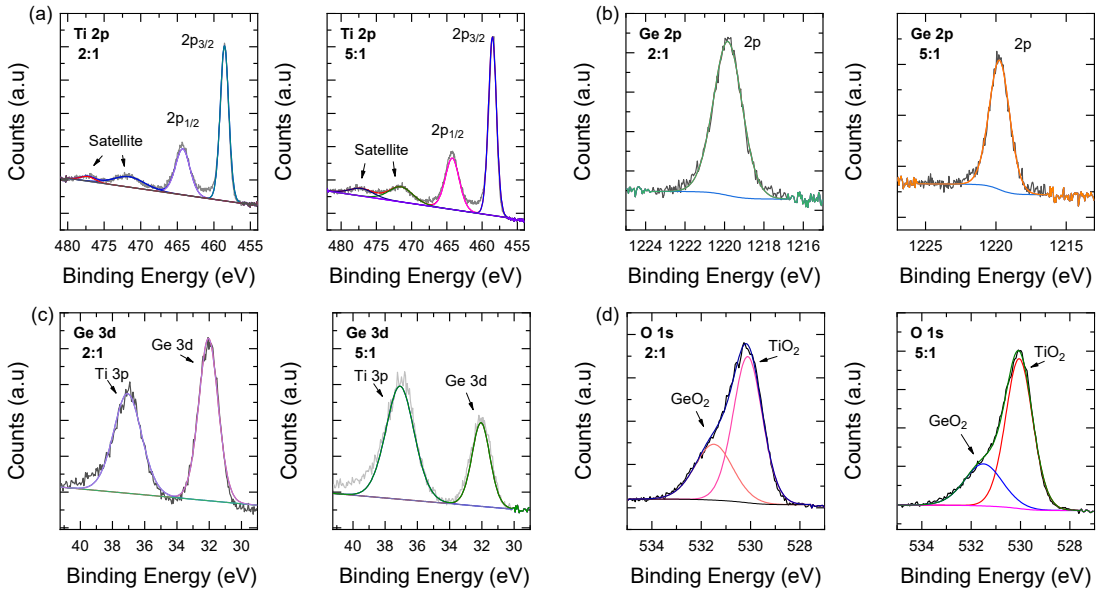

Figure 4.3. XPS analysis for 2:1 (left side) and 5:1 (right side) ratio of TiO_2/GeO_2 inverse opals of (a) Ti 2p (b) Ge 2p (c) Ge 3d, and (d) O 1s core level photoemission.

Depth profiling was carried out on both ratios of IO composites by XPS to examine the subsurface chemistry. Figure 4.4 shows Ti 2p, Ge 2p, Ge 3d and O 1s core level spectra for both ratios after various Ar^+ sputtering times. In the Ti 2p spectrum for both ratios Ti $2p_{3/2}$ and Ti $2p_{1/2}$ spin–orbit split peaks are observed at binding energies of 458.8 eV, and 464.5 eV. Shoulder peaks are seen at 456.9 eV and 462.6 eV, which are shown to increase in area with depth as shown in Figure S3.

The binding energy levels of 458.8 eV and 464.5 eV, which were also present in the initial scan are attributed to Ti^{4+} oxidation state for TiO_2 confirming the stoichiometric phase of the TiO_2. The 456.9 eV and 462.6 eV are artefacts of Ar^+ bombardment, causing localized reduction of the Ti^{4+} species to sub-oxide (Ti^{3+} oxidation state) often by O-vacancy formation.[54, 55] The depth profiles of the Ti 2p core level of the 5:1 ratio composite shows a similar response, and the peaks remain largely unchanged with effects of Ar^+ somewhat more readily observed.

We also analysed the Ge chemical state in each of the composites. The depth profile for the Ge 2p core level in Fig. 4.4 (b) consists of two photoelectron emissions for both the 2:1 and the 5:1 ratio at the 30 s sputtering time. The peaks at ~1219 eV and ~1217 eV are attributed to the +4 oxidation state of germanium (GeO_2) and elemental Ge, respectively.[52] The detected concentration of elemental germanium increases with Ar^+ sputtering time as can be seen in Supplementary material, Fig. S4.4.

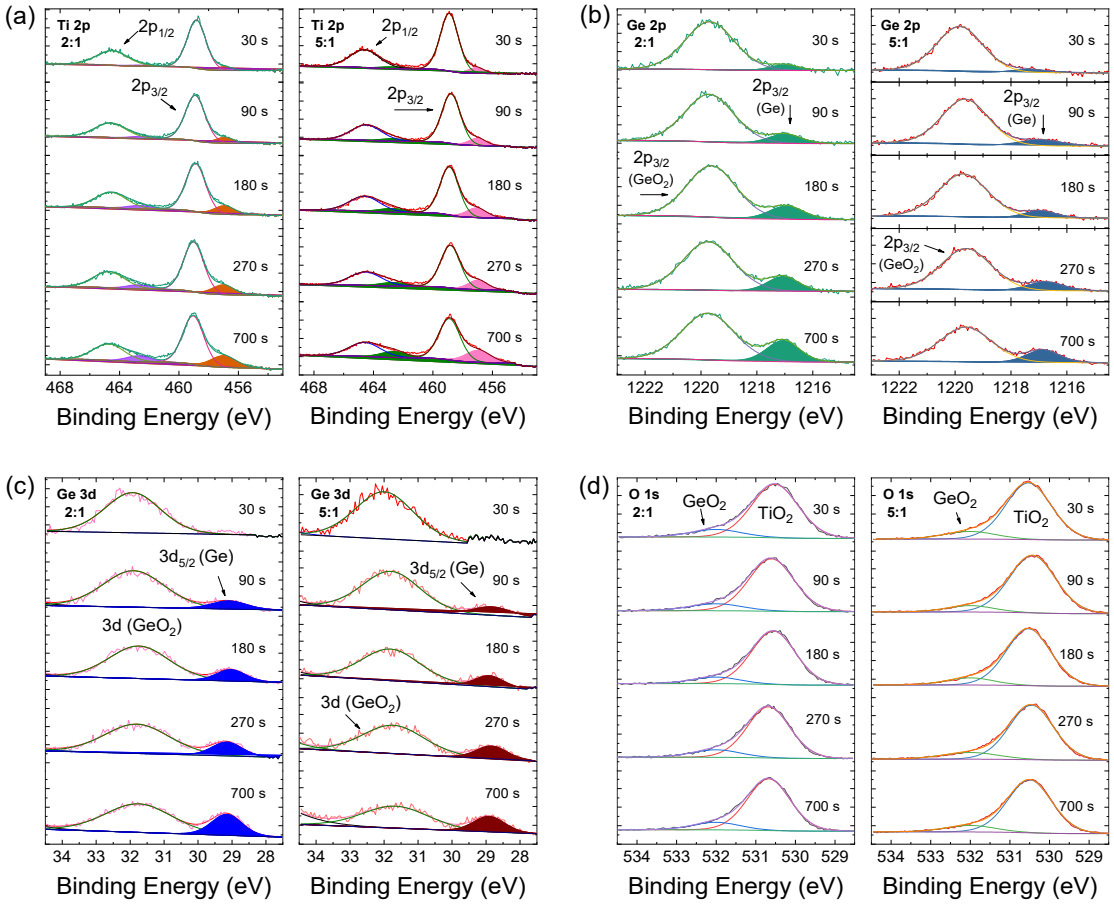

Figure 4.4. XPS depth profiles for (a) Ti 2p, (b) Ge 2p, (c) Ge 3d and (d) O 1s core levels for the 2:1 ratio and the 5:1 ratio of TiO_2/GeO_2 composite inverse opals. Ar^+ sputtering times were between 30 s and 700 s in each case at an energy of 5 keV with a 1.5 mm raster.

For the 2:1 ratio the concentration, at 30 s sputter time, of elemental Ge relative to Ge in a +4 oxidation state is 6.19% which increases to 21.8% at 700 s sputter time. For the 5:1 ratio the relative concentration of elemental Ge is 5.02% at 30 s sputtering

time, increasing to 18.72% at 700 s sputtering time. This is also observed in Fig. 4(c) the Ge 3d level, elemental Ge is not detected until 90 s sputter time, where it appears at a relative concentration of 10.90% for the 2:1 ratio, and 12.5% at the 5:1 ratio as shown in Supplementary material, Fig. S4. By 700 s sputtering time, this relative concentration increases to 24.71% for the 2:1 ratio and 24.56% for the 5:1 ratio. This implies elemental Ge is present deeper within the structure of the TiO_2/GeO_2 inverse opals. The O 1s depth profiles for both ratios are shown in Fig. 4.4(d) and consist of two deconvoluted peaks centered at 530.5 eV and 532 eV which correspond TiO_2 and GeO_2 respectively.

Localized atomic resolution analysis showed amorphous nature with some polycrystalline areas at nanoscale for the samples. Figure 4.5 (a) and (b) show transmission electron microscopy (TEM) images of the inverse opal macrostructure for the 2:1 and 5:1 ratio respectively, and compared to the SEM images in Fig. 4.1, we can see the interconnected structure of the inverse opal in transmission. Interestingly, Fig. 4.5 (c) and (d) show high resolution TEM images of the 2:1 ratio and the 5:1 ratio, respectively, which reveal the dominant amorphous nature of the material. Figure 4.5 (e) and (f) show the selected area electron diffraction (SAED) for the 2:1 ratio composite for two areas of interest, (e) reveals elements of polycrystals with the (004), (105), (107), (200) and (204) planes being observed for anatase TiO_2 and the (011) and (200) plane for hexagonal GeO_2. However, Fig. 4.5 (f) shows the SAED for the same sample indicating an amorphous region. Generally, these macroporous IOs are largely amorphous with localized regions of crystallinity on the nanoscale. Figure 4.5 (g) shows the SAED for the 5:1 ratio, indicating its amorphous nature, no areas of polycrystals were found. Figure 4.5 (i) shows a TEM image of the overlapping walls of the inverse opal structure of for the 2:1 ratio sample and the resulting EDX maps in

Figs 4.5(j-l) of Ge, Ti and O confirm a relatively uniform spatial distributions of the three elements. A similar overall observation is made from measurement of the 5:1 composite ratio material in Figs 4.5(m-p), showing a relatively homogenous mixture within the interaction volume of the electron beam. Pore diameters for the 2:1 ratio were measured at ~397 nm on average, which is in close agreement with the diameter found with SEM, while the pore diameters 5:1 ratio were found to be 457 nm on average (cf. Supplementary material, Fig. S4.1). The walls of the two materials appear to be made up of agglomerated nanoparticles and have varied thickness throughout ranging from 8 – 252 nm with an average of 85 nm for the 2:1 TiO_2/GeO_2 ratio while the walls of the 5:1 ratio of an average thickness of 63 nm, ranging from 17 – 239 nm.

Electron energy loss spectroscopy (EELS) , shown in Fig. S4.5, showed no splitting of the $L_{2,3}$ edge which is common for crystalline TiO_2, and this splitting disappears in amorphous TiO_2 due to the lack of crowding from the octahedral site symmetry. A shift of 5 eV is observed when moving across the analysed region of the 2:1 ratio composite seen in Figure S4.5, with the peak indicating the L_3 edge shifting from 464.4 eV to 460 eV and the Ti L_2 shifting from 470.2 eV to 465.4 eV across the sample area indicated by the orange bar. The oxygen K edge is also observed, recorded at 538.1 eV and shifted to 533.8 eV. The spectrum is in close agreement with the energy loss peaks observed by XPS for Ti^{4+}, the definitive peak without splitting indicates that the sample is predominantly amorphous TiO_2. Relatively little shift in Ti signal is observed for the 5:1 ratio, indicating no change in oxidation state for titanium.

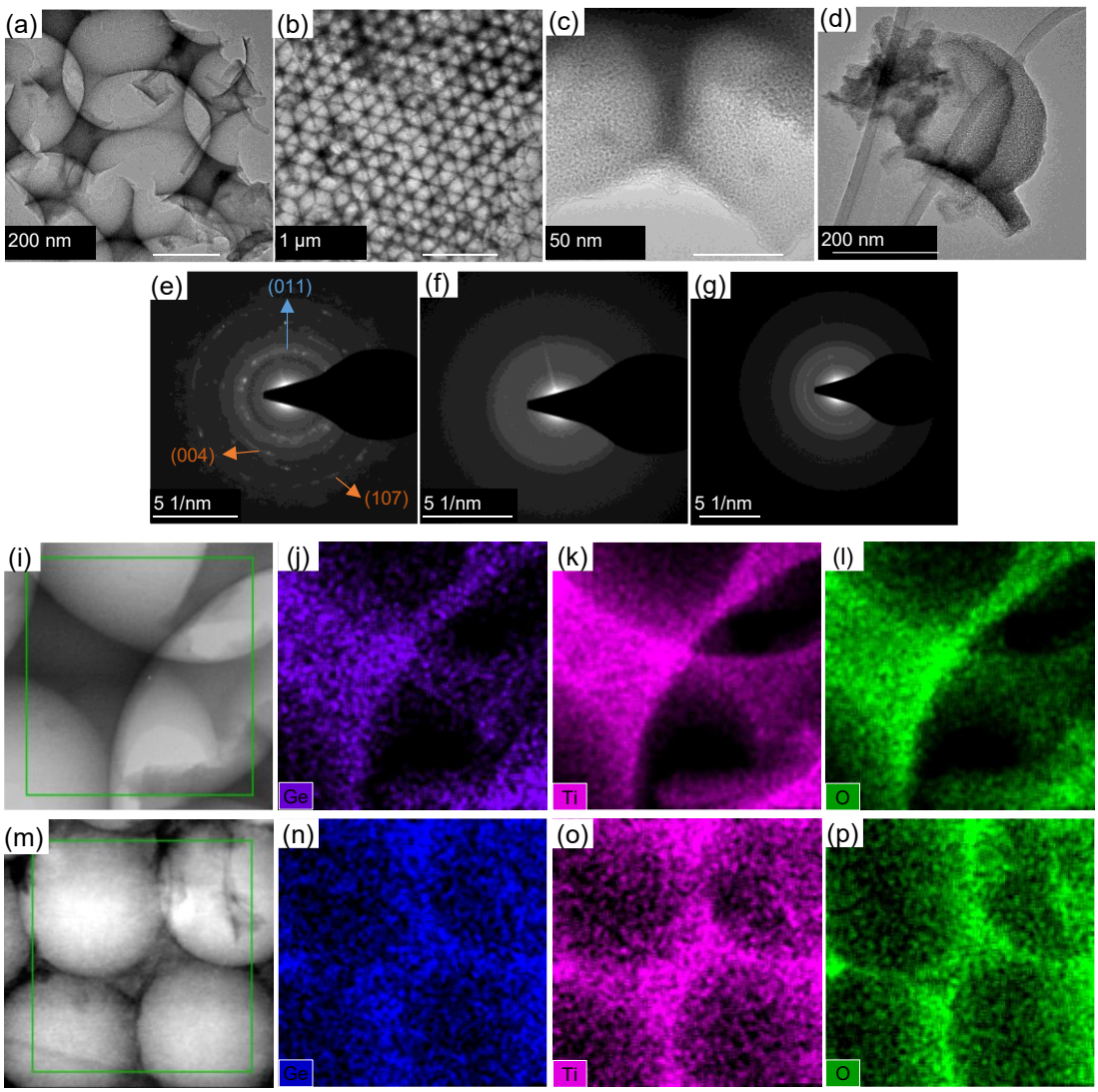

Figure 4.5. TEM images showing macro structure of inverse opals for (a) 2:1 TiO_2/GeO_2 and (b) 5:1 TiO_2/GeO_2. (c, d) HRTEM image showing amorphous nature at nanoscale for the 2:1 ratio and the 5:1 ratio, respectively. (e) SAED pattern showing hints of crystallinity in the 2:1 ratio and (f) SAED pattern showing area of amorphousness for the same sample. (g) SAED showing amorphousness of the 5:1 ratio. (i) TEM image of 2:1 ratio showing an area of overlapping walls of the inverse opal structure and (j),(k) & (l) resulting EDX mapping showing the presence of Ge, Ti, O, respectively. (m) TEM image of 5:1 ratio and corresponding EDX maps showing the presence of (n) Ge, (o) Ti, and (p) O.

4.3.2 Electrochemical Behaviour in Long Life Li-ion Battery Cells

Cyclic voltammograms (CV) were acquired to investigate the Li^+ reaction mechanism for the TiO_2/GeO_2 inverse opals. The 1st, 2nd, 5th, and 10th CV scans for both composite ratios were acquired at a scan rate of 0.1 mV/s and are shown in Fig. 4.6(a,b). For the 2:1 ratio in Fig. 4.6(a), the broad shoulder centered at 1.9 V for the initial cathodic sweep can be attributed to the SEI layer formation, as it does not appear in subsequent cycles. The voltammetric current corresponding to SEI layer formation for the 5:1 ratio (Fig. 4.6(b)), also appears as a small shoulder centered at ~1.87 V. The peak at 1.2 V in Fig. 4.6(a) can be deconvoluted to give two reductions peaks, one at 1.26 V and 1.1 V. The peak at 1.26 V can be attributed to the lithium insertion into TiO_2 to yield Li_xTiO_2.[56] This can be seen to shift to a higher potential with subsequent cycles. The peak at 1.10 V corresponds to the formation of amorphous Li_xGeO_2.[57] In the 5:1 ratio, this peak appears more defined at 1.1 V, and was deconvoluted to contributions at 1.21 V for the lithium insertion into anatase TiO_2 (which is usually seen at a higher potential[58, 59]) and 1.07 V for the formation of amorphous Li_xGeO_2. The strong reduction peak at 0.7 V for the 2:1 ratio and 0.6 V for the 5:1 ratio may correspond to the decomposition of GeO_2 to Ge and the beginning of alloying with Li^+.[60] The sloping region in the cathodic scan from ~ 0.3 to 0.01 V for both ratios corresponds to the lithiation of crystalline Ge.[44, 61]

For the anodic process, distinct voltage regions are observed for the 2:1 and 5:1 ratio of TiO_2/GeO_2 IOs. The first region is between 0.2 – 0.76 V for the 2:1 ratio, and 0.15 – 0.72 V for the 5:1 ratio, corresponding to the dealloying of $Li_xGe \rightarrow xLi + Ge$.[57, 60] The peak observed at 1.1 V for both ratios is attributed to the oxidation of Ge/Li_2O to GeO_2, no shifts in voltage are seen in subsequent cycles indicating the reversibility of the lithiation/delithiation of GeO_2 in the compound.[62] The anodic peak observed for the delithiation of Li_xTiO_2 is seen at 2.02 V for the 2:1 ratio, and 1.98 V

for the 5:1 ratio; this peak is typical for anatase TiO_2. A second, unusual peak is observed at 1.5 V, this has previously been observed for nanostructured TiO_2, however may not be present in bulk TiO_2 CVs.[59, 63, 64]

The lithium storage behavior of the mixed ratio inverse opals was investigated by galvanostatic cycling. Figures 4.6 (c) and (d) show the discharge/charge profiles for the first hundred cycles for the 2:1 TiO_2/GeO_2 IOs and the 5:1 TiO_2/GeO_2 IOs respectively. Initial discharge capacities were recorded as 1994 mAh/g for the 2:1 and 1665 mAh/g for the 5:1 ratio, and the corresponding charge capacities were 1100 mAh/g and 1060 mAh/g, all at 150mA/g specific current. For the 2:1 ratio there were four distinct regions observed (1) a steep voltage drop from OCV to 1.5 V, which corresponds to the insertion into the tetragonal anatase lattice (Li_xTiO_2) and the formation of the SEI layer, (2) a sloping region from 1.5 – 1.0 V where it has been reported that in this region the Li-rich orthorhombic $Li_{0.5}TiO_2$ forms, (3) a sloping region from 1.0 – 0.8 V, which is credited to the formation of amorphous Li_xGeO_2 followed by a plateau at 0.8 V from the reduction of Li_xGeO_2 and GeO_2, and (4) the sloping region from 0.7 – 0.01 V attributed to the alloying of crystalline Ge with Li.[32, 44, 65] These regions are in excellent agreement with the cyclic voltammetry. The same regions are observed for the 5:1 ratio, however there is more distinction seen between regions in the voltage range of 1.5 – 0.8 V, a shorter plateau is observed between 1.5 – 1.2 V which has previously been reported as the lithium insertion into the orthorhombic anatase lattice, and decreased length of this plateau is linked to decreased particle size.[66] The voltage window for the formation of amorphous Li_xGeO_2 in both ratios seems to almost disappear in subsequent cycles, specifically after the 100th cycle. This implies that this reaction no longer occurs and the reversibility of the material cycling comes from the alloying and dealloying of Li with

elemental Ge.[44] An interesting phenomenon is found to occur after 200 cycles that is characteristic for these composites IOs. In Fig. 4.6 (e) for the 2:1 ratio and Fig. 4.6 (f) for the 5:1 ratio, we observe with every 100 cycles or so, the specific capacity increases. For the 100th cycle the discharge capacity is 372 mAh/g for the 2:1 ratio, and 490 mAh/g for the 5:1 ratio of TiO_2/GeO_2 IOs. For the 2:1 ratio, which has a higher relative proportion of Ge content, the specific capacity after 200 cycles is 317 mAh/g, this increases to 360 mAh/g for the 500th cycle and then to ~500 mAh/g by the 1000th cycle, a 58% increase in specific capacity from the 200th cycle. For the 5:1 the increase is found to occur earlier. After the 150th cycle the discharge capacity is 480 mAh/g, and by the 200th cycle we find a specific capacity ~550 mA/g, which continues to increase to reach ~700 mAh/g for the 500th cycle and ~730 mAh/g for the 1000th cycle. This equates to a 32% increase in capacity from the 200th cycle. In all cases, a coulombic efficiency >99% is maintained. This observation could have many possible causes[67], including;

1. Volume expansion, contraction and pulverization happening during the first 100 or so cycles, which may expand the pores and open up new surface and allow better access to some of the higher specific capacity Ge content within the walls of the IO.
2. The region associated with the formation of Li_xGeO_2 is no longer observed after approximately 100 cycles and so the reversibility largely comes from the lithiation/delithiation of elemental germanium. The charge consumed forming this intermediate phase ceases and so a higher capacity is achieved.
3. More elemental Ge is accessed deeper within the structure (detected from XPS depth profiling), and with cycling, it is plausible that Li can access Ge in an oxidation state that allows a higher capacity contribution during cycling

without prior reduction of Ge from its oxide, while not affecting the overall cycle coulombic efficiency.

After the 1000th cycle for the 2:1 ratio the capacity fades off rapidly falling to 292 mAh/g at the 1500th cycle (≈ 60% loss in capacity), decreasing to 123 mAh/g after 2000 cycles. The 5:1 ratio by comparison, is better at retaining its capacity, with a specific capacity of 481 mAh /g after 1500 cycles which equates to a 34% loss in capacity from the 1000th cycle. Overall, a higher GeO_2 content does provide a capacity increase in the composite in general, but we see that in consistently coulombically efficient cycling, a reduction from a 1 part in 3 to 1 part in 6 of GeO_2 content behaves similarly and offers a scaled overall capacity based on the Ge content in the TiO_2/GeO_2 mixture, but the distribution of Ge and its accessibility during cycling has a strong influence on the capacity values during cycling.

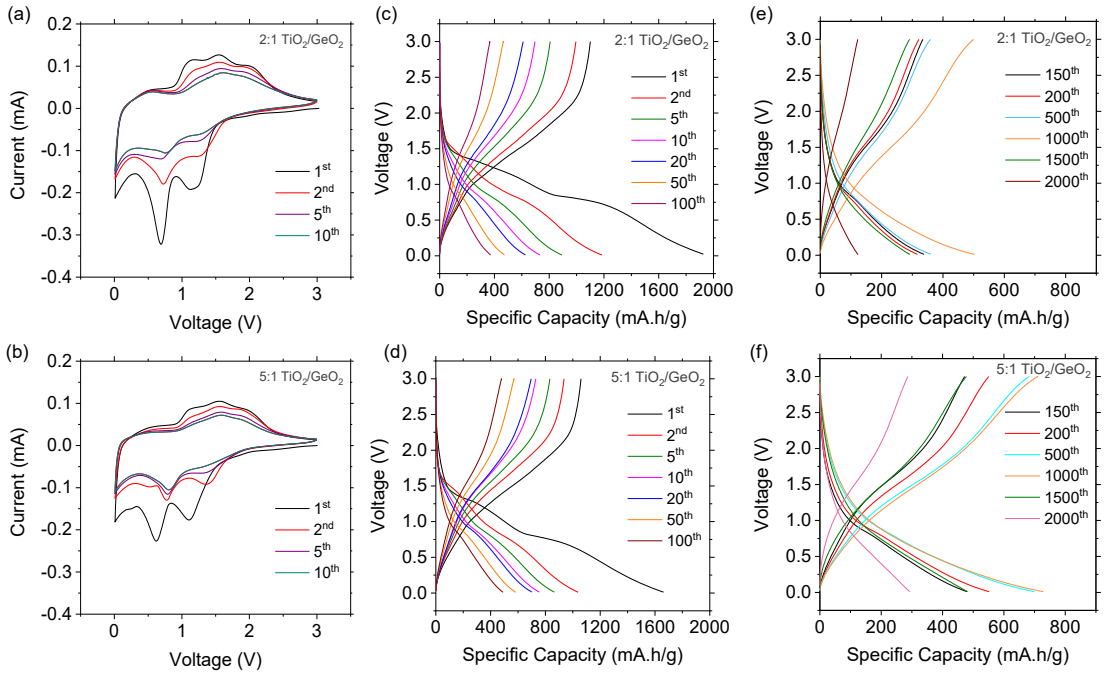

Figure 4.6. Cyclic voltammograms showing the 1st, 2nd, 5th, and 10th cycles for (a) the 2:1 ratio and (b) the 5:1 ratio of TiO_2/GeO_2 IOs. Discharge/charge profiles for 1st, 2nd, 5th, 10th, 50th and 100th cycles for (b) the 2:1 ratio and (c) the 5:1 ratio of TiO_2/GeO_2 IOs cycled at 150mA/g specific current in a potential window of 3.00 - 0.01 V (vs

Li/Li^+). Discharge/charge profiles for (e) the 150^{th}, 200^{th}, 500^{th}, 1000^{th}, 1500^{th} and the 2000^{th} cycles for (e) the 2:1 ratio and (f) the 150^{th}, 200^{th}, 500^{th}, 700^{th}, 900^{th} and 1000^{th} cycles for the 5:1 ratio.

Differential capacity plots (DCPs) were configured to better illustrate the phase transformations occurring in the first 200 cycles for both materials. Figure 4.7 shows the DCPs for the charge and discharge processes for the 2:1 and 5:1 ratio with the corresponding intensity maps for the cycle number. For the discharge process of the 2:1 ratio, and four regions are observed similar to those seen in the CVs, showing that Li insertion takes place over a number of steps. These peaks are seen at 1.5 V, 0.96 V, 0.8 V and a sloping region from 0.4 V – 0.01 V. These peaks are associated with the reduction of TiO_2, the formation of amorphous Li_xGeO_2, the reduction of GeO_2 to crystalline Ge and the lithiation of crystalline Ge, respectively. The peaks associated with the transformation of TiO_2 to Li_xTiO_2 and the formation of amorphous Li_xGeO_2 no longer appear after the first few cycles and only those corresponding to the reduction of GeO_2 and lithiation of crystalline Ge are present. The same four regions are seen in the 5:1 ratio composite, appearing at 1.5 V, 0.94 V, 0.8 V and a sloping region from 0.4 V – 0.01 V. The fading of charge contribution from TiO_2 is also present in the 5:1 ratio, highlighted in the intensity maps in Fig. 4.7.

For delithiation/charge process, four regions are observed: at 0.5 V, 1.1 V, 1.5 V and 1.9 V, for both ratios, for the delithiation of crystalline Ge, the oxidation of Ge to GeO_2 and two peaks associated with the delithiation of TiO_2. These peaks are in excellent agreement with those recorded for the cyclic voltammetry. The peak at 1.9 V that is attributed to the delithiation of TiO_2, fades after the first few cycles as seen in the discharge process. The peak observed at the highest intensity is the peak at 1.5

V, previously observed for nanostructured TiO_2 as mentioned and also for the lithium extraction mechanism for Ge.[68]

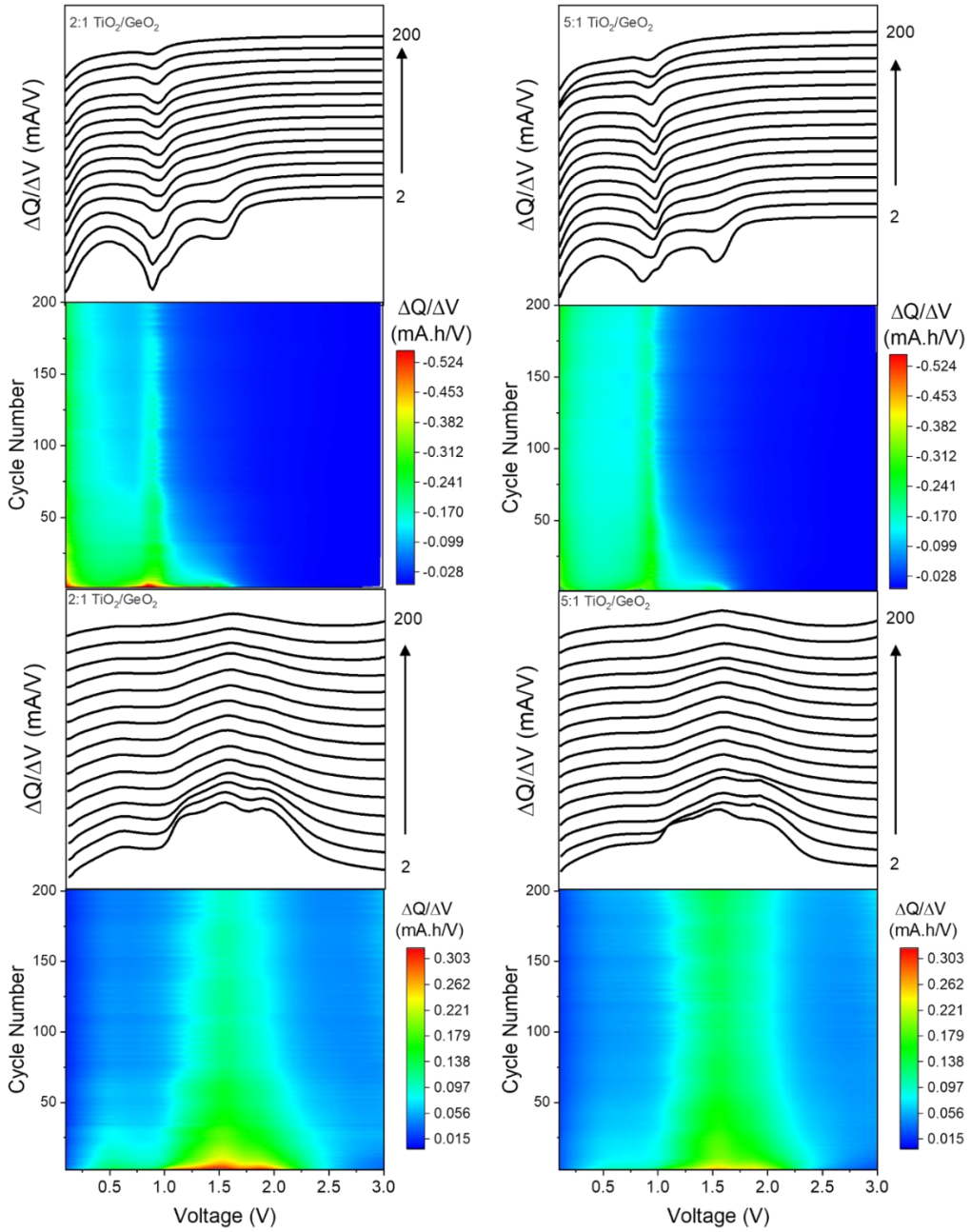

Figure 4.7. Differential capacity plots (DCP) and associated intensity maps for the charge and discharge states of the 2:1 TiO_2/GeO_2 IOs (left) and the 5:1 TiO_2/GeO_2 IOs (right).

Coulombic efficiency during cycling was measured and can be seen in Fig. 4.8 (a) and (b) together with the variation of specific capacity during cycling over ~2000 cycles. The consistent capacity increase over the first ~1000 cycles occurs after the material reaches its first stably reversible composition between 100-150 cycles. Prior to this, the capacity drops until it reaches a stable value, but the CE ~99% is always maintained in this material. The initial Coulombic efficiency (ICE) was ~57% and ~64% for the 2:1 ratio and the 5:1 ratio respectively. The low Coulombic efficiencies are limited to the first cycle and so are attributed to the formation of the SEI layer and Li_2O, low ICE has also been previously observed for Ge-based materials, but once the high CE state is reached the material, even in IO form, has been shown to cycle stably in previous investigations.[11, 43, 62]

As a composite, the 2:1 ratio shows excellent columbic efficiency, between 83% and 99% for the first 20 cycles and maintains an average CE of 99.8% for subsequent cycles. The 5:1 ratio displays better CE initially of >90% for the first 20 cycles and has an average CE of 99.8% for subsequent cycles. The monotonic increase in capacity due to reasons outlined earlier is relatively constant and once it reaches maximum, we then observe a decay in capacity in both composite ratios.

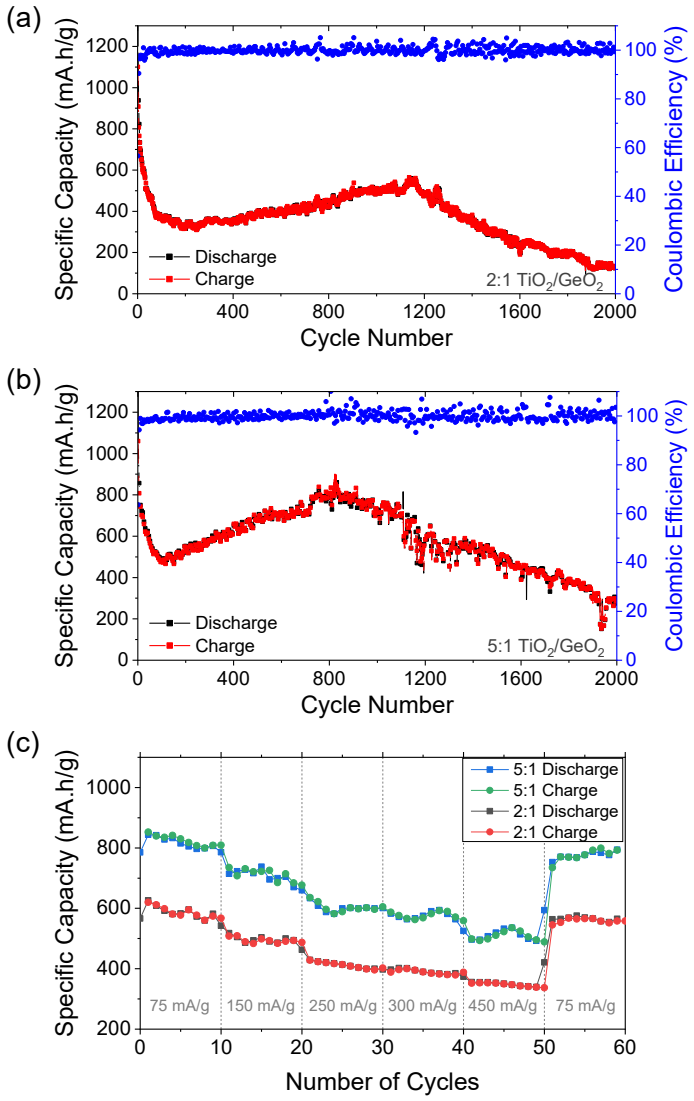

Figure 4.8. Coulombic efficiency graph showing charge and discharge plots at specific current of 150 mA/g for (a) 2:1 ratio of TiO_2/GeO_2 IOs and (b) 5:1 ratio of TiO_2/GeO_2 IOs. (c) Rate capability test for both the 2:1 and 5:1 ratio with various specific currents.

Rate capability tests were also conducted and can be seen in Fig. 4.8(c). These tests involved charging and discharging the cell at various increasing specific currents ranging from 75 – 450 mA/g. Both ratios were cycled for 50 cycles at specific current of 150 mA/g prior to rate testing to eliminate SEI layer and side reactions and to obtain the composition with high (>99%) CE. The results are shown in Fig. 4.8(c) both ratios demonstrated excellent capacity retention and rate performance. The average

discharge capacity at the specific current of 75 mA/g was ~590 mAh/g for the 2:1 and ~920 mAh/g for the 5:1. This decreased to ~500 mAh/g and ~750 mA/g at specific current of 150 mA/g for the 2:1 and 5:1, respectively. The 2:1 ratio better retains its capacity for the 250 mA/g applied current, showing an average of ~420 mAh/g compared to the 5:1 which averaged at ~554 mAh/g. At specific current of 300 mA/g the capacity average was ~390 mAh/g (2:1 ratio) and ~500 mAh/g (5:1 ratio), this decreased slightly to ~350 mAh/g for the 2:1 ratio and ~440 mAh/g for the 5:1 ratio at a specific current of 450 mA/g. When the materials were cycled again at the initial specific current of 75 mA/g, the average specific discharge capacities were recorded as ~550 mA/g for the 2:1 and ~770 mA/g for the 5:1 ratio, proving excellent capacity retention for both materials. The 2:1 ratio loses only 6.1% of its average specific capacity while the 5:1 ratio loses 16.5% of its specific capacity. These results highlight that these TiO_2/GeO_2 IO materials are capable of outstanding reversible capacity, with the 2:1 ratio displaying excellent capacity retention and the 5:1 composite ratio demonstrating that the specific capacity of TiO_2 can be increased with only a small amount of GeO_2.

From the rate capability tests, both composites of the IO materials are able to deliver significantly high capacities at high specific currents, and higher than those of pure TiO_2 or GeO_2 IO under similar conditions. Both the 2:1 and 5:1 TiO_2/GeO_2 samples were cycled at a specific current of 450 mA/g to further investigate the faster-rate performance. The results for these tests are shown in Fig. 4.9. The 2:1 ratio showed a high initial specific discharge capacity of 1406 mAh/g and the charge capacity was 796 mAh/g. The 5:1 ratio had an initial specific discharge capacity of 1633 mAh/g, comparable to the capacity observed at the specific current of 150 mA/g, the specific charge capacity was recorded as 793 mAh/g. This relates to a Coulombic

efficiency of ~ 56 % for the 2:1 ratio and ~ 49 % for the 5:1 ratio during initial lithiation and delithiation. This low Coulombic efficiency is limited to the first cycle and again is attributed to reactions involving SEI formation. While the 5:1 initial capacity is higher, the 2:1 ratio displays better capacity retention at higher rates with the discharge capacities recorded after 100 cycles of ~475 mAh/g for the 2:1 ratio and ~410 mAh/g for the 5:1 ratio. These capacities are comparable to the values recorded at the slower rate and demonstrate that these materials can deliver exceptional performance at high rates.

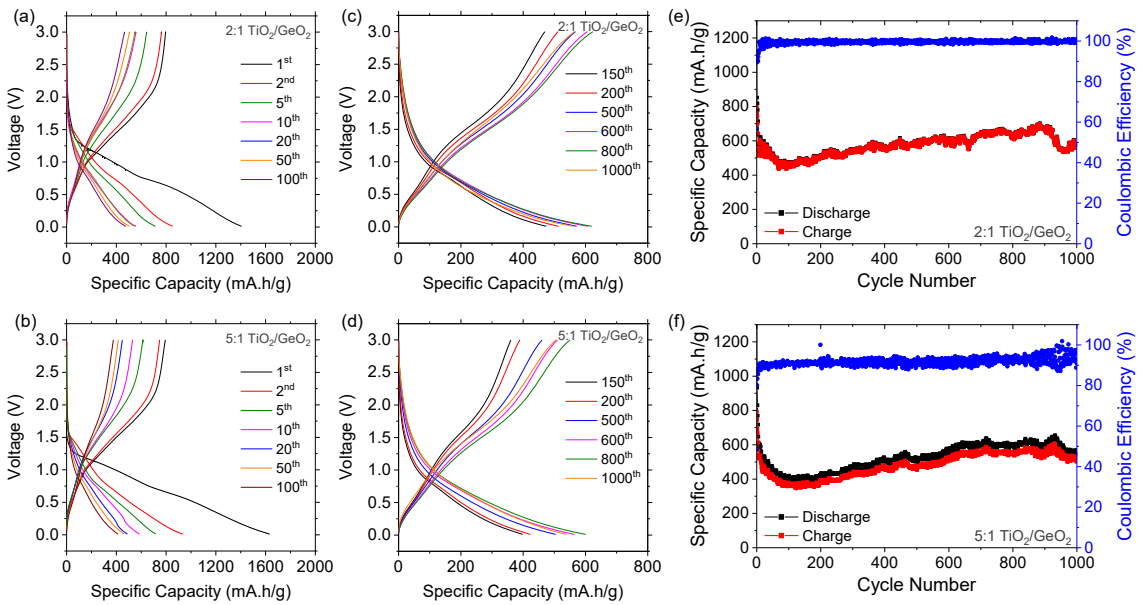

Figure 4.9. Charge and discharge plots at specific current of 450 mA/g for (a) 2:1 ratio of TiO_2/GeO_2 IOs for cycles 1-100. (b) 5:1 ratio of TiO_2/GeO_2 IOs for cycles 1-100. (c) 2:1 ratio of TiO_2/GeO_2 IOs for cycles 150-1000 and (d) 5:1 ratio of TiO_2/GeO_2 IOs for cycles 150-1000.

Beyond the 100th cycle, an increase in capacity is observed again up to ~900 cycles with the 5:1 ratio exhibiting 398 mAh/g for the 150th cycle, increasing to 550 mAh/g for the 800th cycle, a 38% increase in capacity. The capacity was recorded as 538 mAh/g for the 1000th cycle and so an end to the increasing capacity is noted, consistent

with other cells at lower rates in Fig. 4.6. Looking at the 2:1 ratio, an increase in capacity is again noted up until the 900th cycle. After 200 cycles the discharge capacity for the 2:1 ratio is ~510 mAh/g increasing to 670 mAh/g after 900 cycles, a 30% increase in specific capacity. Both composite IO ratio electrodes were stopped after 1000 cycles for the faster rate and so the final capacity for the 2:1 ratio was recorded at ~560 mAh/g. This is greater than the value recorded for the 5:1 ratio and to that seen for the 2:1 ratio at the lower rate of 150 mAh/g, which was ~500 mAh/g. This response may stem from the germanium dioxide which is known to perform well at high rates, including in IO macroporous form, and becomes electrochemically active later in the cycling life as the overall electrode material changes with cycling, as discussed earlier.[69] Figure 4.9 (e) and (f) show the coulombic efficiencies recorded for the faster rate for the 2:1 ratio and the 5:1 ratio, respectively. The 2:1 ratio IO electrode shows stable coulombic efficiency with an ICE of 56% which is limited to the first cycle, and an average of 99.4 % after that. The 5:1 ratio has a lower ICE of 48.6% and an average coulombic efficiency of 91.6 % over the 1000 cycles. This is considerably lower than the 2:1 and also the CE recorded for the 5:1 ratio at the lower specific current of 150 mA/g.

4.3.3 Post-Mortem Structural Analysis of TiO_2/GeO_2 Inverse Opals

As GeO_2 is a conversion/alloying type material, it is known to undergo a large volume change exceeding 300% while TiO_2 IOs have been shown previously to maintain their interconnected structure for over 5000 cycles with isotropic swelling.[11,

[46] The structural changes of the composite TiO_2/GeO_2 IOs after lithiation were studied using scanning electron microscopy (SEM), shown in Fig. 4.10, to investigate volume expansion and structural integrity. After 2000 cycles, the ordered IO structure in both ratios remains intact, although distorted. The 2:1 composite ratio pore diameters were measured to be ~330 nm, having shrunk ~20% in diameter from 406 nm before cycling. While the 5:1 ratio pores were measured to be ~350 nm, a 15% decrease from the 412 nm pore diameter measured before cycling. This is due to the swelling of the walls with lithium insertion which expand into the pores of the IO, helping to prevent pulverization of the overall structure. The interconnectivity of the porous structure is maintained however and while the periodic swelling has deformed the material over extended cycling, the electrolyte-accessible pore structure and the interconnectivity ensure that materials remain electrochemically active, evidenced by the CE and voltage profiles. SEM images taken after 1000 cycles at 450 mA/g for the 2:1 composite ratio and after the rate test for the 5:1 ratio are shown in supplementary material Figs S4.6 and S4.7, respectively. These images show the structural integrity, which is inherent to the inverse opal morphology, remains even with various current densities.

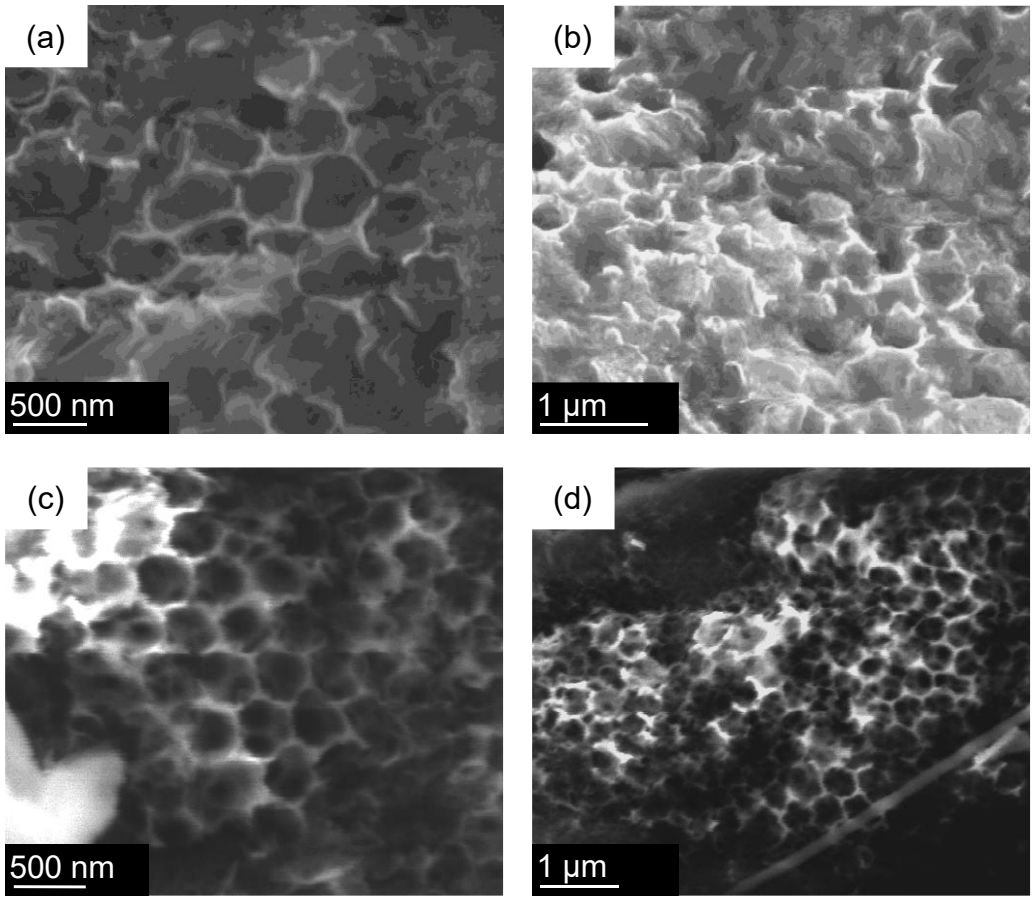

Figure 4.10. SEM images of (a,b) the 2:1 TiO_2/GeO_2 IO material and (c,d) the 5:1 TiO_2/GeO_2 IO material after 2000 cycles showing the interconnected pore structures. Volumetric swelling reduces the pore size. The fibrous material in some images are remnant glass fibers from the separators used in these cells.

4.4 Conclusions

Highly ordered, macroporous inverse opal structures can be made as TiO_2/GeO_2 nanocomposites with various GeO_2 content and provide Coulombic and voltage stable response where the Ge content and its distribution influence the overall capacity at both slow and fast rates. Material characterisation showed anatase TiO_2 and hexagonal GeO_2 phases. GeO_2 incorporation appears to be graded, and XPS identified more elemental Ge below the surface of the IO electrode material.

The introduction of relatively small amounts of germanium improves the specific capacity of TiO_2 with the 2:1 ratio having an initial specific capacity of 1994 mAh/g and the 5:1 ratio reaching 1665 mAh/g at a specific current of 150 mA/g. Both materials displayed interesting behavior between 200 and 900 cycles where we find a characteristic increasing in specific capacities before capacity fading occurs in later cycles. This effect was linked to pulverization that opened fresh material to the electrolyte, including metalloid Ge, and a consistent reduction in the amount of GeO_2 with cycling, so that the charge contribution from its electrochemical reduction to elemental Ge, prior to lithium alloying reaction, reduced. This effect is not seen in either pure TiO_2 or GeO_2 IO electrodes, and a unique observation for composites of these materials. The specific capacity of the 2:1 ratio composite IO increased by 58% from ~310 mAh/g at 200 cycles to ~500 mAh/g for the 1000^{th} cycle before fading to ~120 mAh/g by the 2000^{th} cycle, having run for almost 10,000 hours. The 5:1 ratio capacity increased from 480 mAh/g (150^{th} cycle) to ~730 mAh/g (1000^{th} cycle) which is a 52% increase before fading to ~330 mAh/g by the 1720^{th} cycle, showing superior capacity retention when compared to the 2:1 ratio. While IO electrodes offer consistent and stable cycling behavior, this work identified features in composites that allow for capacity increases with cycling, while retaining coulombic efficiencies of >99% during this period of capacity increase. However, a maximum capacity is reached in all cases, followed by a more severe capacity fading than is normally seen in the pure TiO_2 and GeO_2 electrodes under similar conditions.

Rate testing was performed at intervals of 10 cycles with specific currents ranging from 75 mA/g to 450 mA/g. Both materials displayed good capacity retention, with the 2:1 composite ratio retaining 94% capacity while the 5:1 ratio retained 83.5% of its capacity. Dedicated fast rate cycling was performed at 450 mA/g for 1000 cycles

with the 2:1 ratio exhibiting ~1400 mAh/g for the initial discharge, and ~1630 mAh/g for the 5:1 ratio. The 2:1 ratio IO behaved well under fast rate conditions displaying a reversible capacity of ~500 mAh/g with an average coulombic efficiency (CE) of 99.4 %. For the 5:1 ratio displayed high capacity values (with a reversible capacity of ~400 – 500 mAh/g), the coulombic efficiency plot highlights issues with the average CE measured at 91.6 %. Post cycling material characterisation was done via SEM imaging and showed the structure is partially retained after 2000 cycles for the 2:1 ratio. These findings demonstrate that composites of well-behaved interconnected macroporous Li-ion battery anode materials exhibit unusual behavior even when coulombically efficient, and with stable and well-known voltage profiles. The accessibility and spatial distribution of the Ge is a key factor here, but difficult to control from solution mixing processes. Cycling does relieve this Ge content to become accessible and electrochemically active, with the results showing that a small Ge content has a significant influence on the behavior of the composite. An intriguing finding for dual phase composites such as these is that some reversible lithium reaction with the GeO_2 becomes self-limiting, and the system preferentially allows reversible alloying with metalloid germanium in the TiO_2/GeO_2 composites. In tandem, the capacity, once stabilized to >99% coulombic efficiency post-SEI formation, is seen to continually increase even with >99% efficiency, followed by a sharp fading of capacity with cycling. The data highlights some benefits of tailoring porous material and their compositions to improve capacity and rate-behavior, but also shows how sensitive and different reversible reactions can lead to efficient but variable specific capacities.

The data shows that a composite of intercalation and alloying compounds can provide good capacity and excellent coulombic efficiency, even with low quantities of the higher capacity alloying compound. Further, gradients from spatial

heterogeneities are shown to affect capacity in cycling life, where increasing capacity are found as the higher capacity material is relieved within the composite matrix as the material is modified during cycling, while remaining ideally coulombically efficient. Composites using dissimilar Li reactions and the concentrations are potentially useful, but care is needed to ensure homogeneous formulation for cycling stability of the capacity values.

4.5 Appendix: Supplementary Information

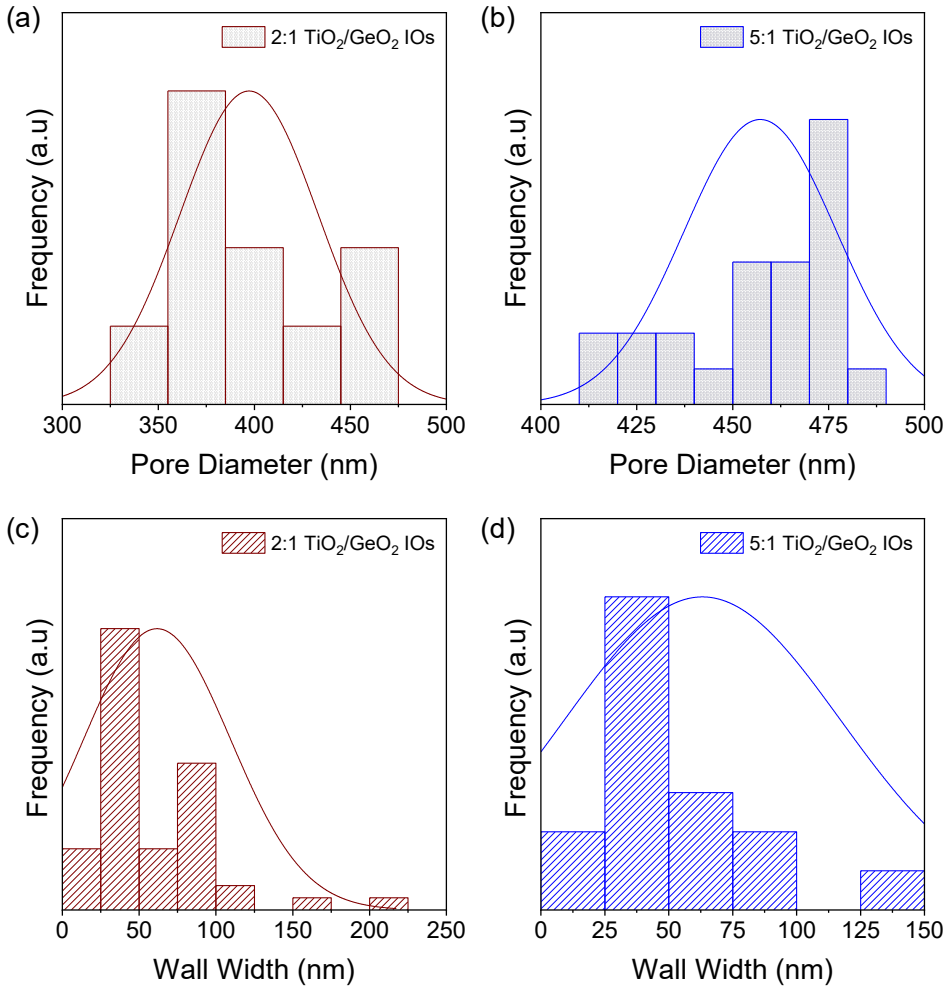

Figure S4.1. Histograms showing the distribution of pore diameters of (a) 2:1 TiO_2/GeO_2 and (b) 5:1 TiO_2/GeO_2. Histogram showing distribution of wall thickness of (c) 2:1 TiO_2/GeO_2 and (d) 5:1 TiO_2/GeO_2.

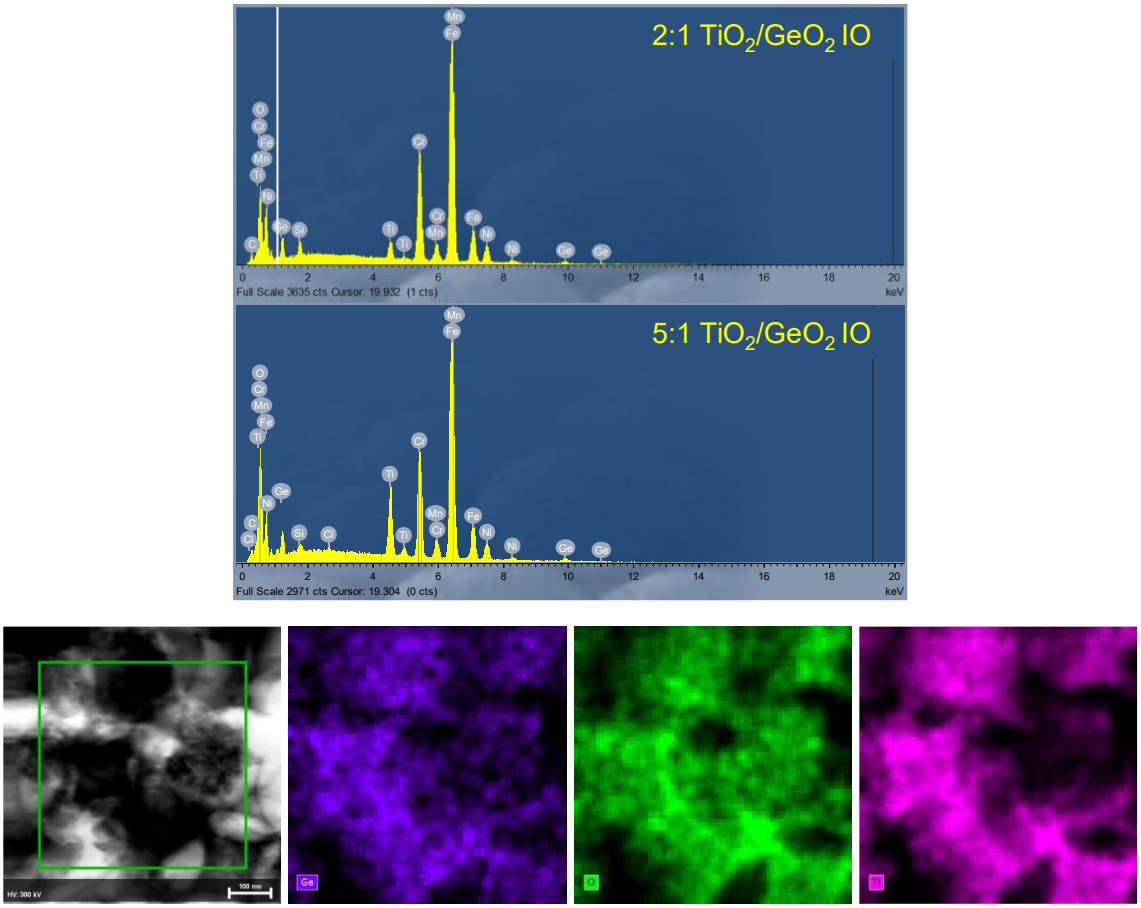

Figure S4.2. EDX spectra of the 2:1 and 5:1 TiO_2/GeO_2 inverse opal materials. Trace elements are also detected from the underlying stainless steel current collector. EDX mapping also confirmed the distribution of Ti, Ge, and O throughout the structure.

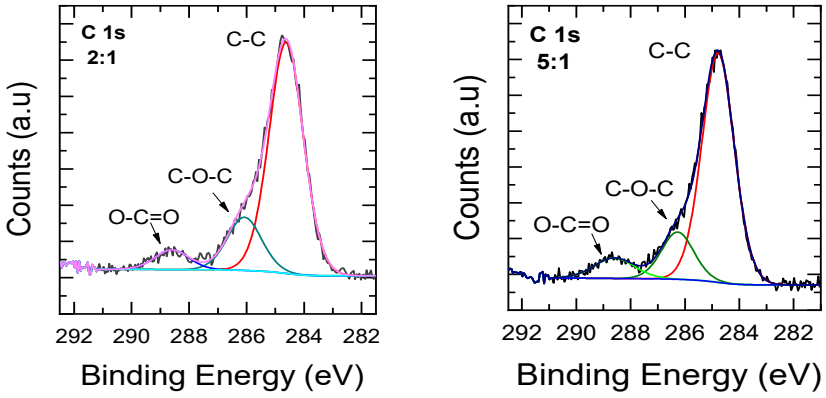

Figure S4.3. XPS analysis of C1s level for the 2:1 ratio of TiO_2/GeO_2 inverse opals (left) and the 5:1 ratio of TiO_2/GeO_2 inverse opals (right).

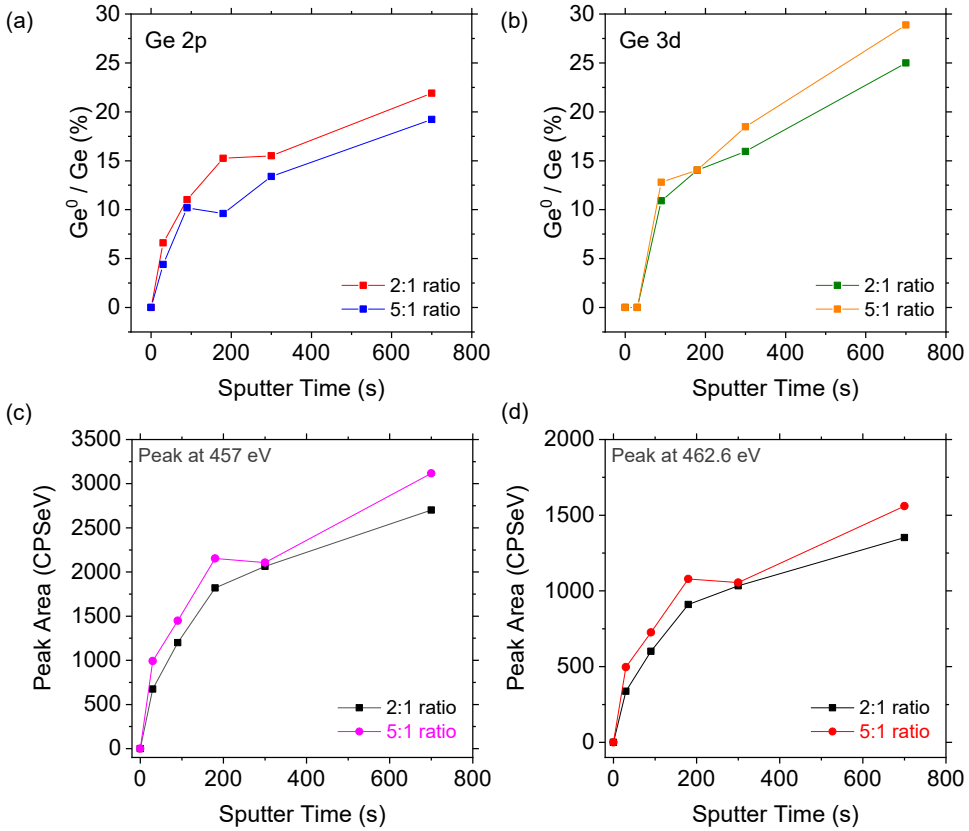

Figure S4.4. XPS sputter depth profiles: Atomic percentage of elemental Ge relative to total Ge present as a function of sputter time for (a) the Ge 2p core level and (b) the Ge 3d core level. Peak area vs sputter time for peak observed at (c) 457 eV and (d) 462.6 eV for Ti 2p core level.

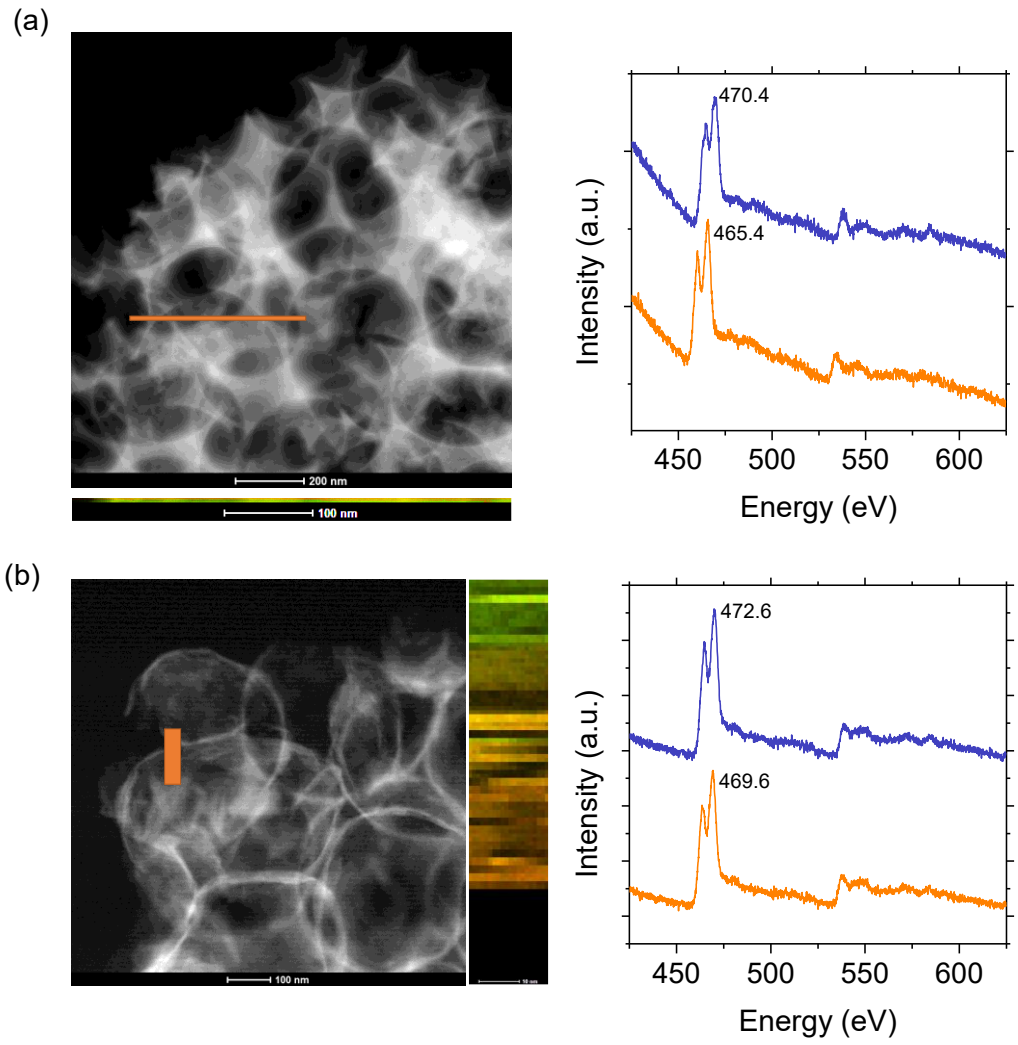

Figure S4.5. Darkfield TEM images and corresponding EELS spectra for (a) 2:1 ratio and (b) 5:1 ratio.

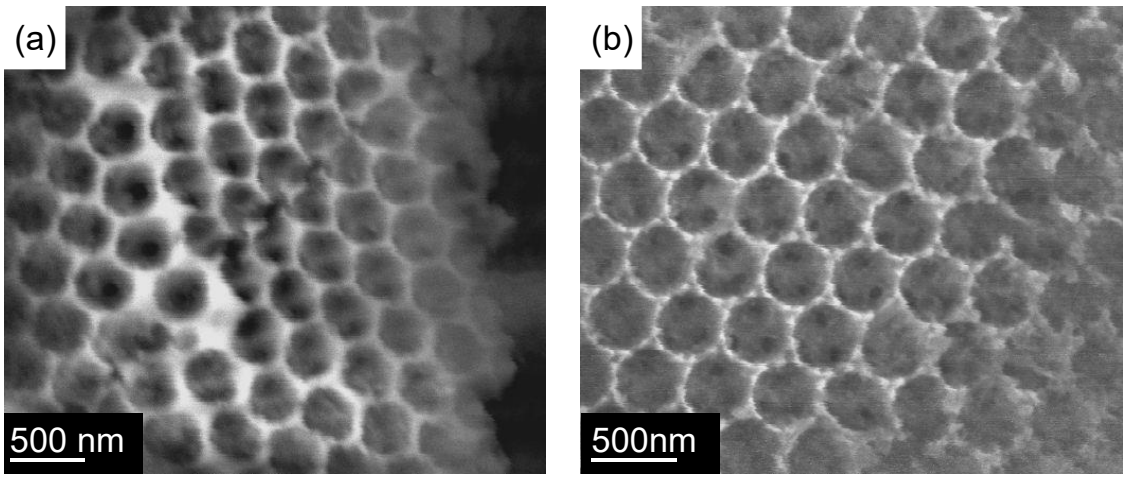

Figure S4.6. (a) and (b) SEM images of the 2:1 ratio after 1000 cycles at 450 mA/g.

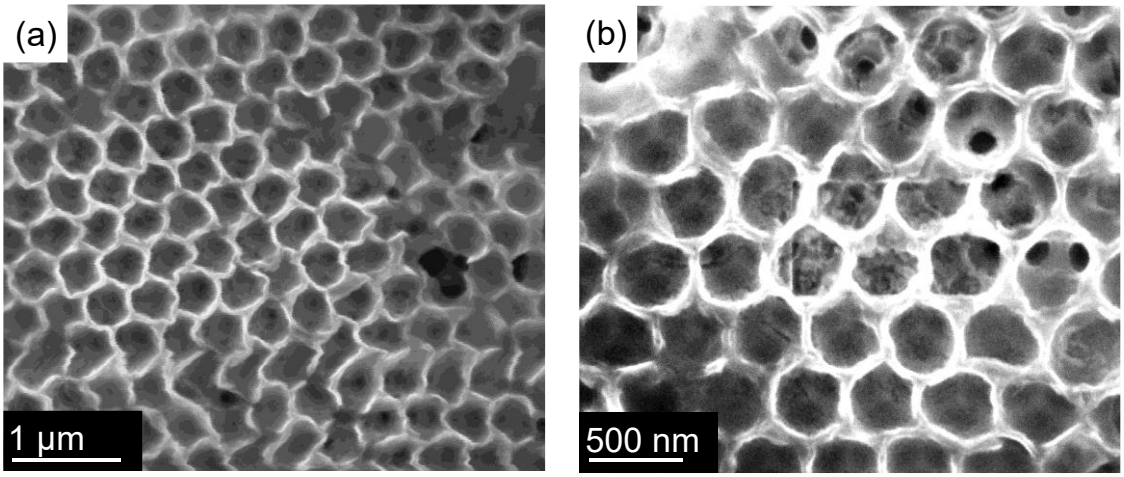

Figure S4.7. (a) and (b) SEM images of 5:1 ratio after rate test. As with the IO composite after 1000 cycles, the structure is maintained with some buckling and thickening of the IO walls in places.

4.6 References

(1) Goodenough, J. B.; Kim, Y. Challenges for Rechargeable Li Batteries. *Chemistry of Materials* **2010**, *22* (3), 587-603. DOI: 10.1021/cm901452z.
(2) Tarascon, J. M.; Armand, M. Issues and challenges facing rechargeable lithium batteries. *Nature* **2001**, *414* (6861), 359-367, Review. DOI: 10.1038/35104644 Scopus.
(3) Choi, J. W.; Aurbach, D. Promise and reality of post-lithium-ion batteries with high energy densities. *Nature Reviews Materials* **2016**, *1* (4), 16013. DOI: 10.1038/natrevmats.2016.13.
(4) Wang, K.; Hua, W.; Huang, X.; Stenzel, D.; Wang, J.; Ding, Z.; Cui, Y.; Wang, Q.; Ehrenberg, H.; Breitung, B.; et al. Synergy of cations in high entropy oxide lithium ion battery anode. *Nature Communications* **2023**, *14* (1), 1487. DOI: 10.1038/s41467-023-37034-6.
(5) Bauer, C.; Burkhardt, S.; Dasgupta, N. P.; Ellingsen, L. A.-W.; Gaines, L. L.; Hao, H.; Hischier, R.; Hu, L.; Huang, Y.; Janek, J.; et al. Charging sustainable batteries. *Nature Sustainability* **2022**, *5* (3), 176-178. DOI: 10.1038/s41893-022-00864-1.
(6) Harlow, J.; Ma, X.; Li, J.; Logan, E.; Liu, Y.; Zhang, N.; Ma, L.; Glazier, S.; Cormier, M.; Genovese, M.; et al. A Wide Range of Testing Results on an Excellent Lithium-Ion Cell Chemistry to be used as Benchmarks for New Battery Technologies. *Journal of The Electrochemical Society* **2019**, *166*, A3031-A3044. DOI: 10.1149/2.0981913jes.
(7) Eldesoky, A.; Logan, E.; Louli, A.; Song, W.; Weber, R.; Hy, S.; Petibon, R.; Harlow, J.; Azam, S.; Zsoldos, E. Impact of graphite materials on the lifetime of NMC811/graphite pouch cells: part II. long-term cycling, stack pressure growth, isothermal microcalorimetry, and lifetime projection. *Journal of The Electrochemical Society* **2022**, *169* (1), 010501.
(8) Liao, J. Y.; Manthiram, A. Mesoporous TiO2-Sn/C Core-Shell Nanowire Arrays as High-Performance 3D Anodes for Li-Ion Batteries. *Advanced Energy Materials* **2014**, *4* (14), 1400403-n/a. DOI: 10.1002/aenm.201400403.
(9) Dylla, A. G.; Henkelman, G.; Stevenson, K. J. Lithium Insertion in Nanostructured TiO2(B) Architectures. *Accounts of Chemical Research* **2013**, *46* (5), 1104-1112. DOI: 10.1021/ar300176y.
(10) Wang, Y.-Q.; Gu, L.; Guo, Y.-G.; Li, H.; He, X.-Q.; Tsukimoto, S.; Ikuhara, Y.; Wan, L.-J. Rutile-TiO2 nanocoating for a high-rate Li4Ti5O12 anode of a lithium-ion battery. *Journal of the American Chemical Society* **2012**, *134* (18), 7874-7879.
(11) Chan, C. K.; Zhang, X. F.; Cui, Y. High Capacity Li Ion Battery Anodes Using Ge Nanowires. *Nano Letters* **2008**, *8* (1), 307-309. DOI: 10.1021/nl0727157.
(12) Seng, K. H.; Park, M. H.; Guo, Z. P.; Liu, H. K.; Cho, J. Self-Assembled Germanium/Carbon Nanostructures as High-Power Anode Material for the Lithium-Ion Battery. *Angewandte Chemie International Edition* **2012**, *51* (23), 5657-5661. DOI: 10.1002/anie.201201488.
(13) Kumar Sen, U.; Shaligram, A.; Mitra, S. Intercalation Anode Material for Lithium Ion Battery Based on Molybdenum Dioxide. *ACS Applied Materials & Interfaces* **2014**, *6* (16), 14311-14319. DOI: 10.1021/am503605u.
(14) Zhu, Z. Q.; Wang, S. W.; Du, J.; Jin, Q.; Zhang, T. R.; Cheng, F. Y.; Chen, J. Ultrasmall Sn Nanoparticles Embedded in Nitrogen-Doped Porous Carbon As High-Performance Anode for Lithium-Ion Batteries. *Nano Letters* **2014**, *14* (1), 153-157. DOI: 10.1021/nl403631h.

(15) Armstrong, E.; O'Dwyer, C. Artificial opal photonic crystals and inverse opal structures – fundamentals and applications from optics to energy storage. *Journal of Materials Chemistry C* **2015**, *3* (24), 6109-6143, 10.1039/C5TC01083G. DOI: 10.1039/C5TC01083G.
(16) Armstrong, E.; McNulty, D.; Geaney, H.; O'Dwyer, C. Electrodeposited Structurally Stable V2O5 Inverse Opal Networks as High Performance Thin Film Lithium Batteries. *ACS Applied Materials & Interfaces* **2015**, *7* (48), 27006-27015. DOI: 10.1021/acsami.5b09511.
(17) Phillips, K. R.; Shirman, T.; Shirman, E.; Shneidman, A. V.; Kay, T. M.; Aizenberg, J. Nanocrystalline Precursors for the Co-Assembly of Crack-Free Metal Oxide Inverse Opals. *Advanced Materials* **2018**, *30* (19), 1706329. DOI: https://doi.org/10.1002/adma.201706329 (acccessed 2023/11/22).
(18) Mukhopadhyay, A.; Sheldon, B. W. Deformation and stress in electrode materials for Li-ion batteries. *Progress in Materials Science* **2014**, *63*, 58-116, Review. DOI: 10.1016/j.pmatsci.2014.02.001 Scopus.
(19) Liu, N.; Wu, H.; McDowell, M. T.; Yao, Y.; Wang, C.; Cui, Y. A Yolk-Shell Design for Stabilized and Scalable Li-Ion Battery Alloy Anodes. *Nano Letters* **2012**, *12* (6), 3315-3321. DOI: 10.1021/nl3014814.
(20) Zhang, Y.; Tang, Y.; Li, W.; Chen, X. Nanostructured TiO2-Based Anode Materials for High-Performance Rechargeable Lithium-Ion Batteries. *ChemNanoMat* **2016**, *2* (8), 764-775. DOI: 10.1002/cnma.201600093 (acccessed 2020/02/11).
(21) Li, D.; Wang, H.; Liu, H. K.; Guo, Z. A New Strategy for Achieving a High Performance Anode for Lithium Ion Batteries—Encapsulating Germanium Nanoparticles in Carbon Nanoboxes. *Advanced Energy Materials* **2016**, *6* (5), 1501666. DOI: https://doi.org/10.1002/aenm.201501666.
(22) Collins, G.; Armstrong, E.; McNulty, D.; O'Hanlon, S.; Geaney, H.; O'Dwyer, C. 2D and 3D photonic crystal materials for photocatalysis and electrochemical energy storage and conversion. *Science and Technology of Advanced Materials* **2016**, *17* (1), 563-582. DOI: 10.1080/14686996.2016.1226121.
(23) Sakamoto, J. S.; Dunn, B. Hierarchical battery electrodes based on inverted opal structures. *Journal of Materials Chemistry* **2002**, *12* (10), 2859-2861, 10.1039/B205634H. DOI: 10.1039/B205634H.
(24) O'Dwyer, C. Color-Coded Batteries – Electro-Photonic Inverse Opal Materials for Enhanced Electrochemical Energy Storage and Optically Encoded Diagnostics. *Advanced Materials* **2016**, *28* (27), 5681-5688. DOI: 10.1002/adma.201503973 (acccessed 2019/10/01).
(25) Osiak, M.; Geaney, H.; Armstrong, E.; O'Dwyer, C. Structuring materials for lithium-ion batteries: advancements in nanomaterial structure, composition, and defined assembly on cell performance. *Journal of Materials Chemistry A* **2014**, *2* (25), 9433-9460, 10.1039/C4TA00534A. DOI: 10.1039/C4TA00534A.
(26) Lonergan, A.; O'Dwyer, C. Many Facets of Photonic Crystals: From Optics and Sensors to Energy Storage and Photocatalysis. *Advanced Materials Technologies* **2023**, *8* (6), 2201410, https://doi.org/10.1002/admt.202201410. DOI: https://doi.org/10.1002/admt.202201410 (acccessed 2023/07/05).
(27) McNulty, D.; Lonergan, A.; O'Hanlon, S.; O'Dwyer, C. 3D open-worked inverse opal TiO2 and GeO2 materials for long life, high capacity Li-ion battery anodes. *Solid State Ionics* **2018**, *314*, 195-203. DOI: https://doi.org/10.1016/j.ssi.2017.10.008.
(28) Vu, A.; Qian, Y.; Stein, A. Porous Electrode Materials for Lithium-Ion Batteries – How to Prepare Them and What Makes Them Special. *Advanced Energy Materials*

2012, *2* (9), 1056-1085, https://doi.org/10.1002/aenm.201200320. DOI: https://doi.org/10.1002/aenm.201200320 (acccessed 2023/06/22).
(29) Zhang, H.; Yu, X.; Braun, P. V. Three-dimensional bicontinuous ultrafast-charge and -discharge bulk battery electrodes. *Nature Nanotechnology* **2011**, *6* (5), 277-281. DOI: 10.1038/nnano.2011.38.
(30) Reiman, K. H.; Brace, K. M.; Gordon-Smith, T. J.; Nandhakumar, I.; Attard, G. S.; Owen, J. R. Lithium insertion into TiO2 from aqueous solution–Facilitated by nanostructure. *Electrochemistry communications* **2006**, *8* (4), 517-522.
(31) Wu, M.-S.; Wang, M.-J.; Jow, J.-J.; Yang, W.-D.; Hsieh, C.-Y.; Tsai, H.-M. Electrochemical fabrication of anatase TiO2 nanostructure as an anode material for aqueous lithium-ion batteries. *Journal of Power Sources* **2008**, *185* (2), 1420-1424.
(32) Dambournet, D.; Belharouak, I.; Amine, K. Tailored Preparation Methods of TiO2 Anatase, Rutile, Brookite: Mechanism of Formation and Electrochemical Properties. *Chemistry of Materials* **2010**, *22* (3), 1173-1179. DOI: 10.1021/cm902613h.
(33) Legrain, F.; Malyi, O.; Manzhos, S. Insertion energetics of lithium, sodium, and magnesium in crystalline and amorphous titanium dioxide: A comparative first-principles study. *Journal of Power Sources* **2015**, *278*, 197-202. DOI: https://doi.org/10.1016/j.jpowsour.2014.12.058.
(34) Liang, S.; Wang, X.; Cheng, Y.-J.; Xia, Y.; Müller-Buschbaum, P. Anatase titanium dioxide as rechargeable ion battery electrode - A chronological review. *Energy Storage Materials* **2022**, *45*, 201-264. DOI: https://doi.org/10.1016/j.ensm.2021.11.023.
(35) Wei, Z.; Li, R.; Huang, T.; Yu, A. Fabrication and electrochemical properties of Si/TiO2 nanowire array composites as lithium ion battery anodes. *Journal of Power Sources* **2013**, *238*, 165-172. DOI: https://doi.org/10.1016/j.jpowsour.2013.03.080.
(36) Zhu, Q.; Hu, H.; Li, G.; Zhu, C.; Yu, Y. TiO2 Nanotube Arrays Grafted with MnO2 Nanosheets as High-Performance Anode for Lithium Ion Battery. *Electrochimica Acta* **2015**, *156*, 252-260. DOI: https://doi.org/10.1016/j.electacta.2015.01.023.
(37) Chen, K.; Tan, Y.; Gao, Y.; Chen, Y. Y. Carbon-coated SiOx/TiO2 composite nanospheres with conductive TiO2 nanocrystals as anode materials for lithium-ion batteries. *Electrochimica Acta* **2023**, *450*, 142165. DOI: https://doi.org/10.1016/j.electacta.2023.142165.
(38) Bai, Y.; Yan, D.; Yu, C.; Cao, L.; Wang, C.; Zhang, J.; Zhu, H.; Hu, Y.-S.; Dai, S.; Lu, J.; et al. Core-shell Si@TiO2 nanosphere anode by atomic layer deposition for Li-ion batteries. *Journal of power sources* **2016**, *308*, 75-82. DOI: 10.1016/j.jpowsour.2016.01.049.
(39) Jiang, M.; Zhang, F.; Zhu, G.; Ma, Y.; Luo, W.; Zhou, T.; Yang, J. Interface-Amorphized Ti3C2@Si/SiOx@TiO2 Anodes with Sandwiched Structures and Stable Lithium Storage. *ACS Applied Materials & Interfaces* **2020**, *12* (22), 24796-24805. DOI: 10.1021/acsami.0c05116.
(40) Lotfabad, E. M.; Kalisvaart, P.; Cui, K.; Kohandehghan, A.; Kupsta, M.; Olsen, B.; Mitlin, D. ALD TiO 2 coated silicon nanowires for lithium ion battery anodes with enhanced cycling stability and coulombic efficiency. *Physical Chemistry Chemical Physics* **2013**, *15* (32), 13646-13657.
(41) Wang, D.; Chang, Y.-L.; Wang, Q.; Cao, J.; Farmer, D. B.; Gordon, R. G.; Dai, H. Surface Chemistry and Electrical Properties of Germanium Nanowires. *Journal of the American Chemical Society* **2004**, *126* (37), 11602-11611. DOI: 10.1021/ja047435x.

(42) Yue, G. H.; Zhang, X. Q.; Zhao, Y. C.; Xie, Q. S.; Zhang, X. X.; Peng, D. L. High performance of Ge@C nanocables as the anode for lithium ion batteries. *RSC Advances* **2014**, *4* (41), 21450-21455, 10.1039/C4RA01512F. DOI: 10.1039/C4RA01512F.
(43) Yang, L. C.; Gao, Q. S.; Li, L.; Tang, Y.; Wu, Y. P. Mesoporous germanium as anode material of high capacity and good cycling prepared by a mechanochemical reaction. *Electrochemistry Communications* **2010**, *12* (3), 418-421. DOI: https://doi.org/10.1016/j.elecom.2010.01.008.
(44) McNulty, D.; Geaney, H.; Buckley, D.; O'Dwyer, C. High capacity binder-free nanocrystalline GeO2 inverse opal anodes for Li-ion batteries with long cycle life and stable cell voltage. *Nano Energy* **2018**, *43*, 11-21. DOI: https://doi.org/10.1016/j.nanoen.2017.11.007.
(45) McNulty, D.; Carroll, E.; O'Dwyer, C. Rutile TiO2 Inverse Opal Anodes for Li-Ion Batteries with Long Cycle Life, High-Rate Capability, and High Structural Stability. *Advanced Energy Materials* **2017**, *7* (12), 1602291. DOI: 10.1002/aenm.201602291.
(46) McNulty, D.; Carroll, E.; O'Dwyer, C. Rutile TiO2 Inverse Opal Anodes for Li-Ion Batteries with Long Cycle Life, High-Rate Capability, and High Structural Stability. *Advanced Energy Materials* **2017**, *7* (12), n/a-n/a. DOI: 10.1002/aenm.201602291.
(47) Pang, Y.; Xu, G.; Feng, Q.; Lv, J.; Qin, Y.; Zhang, Y.; Zheng, Z.; Wu, Y. Crystalline orientation preference for TiO2 nanotube arrays with efficient photoelectrochemical properties. *Physics Letters A* **2018**, *382* (38), 2759-2762. DOI: https://doi.org/10.1016/j.physleta.2018.07.021.
(48) Choi, H. C.; Jung, Y. M.; Kim, S. B. Size effects in the Raman spectra of TiO2 nanoparticles. *Vibrational Spectroscopy* **2005**, *37* (1), 33-38. DOI: https://doi.org/10.1016/j.vibspec.2004.05.006.
(49) Scott, J. F. Raman Spectra of Ge${\mathrm{O}}_{2}$. *Physical Review B* **1970**, *1* (8), 3488-3493. DOI: 10.1103/PhysRevB.1.3488.
(50) Loechelt, G. H.; Cave, N. G.; Menéndez, J. Polarized off-axis Raman spectroscopy: A technique for measuring stress tensors in semiconductors. *Journal of Applied Physics* **1999**, *86* (11), 6164-6180. DOI: 10.1063/1.371670 (acccessed 2023/01/14).
(51) Pan, L.; Wang, S.; Zou, J.-J.; Huang, Z.-F.; Wang, L.; Zhang, X. Ti3+-defected and V-doped TiO2 quantum dots loaded on MCM-41. *Chemical Communications* **2014**, *50* (8), 988-990, 10.1039/C3CC47752E. DOI: 10.1039/C3CC47752E.
(52) Morgan, W. E.; Van Wazer, J. R. Binding energy shifts in the x-ray photoelectron spectra of a series of related Group IVa compounds. *The Journal of Physical Chemistry* **1973**, *77* (7), 964-969. DOI: 10.1021/j100626a023.
(53) McNulty, D.; Geaney, H.; Ramasse, Q.; O'Dwyer, C. Long Cycle Life, Highly Ordered SnO2/GeO2 Nanocomposite Inverse Opal Anode Materials for Li-Ion Batteries. *Advanced Functional Materials* **2020**, *30* (51), 2005073, https://doi.org/10.1002/adfm.202005073. DOI: https://doi.org/10.1002/adfm.202005073 (acccessed 2021/02/22).
(54) Hernan, L.; Morales, J.; Sanchez, L.; Tirado, J. L.; Espinos, J. P.; Gonzalez Elipe, A. R. Diffraction and XPS Studies of Misfit Layer Chalcogenides Intercalated with Cobaltocene. *Chemistry of Materials* **1995**, *7* (8), 1576-1582. DOI: 10.1021/cm00056a026.
(55) Diebold, U. The surface science of titanium dioxide. *Surface Science Reports* **2003**, *48* (5), 53-229. DOI: https://doi.org/10.1016/S0167-5729(02)00100-0.

(56) Sugiawati, V. A.; Vacandio, F.; Galeyeva, A.; Kurbatov, A. P.; Djenizian, T. Enhanced Electrochemical Performance of Electropolymerized Self-Organized TiO2 Nanotubes Fabricated by Anodization of Ti Grid. *Frontiers in Physics* **2019**, *7* (179), Original Research. DOI: 10.3389/fphy.2019.00179.
(57) Zeng, L.; Huang, X.; Chen, X.; Zheng, C.; Qian, Q.; Chen, Q.; Wei, M. Ge/GeO2-Ordered Mesoporous Carbon Nanocomposite for Rechargeable Lithium-Ion Batteries with a Long-Term Cycling Performance. *ACS Applied Materials & Interfaces* **2016**, *8* (1), 232-239. DOI: 10.1021/acsami.5b08470.
(58) Bao, S.-J.; Bao, Q.-L.; Li, C.-M.; Zhi-Li, D. Novel porous anatase TiO2 nanorods and their high lithium electroactivity. *Electrochemistry Communications* **2007**, *9* (5), 1233-1238. DOI: https://doi.org/10.1016/j.elecom.2007.01.028.
(59) Kavan, L.; Grätzel, M.; Gilbert, S. E.; Klemenz, C.; Scheel, H. J. Electrochemical and Photoelectrochemical Investigation of Single-Crystal Anatase. *Journal of the American Chemical Society* **1996**, *118* (28), 6716-6723. DOI: 10.1021/ja9541721.
(60) Yan, S.; Song, H.; Lin, S.; Wu, H.; Shi, Y.; Yao, J. GeO2 Encapsulated Ge Nanostructure with Enhanced Lithium-Storage Properties. *Advanced Functional Materials* **2019**, *29* (8), 1807946, https://doi.org/10.1002/adfm.201807946. DOI: https://doi.org/10.1002/adfm.201807946 (acccessed 2022/06/28).
(61) Arro, C. R.; Mohamed, A. T. I.; Bensalah, N. Impact of Ge content on the electrochemical performance of Germanium Oxide/Germanium/ reduced graphene (GeO2/Ge/r-GO) hybrid composite anodes for lithium-ion batteries. *Materials Today Communications* **2022**, *30*, 103151. DOI: https://doi.org/10.1016/j.mtcomm.2022.103151.
(62) Ngo, D. T.; Kalubarme, R. S.; Chourashiya, M. G.; Park, C.-N.; Park, C.-J. Electrochemical Performance of GeO2/C Core Shell based Electrodes for Li-ion Batteries. *Electrochimica Acta* **2014**, *116*, 203-209. DOI: https://doi.org/10.1016/j.electacta.2013.11.031.
(63) Kavan, L.; Rathouský, J.; Grätzel, M.; Shklover, V.; Zukal, A. Surfactant-Templated TiO2 (Anatase): Characteristic Features of Lithium Insertion Electrochemistry in Organized Nanostructures. *The Journal of Physical Chemistry B* **2000**, *104* (50), 12012-12020. DOI: 10.1021/jp003609v.
(64) Zachau-Christiansen, B.; West, K.; Jacobsen, T.; Atlung, S. Lithium insertion in different TiO2 modifications. *Solid State Ionics* **1988**, *28-30*, 1176-1182. DOI: https://doi.org/10.1016/0167-2738(88)90352-9.
(65) Gentili, V.; Brutti, S.; Hardwick, L. J.; Armstrong, A. R.; Panero, S.; Bruce, P. G. Lithium Insertion into Anatase Nanotubes. *Chemistry of Materials* **2012**, *24* (22), 4468-4476. DOI: 10.1021/cm302912f.
(66) Wagemaker, M.; Borghols, W. J. H.; Mulder, F. M. Large Impact of Particle Size on Insertion Reactions. A Case for Anatase LixTiO2. *Journal of the American Chemical Society* **2007**, *129* (14), 4323-4327. DOI: 10.1021/ja067733p.
(67) Jiang, M.; Chen, J.; Zhang, Y.; Song, N.; Jiang, W.; Yang, J. Assembly: A Key Enabler for the Construction of Superior Silicon-Based Anodes. *Advanced Science* **2022**, *9* (30), 2203162. DOI: https://doi.org/10.1002/advs.202203162 (acccessed 2023/11/22).
(68) Tan, L. P.; Lu, Z.; Tan, H. T.; Zhu, J.; Rui, X.; Yan, Q.; Hng, H. H. Germanium nanowires-based carbon composite as anodes for lithium-ion batteries. *Journal of Power Sources* **2012**, *206*, 253-258. DOI: https://doi.org/10.1016/j.jpowsour.2011.12.064.

(69) Li, X.; Yang, Z.; Fu, Y.; Qiao, L.; Li, D.; Yue, H.; He, D. Germanium Anode with Excellent Lithium Storage Performance in a Germanium/Lithium–Cobalt Oxide Lithium-Ion Battery. *ACS Nano* **2015**, *9* (2), 1858-1867. DOI: 10.1021/nn506760p.

Chapter 5

Three–Dimensionally Ordered Macroporous Amorphous C/TiO_2 Composite Electrodes for Li-ion Batteries

Adapted from : Three – Dimensionally Ordered Macroporous Amorphous C/TiO2 Composite Electrodes for Lithium-ion Batteries.

ECS Advances **2024**, *3* (1), 010502. DOI: 10.1149/2754-2734/ad248e.

Abstract

A facile method utilizing colloidal templating and sucrose as a carbon precursor is used to synthesize highly ordered, porous inverse opal structures as C/TiO_2 nanocomposites. Material characterization shows amorphous TiO_2 and large pore size of ~400 nm allowing for enhanced electrolyte penetration. C/TiO_2 inverse opals materials as electrodes in Li-ion battery half cells demonstrate discharge and charge capacities of ~870 mAh/g and 470 mAh/g, respectively, at a current density of 150 mA/g. The enhanced capacities, which surpass theoretical limits for TiO_2 and carbon based on intercalation reactions, are analysed under voltammetric conditions to assess relative contributions to capacity from diffusion-limited intercalations and capacitive charge compensation reactions. The porous structure contributes to excellent capacity retention, rate performance and improved Coulombic efficiency (99.6% after 250 cycles), compared to individual carbon and TiO_2 inverse opals.

5.1 Introduction

The development of high–performance lithium-ion batteries (LIBs) has revolutionized modern portable electronics and electric vehicle technology.[1-4] The key to the outstanding performance of LIBs lies in the design and engineering of their electrodes.[5-8] As the demand for higher energy density, faster charging capabilities and longer cycle life continues to grow, the need for advanced electrode materials[9, 10] and designs becomes increasingly crucial. Large-scale production of carbon-based materials has made them a prevalent choice as anodes in LIBs, widely used in both portable and stationary devices due to their cost-effectiveness, abundance, electrical conductivity, and low toxicity.[11-13] However, carbon based materials are prone to dendrite formation due to their low intercalation potential, which can cause poor cycling stability, and safety issues. Conversely, TiO_2 has shown good chemical and physical properties and has garnered attention as a promising material in LIBs[14-16] and other electrochemical technologies, nonetheless, TiO_2 suffers from limited li-ion and electron transport capabilities which results in low capacity retention and poor rate performances.[17, 18]

Composites materials have garnered significant attention as a means to harness the advantages of multiple materials, often resulting in synergistic outcomes.[19-22] Nevertheless, many commercial materials are slurry-based, comprising of active material particles, binders and conductive additives that are randomly arranged and densely packed, affording limited control over their structural attributes.[23] They exhibit an adverse relationship between tortuosity and porosity, leading to a trade-off between energy density and power density.[24, 25] Consequently, nanostructuring both TiO_2 and carbon materials have been investigated as a method of improving Li^+

diffusion and electrical conductivity as well as increase specific capacity, and examining the relative influence of these parameters.[26-31] Three-dimensional ordered macroporous (3DOM) materials represent a promising avenue in this pursuit, characterized by interconnected pore and wall structures with wall thicknesses of a few tens of nanometers.[32-37] Among these materials, inverse opals (IOs) are a subtype of 3DOMs, formed via a sacrificial template of polymer spheres such as polystyrene.[38, 39] IOs offer the benefit of shorter diffusion lengths for lithium ions and can improve charge transfer rates because of a larger surface area. The porous architecture facilitates rapid Li^+ movement and diffusion within the electrolyte, all while preserving the structural integrity, thus preventing volume swelling or material degradation. Notably, IOs can be prepared directly onto the current collector and so removes the need for any binders or additives.

In this chapter, C/TiO_2 composite inverse opal electrodes with a robust 3D structure and high surface area were synthesized using a solvent infiltration method. Structural characterization in the form of X-ray diffraction (XRD) and selected area electron diffraction (SAED) reveals the amorphous nature of the material. We investigate the effect of combining carbon and TiO_2 by conducting a comparative electrochemical analysis of the composite IO electrode alongside their individual IO counterparts. The electrochemical performances of both materials are analyzed by cyclic voltammetry (CV), galvanostatic cycling (GCPL) and rate testing. Our findings demonstrate that the C/TiO_2 IOs offer increased capacities and improved capacity retention over 250 cycles compared to pure TiO_2 and carbon IOs. Our composite electrodes exhibit stable Coulombic efficiency even at high current densities, showcasing impressive high-rate performance. Furthermore, post-mortem evaluation

underscores the structural stability of the IOs, as they maintain their structural integrity after cycling.

5.2 Experimental

5.2.1 Materials Preparation

The substrates used were stainless steel (SS) discs (grade 304) with a diameter of 15.5 mm. The opal template was fabricated using the evaporation induced self-assembly (EISA) method, which involved suspending the SS discs in a 0.2% solution of polystyrene spheres (500 nm diameter) and deionized water and placing in a convection oven at 60°C overnight. TiO_2 and carbon IO samples were prepared for the purpose of conducting structural and crystallinity comparison analyses, as well as for making electrochemical comparisons with the composite materials.

C/TiO_2 IO Preparation

A 0.1M solution of titanium(IV) chloride tetrahydrofuran ($TiCl_4$.2THF) was prepared in IPA while the carbon precursor solution consisted of sucrose, ethanol (EtOH), deionized water and sulphuric acid (18 M, Sigma Aldrich). These were mixed in mass ratios of 1 : 35.5 : 5 : 0.18, respectively. The dried PS sphere templates were then infilled by drop casting a volume of the carbon precursor (~15 μL) followed by an equal volume of the TiO_2 precursor. The samples were placed in a convection oven at 70 ℃ for 25 min before being heated to 100 ℃ for 5 hours in air. After 5 hours the samples were placed in a tube furnace under Ar and heated to 500 ℃ at a ramp rate of 5 ℃/min. The samples were held at 500 ℃ for 2 hours.

Carbon IO Preparation

The dried PS spheres were infilled with ~30 μL of the sucrose solution before being placed in a convection oven at 70 ℃ for 25 min. The carbon samples were then heated to 100 ℃ for 5 hours in air before being heated to 900 ℃ under Ar and held for 2 hours.

TiO_2 IO Preparation

The dried PS spheres were infilled with ~30 μL of the $TiCl_4$.2THF solution before being placed in a convection oven at 70 ℃ for 25 min. The samples were then heated to 500 ℃ in air at a ramp rate of 5 ℃/min and held for 1 hour.

5.2.2 Material Characterisation

SEM analysis was performed on FEI Quanta 650 FEG high resolution SEM at an accelerating voltage of 10 kV. EDS analysis was performed using a FEI Quanta 650 FEG high resolution SEM at an accelerating voltage of 20 kV. EDS mapping was performed on Zeiss Supra 40 high resolution SEM at an accelerating voltage of 20 kV. SEM images and feature dimensions were analyzed using ImageJ software. Raman scattering was performed on an Ocean Optics QE65PRO Raman Spectrometer using a 40 mW Ar^+ laser at 532 nm excitation. The laser was focused onto the samples using a 40× objective lens and spectra were collected using a CCD camera. X-ray diffraction (XRD) was conducted using a PANalytical XPERT PRO PW3050 diffractometer using a Cu anode, Kα radiation with wavelength λ = 0.15406 nm, operation voltage 40 kV, current 20 mA, with the samples being scanned from 2θ = 5 – 80°. TEM analysis was conducted using a JEOL JEM-2100F TEM operating at 200 kV.

5.2.3 Electrochemical Characterisation

All electrochemical characterization was performed using BioLogic VSP Potentiostat/Galvanostat. All IOs were investigated in a half cell configuration against a pure Li counter, using a stainless-steel PAT-cell from EL-Cell in a two-electrode configuration. The electrolyte used was lithium hexafluorophosphate solution, in ethylene carbonate and diethyl carbonate, 1.0 M $LiPF_6$ in EC/DEC=50/50 (v/v), battery grade from Sigma Aldrich. The separator used was glass microfiber from Whatman Grade GF/A cut to size. The typical loading mass of the samples were between 0.4 mg – 0.7 mg. C/TiO_2 electrochemical tests were investigated in a potential window of 3.0 V – 0.01 V. Supplementary electrochemical tests for carbon and TiO_2 IOs were investigated in a potential window of 3.0 V – 0.01 V unless stated otherwise. Cyclic voltammetry was performed at various scan rates for C/TiO_2 and galvanostatic cycling was performed using various specific currents as mentioned in this report (0.05 mV/s – 1000 mV/s, 75 mA/g – 450 mA/g).

5.3 Results and discussion

5.3.1 Material and Structural Characterisation

The carbon/TiO_2 inverse opal (IO) samples were prepared by evaporation induced self-assembly (EISA) as described by Colvin et al. with a volume fraction of 0.2%.[40] The polystyrene sphere opal templates were then infilled with 15 µL of the sucrose solution and 15µL of the TiO_2 precursor. The samples were then dried at 70 °C for 30 mins to evaporate the solvents in the precursor followed by a pre-carbonization step which involved heating the samples to 100 °C in air and held for 5 hours. The samples

were then placed in a tube furnace and heated to 500 °C under Ar and held for 2 hours. The sacrificial sphere template decomposed with the high temperature which allowed the IO structure to form and produce highly ordered porous structures which can be seen in the SEM images in Figs 5.1 (a-d). The thickness of the inverse opal structure is ~17 μm thick and contains pores with an average diameter of 363 nm (shown in Supplementary material, Fig. S5.1). The various layers that form the (111)-oriented inverse of the apparent face centered cubic (fcc) opal template can be seen through the pores of the samples from the SEM images. The atomic ratio of carbon to TiO_2 was found to be between 8:1 and 10:1, the variance in ratio may be due to remnant or adventitious carbon from the polystyrene spheres.

Raman scattering spectroscopy in Fig. 5.1 (e) detected peaks at 173.8 cm^{-1}, 427.9 cm^{-1}, 611.3 cm^{-1}, 801.3 cm^{-1} and 316.7 cm^{-1} for modes B_{1g}, E_g, A_{1g}, B_{2g} and second order scattering indicative of rutile TiO_2. Peaks at 1372.7 cm^{-1} and 1597.2 cm^{-1} show the D (disorder)- and G (graphitic) bands for carbon, respectively. The G band is due to the in-plane stretching of C sp^2 bonded atoms for both chain and rings, while the D band indicates disorder is present, and its intensity is correlated to the presence of sixfold aromatic rings.[41] The I_D/I_G ratio was found to be 0.71 compared to the I_D/I_G ratio of 1.00 for the carbon-only IO spectra. This decrease in ratio indicates a reduction in order and may indicate increasing amorphization of the carbon. X-ray diffraction (XRD) measurements of the IO structure suggested that the materials are predominantly amorphous, showing no distinct peaks in the XRD pattern other than those for the stainless-steel substrate. Localized laser-induced heating allowed us to see the crystallized form of both materials, but the as-prepared composite IO is an amorphous material.[42, 43] Notably the XRD patterns align with the electron diffraction patterns depicted in Fig. 5.2.

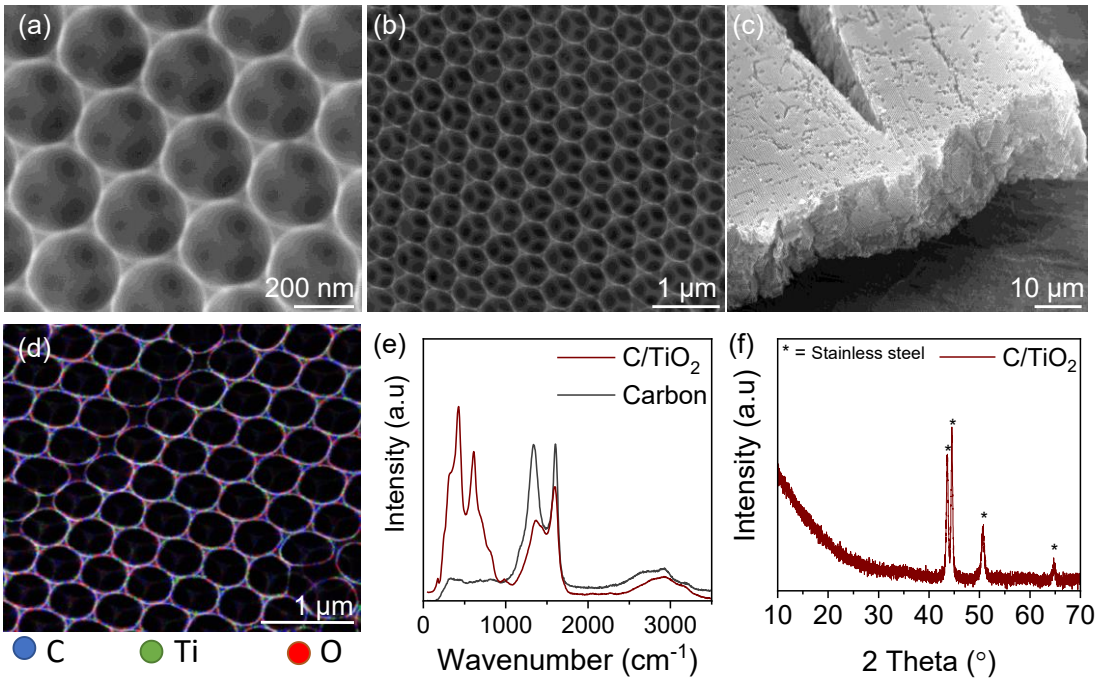

Figure 5.1. (a) – (c) SEM images of C/TiO_2 inverse opals at various magnifications. (d) EDX mapping of key elements overlayed onto an SEM image. (e) Raman spectra of C/TiO_2 IO and carbon only IO, showing rutile TiO_2 and D and G bands for carbon. (f) XRD pattern depicting amorphous C/TiO_2, peaks labelled * correspond to the stainless-steel substrate.

Transmission electron microscopy (TEM) analysis was employed to gain further insight into the porous structure of the C/TiO_2 composites. In Fig. 5.2 (a,b), TEM images of the C/TiO_2 composite at different magnifications reveal a hierarchical porous structure characterized by macroscopic pores. The wall diameters were measured to be ~30 nm on average, compared to ~26 nm for carbon IOs and ~12 nm for TiO_2 IOs (shown in Supplementary material, Fig. S5.2). The high-resolution TEM (HRTEM) image in Fig. 5.2 (c) has no discernible lattice fringe indicating the amorphous nature, which is confirmed by the selected area electron diffraction (SAED) pattern in Fig. 5.2 (d). By comparison, pure TiO_2-only IOs are crystalline in the anatase phase, and pure carbon-only IOs are amorphous. Further HRTEM details on the crystalline TiO_2-only IOs are shown in Supplementary material, Fig. S5.3. The dark-field TEM image and the corresponding EDS elemental mapping images can be

seen in Figs. 5.2 (e-h), revealing a notably uniform dispersion of carbon (C), oxygen (O), and titanium (Ti) species. Figure 5.2 (i) show an SEM image of the C/TiO_2 IO material and the resulting EDS line scan revealing a generally homogenous and consistent dispersion of carbon (C), oxygen (O), and titanium (Ti) species across the trace line.

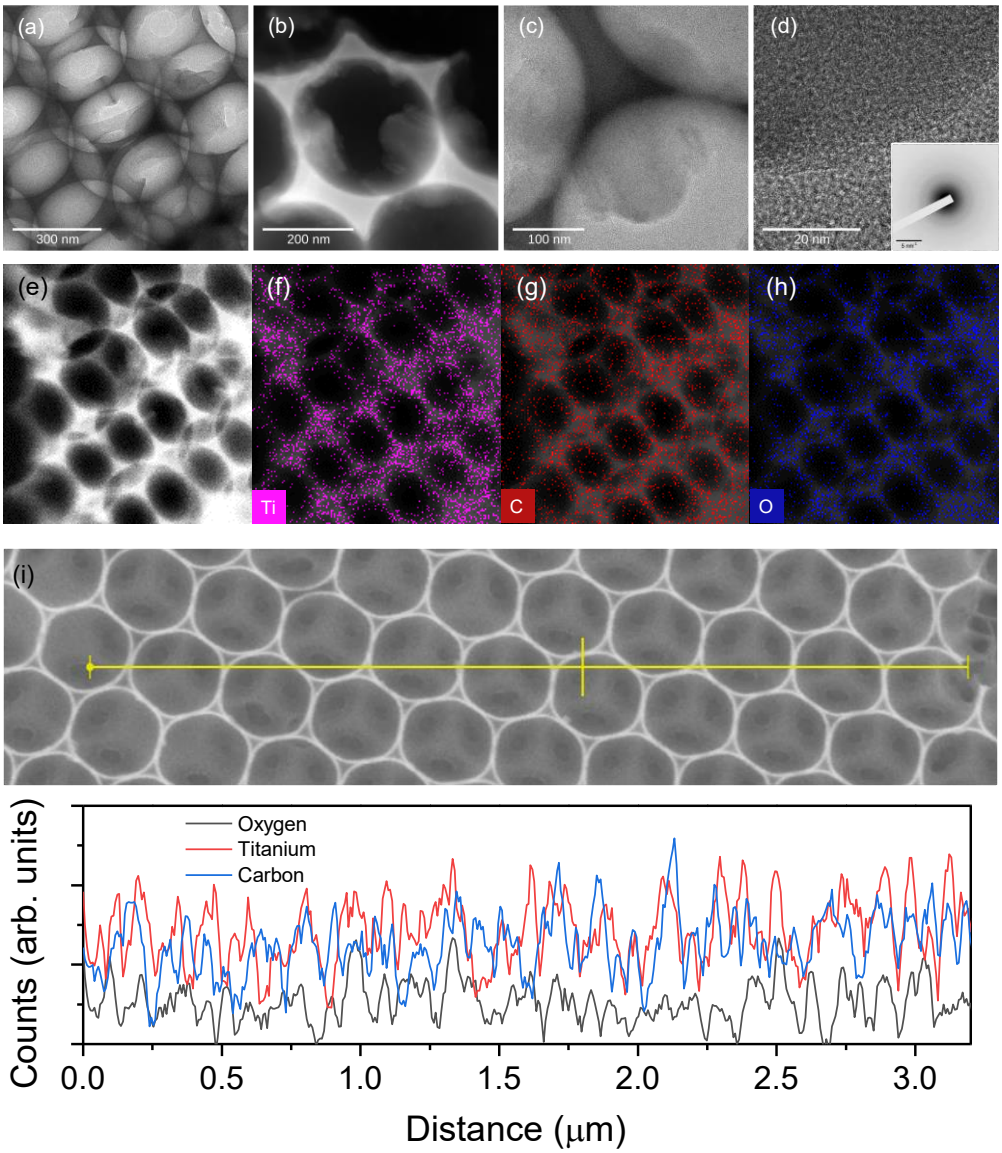

Figure 5.2. (a,b) Bright and dark field TEM images of C/TiO_2 IO material showing the interconnected structure and a local pore. (c) HRTEM image of C/TiO_2 material showing no distinct lattice fringes and (d) resulting SAED indicating dominant amorphous nature. (e) Dark field TEM of C/TiO_2 IO and resulting EDS mapping showing distribution of (f) titanium, (g) carbon, and (h) oxygen. (i) SEM image and corresponding EDS line scan (yellow line shows the line scan trace) of carbon (blue), oxygen (grey) and titanium (red).

5.3.2 Electrochemical Characterisation

The electrochemical behavior of the material was characterized in a half cell system against a Li metal counter electrode. Figure 5.3 (a) shows the cyclic voltammetry (CV) curves at a scan rate of 0.05 mV/s in the potential window 3 V – 0.015 V. Four regions of interest in the cathodic scan include the peaks at 1.4 V, 1.28 V, 0.73 V and the sloping region from 0.49 V – 0.015 V. These peaks correlate to major lithiation reactions with C/TiO_2. The cathodic reduction peak at 1.4 V and the anodic oxidation peak at 1.86 V are associated with the lithiation/delithiation of TiO_2, which follows equation 5.1:

$$Li_xTiO_2 \leftrightarrow TiO_2 + xLi + + xe^- \quad \text{……Eq. 5.1}$$

Evidence of SEI layer formation is found at 1.3 V as this peak is only visible for the first cycle. The peak centered at 0.73 V suggests lithium insertion into the carbon material and is observed in CVs for carbon only IOs (Fig. 5.3(b)). The sloping region from 0.49 V to 0.015 V correlates to the lithiation of carbon, which follows reaction Eq. 5.2 :

$$LiC_x \leftrightarrow Li^+ + xC + e^- \quad \text{Eq. 5.2}$$

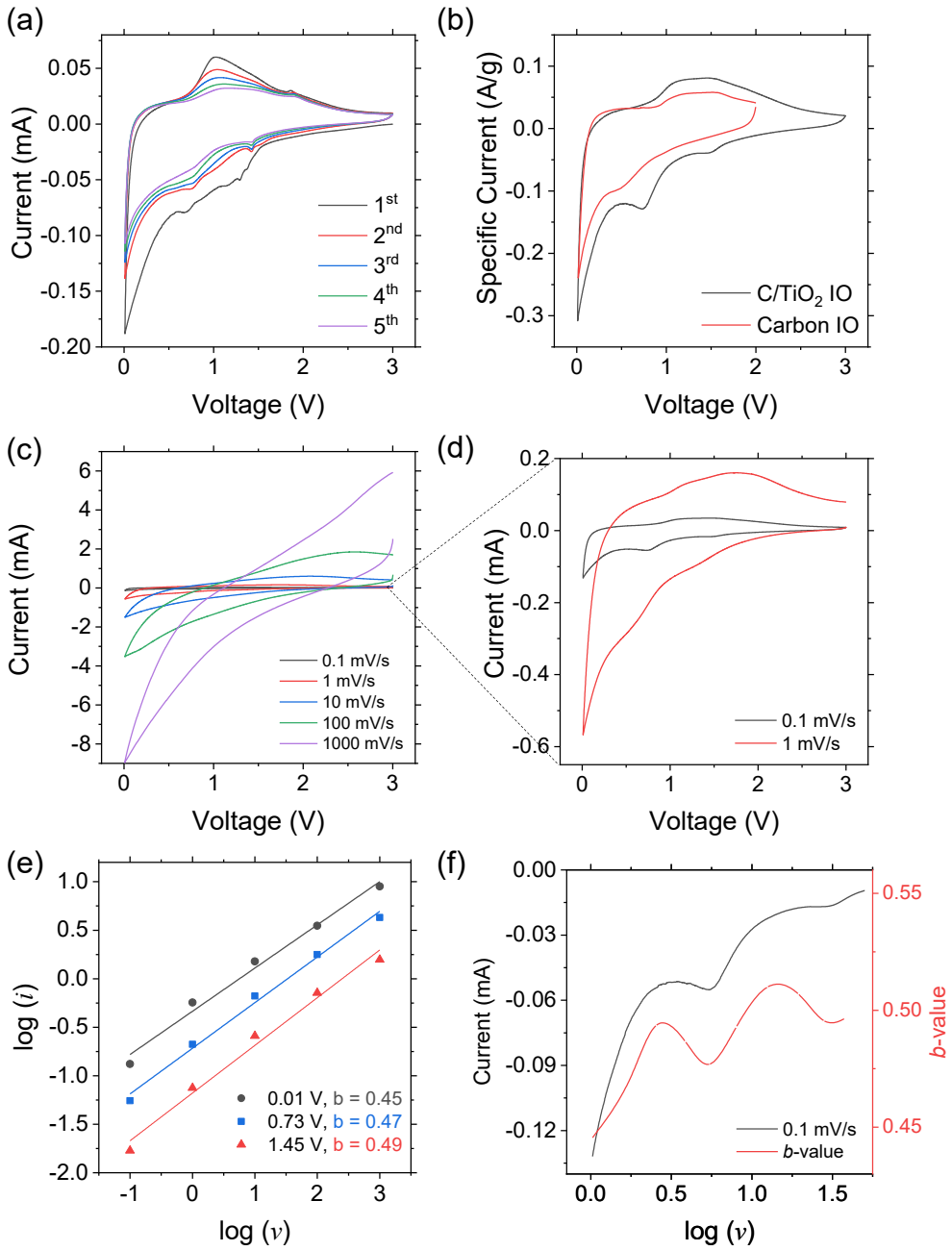

Figure 5.3. (a) CV of C/TiO_2 IO for the first five scan at scan rate 0.05 mV/s. (b) CV of C/TiO_2 IO compared to carbon only at 0.1 mV/s. (c) CV of C/TiO_2 IO at various scan rates from 0.1 – 1000 mV/s, (d) is magnified (c) to show curves at 0.1 and 1 mV/s. (e) *b*-values for log (*i*) as a function of log (*v*) for C/TiO_2 IOs at key insertion voltages (f) calculated *b*-values for C/TiO_2 IO overlaid on the first cathodic scan at a scan rate of 0.1 mV/s.

The anodic peak at 1.16 V is attributed to the delithiation of carbon, and the delithiation of TiO_2 is shown by the peak at 1.86 V. While TiO_2 is described as an intercalation mode material, hard carbons react with lithium by capacitive

ionization/deionization and adsorption/desorption processes. C/TiO_2 IOs were compared to carbon IOs that were cycled between 2 V – 0.01 V in Fig. 5.3(b), highlighting the increased current density arising from the addition of TiO_2. To investigate charge storage properties for C/TiO_2, CVs were taken at various scan rates from 0.1 mV/s to 1000 mV/s in the voltage range of 0.015 V to 3 V as shown in Fig. 5.3(c). The total stored charge can be separated into faradaic and non-faradaic processes, faradaic processes involve a transfer of charge at the electrode-electrolyte interface, such as intercalation and/or alloying, while non-faradaic processes[44-48] involve electrostatic interactions without significant chemical changes.[49]

Capacitive effects can be characterized by analyzing the CV at various scan rates according to [50]

$$i(V,t) = av^b \qquad \text{Eq. 5.3}$$

where i is the current (mA), v is the scan rate (mV/s) and a, b are adjustable values. The b-values can be obtained by setting a log on both sides of equation 5.3,

$$\log i = \log a + b \log v \qquad \text{Eq. 5.4}$$

and finding the slope (Fig. 5.3 (e,f)). When b = 0.5, the process is considered diffusion limited and when the b-value approaches 1.0, capacitive behavior is dominant.[51] In Fig. 5.3 (e) we show the plot of log(i) vs log (v) for the 3 cathodic peaks observed in the CV, and for a range of currents from the CVs in Fig. 5.3 (f). All 3 voltage points show a b-value below 0.5, indicating that the current response is primarily due to intercalation reactions rather than capacitive.

The total current (i) at a specific potential (V) is the sum of both the diffusion-controlled and capacitive reactions according to:

$$i(V,t) = k_1 v + k_2 v^{1/2} \quad \text{Eq. 5.5}$$

where $k_1 v$ and $k_2 v^{1/2}$ correspond to the current attributed to capacitive and diffusion-controlled process respectively. By rearranging this equation to

$$\frac{i}{v^{1/2}} = k_1 v^{1/2} + k_2 \quad \text{Eq. 5.6}$$

we can find k_1 and k_2 through the linear fit of $\frac{i}{v^{1/2}}$ vs $v^{1/2}$. It is then possible to distinguish between currents arising from Li^+ insertion and those occurring from capacitive-like processes.[52, 53] Figure 5.4 shows the voltage profiles for the intercalation (red) and capacitive (green) currents compared to the measured current (grey) for scan rates 0.1 mV/s – 1000 mV/s. Diffusion processes account for ~99.5% of the current measured for the 0.1 mV/s scan as per Fig. 5.4(a,f), this decreases slightly to ~98% for the 1 mV/s scan showing little contribution from capacitive processes. This is in excellent agreement with the *b*-values calculated for the cathodic peaks which were on or below 0.50. Once a scan rate of 100 mV/s is reached (Fig. 5.4(d,f)) we observe pseudocapacitive behavior at the surface, with ~21% of the current arising from capacitive-like processes. Intercalation is a slower process than capacitive charge compensation at the surface,[51] which could explain the drop in specific capacity under fast voltage scanning conditions to 9.8 mAh/g as shown in Supplementary material, Fig. S5.4. Specific capacity for the cell was found using the following equation,

$$C = \frac{1}{mv(V_c - V_a)} \int_{V_a}^{V_c} I(V) dV \quad \text{Eq. 5.7}$$

where V_c and V_a are the cathodic and anodic voltage limits respectively, m is the mass loading of the electrode and v is the scan rate. At 1000 mV/s we find almost 50:50 contribution from capacitive and diffusion reactions. The presence of capacitance contributions occurring with an opposite polarity of current (or beyond the region covered by the measured current in grey), results from the deconvolution process applied to the measured current. The sum total of the inferred intercalation and capacitive contributions at each given potential corresponds to the observed current (grey).

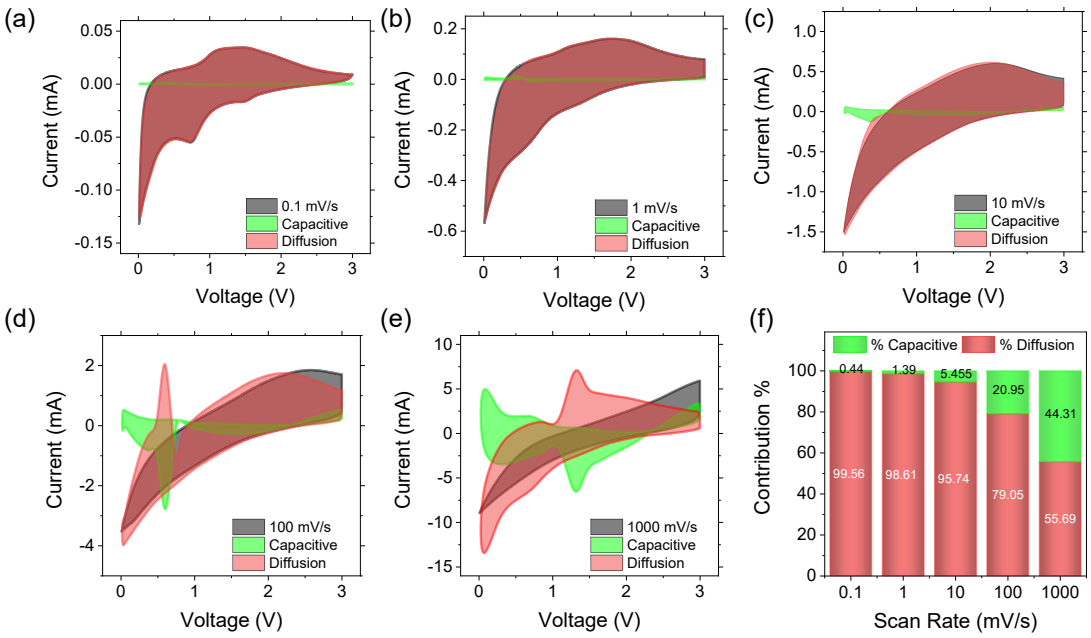

Figure 5.4. Intercalation (red) and capacitive (green) contributions to the total measured current (*grey*) for C/TiO_2 IOs at scans rates of (a) 0.1 mV/s, (b) 1 mV/s, (c) 10 mV/s, (d) 100 mV/s and (e) 1000 mV/s. The sum of these contributions at each potential equals the actual measured current.

Figure 5.5 (a) shows the discharge/charge voltage profile of the C/TiO_2 composites at a current density of 150 mA/g in a potential window of 0.014 – 3 V. All capacities were calculated based on the loading mass of the C/TiO_2 active material. Galvanostatic cycling shows initial capacities of 869 mAh/g and 472 mAh/g for the discharge and charge, respectively, with an initial coulombic efficiency (ICE) of

54.3%. This discharge capacity exceeds the theoretical capacity of both TiO_2 (336 mAh/g for $LiTiO_2$) and for carbon (372 mAh/g for LiC_6). The higher capacities observed mainly stem from the presence of defects formed during calcination which serve as additional charge compensation sites for lithium. A weak plateau was observed during the initial charge, from 1.50 – 1.15 V, followed a sloping region from 1.00 V – 0.45 V, and another sloping region extending to the lower potential limit, which is in close agreement with the cathodic peaks observed in the CV. The low coulombic efficiency is limited to the first cycle and caused by irreversible side reactions such as the SEI layer formation. In comparison, for carbon only and TiO_2 inverse opal electrodes tested under the same conditions, the initial discharge(charge) capacities for carbon IOs were 835 mAh/g (299 mAh/g), with an ICE of 36% and TiO_2 IOs showed 648 mAh/g (312 mAh/g), with an ICE of 48%. The C/TiO_2 IOs display impressive capacity retention qualities with a discharge capacity of 420 mAh/g after 100 cycles, reaching 471 mAh/g on the 250th cycle. This slight increase in capacity may be attributed to the retention of electrolyte decomposition byproducts within the walls of the macroporous structure.[54] While initial coulombic efficiency was 54.3%, this increased to 97% by the 10th cycle and had an average of 99.6% for the 250 cycles. This is an improvement on the average 98.5% coulombic efficiency recorded for the carbon only IOs and the 96.4% CE recorded for the TiO_2 IOs. The capacity values achieved surpass previous research reported for nanocomposite carbon and TiO_2 materials prepared under comparable temperature conditions (see Supplementary material, Table S5.1).[55, 56] This improved reversibility may be due to the porous nature of our inverse opal structures which alleviates volumetric stress arising from the swelling and contracting of the material during cycling under galvanostatic conditions where the reactions are diffusion- limited intercalation.

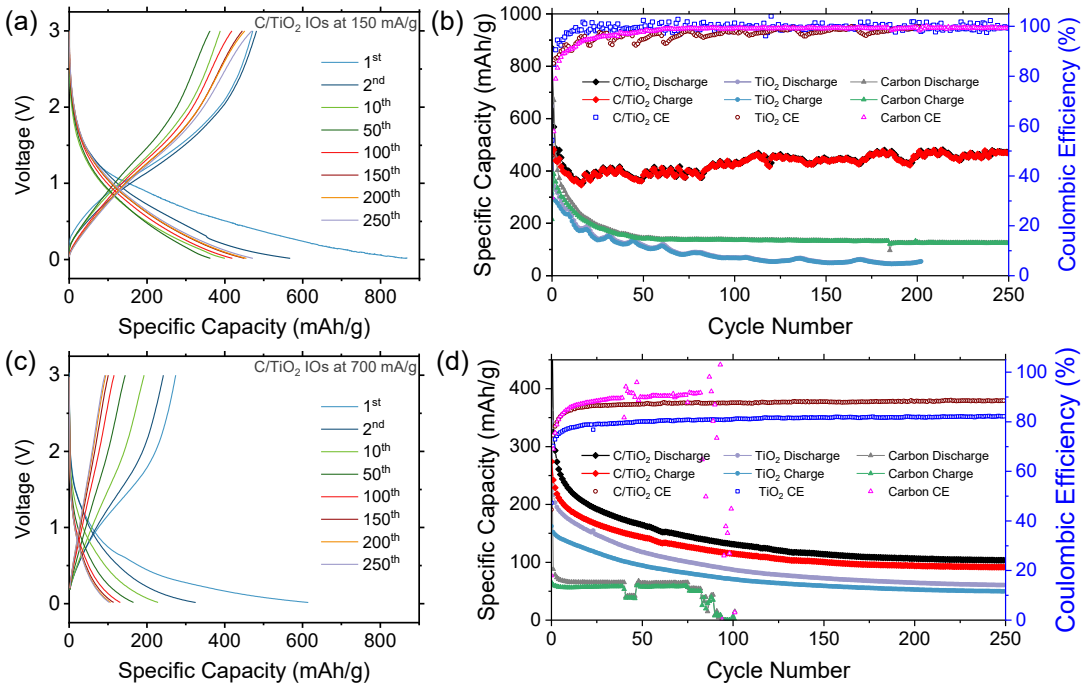

Figure 5.5. (a) Discharge/charge profiles for 1st, 2nd, 10th, 50th, 100th, 150th, 200th and 250th cycles at a current density of 150 mA/g. (b) Coulombic efficiency graph comparing the performance of C/TiO2, TiO2 and carbon IOs cycled at 150 mA/g. (c) Discharge/charge profiles for 1st, 2nd, 10th, 50th, 100th, 150th, 200th and 250th cycles at a current density of 700 mA/g. (d) Coulombic efficiency graph comparing C/TiO2, TiO2 and carbon IOs cycled at 700 mA/g.

The galvanostatic discharge and charge curves for the composite C/TiO2 IOs at a high current density of 700 mA/g in a voltage window of 0.014V – 3 V are shown in Fig. 5.5(c). Initial discharge capacity was 614.8 mAh/g with a charge capacity of 273.9 mAh/g resulting in an ICE of 44.6%. The capacity decreases to 228.7 mAh/g by the 10th cycle, and experiences a steady decrease, falling to 103.43 mAh/g by the 250th cycle. Our composite material shows higher overall capacity as well as capacity retention when compared to TiO2 IOs and carbon IOs shown in Fig. 5.5(d). The TiO2 IO had an initial discharge and charge capacity of 343 and 162 mAh/g respectively, falling to 60.45 and 49.7 mAh/g for the final discharge and charge. While the carbon IOs showed 3645 mAh/g for the first discharge with an ICE of 18%, falling to 65 mAh/g by the 10th cycle and failing before the 100th cycle. The C/TiO2 material

experienced a capacity loss of 68% from the 2nd to 250th cycle, excluding the first cycle because of SEI layer formation, while TiO_2 experienced 72% loss. This better performance at high rates may be due to the conductivity of carbon in our C/TiO_2 material. While we do see relatively low coulombic efficiency for both materials, our C/TiO_2 possesses an average CE of 87.3% over the 250 cycles while the TiO_2 had an average CE was 80.7%.

The rate performances of C/TiO_2, TiO_2 and carbon inverse opals at the current rates of 0.2 – 1.5 C are compared in Fig. 5.6(a). The C rates were calculated from the theoretical capacity of the composite material arising from the weight percentages, which equates to ~70.4 wt. % of carbon. The C/TiO_2 IO displayed good stability at high rates however, surprisingly, suffered greater capacity loss than its individual C and TiO_2 counterparts. Our composite material achieved average capacities of 461.5, 377.4, 324.8, 309.0, and 285.8 mAh/g for the 0.2, 0.5, 0.8, 1, and 1.5 C rates, respectively. This performance at high current density demonstrates that the incorporation of carbon enhances both cycling stability and high-rate performance when compared to TiO_2 IOs, under galvanostatic conditions. The TiO_2 IOs showed capacities of 243.9, 157.7, 131.2, 119 and 99.2 mAh/g for the same current densities, while carbon IOs achieved 393.5, 338.8, 273.7, 252, and 209.2 mAh/g, respectively. The reversible capacity of C/TiO_2 IOs recovered to 402.6 mAh/g when the current density was reverted to 70 mA/g. This equates to a 12.8% loss in capacity after the specific current was returned to 0.2 C. This is similar, if not better, to rate performances recorded for other C/TiO_2 macroporous structures.[30, 55] In comparison, TiO_2 IOs and carbon IOs lost 6.7% and 9.7% of their initial capacity, respectively, after the specific current was returned to the lower rate.

While the composite material exhibits lower capacity retention during the rate test compared to the individual carbon and TiO_2 IOs, an analysis of the charge/discharge curves at each specific current as shown in Fig. 5.6 (b), reveals that the composite material maintains a coulombic efficiency of ~99% when the current is returned to 0.2 C. Extended cycling at 70 mA/g for the C/TiO_2 IOs can be found in Fig. S5.5, along with the associated coulombic efficiencies.

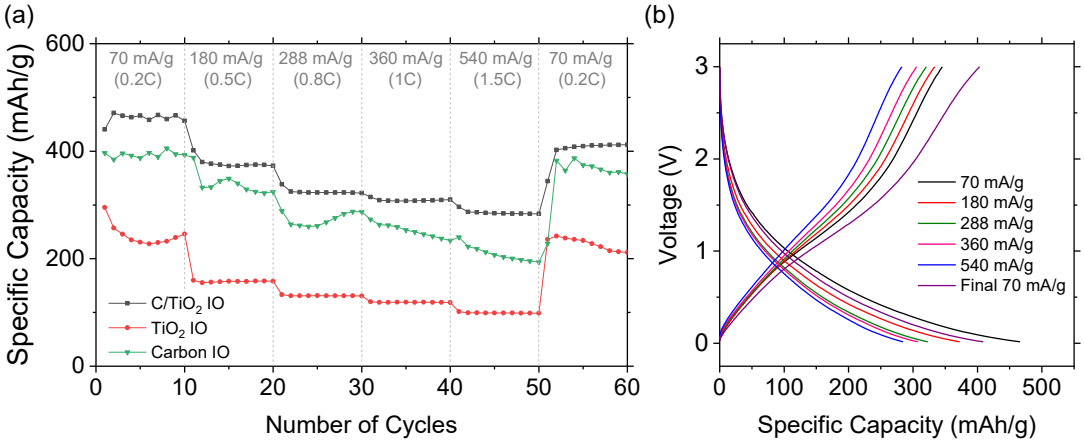

Figure 5.6. (a) Rate capability test for C/TiO_2, pure TiO_2 and carbon inverse opals with various specific currents ranging from 70 – 540 mA/g. (b) Charge/Discharge curves for the 5th cycle of C/TiO_2 IOs at each current density in the rate test.

5.3.3 Post-Cycling Structural Characterisation

After electrochemical testing, the cells were disassembled for structural analysis using SEM to identify any changes resulting from cycling. Figure 7 shows line-scan profiles acquired from grey-scale SEM images of C/TiO_2 IO materials before and after cycling at current densities of 150 mA/g and 700 mA/g. These profiles clearly reveal the periodicity of the materials and illustrate the minimal volume expansion observed in the IO material post cycling. Specifically, after 250 cycles at 150 mA/g (Fig. 5.7(a)) there was a negligible change (<1% increase) in wall diameter.

Even at the higher rate of 700 mA/g, the samples retained their structural integrity, experiencing only a 19% volume expansion, with a pore diameter of ~ 500 nm for the pristine material to ~ 405 nm diameter for the same material after cycling. Several factors likely contribute to these outcomes. Firstly, the C/TiO_2 IO materials feature a substantial specific surface area and a network of interconnected pore structures. Consequently, the lithiation/delithiation process occurs within the porous channels as well as uniformly on the material surface, promoting the formation of stable SEI layers.[57, 58] Secondly, the honeycomb-like IO skeleton reduces the Li^+ transport resistance between the electrode and electrolyte.[54] Lastly, the carbon addition enhances the overall conductivity of TiO_2, allowing the IO structure to serve as a continuous carrier for electron transport at higher rates under galvanostatic conditions where the voltage change is slow.

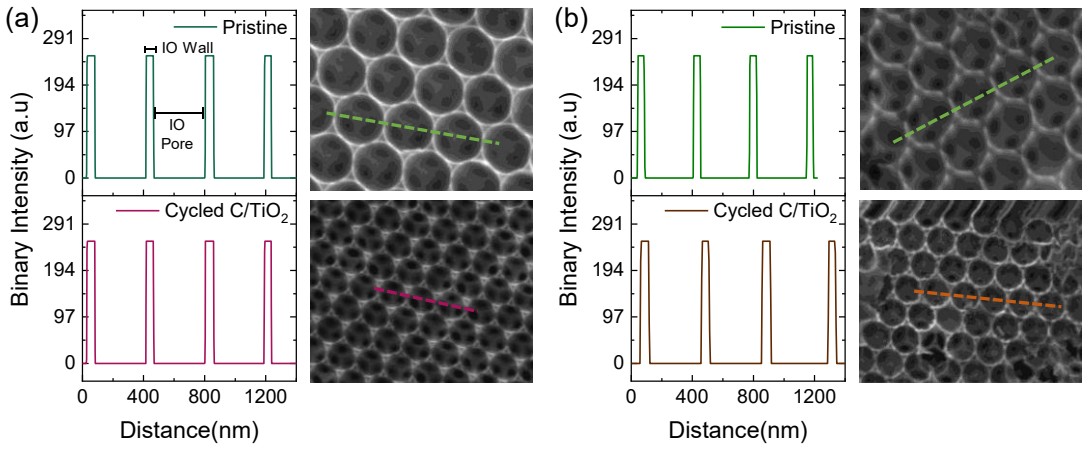

Figure 5.7. Line-scan profiles acquired from binary conversions of SEM images of C/TiO_2 IO anodes as prepared and after 250 cycles at (a) 150 mA/g and (b) 700 mA/g.

5.4 Conclusions

Highly ordered, porous inverse opal structures can be made as C/TiO_2 nanocomposites using a facile method that involves a colloidal templating approach and sucrose as the carbon precursor. Material characterization showed amorphous TiO_2 at the atomic scale with 3D architecture at the macro scale. EDS shows uniform distribution of C, Ti and O elements.

The C/TiO_2 inverse opal electrodes exhibited high initial discharge and charge capacities of 869 mAh/g and 472 mAh/g, exceeding theoretical limits for TiO_2 and carbon. This enhanced performance could potentially be linked to defects formed during calcination, which provide additional charge compensation sites for lithium. The porous structure contributed to remarkable capacity retention and improved coulombic efficiency (99.6% after 250 cycles), outperforming the individual carbon and TiO_2 materials. Despite a 68% loss in capacity from the 2^{nd} to 250^{th} cycle at a high current density of 700 mA/g, C/TiO_2 maintained an average Coulombic efficiency of 87.3%, surpassing that of pure TiO_2 IO at ~ 81%. Rate testing further revealed our C/TiO_2 IO material's specific capacities when compared to both TiO_2 and carbon IOs at various specific currents. Despite experiencing greater capacity loss than the individual counterparts, C/TiO_2 maintained stable CE at all currents.

Post-mortem analysis shows our C/TiO_2 IOs maintain a high-quality inverse opal architecture after cycling, indicating minimal expansion (1% and 19%) after 250 cycles at 150 mA/g and 700 mA/g, respectively. The impressive electrochemical and physical properties of C/TiO_2 IOs are attributed to the ordered interconnected macroporous structure that can help with rapid electrolyte diffusion, increased surface area, interconnected pores which accommodate for volume expansion and reduce Li^+

transport resistance. While capacitive effects from the composite are seen under voltammetric conditions at higher rates, slower scan rates and all galvanostatic measurements are primarily diffusion limited and promote intercalation reactions. The data highlights some benefits of tailoring porous material and their compositions to improve capacity and rate-behavior.

5.5 Appendix: Supplementary Information

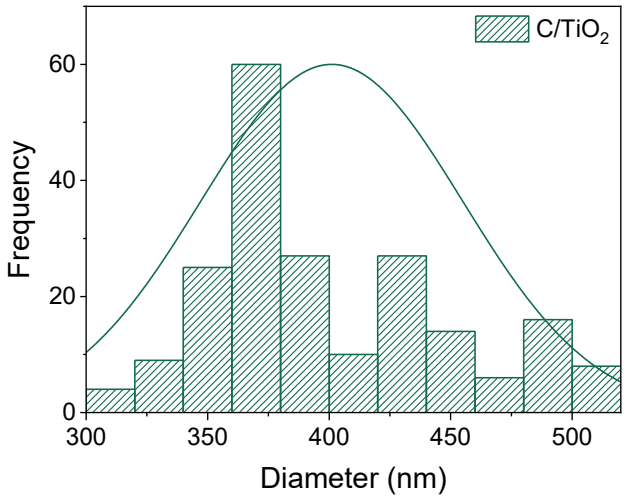

Figure S5.1. Histograms showing the distribution of pore diameters of the inverse opal structure for C/TiO_2.

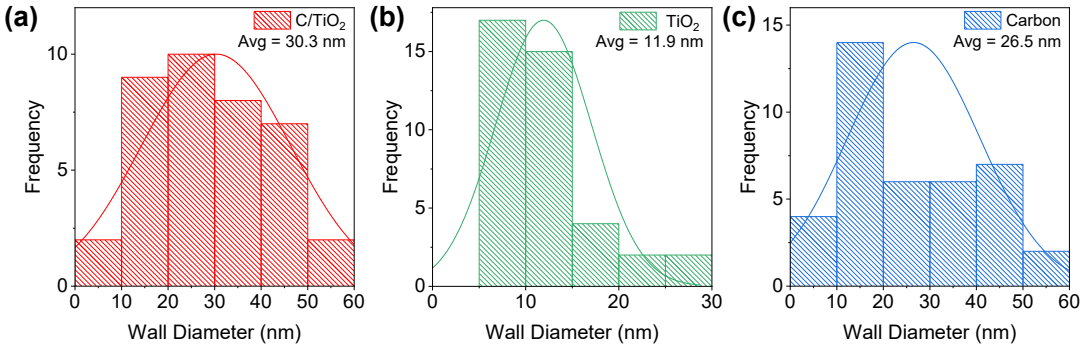

Figure S5.2. Histograms showing the distribution of diameters for walls of the inverse opal structure for (a) C/TiO_2, (b) TiO_2 and (c) carbon.

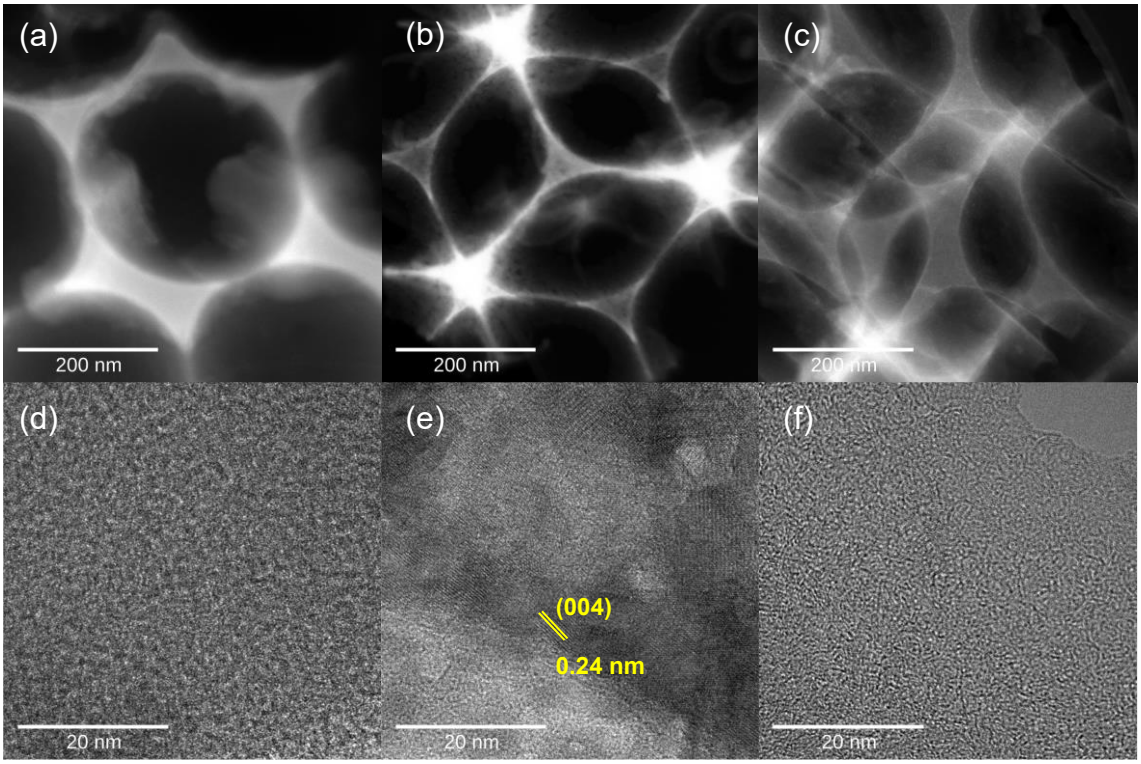

Figure S5.3. Dark field TEM images of (a) C/TiO_2, (b) TiO_2 and (c) Carbon IOs. Respective HRTEM images of (a) amorphous C/TiO_2, (b) anatase TiO_2 showing lattice fringes, and (c) amorphous carbon.

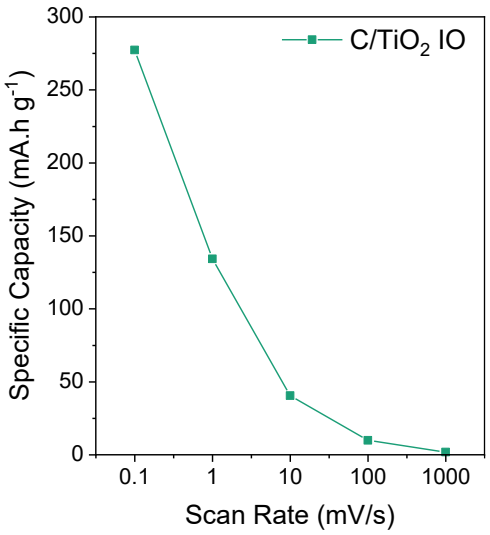

Figure S5.4. Specific capacity vs scan rate for C/TiO_2 IOs as calculated from cyclic voltammetry.

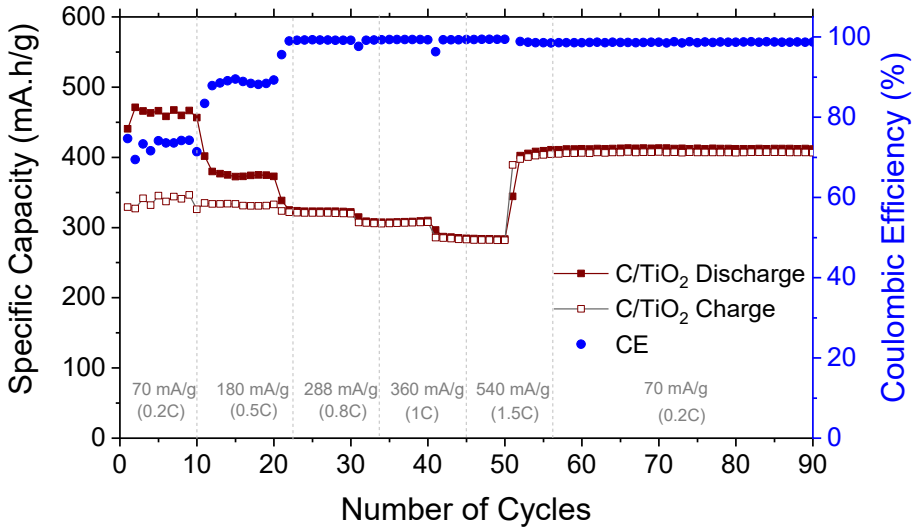

Figure S5.5. Rate test for C/TiO_2 as per Fig.6 (a) in the main text with extended cycling at 70 mA/g showing coulombic efficiency (blue).

Table S5.1. Comparison of charge capacities obtained for various C/TiO_2 composites nanostructures from the literature with values obtained in this study.

		Discharge Capacity mAh/g					
Material	**C-rate**	**1st**	**2nd**	**50th**	**100th**	**250th**	**Ref.**
C/TiO_2 Inverse Opal	150 mA/g	869	568	363	419	472	This work
C@TiO_2 nanocomposites	100 mA/g	755	389	252	237		[55]
Carbon Coated Mesoporous TiO_2	100 mA/g	225	200		178		[59]
TiO_2/carbon nanotubes	100 mA/g	302			185		[60]
3D TiO_2-Graphene-CNT	1 C	164					[61]
Carbon-coated TiO_2 nanocrystals	C/25	278					[62]
Porous TiO_2/C nanocomposite	0.1 C	415.5	288.2				[63]
Macroporous TiO_2/C composite	C/2				180		[64]
3DOM TiO_2-carbon nanocomposite	0.2 C				549		[30]
C@TiO_2/3D hollow sphere	1 C				104		[65]
TiO_2-rGO nanocomposite	100 mA/g	267		195			[29]
Ball-milled C-TiO_2	335 mA/g	361		147	148		[66]

5.6 References

(1) Murdock, B. E.; Toghill, K. E.; Tapia-Ruiz, N. A Perspective on the Sustainability of Cathode Materials used in Lithium-Ion Batteries. *Advanced Energy Materials* **2021**, *11* (39), 2102028. DOI: https://doi.org/10.1002/aenm.202102028 (acccessed 2023/11/29).
(2) Goodenough, J. B.; Kim, Y. Challenges for Rechargeable Li Batteries. *Chemistry of Materials* **2010**, *22* (3), 587-603. DOI: 10.1021/cm901452z.
(3) Harlow, J.; Ma, X.; Li, J.; Logan, E.; Liu, Y.; Zhang, N.; Ma, L.; Glazier, S.; Cormier, M.; Genovese, M.; et al. A Wide Range of Testing Results on an Excellent Lithium-Ion Cell Chemistry to be used as Benchmarks for New Battery Technologies. *Journal of The Electrochemical Society* **2019**, *166*, A3031-A3044. DOI: 10.1149/2.0981913jes.
(4) Liao, J.-Y.; Manthiram, A. Mesoporous TiO2-Sn/C Core-Shell Nanowire Arrays as High-Performance 3D Anodes for Li-Ion Batteries. *Advanced Energy Materials* **2014**, *4* (14), 1400403. DOI: 10.1002/aenm.201400403 (acccessed 2020/02/14).
(5) Tarascon, J. M.; Armand, M. Issues and challenges facing rechargeable lithium batteries. *Nature* **2001**, *414* (6861), 359-367, Review. DOI: 10.1038/35104644 Scopus.
(6) Armand, M.; Tarascon, J.-M. Building better batteries. *nature* **2008**, *451* (7179), 652-657.
(7) Bruce, P. G.; Scrosati, B.; Tarascon, J. M. Nanomaterials for rechargeable lithium batteries. *Angewandte Chemie International Edition* **2008**, *47* (16), 2930-2946.
(8) Zhang, S. S. A review on electrolyte additives for lithium-ion batteries. *Journal of Power Sources* **2006**, *162* (2), 1379-1394.
(9) Chan, C. K.; Zhang, X. F.; Cui, Y. High Capacity Li Ion Battery Anodes Using Ge Nanowires. *Nano Letters* **2008**, *8* (1), 307-309. DOI: 10.1021/nl0727157.
(10) Dylla, A. G.; Henkelman, G.; Stevenson, K. J. Lithium insertion in nanostructured TiO2 (B) architectures. *Accounts of chemical research* **2013**, *46* (5), 1104-1112.
(11) McCreery, R. L. Advanced carbon electrode materials for molecular electrochemistry. *Chemical reviews* **2008**, *108* (7), 2646-2687.
(12) Endo, M.; Kim, C.; Nishimura, K.; Fujino, T.; Miyashita, K. Recent development of carbon materials for Li ion batteries. *Carbon* **2000**, *38* (2), 183-197.
(13) Lee, K. T.; Lytle, J. C.; Ergang, N. S.; Oh, S. M.; Stein, A. Synthesis and Rate Performance of Monolithic Macroporous Carbon Electrodes for Lithium-Ion Secondary Batteries. *Advanced Functional Materials* **2005**, *15* (4), 547-556. DOI: https://doi.org/10.1002/adfm.200400186 (acccessed 2023/09/15).
(14) Liang, S.; Wang, X.; Cheng, Y.-J.; Xia, Y.; Müller-Buschbaum, P. Anatase titanium dioxide as rechargeable ion battery electrode - A chronological review. *Energy Storage Materials* **2022**, *45*, 201-264. DOI: https://doi.org/10.1016/j.ensm.2021.11.023.
(15) Zachau-Christiansen, B.; West, K.; Jacobsen, T.; Atlung, S. Lithium insertion in different TiO2 modifications. *Solid State Ionics* **1988**, *28-30*, 1176-1182. DOI: https://doi.org/10.1016/0167-2738(88)90352-9.
(16) Zhang, Y.; Tang, Y.; Li, W.; Chen, X. Nanostructured TiO2-Based Anode Materials for High-Performance Rechargeable Lithium-Ion Batteries. *ChemNanoMat* **2016**, *2* (8), 764-775. DOI: 10.1002/cnma.201600093 (acccessed 2020/02/11).

(17) Chen, Z.; Belharouak, I.; Sun, Y. K.; Amine, K. Titanium-based anode materials for safe lithium-ion batteries. *Advanced Functional Materials* **2013**, *23* (8), 959-969.
(18) Shin, J.-Y.; Joo, J. H.; Samuelis, D.; Maier, J. Oxygen-deficient TiO2− δ nanoparticles via hydrogen reduction for high rate capability lithium batteries. *Chemistry of Materials* **2012**, *24* (3), 543-551.
(19) Xu, Y.; Zhu, Y.; Liu, Y.; Wang, C. Electrochemical performance of porous carbon/tin composite anodes for sodium-ion and lithium-ion batteries. *Advanced Energy Materials* **2013**, *3* (1), 128-133.
(20) Lin, J.; Peng, Z.; Xiang, C.; Ruan, G.; Yan, Z.; Natelson, D.; Tour, J. M. Graphene nanoribbon and nanostructured SnO2 composite anodes for lithium ion batteries. *ACS nano* **2013**, *7* (7), 6001-6006.
(21) Yu, Y.; Chen, C. H.; Shui, J. L.; Xie, S. Nickel-foam-supported reticular CoO–Li2O composite anode materials for lithium ion batteries. *Angewandte Chemie International Edition* **2005**, *44* (43), 7085-7089.
(22) Dou, F.; Shi, L.; Chen, G.; Zhang, D. Silicon/carbon composite anode materials for lithium-ion batteries. *Electrochemical Energy Reviews* **2019**, *2*, 149-198.
(23) Moshtev, R.; Johnson, B. State of the art of commercial Li ion batteries. *Journal of Power Sources* **2000**, *91* (2), 86-91. DOI: https://doi.org/10.1016/S0378-7753(00)00458-4.
(24) Ebner, M.; Chung, D. W.; García, R. E.; Wood, V. Tortuosity anisotropy in lithium-ion battery electrodes. *Advanced Energy Materials* **2014**, *4* (5), 1301278.
(25) Bae, C.-J.; Erdonmez, C. K.; Halloran, J. W.; Chiang, Y.-M. Design of Battery Electrodes with Dual-Scale Porosity to Minimize Tortuosity and Maximize Performance. *Advanced Materials* **2013**, *25* (9), 1254-1258. DOI: https://doi.org/10.1002/adma.201204055 (acccessed 2023/10/05).
(26) Wu, H. B.; Chen, J. S.; Hng, H. H.; Wen Lou, X. Nanostructured metal oxide-based materials as advanced anodes for lithium-ion batteries. *Nanoscale* **2012**, *4* (8), 2526-2542, 10.1039/C2NR11966H. DOI: 10.1039/C2NR11966H.
(27) McNulty, D.; Carroll, E.; O'Dwyer, C. Rutile TiO2 Inverse Opal Anodes for Li-Ion Batteries with Long Cycle Life, High-Rate Capability, and High Structural Stability. *Advanced Energy Materials* **2017**, *7* (12), 1602291. DOI: 10.1002/aenm.201602291.
(28) Yu, X.-Y.; Wu, H. B.; Yu, L.; Ma, F.-X.; Lou, X. W. Rutile TiO2 Submicroboxes with Superior Lithium Storage Properties. *Angewandte Chemie International Edition* **2015**, *54* (13), 4001-4004. DOI: 10.1002/anie.201411353 (acccessed 2020/02/14).
(29) Kim, H.-K.; Mhamane, D.; Kim, M.-S.; Roh, H.-K.; Aravindan, V.; Madhavi, S.; Roh, K. C.; Kim, K.-B. TiO2-reduced graphene oxide nanocomposites by microwave-assisted forced hydrolysis as excellent insertion anode for Li-ion battery and capacitor. *Journal of Power Sources* **2016**, *327*, 171-177. DOI: https://doi.org/10.1016/j.jpowsour.2016.07.053.
(30) Song, L.; Li, L.; Gao, X.; Zhao, J.; Lu, T.; Liu, Z. A facile synthesis of a uniform constitution of three-dimensionally ordered macroporous TiO 2–carbon nanocomposites with hierarchical pores for lithium ion batteries. *Journal of Materials Chemistry A* **2015**, *3* (13), 6862-6872.
(31) Landi, B. J.; Ganter, M. J.; Cress, C. D.; DiLeo, R. A.; Raffaelle, R. P. Carbon nanotubes for lithium ion batteries. *Energy & Environmental Science* **2009**, *2* (6), 638-654.
(32) Stein, A. Batteries take charge. *Nature Nanotechnology* **2011**, *6* (5), 262-263.

(33) Zhang, H.; Braun, P. V. Three-Dimensional Metal Scaffold Supported Bicontinuous Silicon Battery Anodes. *Nano Letters* **2012**, *12* (6), 2778-2783. DOI: 10.1021/nl204551m.
(34) Armstrong, E.; McNulty, D.; Geaney, H.; O'Dwyer, C. Electrodeposited Structurally Stable V2O5 Inverse Opal Networks as High Performance Thin Film Lithium Batteries. *ACS Applied Materials & Interfaces* **2015**, *7* (48), 27006-27015. DOI: 10.1021/acsami.5b09511.
(35) Osiak, M.; Geaney, H.; Armstrong, E.; O'Dwyer, C. Structuring materials for lithium-ion batteries: advancements in nanomaterial structure, composition, and defined assembly on cell performance. *Journal of Materials Chemistry A* **2014**, *2* (25), 9433-9460, 10.1039/C4TA00534A. DOI: 10.1039/C4TA00534A.
(36) McNulty, D.; Geaney, H.; Buckley, D.; O'Dwyer, C. High capacity binder-free nanocrystalline GeO2 inverse opal anodes for Li-ion batteries with long cycle life and stable cell voltage. *Nano Energy* **2018**, *43*, 11-21. DOI: https://doi.org/10.1016/j.nanoen.2017.11.007.
(37) McNulty, D.; Geaney, H.; Ramasse, Q.; O'Dwyer, C. Long Cycle Life, Highly Ordered SnO2/GeO2 Nanocomposite Inverse Opal Anode Materials for Li-Ion Batteries. *Advanced Functional Materials* **2020**, *30* (51), 2005073, https://doi.org/10.1002/adfm.202005073. DOI: https://doi.org/10.1002/adfm.202005073 (acccessed 2021/02/22).
(38) Phillips, K. R.; Shirman, T.; Shirman, E.; Shneidman, A. V.; Kay, T. M.; Aizenberg, J. Nanocrystalline Precursors for the Co-Assembly of Crack-Free Metal Oxide Inverse Opals. *Advanced Materials* **2018**, *30* (19), 1706329. DOI: https://doi.org/10.1002/adma.201706329 (acccessed 2023/11/22).
(39) McNulty, D.; Landgraf, V.; Trabesinger, S. The importance of sulfur host structural preservation for lithium–sulfur battery performance. *Journal of Materials Chemistry A* **2020**, *8* (48), 26085-26097.
(40) Jiang, P.; Bertone, J. F.; Hwang, K. S.; Colvin, V. L. Single-Crystal Colloidal Multilayers of Controlled Thickness. *Chemistry of Materials* **1999**, *11* (8), 2132-2140. DOI: 10.1021/cm990080+.
(41) Ferrari, A.; Robertson, J. Interpretation of Raman spectra of disordered and amorphous carbon. *Physical Review B - Condensed Matter and Materials Physics* **2000**, *61* (20), 14095-14107, Article. DOI: 10.1103/PhysRevB.61.14095 Scopus.
(42) Benavides, J. A.; Trudeau, C. P.; Gerlein, L. F.; Cloutier, S. G. Laser Selective Photoactivation of Amorphous TiO2 Films to Anatase and/or Rutile Crystalline Phases. *ACS Applied Energy Materials* **2018**, *1* (8), 3607-3613. DOI: 10.1021/acsaem.8b00171.
(43) Siuzdak, K.; Haryński, Ł.; Wawrzyniak, J.; Grochowska, K. Review on robust laser light interaction with titania – Patterning, crystallisation and ablation processes. *Progress in Solid State Chemistry* **2021**, *62*, 100297. DOI: https://doi.org/10.1016/j.progsolidstchem.2020.100297.
(44) Simon, P.; Gogotsi, Y.; Dunn, B. Where do batteries end and supercapacitors begin? *Science* **2014**, *343* (6176), 1210-1211.
(45) Augustyn, V.; Simon, P.; Dunn, B. Pseudocapacitive oxide materials for high-rate electrochemical energy storage. *Energy & Environmental Science* **2014**, *7* (5), 1597-1614.
(46) Augustyn, V.; Come, J.; Lowe, M. A.; Kim, J. W.; Taberna, P.-L.; Tolbert, S. H.; Abruña, H. D.; Simon, P.; Dunn, B. High-rate electrochemical energy storage through Li+ intercalation pseudocapacitance. *Nature materials* **2013**, *12* (6), 518-522.

(47) Brousse, T.; Bélanger, D.; Long, J. W. To be or not to be pseudocapacitive? *Journal of The Electrochemical Society* **2015**, *162* (5), A5185.
(48) McNulty, D.; Buckley, D. N.; O'Dwyer, C. Comparative electrochemical charge storage properties of bulk and nanoscale vanadium oxide electrodes. *Journal of Solid State Electrochemistry* **2016**, *20*, 1445-1458.
(49) Dupont, M. F.; Donne, S. W. Separating faradaic and non-faradaic charge storage contributions in activated carbon electrochemical capacitors using electrochemical methods: I. step potential electrochemical spectroscopy. *Journal of the Electrochemical Society* **2015**, *162* (7), A1246.
(50) Kim, T.; Choi, W.; Shin, H.-C.; Choi, J.-Y.; Kim, J. M.; Park, M.-S.; Yoon, W.-S. Applications of Voltammetry in Lithium Ion Battery Research. *J. Electrochem. Sci. Technol* **2020**, *11* (1), 14-25. DOI: 10.33961/jecst.2019.00619.
(51) Liu, J.; Wang, J.; Xu, C.; Jiang, H.; Li, C.; Zhang, L.; Lin, J.; Shen, Z. X. Advanced energy storage devices: basic principles, analytical methods, and rational materials design. *Advanced science* **2018**, *5* (1), 1700322.
(52) Wang, J.; Polleux, J.; Lim, J.; Dunn, B. Pseudocapacitive contributions to electrochemical energy storage in TiO2 (anatase) nanoparticles. *The Journal of Physical Chemistry C* **2007**, *111* (40), 14925-14931.
(53) Fleischmann, S.; Mitchell, J. B.; Wang, R.; Zhan, C.; Jiang, D.-e.; Presser, V.; Augustyn, V. Pseudocapacitance: from fundamental understanding to high power energy storage materials. *Chemical Reviews* **2020**, *120* (14), 6738-6782.
(54) Vu, A.; Qian, Y.; Stein, A. Porous Electrode Materials for Lithium-Ion Batteries – How to Prepare Them and What Makes Them Special. *Advanced Energy Materials* **2012**, *2* (9), 1056-1085, https://doi.org/10.1002/aenm.201200320. DOI: https://doi.org/10.1002/aenm.201200320 (acccessed 2023/06/22).
(55) Chen, J.; Li, Y.; Mu, J.; Zhang, Y.; Yu, Z.; Han, K.; Zhang, L. C@TiO2 nanocomposites with impressive electrochemical performances as anode material for lithium-ion batteries. *Journal of Alloys and Compounds* **2018**, *742*, 828-834. DOI: https://doi.org/10.1016/j.jallcom.2018.01.359.
(56) Ji, W.; Mei, Y.; Yang, M.; Liu, H.; Wang, S.; Shan, Z.; Ding, F.; Liu, X.; Gao, X.; Li, X. The core-shell mesoporous titanium dioxide with in-situ nitrogen doped carbon as the anode for high performance lithium-ion battery. *Journal of Alloys and Compounds* **2019**, *806*, 946-952. DOI: https://doi.org/10.1016/j.jallcom.2019.07.225.
(57) Sun, X.; Wang, Z.; Zhang, H.; Si, K.; Wang, X.; Zhang, X. Honeycomb-like 3D ordered macroporous SiOx/C nanoarchitectures with carbon coating for high-performance lithium storage. *Journal of Colloid and Interface Science* **2023**, *651*, 394-403. DOI: https://doi.org/10.1016/j.jcis.2023.07.199.
(58) Liu, Z.; Yuan, X.; Zhang, S.; Wang, J.; Huang, Q.; Yu, N.; Zhu, Y.; Fu, L.; Wang, F.; Chen, Y.; et al. Three-dimensional ordered porous electrode materials for electrochemical energy storage. *NPG Asia Materials* **2019**, *11* (1), 12. DOI: 10.1038/s41427-019-0112-3.
(59) Liu, H.; Li, W.; Shen, D.; Zhao, D.; Wang, G. Graphitic Carbon Conformal Coating of Mesoporous TiO2 Hollow Spheres for High-Performance Lithium Ion Battery Anodes. *Journal of the American Chemical Society* **2015**, *137* (40), 13161-13166. DOI: 10.1021/jacs.5b08743.
(60) Liu, J.; Feng, H.; Jiang, J.; Qian, D.; Li, J.; Peng, S.; Liu, Y. Anatase-TiO2/CNTs nanocomposite as a superior high-rate anode material for lithium-ion batteries. *Journal of Alloys and Compounds* **2014**, *603*, 144-148. DOI: https://doi.org/10.1016/j.jallcom.2014.03.089.

(61) Shen, L.; Zhang, X.; Li, H.; Yuan, C.; Cao, G. Design and Tailoring of a Three-Dimensional TiO2–Graphene–Carbon Nanotube Nanocomposite for Fast Lithium Storage. *The Journal of Physical Chemistry Letters* **2011**, *2* (24), 3096-3101. DOI: 10.1021/jz201456p.
(62) Xia, T.; Zhang, W.; Wang, Z.; Zhang, Y.; Song, X.; Murowchick, J.; Battaglia, V.; Liu, G.; Chen, X. Amorphous carbon-coated TiO2 nanocrystals for improved lithium-ion battery and photocatalytic performance. *Nano Energy* **2014**, *6*, 109-118. DOI: https://doi.org/10.1016/j.nanoen.2014.03.012.
(63) Wang, W.; Sa, Q.; Chen, J.; Wang, Y.; Jung, H.; Yin, Y. Porous TiO2/C Nanocomposite Shells As a High-Performance Anode Material for Lithium-Ion Batteries. *ACS Applied Materials & Interfaces* **2013**, *5* (14), 6478-6483. DOI: 10.1021/am402350n.
(64) Petkovich, N. D.; Rudisill, S. G.; Wilson, B. E.; Mukherjee, A.; Stein, A. Control of TiO2 Grain Size and Positioning in Three-Dimensionally Ordered Macroporous TiO2/C Composite Anodes for Lithium Ion Batteries. *Inorganic Chemistry* **2014**, *53* (2), 1100-1112. DOI: 10.1021/ic402648f.
(65) Zhang, Y.; Zhang, N.; Chen, J.; Zhang, T.; Ge, W.; Zhang, W.; Xie, G.; Zhang, L.; He, Y. Preparation and lithium storage properties of C@TiO2/3D carbon hollow sphere skeleton composites. *Journal of Alloys and Compounds* **2020**, *815*, 152511. DOI: https://doi.org/10.1016/j.jallcom.2019.152511.
(66) Chen, Y.; Ma, X.; Cui, X.; Jiang, Z. In situ synthesis of carbon incorporated TiO2 with long-term performance as anode for lithium-ion batteries. *Journal of Power Sources* **2016**, *302*, 233-239. DOI: https://doi.org/10.1016/j.jpowsour.2015.10.057.

Chapter 6

Carbon Inverse Opals as Monolithic Structures for Sodium-ion and Potassium-ion Batteries

Adapted from: Carbon Inverse Opal Macroporous Monolithic Structures as Electrodes for Na-ion and K-ion Batteries.

Journal of The Electrochemical Society **2024**, *171* (3), 030529. DOI: 10.1149/1945-7111/ad3399.

Abstract

Highly ordered three-dimensional carbon inverse opals (IOs) are produced from sucrose. The walls of the ordered porous carbon structure containing disordered nanostructures with short-range graphitic areas. The face-centred cubic (FCC) interconnected open-worked structure defines a conductive macroporous monolithic electrode with high surface area-to-volume ratio that is easily wetted by electrolytes for Na-ion and K-ion systems. Electrochemical characterization in half-cells against Na metal electrodes reveals stable discharge capacities of 25 mAh g^{-1} at 35 mA g^{-1} and 40 mAh g^{-1} at 75 mA g^{-1} and 185 mA g^{-1}. While in K-ion half cells, the carbon IO delivers capacities of 32 mAh g^{-1} at 35 mA g^{-1} and ~25 mAh g^{-1} at 75 mA g^{-1} and 185 mA g^{-1}. The IOs demonstrate storage mechanisms involving both capacitive and diffusion-controlled processes. Comparison with non-templated carbon thin films highlights the superior capacity retention (72% for IO vs 58 % for thin film) and cycling stability of the IO structure in Na-ion cells. Robust structural integrity against volume changes with larger ionic radius of potassium ions is maintained after 250 cycles in K-ion cells. The carbon IOs exhibit stable coulombic efficiency (>99%) in sodium-ion batteries (SIBs) and self-improving coulombic efficiency with cycling in potassium-ion batteries (PIBs). The structural design facilitates efficient electrolyte infiltration, ability to withstand structural stresses ,and along with the dual storage mechanism, positions the IOs as promising electrode structures for SIBs and PIBs.

6.1 Introduction

The growing demand for large-scale lithium-ion battery (LIB) production for electric vehicles and smart grids is constrained by limited lithium resources and high costs.[1-3] Sodium-ion batteries (SIBs) emerge as a promising alternative due to abundant sodium resources.[4-7] Despite the vast abundance of sodium and potassium compared to lithium, potassium-ion batteries (PIBs) have received less attention until recently.[8-10] PIBs offer advantages such as abundant resources and a closer redox potential to Li/Li^+ than SIBs, suggesting higher voltage plateau and energy density over sodium-ion batteries. However, PIBs face challenges, such as the larger size of K ions hindering efficient intercalation into some electrode materials.[11] The performance of SIBs and PIBs therefore depends on electrode materials, prompting focused efforts to develop materials with specific properties, such as mechanical strength, chemical stability, high surface area, and conductivity.[12-15]

Among various electrode materials, carbon materials, with their chemical stability, large specific surface, high electrical conductivity, and cost-effectiveness, have garnered attention. The development of nanostructured carbons, such as carbon nanotubes[16], graphene[17], carbon nanowires, porous carbons[18], and hollow carbon spheres[19], has become an important material set for rechargeable battery anodes. While graphite has been used universally as an anode for LIBs exhibiting a capacity of 370 mAh g^{-1}, it does not work well in SIBs (35 mAh g^{-1}).[20] While K-ions can insert into graphite, the theoretical capacity is lower for PIBs than LIBs and repeated cycling can cause extensive volume expansion (~61%) and pulverisation of the graphite structure.[21] Hard carbon, a prospective anode for SIBs[22, 23], exhibit reversible capacities of 296 – 353 mAh g^{-1} in Na-ion cells with heat-treated variants reaching

~430 mAh g^{-1}.[24, 25] In potassium-ion batteries, the hard carbon electrode falls short of the theoretical KC_8 capacity (280 mAh g^{-1}), highlighting the need for increased potassiation capacity to demonstrate higher energy density.[26]

Three-dimensional ordered macroporous structures exhibit promise as electrode materials for sodium-ion and potassium-ion batteries. These structures, previously explored in the realm of lithium-ion batteries, have demonstrated their capacity to enhance rate performance and longevity.[27-31] The ordered macroporous design offers advantages such as improved structural integrity, providing a stable framework that mitigates volume expansion during charge-discharge cycles. This inherent stability contributes to sustained electrochemical performance over extended cycles. Translating these benefits to Na-ion and K-ion batteries holds significant potential, addressing challenges posed by the larger size of sodium and potassium ions. Specifically in K-ion batteries, where capacity fading has been reported due to suspected large volume changes with cycling.[32, 33] The ordered macroporous architecture facilitates efficient ion diffusion and electrolyte permeation, factors critical for optimizing the electrochemical performance of Na-ion and K-ion batteries. By harnessing the structural advantages observed in lithium-ion batteries, three-dimensional ordered macroporous structures emerge as a promising avenue for advancing the capabilities of Na-ion and K-ion batteries, aligning with the growing demand for sustainable and high-performance energy storage solutions.

In this chapter, we present a three-dimensional inverse opal structure of carbon and systematically evaluate its performance in sodium and potassium ion cells. Our investigation delves into the impact of this unique macroporous structure on the electrochemical behavior of these cells, specifically examining galvanostatic charge/discharge profiles and distinguishing between capacitive and diffusion-

controlled processes. By studying the intricate interplay between the 3D inverse opal structure and the electrochemical characteristics in sodium and potassium ion cells, our aim is to discern the potential of these macroporous structures as versatile scaffolding or model architectures. This investigation is essential for unlocking the potential of utilizing these structures in 'post-lithium' technologies, contributing to the ongoing progress of advanced energy storage systems.

6.2 Experimental

6.2.1 Materials Preparation

Stainless steel (SS) discs (grade 304) with a diameter of 15.5 mm were used as substrates. The opal template was fabricated using the evaporation induced self-assembly (EISA) method, which involved suspending the SS discs in a 0.2% solution of polystyrene spheres (500 nm diameter) and deionized water. The suspended discs were placing in a convection oven at 60°C overnight. The dried PS spheres were infilled with ~35 µL of the sucrose solution before being placed in a convection oven at 70 ℃ for 25 min. The carbon samples were then heated to 100 ℃ for 5 hours in air before being heated to 900 ℃ at a ramp rate of 5 ℃ min^{-1} under Ar and held for 2 hours.

Carbon electrodes in thin film form were prepared using the same method, excluding the use of polystyrene spheres as a structural template.

6.2.2 Material Characterisation

SEM analysis was performed on FEI Quanta 650 FEG high resolution SEM at an accelerating voltage of 10 kV. SEM images and feature dimensions were analysed using ImageJ software. Raman scattering was performed on an Ocean Optics QE65PRO Raman Spectrometer using a 40 mW Ar^+ laser at 532 nm excitation. The laser was focused onto the samples using a 40× objective lens and spectra were collected using a CCD camera. TEM analysis was conducted using a JEOL JEM-2100F TEM operating at 200 kV.

6.2.3 Electrochemical Characterisation

All electrochemical characterization was performed using BioLogic VSP Potentiostat/Galvanostat. The loading mass of active materials was between 0.5 mg – 0.8mg for all electrodes. The carbon inverse opal material was investigated in a half cell configuration against a pure Li, Na, or K counter electrode using a stainless-steel PAT cell from EL-Cell in a two-electrode configuration. The electrolyte used was 1.0 M $LiPF_6$ in EC/DMC=50/50 (v/v) (Sigma Aldrich), 1.0 M $NaClO_4$ in PC with 5 vol. % fluoroethylene carbonate (FEC) additive, and 1.0 M KPF_6 in EC/DMC =50/50 (v/v) for the lithium, sodium, and potassium cells, respectively. The separator used was glass microfiber from Whatman Grade GF/A cut to size. All electrochemical tests were investigated in a potential window of 2.0 V – 0.014 V.

6.3 Results and discussion

6.3.1 Material Characterisation Analysis

The carbon inverse opal (IO) samples were grown by calcination of a sacrificial self-assembled opal film infilled with a sucrose solution. Details of the structure and morphology are demonstrated by scanning electron microscopy (SEM) images in Fig. 6.1 (a) and (b). The images show IOs on the current collector, and the morphology is typically islands of three-dimensional ordered macroporous architecture. These IOs are characterized by highly ordered interconnected layers of carbon with face-centred cubic (FCC) symmetry. The growth of the opal template is perpendicular to the (111) plane of the FCC lattice[34], with the various layers seen through the pores of the samples. Cross-sectional SEM imaging of the carbon IO in Fig. 6.1 (d) shows the thickness of the material is ~17.5 μm. High resolution transmission electron microscopy (HRTEM) is shown in Fig. 6.1 (d), a disordered nanostructure was observed in the carbon inverse opal samples featuring curved, short-range graphitic areas within the IO walls. Selected area electron diffraction (SAED) pattern shows dispersive diffraction rings. The disordered microstructure of the carbon IOs is characterized by local regions of puckered layered graphitic structures and their relative orientations contribute to the (100) and (110) planes in the polycrystalline SAED pattern.[35] Structural measurements were extracted from the SEM images, captured at various locations across the sample surface. To mitigate the influence of potential isotropic swelling, measurements were systematically obtained from various directions across each feature, as seen in Fig. 6.1(a). The material had a bimodal distribution in recorded pore diameter, as shown by the histogram in Fig. 6.1 (e). from the regions examined this equates to 68% of the pores being ~495 nm in diameter on average and 32% being ~355 nm in diameter on average. A histogram of wall thickness measurements can be found in Fig. S6.1, where the thickness is measured to be 26.5 nm on average.

The macroporosity induces a high surface area-to-volume ratio, offering ample space for optimal electrolyte infiltration. The specific surface area is approximated by considering the ratio of average macropore diameters (68 % being 495 nm, and 32 % being 355 nm), assuming perfect FCC symmetry and disregarding micropores and mesopores within the IO walls. With each FCC unit cell containing 4 macropores with the area per pore is equal to $4\pi r^2$ and a volume approximated as a^3 (where $a = D\sqrt{2}$), the specific surface area per unit volume is derived as 10.17 m^3 cm^{-3}. Using the density of hard carbon (1.5 g cm^{-3})[36] and the volume faction of perfectly ordered FCC arranged inverse opals[37], the specific area per unit mass was calculated to be 25.59 m^2 g^{-1}. With an average mass loading of 0.65 mg, yields a specific surface area of 0.02 m^2 for these electrodes. While this approximation yields a lower specific surface area compared to other measurements based on N_2 adsorption for carbon IOs[38-40], it is worth noting that this calculation does not consider any potential additional meso-/microporosity of the surface and is a lower bound value for the geometrical surface area of the electrode. Such porosity often constitutes a significant contribution to the surface area values determined by gas adsorption.[41, 42]

Raman spectroscopy, Fig. 6.1 (f), shows clear peaks at ~1347 cm^{-1} and ~1604 cm^{-1} for the D (disorder) and G (graphitic) bands of carbon, respectively. These bands are associated with the vibrational modes of carbon atoms, the D band is characteristic of disorder induced by sp^3 hybridization and is activated in the presence of structural defects, disorder, or the presence of amorphous carbon.[43] The G band is associated with the E_{2g} vibrational mode of sp^2-bonded carbon atoms present in graphitic structures, the intensity of the D band compared to the G band (I_D/I_G), which was 0.97, suggests a combination of ordered and disordered regions in the carbon IO.[44] The full width at half maximum for the D and G bands are 174.3 cm^{-1} and 72.7 cm^{-1} based on

Gaussian models, which could indicate the coexistence of amorphous carbon/disordered regions with graphitic structures.[45-47] This observation agrees with the HRTEM and SAED data where the IO structural walls comprise carbon interspersed with localized regions of layered graphitic structures. The broad peak at 2810 cm^{-1} is known as the 2D peak and originates from second order two phonons process, with the weak intensity and broad width indicating defects in the IO.[48]

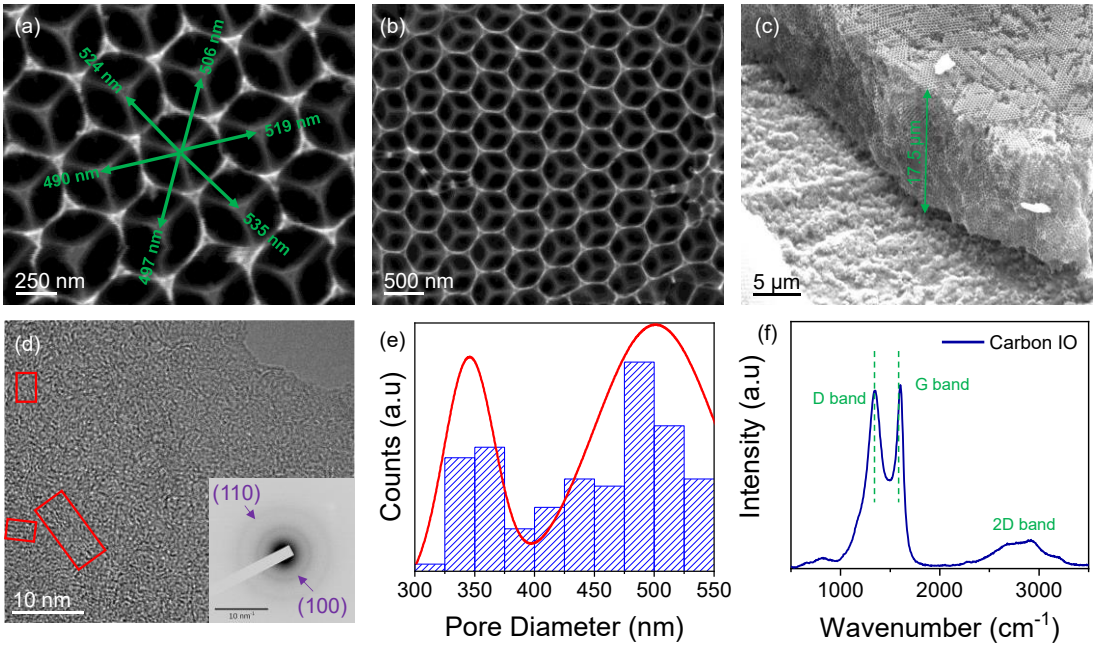

Figure 6.1. SEM images of carbon inverse opals at various magnitudes highlighting (a) pore size, (b) high degree of order and (c) thickness. (d) HRTEM of carbon IOs with graphitic areas in red, (Inset) SAED showing diffuse rings corresponding to (100) and (110) planes of localized layered graphitic regions. (e) Histogram showing bimodal distribution of pore diameters. (f) Raman spectrum of carbon IOs.

6.3.2 Electrochemical Characterization Analysis

The electrochemical behavior of the material was characterized in a half cell system against either a Na or K metal counter electrode. Figure 6.2 shows the cyclic voltammetry (CV) curves at a scan rate of 0.1 mV/s in the potential window 2 V – 0.014 V. The first cycle for carbon IO vs sodium, Fig. 6.2 (a), shows cathodic peaks at 1.08 V and 0.49 V that disappear in subsequent cycles, and are ascribed to the

irreversible reaction between sodium ions and surface functional groups, the decomposition of the electrolyte, the SEI layer formation, and various irreversible side reactions.[49-51] The cathodic peak at 0.02 V is attributed to the sodium insertion into carbon materials.[52] From the 2nd cycle onwards, Fig. 6.2 (b) – (d), a broad cathodic peak at 0.7 V can be seen in the cathodic scan, this is seen for reversible sodiation of oxides on the surface, and the corresponding anodic peak at 1.4 V.[53] For the desodiation of carbon, a broad peak from 0.014 V - 0.9 V is observed, indicating the extraction of sodium takes place across a wide potential range.[54]

The CVs for the carbon IO vs potassium are shown in Fig. 6 (in green), the initial scan shows cathodic peaks at 1.08 V and a broad peak from ~ 0.7 V – 0.2 V. This broad peak contains a peak at ~ 0.6 V which is associated with the irreversible reactions such as SEI layer formation and decomposition of electrolyte, the peak at 1.08 V is also ascribed to the SEI layer, as these disappear after the first and second cycle. The potassiation of carbon appears to occur from 0.2 V – 0.014 V, with the depotassiation occurring over a wide voltage range similar to that observed in the sodium system. A higher current density is seen in the voltage region of 1.0 V – 1.5 V, this has been observed in graphene oxide materials[55-57] and could indicate extraction reactions with surface oxides as seen compared to the same measurements in the Na-cell.

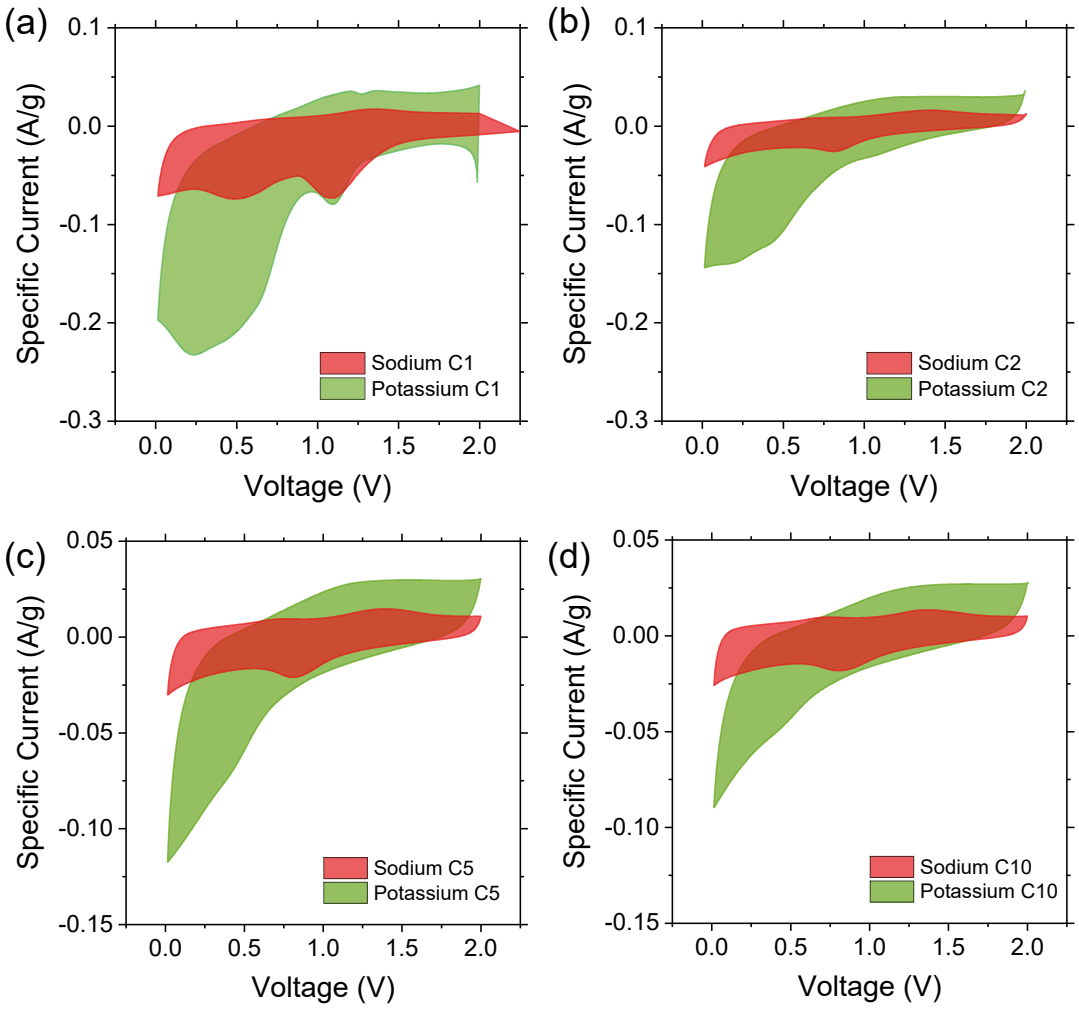

Figure 6.2. Cyclic voltammograms of (a) 1st scan (C1), (b) 2nd scan (C2), (c) 5th scan (C5) and (d) 10th scan (C10) for carbon inverse opals in sodium and potassium half cells.

The electrochemical storage performances of the carbon IOs were examined through galvanostatic cycling for both systems, and the data is shown in Fig. 6.3. Three rates were examined, 35 mA g^{-1}, 75 mA g^{-1}, and 185 mA g^{-1}, with all cells cycled 250 times to analyze specific capacities and stability in sodium-ion and potassium-ion battery cells. The initial discharges of all cells can be found in Fig. S6.2. Figure 6.3 (a) – (c) shows the carbon IO vs Na GCPL from the 2nd to the 250th cycle. The initial discharge was 255 mAh g^{-1} at a current density of 35 mA g^{-1}, which then decreased to ~40 mAh g^{-1} for the 2nd discharge, achieving a coulombic efficiency of 68%. The

specific capacity was stable by the 10th cycle at 27 mAh g^{-1} and maintained this capacity for the 250 cycles with an average coulombic efficiency of 98.6%. The 2nd cycle at 75 mA g^{-1}, shown in Fig. 6.2 (b), displayed a discharge and charge capacity of 48.5 mAh g^{-1} and 38.5 mAh g^{-1}, respectively, with a coulombic efficiency of ~79%. The discharge capacity after the 10th cycle was 40 mAh g^{-1}which remained stable over the next 240 cycles, falling to 35 mAh g^{-1} which equated to a 12.5% loss in capacity. When the current density was 185 mA g^{-1}, the carbon IOs showed impressive capacity retention for the 250 cycles, losing just over 1% in specific capacity from 38.5 mAh g^{-1} at the 10th cycle to 38 mAh g^{-1} at the 250th cycle. This was accompanied by a coulombic efficiency of 99.7% on average, indicating stable and reliable cycling at the 185 mA g^{-1} current density.

For the potassium-ion system, carbon inverse opals were cycled at the same rates as outlined for the sodium-ion cells, these are seen in Fig. 6.3 (d) – (f). A weak plateau was observed during the second cycle at 35 mA g^{-1} (Fig. 6.3 (d)), from 0.7 – 0.4 V, followed a sloping region from 0.4V – 0.42 V, and another sloping region extending to the lower potential limit, which is in close agreement with the cathodic peaks observed in the CV. However, capacity fading is more obvious in the K-ion battery compared to the Na-ion, with an initial discharge capacity of 1667 mAh g^{-1} (ICE of ~5%) (Fig. S6.2 (d)), which falls to 208 mAh g^{-1} for the 2nd cycle and continues to fade reaching 32 mAh g^{-1} for the 250th cycle with an average Coulombic efficiency of ~83%. The 75 mA g^{-1} rate shows an initial discharge capacity of 554 mAh g^{-1} with an ICE of ~ 9%, which is lower than other carbon materials reported for potassium-ion batteries.[55, 58] The 2nd, 10th, and 50th cycles show discharge capacities of 82 mAh g^{-1}, 49 mAh g^{-1} and 38 mAh g^{-1}, respectively. The capacity fades to 24 mAh g^{-1} for the 250th cycle, however the Coulombic efficiency continuously improves reaching 97%

by the 250th cycle. The 185 mA g^{-1} rate, Fig. 6.3 (f), showed slightly higher ICE (~13%) with specific capacities of 421 mAh g^{-1} and 53 mAh g^{-1} for the discharge and charge, respectively. The carbon IOs exhibited a discharge capacity of 28 mAh g^{-1}, with a charge capacity of 26 mAh g^{-1} after 250 cycles, showing a Coulombic efficiency of ~92%.

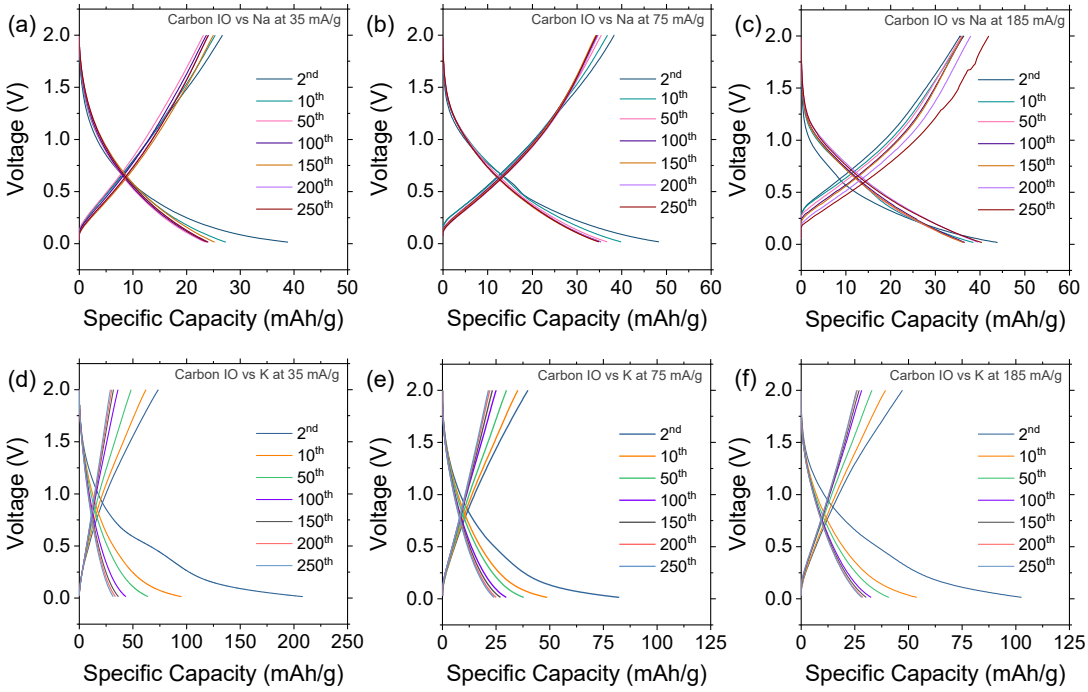

Figure 6.3. Galvanostatic charge–discharge profiles between 2.0 – 0.014 V for carbon IOs vs sodium at (a) 35 mA g^{-1}, (b) 75 mA g^{-1}, (c) 185 mA g^{-1}. Charge–discharge profiles for carbon IOs vs potassium at (d) 35 mA g^{-1}, (e) 75 mA g^{-1}, and (f) 185 mA g^{-1}.

The carbon IOs demonstrated a disparity in the K-ion batteries relative to their efficacy in Na-ion batteries. Previous studies have suggested that defects in the electrode structure can enhance specific capacity.[59, 60] While the capacities achieved may not match those recorded for other hard carbon structure (100 – 300 mAh g^{-1})[61, 62], incorporating heteroatom-doping or composite additions could prove beneficial in this context, leading to an enhancement in specific capacity.[63, 64]

As a comparison, we also acquired galvanostatic charge-discharge curves of the carbon IOs for lithium-ion half cells at current densities of 75 mA $g^{-1}$and 185 mA g^{-1}, and the data are shown in Fig. S6.3. At a 75 mA g^{-1} current density, the cell shows an initial Coulombic efficiency of 32% for the carbon inverse opals vs Li, corresponding to a discharge and charge capacity of 731 mAh g^{-1} and 234 mAh g^{-1}, respectively. However, this low Coulombic efficiency is limited to the first few cycles, averaging out to 99% for the 250 cycles. A stable specific capacity is obtained after 10 cycles with a reversible capacity of ~100 mAh g^{-1}. For the 185 mA g^{-1} rate, a lower ICE of 27% was recorded with capacities of 383 mAh g^{-1} and 102 mAh g^{-1} for the discharge and charge. Similar curves are observed for the carbon IOs in all three systems with a sloping voltage region exhibited at ~1.5 V, which is generally associated with surface electrochemical reactions; these processes involve interactions with edge and defect sites as well as adsorption onto the surface of pores.[65, 66] Lithium readily intercalates into the interlayer spacing of graphite, forming LiC_6 at full charge.[67] However, sodium faces challenges due to its larger ionic radius, leading to thermodynamically unstable graphitic intercalation compounds (GICs).[68] Potassium intercalation is further hindered, and while sodium interactions are described by an "adsorption–intercalation–pore filling" mechanism, potassium storage in hard carbons is primarily attributed to surface adsorption.[66, 69-71]

To examine how the macroporous structure affected electrochemical behaviour, non-templated carbon thin films were tested vs sodium and potassium at a current density of 75 mA g^{-1}, shown in Fig. 6.4. SEM images showing the difference in morphology of the carbon inverse opal and carbon thin film is shown in Figs. 6.4 (c) and (d). Additional SEM images showing the morphology of carbon thin films are shown in Fig. S6.4. Initial Coulombic efficiencies showed an improvement in

irreversible capacities for the IOs in the sodium ion cell, registering 19% CE for the carbon IO and 6% CE for the carbon thin film. Comparable discharge capacities of approximately 215 mAh g^{-1} are noted for both materials in the first cycle. However, the thin film exhibits more significant capacity fading, recording 26 mAh g^{-1} in the 2nd discharge compared to 48 mAh g^{-1} in the carbon IO-containing cell. Impressively, the IO maintains consistent discharge capacities of 40 mAh g^{-1}, 35 mAh g^{-1}, and 35 mAh g^{-1} for the 10th, 100th, and 250th cycles, while the thin film shows 20 mAh g^{-1}, 16 mAh g^{-1}, and 15 mAh g^{-1} for the same cycles. This equates to a 28 % loss in capacity, from the 2nd to 250th cycle, for the IO structure versus 42 % loss in capacity for the thin film. Coulombic efficiencies recorded from the 2nd to the 250th cycle show improved reversibility for the carbon IO with an average CE of 97% while the thin film averaged 89% Coulombic efficiency. Notably, the macroporous carbon doubles the specific capacity relative to the thin film, potentially attributed to the inverse opal structure's facilitation of improved electrolyte penetration, shorter diffusion distances, and a higher surface area, providing additional charge compensation sites for sodium. The IO architecture enables efficient mass transport of ions and electrodes which promotes uniform electrochemical reactions and aids in improving Coulombic efficiency.[72-74]

Figure 6.4 (b) illustrates the comparison between the carbon thin film and carbon IO in a potassium-ion half-cell. Notably, the initial coulombic efficiency is higher in the thin film, reaching 22%, compared to the carbon IO's 9%. Despite the IO exhibiting higher 1st and 2nd discharge capacities (554 mAh g^{-1} and 82 mAh g^{-1}) in contrast to the thin film (112 mAh g^{-1} and 35 mAh g^{-1}), a more pronounced capacity fading is observed in the IO material. The carbon IO retained 30% capacity from the 2nd cycle to the 250th, compared to the thin film's retention recorded at 51 %. This observation implies potential structural stresses or damage to the IO walls. Notably,

this marks the first report of carbon inverse opals being tested in potassium-ion batteries. The potential reason for the IO wall damage could be attributed to the larger ionic radius of potassium compared to lithium and sodium, for which carbon IOs have previously demonstrated efficacy.[29, 75, 76] However, a noteworthy trend emerges as the IO structure consistently improves in reversibility throughout the 250 cycles, surpassing the Coulombic efficiency of the thin film. The final Coulombic efficiencies are recorded as 97% for the IO and 93% for the thin film.

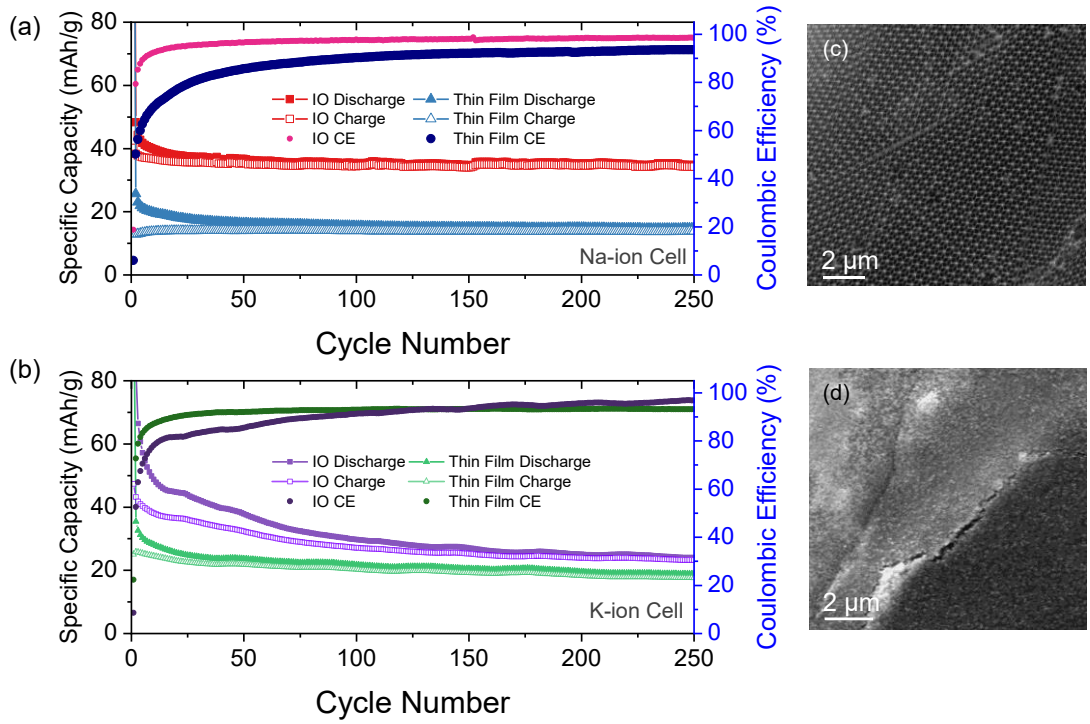

Figure 6.4. Comparison of (a) carbon IO and carbon thin film vs sodium at 75 mA g^{-1}, and (b) carbon IO and carbon thin film vs potassium at 75 mA g^{-1}. SEM images showing morphology of (c) carbon IO electrode, and (d) carbon thin film electrode.

6.3.3 Electrochemical Kinetics

To further analyse the storage mechanism for carbon inverse opals in Na-ion and K-ion batteries, CV techniques were employed. The CV curves for carbon IO at various scan rates from 0.1 – 100 mV/s are shown in Fig. 6.5. While the CVs were set in a potential window of 2 V – 0.014 V, a drift to higher voltages at the end of each cycle

is observed. The curves for both systems exhibit a consistent shape with redox peaks in a lower potential region and a rectangular shape in a high potential region. These features are attributed to the diffusion-controlled intercalation process and surface-induced double layer capacitance, respectively.[77] To assess the specific contribution of these processes, capacitive effects were analysed using the power-law formula,

$$i(V,t) = av^b \quad \text{Eq. 6.1}$$

where *i* is the current (mA), *v* is the scan rate (mV/s) and *a*, *b* are adjustable values. The *b*-values can be derived from a plot of log(*i*) vs log(*v*) a log on both sides of equation 6.1. A value of $b = 0.5$ signifies a current that is diffusion-controlled, indicative of a Faradaic intercalation process.[78, 79] On the other hand, when $b = 1$, it denotes a capacitive response, where the capacitive current shows a linear proportionality to the scan rate. The *b*-values at the end of the voltage window (0.014 V) were found to be 0.65 and 0.59 for the carbon IOs in Na-ion and K-ion systems, respectively, this plot can be found in Fig. S6.5. These values indicate that both double-layer capacitance and Faradaic intercalation processes are utilized with more current coming from the diffusion-controlled processes.[80]

The currents arising from capacitive and diffusion processes can be explicitly determined using the following equation,

$$i(V,t) = k_1 v + k_2 v^{1/2} \quad \text{Eq. 6.2}$$

where *i* represents the current, *v* is the scan rate, and k_1 and k_2 are coefficients corresponding to the capacitive and diffusion-controlled processes, respectively. Figure 6.5 shows the calculated contributions from Faradaic and non-Faradaic processes, at scan rates of 10 mV s^{-1} and 100 mV s^{-1}, in both Na-ion and K-ion cells. Calculated contributions for all scan rates can be found in supplementary information,

Figs. S6.5 and S6.7. For the carbon IOs in Na-ion cells, diffusion-controlled processes account for 97%, 85%, 83% 70%, and 67% of the current contribution for scan rates 0.1 , 0.5, 1, 5, and 10 mV s^{-1}. Once the scan rate reaches 50 mV s^{-1} in these tests, we note the onset of a greater current contribution from capacitive reactions, which account for 54% of the current response and increase to 60% for 100 mV s^{-1}, Fig. S6.7. On the other hand, double-layer capacitance accounts for a larger proportion of the current response for the carbon IOs in the K-ion cell. As can be seen from Fig. 6.5 (e) and (f), a large portion of the current response at the higher voltage region is from capacitive processes. For each scan rate, diffusion-controlled processes accounted for 87%, 78%, 76%, 72%, 48%, 29% and 24% for the 0.1, 0.5, 1, 5, 10, 50, and 100 mV s^{-1} scan rate, respectively (Fig. S6.7).

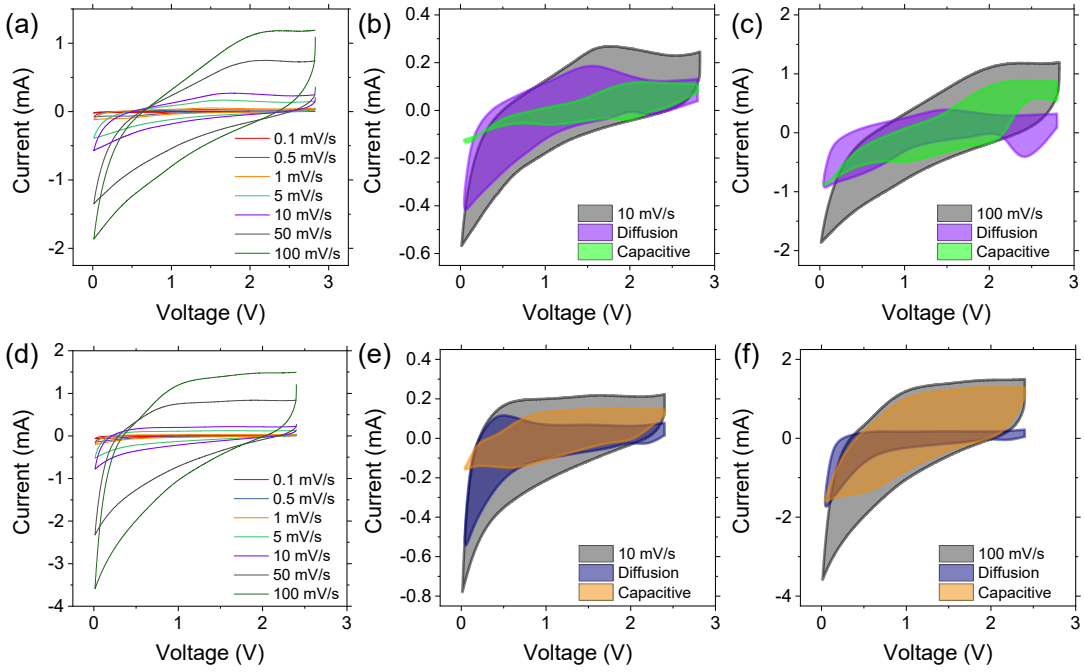

Figure 6.5. (a) CV of carbon IO in Na-ion cell at various scan rates. Intercalation (purple) and capacitive (green) contributions to the total measured current (*grey*) for carbon IO at scans rates of (b) 10 mV s^{-1} and (c) 100 mV s^{-1}. The sum of these contributions at each potential equals the actual measured current. (d) CV of carbon IO in K-ion cell. (e) . Intercalation (blue) and capacitive (orange) processes compared to the total measured current (*grey*) for carbon IO in K-ion cell at scans rates of (b) 10 mV s^{-1} and (c) 100 mV s^{-1}.

6.3.4 Post-Mortem Structural Analysis

Post-mortem analysis involved SEM examination of the structural integrity of carbon IOs in sodium and potassium-ion cells. Given the substantial specific surface area and interconnected pore structure that demonstrated durability in lithium-ion cells, we sought to assess their performance in sodium and potassium-ion cells. After 250 cycles at 75 mA g^{-1} and 185 mA g^{-1} rates, cells were disassembled, washed with electrolyte solution, and examined. For sodium-ion cells (Fig. 6.6 (a) and (b)), despite observing distortion and slight swelling in sodium-ion cells, the structural integrity of the inverse opal remained. Significantly, the structural integrity persisted despite volume expansion of the inverse opal walls. Initially measured at 26.5 nm before cycling, the wall thickness increased by 40% (to ~37 nm) and 77% (to ~47 nm) at rates of 75 mA g^{-1} and 185 mA g^{-1}, respectively.

The carbon inverse opals after potassiation are shown in Fig. 6.6 (c) and (d). The carbon IOs exhibited more pronounced volume expansion during cycling relative to the sodium-ion cell. Measurements from SEM images indicated a wall thickness of ~48 nm after 250 cycles at the 75 mA g^{-1} rate and 55 nm for the 185 mA g^{-1} rate. While the majority of the electrode maintained its structure, SEM images revealed localized swelling and breakage in certain areas, as depicted in supplementary information (Fig. S6.8). Additional SEM images of all electrodes post-cycling can be found here as well. Intriguingly, this structural breakdown occurred primarily at the slower rate of 75 mA g^{-1}, despite a wall thickness swelling of only 81%, compared to the faster rates showing an ~106% increase.

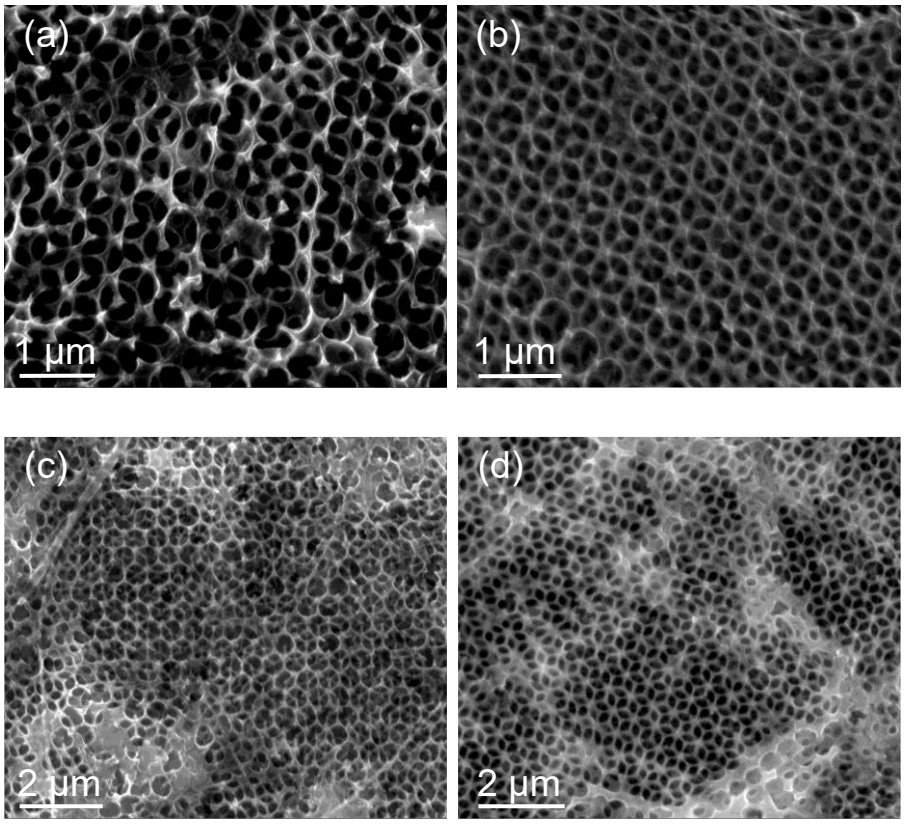

Figure 6.6. Post-mortem SEM analysis of carbon inverse opals after 250 cycles at (a) 75 mA g^{-1} vs Na, (b) 185 mA g^{-1} vs Na, (c) 75 mA g^{-1} vs K, (d) 185 mA g^{-1} vs K.

This structural integrity is innate to the inverse opal architecture, evident in the accommodation of volumetric swelling within the macropores during cycling, as illustrated in SEM images. Previously, inverse opal structures have been shown to withstand thousands of cycles in lithium-ion batteries[29], and reports have shown resistance to volumetric swelling over 500 cycles in sodium-ion cells[81]. This report extends the scope by showcasing their resilience against potassium ions, which exhibit larger ionic radii and are more susceptible to cause volume expansion.[82] These findings contribute valuable insights into the potential viability of inverse opal structures for sustained performance and longevity in 'beyond-lithium' battery applications.

6.4 Conclusion

Carbon inverse opals were synthesized from sucrose to produce highly ordered, three-dimensional macroporous architecture. The macroporous structure was characterized by interconnected layers with face-centred cubic (FCC) symmetry, providing a high surface area-to-volume ratio. High-resolution transmission electron microscopy (HRTEM) revealed a disordered nanostructure with curved, short-range graphitic areas, and selected area electron diffraction (SAED) confirmed the disordered microstructure. Structural measurements indicated two mean averages of pore diameters of ~495 nm and ~355 nm, and an electrode coating thickness of approximately 17.5 μm.

The electrochemical characterization of the carbon IOs in sodium-ion (Na-ion) and potassium-ion (K-ion) battery cells showed promising results. Cyclic voltammetry (CV) curves exhibited reversible sodiation and potassiation processes. Galvanostatic cycling at various rates demonstrated stable specific capacities and Coulombic efficiencies in Na-ion cells. However, in K-ion cells, a more pronounced capacity fading was observed, suggesting potential challenges associated with the larger ionic radius of potassium.

Electrochemical kinetics analysis indicated that both diffusion-controlled intercalation and surface-induced double-layer capacitance contributed to the charge storage mechanism. Post-mortem structural analysis revealed the remarkable structural integrity of the carbon IOs, even after 250 cycles in both Na-ion and K-ion cells. The inverse opal architecture accommodated volumetric swelling within the macropores, showcasing resilience against the challenges posed by sodium and potassium ions.

These findings underscore the potential of three-dimensional ordered macroporous structures, such as carbon inverse opals, as promising electrode structures for 'beyond-lithium' battery technologies and also provide an electrode structure that allows examination of charge storage mechanisms and fundamental response to charging and discharging in the absence of physical additives such as additional conductivity enhancers or binders. The unique architecture not only facilitates stable electrochemical performance in sodium-ion cells but also demonstrates notable durability and resistance to structural breakdown, even in the presence of larger potassium ions.

6.5 Appendix : Supplementary Information

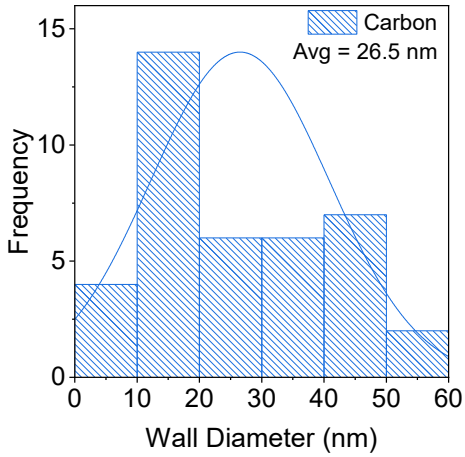

Figure S6.1. Histogram illustrating distribution of measured wall thickness for pristine carbon IO.

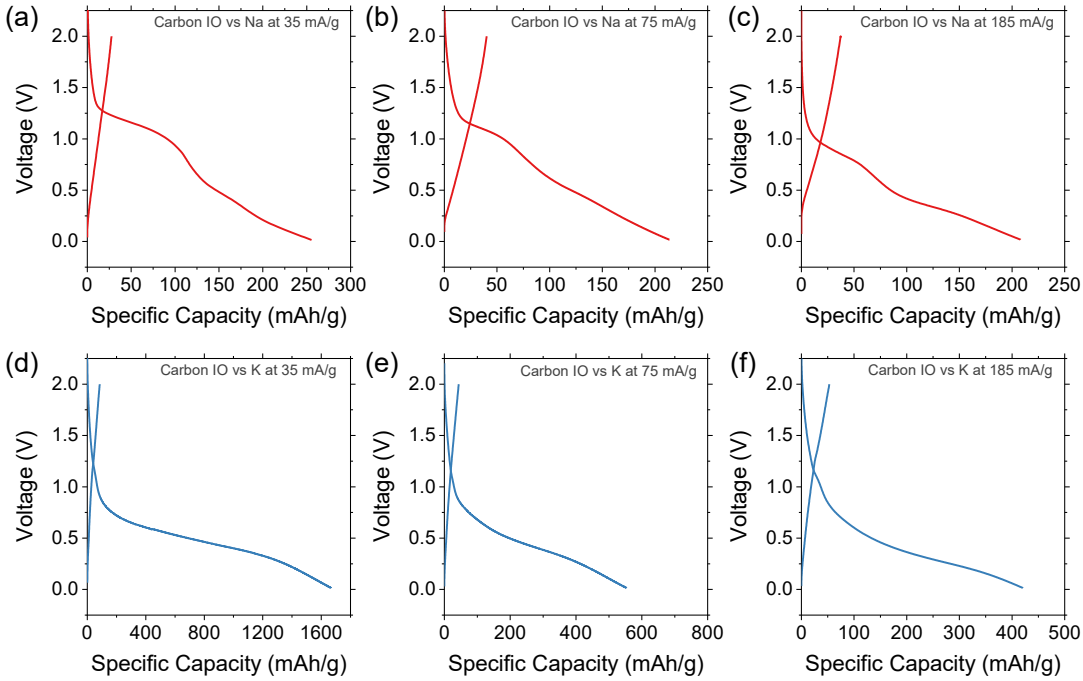

Figure S6.2 Initial discharge and charge plots for carbon inverse opals in (a) Na-ion cell at 35 mA g^{-1}, (b) Na-ion cell at 75 mA g^{-1}, (c) Na-ion cell at 185 mA g^{-1}, (d) K-ion cell at 35 mA g^{-1}, (e) K-ion cell at 75 mA g^{-1}, and (f) K-ion cell at 185 mA g^{-1}.

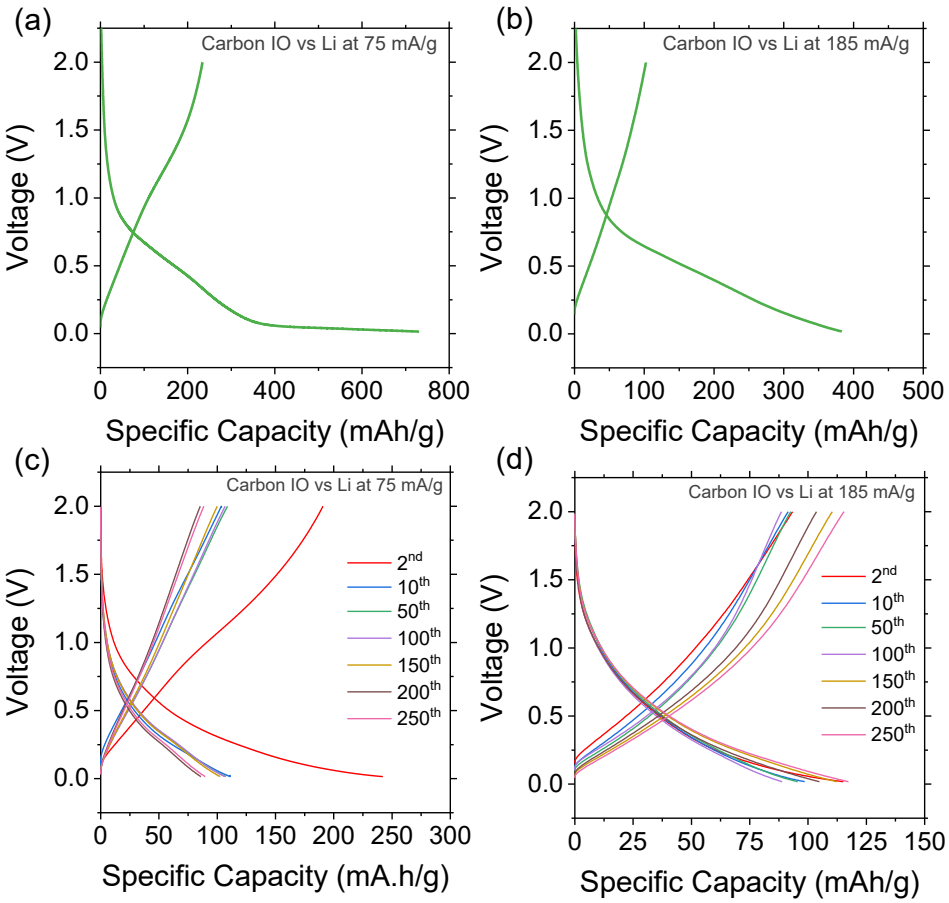

Figure S6.3. Initial discharge/charge plots for carbon IO vs lithium at (a) 75 mA g^{-1}, and (b) 185 mA g^{-1}. Galvanostatic cycling profiles of carbon IOs in lithium-ion cells for the 2nd, 10, 50th, 100th, 150th, 200th, and 250th cycle at (c) 75 mA g^{-1} and (d) 185 mA g^{-1}.

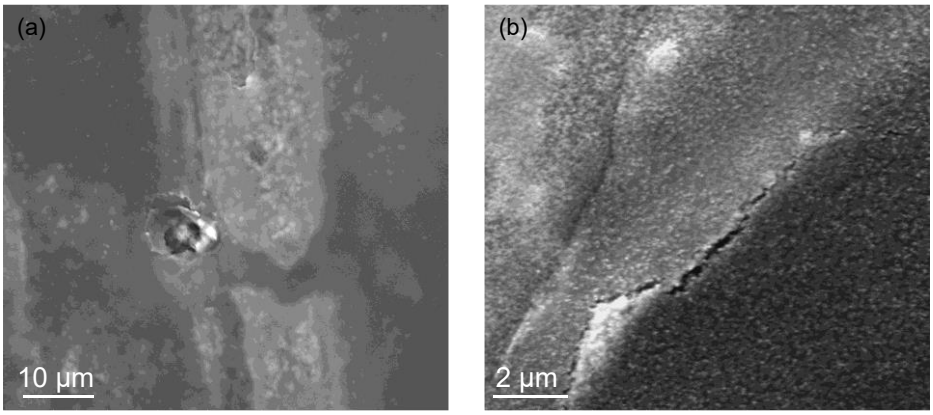

Figure S6.4 SEM images of carbon thin film at different magnifications illustrating lack of macrostructure and pores.

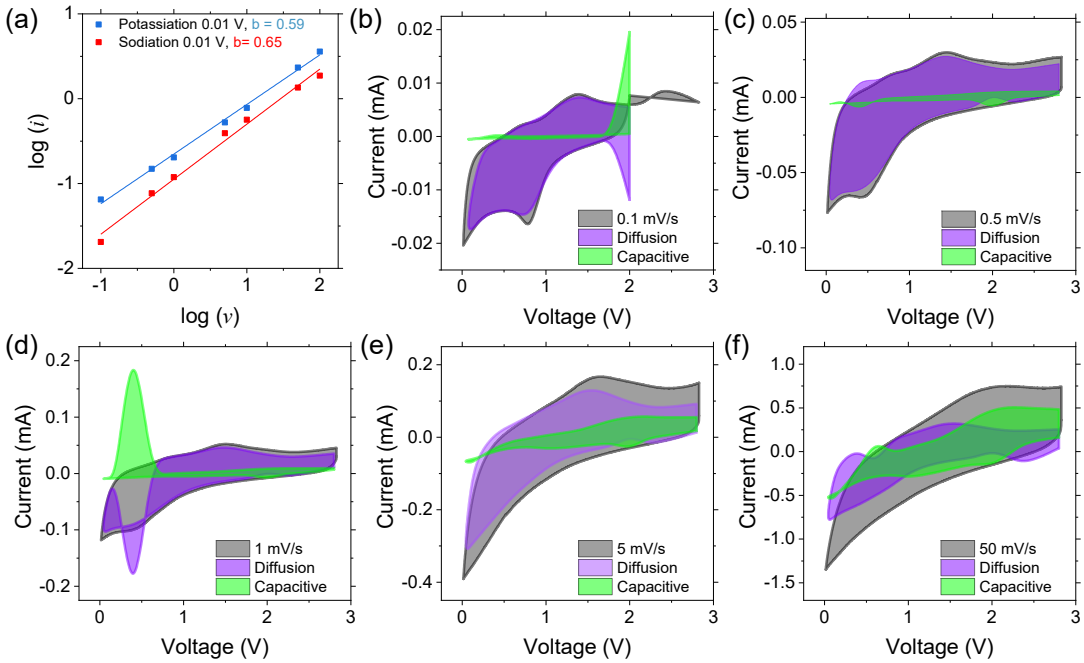

Figure S6.5. (a) *b*-values for log (*i*) as a function of log (*v*) for carbon IOs at insertion voltage 0.01 V in sodium-ion cell (red) and potassium-ion cell (blue). Intercalation (purple) and capacitive (green) contributions to the total measured current (*grey*) for carbon IOs vs sodium at scans rates of (b) 0.1 mV s^{-1}, (c) 0.5 mV s^{-1}, (d) 1 mV s^{-1}, (e) 5 mV $s^{-1}$and (f) 50 mV s^{-1}. The sum of these contributions at each potential equals the actual measured current.

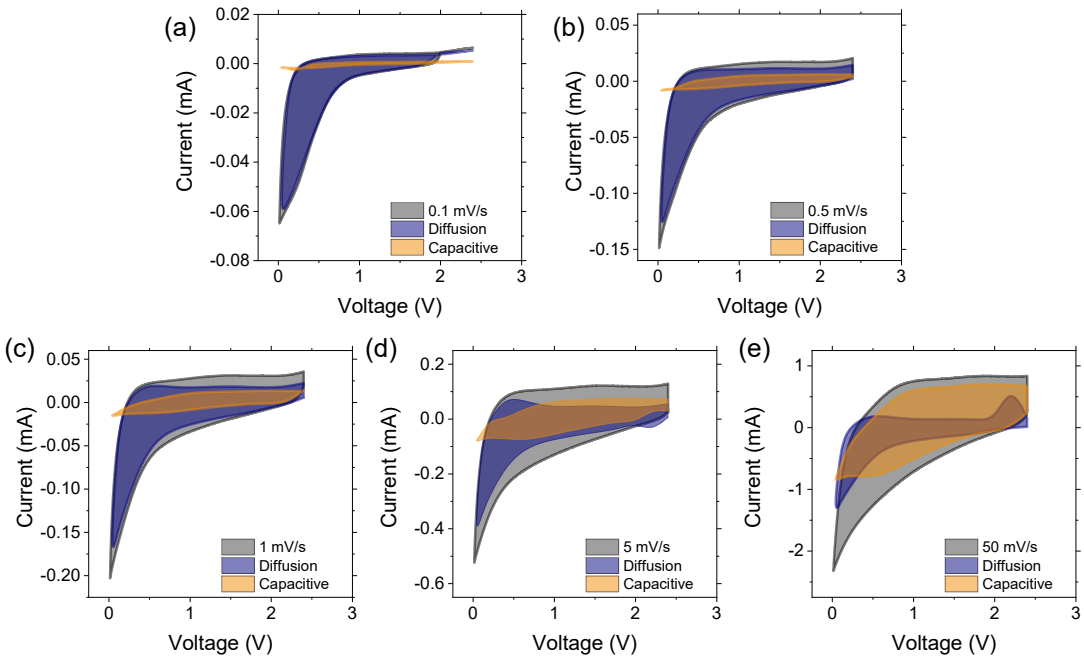

Figure S6.6. Intercalation (blue) and capacitive (orange) contributions to the total measured current (*grey*) for carbon IOs vs potassium at scans rates of (a) 0.1 mV s^{-1}, (b) 0.5 mV s^{-1}, (c) 1 mV s^{-1}, (d) 5 mV $s^{-1}$and (e) 50 mV s^{-1}. The sum of these contributions at each potential equals the actual measured current.

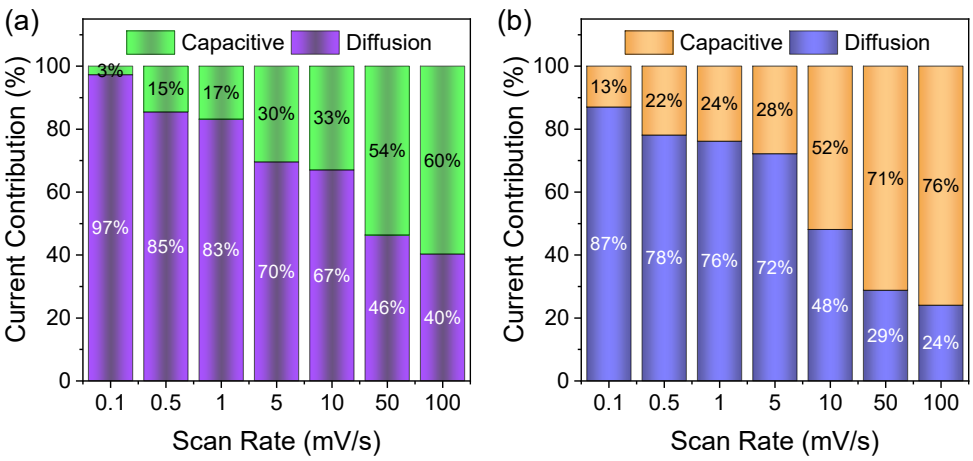

Figure S6.7. Percentage contributions to total current at each scan rate for (a) carbon IOs vs sodium, and (b) carbon IOs vs potassium.

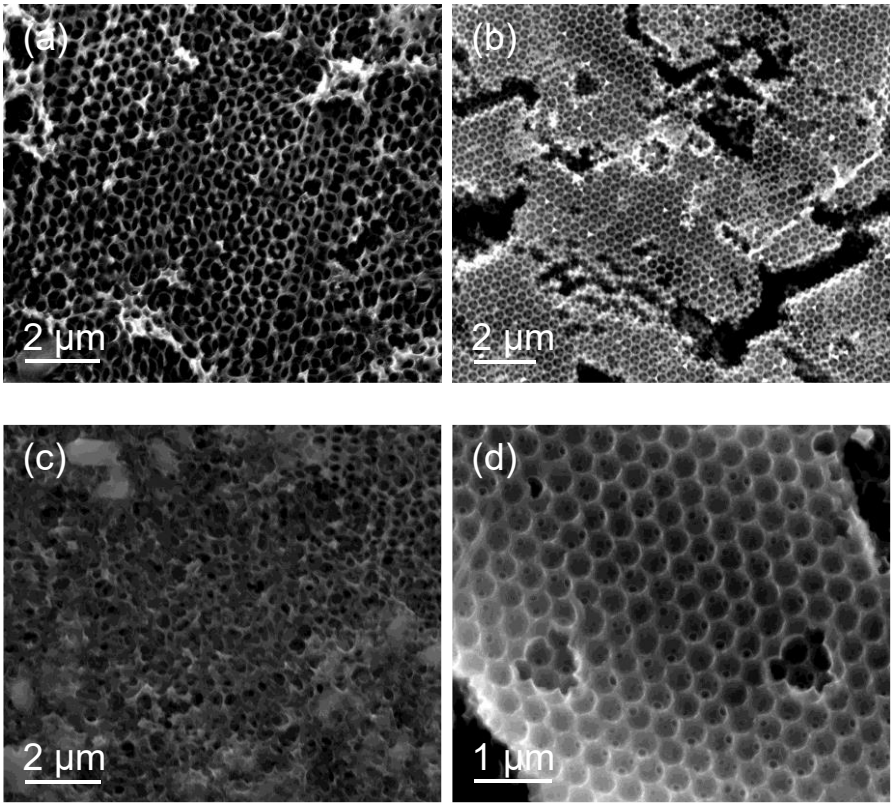

Figure S6.8. Additional post-mortem SEM images after 250 cycles (a) vs Na at 75 mA g^{-1}, (b) vs Na at 185 mA g^{-1}, (c) vs at 75 mA g^{-1}, showing major distortion and localized breakage of the IO architecture, and (d) vs K at 185 mA g^{-1}.

6.6 References

(1) Tarascon, J. M.; Armand, M. Issues and challenges facing rechargeable lithium batteries. *Nature* **2001**, *414* (6861), 359-367, Review. DOI: 10.1038/35104644 Scopus.
(2) Larcher, D.; Tarascon, J.-M. Towards greener and more sustainable batteries for electrical energy storage. *Nature chemistry* **2015**, *7* (1), 19-29.
(3) Huang, B.; Pan, Z.; Su, X.; An, L. Recycling of lithium-ion batteries: Recent advances and perspectives. *Journal of Power Sources* **2018**, *399*, 274-286.
(4) Nayak, P. K.; Yang, L.; Brehm, W.; Adelhelm, P. From lithium-ion to sodium-ion batteries: advantages, challenges, and surprises. *Angewandte Chemie International Edition* **2018**, *57* (1), 102-120.
(5) Delmas, C. Sodium and sodium-ion batteries: 50 years of research. *Advanced Energy Materials* **2018**, *8* (17), 1703137.
(6) Hwang, J.-Y.; Myung, S.-T.; Sun, Y.-K. Sodium-ion batteries: present and future. *Chemical Society Reviews* **2017**, *46* (12), 3529-3614.
(7) Yabuuchi, N.; Kubota, K.; Dahbi, M.; Komaba, S. Research Development on Sodium-Ion Batteries. *Chemical Reviews* **2014**, *114* (23), 11636-11682. DOI: 10.1021/cr500192f.
(8) Min, X.; Xiao, J.; Fang, M.; Wang, W. A.; Zhao, Y.; Liu, Y.; Abdelkader, A. M.; Xi, K.; Kumar, R. V.; Huang, Z. Potassium-ion batteries: outlook on present and future technologies. *Energy & Environmental Science* **2021**, *14* (4), 2186-2243.
(9) Rajagopalan, R.; Tang, Y.; Ji, X.; Jia, C.; Wang, H. Advancements and challenges in potassium ion batteries: a comprehensive review. *Advanced Functional Materials* **2020**, *30* (12), 1909486.
(10) Pramudita, J. C.; Sehrawat, D.; Goonetilleke, D.; Sharma, N. An initial review of the status of electrode materials for potassium-ion batteries. *Advanced energy materials* **2017**, *7* (24), 1602911.
(11) Vaalma, C.; Buchholz, D.; Passerini, S. Non-aqueous potassium-ion batteries: a review. *Current Opinion in Electrochemistry* **2018**, *9*, 41-48.
(12) Oszajca, M. F.; Bodnarchuk, M. I.; Kovalenko, M. V. Precisely Engineered Colloidal Nanoparticles and Nanocrystals for Li-Ion and Na-Ion Batteries: Model Systems or Practical Solutions? *Chemistry of Materials* **2014**, *26* (19), 5422-5432. DOI: 10.1021/cm5024508.
(13) Zhang, W.; Liu, Y.; Guo, Z. Approaching high-performance potassium-ion batteries via advanced design strategies and engineering. *Science Advances 5* (5), eaav7412. DOI: 10.1126/sciadv.aav7412 (acccessed 2023/09/06).
(14) Xu, Y.-S.; Guo, S.-J.; Tao, X.-S.; Sun, Y.-G.; Ma, J.; Liu, C.; Cao, A.-M. High-Performance Cathode Materials for Potassium-Ion Batteries: Structural Design and Electrochemical Properties. *Advanced Materials* **2021**, *33* (36), 2100409. DOI: https://doi.org/10.1002/adma.202100409 (acccessed 2023/12/14).
(15) Fang, Y.; Yu, X.-Y.; Lou, X. W. D. Nanostructured electrode materials for advanced sodium-ion batteries. *Matter* **2019**, *1* (1), 90-114.
(16) Landi, B. J.; Ganter, M. J.; Cress, C. D.; DiLeo, R. A.; Raffaelle, R. P. Carbon nanotubes for lithium ion batteries. *Energy & Environmental Science* **2009**, *2* (6), 638-654, 10.1039/B904116H. DOI: 10.1039/B904116H.
(17) Bi, J.; Du, Z.; Sun, J.; Liu, Y.; Wang, K.; Du, H.; Ai, W.; Huang, W. On the Road to the Frontiers of Lithium-Ion Batteries: A Review and Outlook of Graphene Anodes.

Advanced Materials **2023**, *35* (16), 2210734. DOI: https://doi.org/10.1002/adma.202210734 (acccessed 2024/04/08).
(18) Cheng, X.; Tang, C.; Yan, C.; Du, J.; Chen, A.; Liu, X.; Jewell, L.; Zhang, Q. Preparation of porous carbon spheres and their application as anode materials for lithium-ion batteries: A review. *Materials Today Nano* **2023**, *22*, 100321. DOI: https://doi.org/10.1016/j.mtnano.2023.100321.
(19) Yan, K.; Lu, Z.; Lee, H.-W.; Xiong, F.; Hsu, P.-C.; Li, Y.; Zhao, J.; Chu, S.; Cui, Y. Selective deposition and stable encapsulation of lithium through heterogeneous seeded growth. *Nature Energy* **2016**, *1* (3), 1-8.
(20) Stevens, D.; Dahn, J. The mechanisms of lithium and sodium insertion in carbon materials. *Journal of The Electrochemical Society* **2001**, *148* (8), A803.
(21) Wang, L.; Yang, J.; Li, J.; Chen, T.; Chen, S.; Wu, Z.; Qiu, J.; Wang, B.; Gao, P.; Niu, X. Graphite as a potassium ion battery anode in carbonate-based electrolyte and ether-based electrolyte. *Journal of Power Sources* **2019**, *409*, 24-30.
(22) Dou, X.; Hasa, I.; Saurel, D.; Vaalma, C.; Wu, L.; Buchholz, D.; Bresser, D.; Komaba, S.; Passerini, S. Hard carbons for sodium-ion batteries: Structure, analysis, sustainability, and electrochemistry. *Materials Today* **2019**, *23*, 87-104.
(23) Kamiyama, A.; Kubota, K.; Nakano, T.; Fujimura, S.; Shiraishi, S.; Tsukada, H.; Komaba, S. High-Capacity Hard Carbon Synthesized from Macroporous Phenolic Resin for Sodium-Ion and Potassium-Ion Battery. *ACS Applied Energy Materials* **2020**, *3* (1), 135-140. DOI: 10.1021/acsaem.9b01972.
(24) Yamamoto, H.; Muratsubaki, S.; Kubota, K.; Fukunishi, M.; Watanabe, H.; Kim, J.; Komaba, S. Synthesizing higher-capacity hard-carbons from cellulose for Na-and K-ion batteries. *Journal of Materials Chemistry A* **2018**, *6* (35), 16844-16848.
(25) Kubota, K.; Dahbi, M.; Hosaka, T.; Kumakura, S.; Komaba, S. Towards K-Ion and Na-Ion Batteries as "Beyond Li-Ion". *The Chemical Record* **2018**, *18* (4), 459-479. DOI: https://doi.org/10.1002/tcr.201700057 (acccessed 2023/11/10).
(26) Jian, Z.; Xing, Z.; Bommier, C.; Li, Z.; Ji, X. Hard Carbon Microspheres: Potassium-Ion Anode Versus Sodium-Ion Anode. *Advanced Energy Materials* **2016**, *6* (3), 1501874. DOI: https://doi.org/10.1002/aenm.201501874 (acccessed 2023/12/19).
(27) McNulty, D.; Geaney, H.; O'Dwyer, C. Carbon-Coated Honeycomb Ni-Mn-Co-O Inverse Opal: A High Capacity Ternary Transition Metal Oxide Anode for Li-ion Batteries. *Scientific Reports* **2017**, *7* (1), 42263. DOI: 10.1038/srep42263.
(28) Armstrong, E.; McNulty, D.; Geaney, H.; O'Dwyer, C. Electrodeposited Structurally Stable V2O5 Inverse Opal Networks as High Performance Thin Film Lithium Batteries. *ACS Applied Materials & Interfaces* **2015**, *7* (48), 27006-27015. DOI: 10.1021/acsami.5b09511.
(29) McNulty, D.; Carroll, E.; O'Dwyer, C. Rutile TiO2 Inverse Opal Anodes for Li-Ion Batteries with Long Cycle Life, High-Rate Capability, and High Structural Stability. *Advanced Energy Materials* **2017**, *7* (12), 1602291. DOI: 10.1002/aenm.201602291.
(30) Li, Z.; Zhao, T.; Zhan, X.; Gao, D.; Xiao, Q.; Lei, G. High capacity three-dimensional ordered macroporous CoFe2O4 as anode material for lithium ion batteries. *Electrochimica Acta* **2010**, *55* (15), 4594-4598.
(31) Esmanski, A.; Ozin, G. A. Silicon inverse-opal-based macroporous materials as negative electrodes for lithium ion batteries. *Advanced Functional Materials* **2009**, *19* (12), 1999-2010.
(32) Jian, Z.; Luo, W.; Ji, X. Carbon electrodes for K-ion batteries. *Journal of the American chemical society* **2015**, *137* (36), 11566-11569.

(33) Wang, Q.; Zhao, X.; Ni, C.; Tian, H.; Li, J.; Zhang, Z.; Mao, S. X.; Wang, J.; Xu, Y. Reaction and Capacity-Fading Mechanisms of Tin Nanoparticles in Potassium-Ion Batteries. *The Journal of Physical Chemistry C* **2017**, *121* (23), 12652-12657. DOI: 10.1021/acs.jpcc.7b03837.
(34) Armstrong, E.; O'Dwyer, C. Artificial opal photonic crystals and inverse opal structures – fundamentals and applications from optics to energy storage. *Journal of Materials Chemistry C* **2015**, *3* (24), 6109-6143, 10.1039/C5TC01083G. DOI: 10.1039/C5TC01083G.
(35) Wang, K.; Jin, Y.; Sun, S.; Huang, Y.; Peng, J.; Luo, J.; Zhang, Q.; Qiu, Y.; Fang, C.; Han, J. Low-cost and high-performance hard carbon anode materials for sodium-ion batteries. *ACS omega* **2017**, *2* (4), 1687-1695.
(36) Tokumitsu, K.; Mabuchi, A.; Fujimoto, H.; Kasuh, T. Electrochemical insertion of lithium into carbon synthesized from condensed aromatics. *Journal of the Electrochemical Society* **1996**, *143* (7), 2235.
(37) Zhang, Y. S.; Zhu, C.; Xia, Y. Inverse Opal Scaffolds and Their Biomedical Applications. *Advanced Materials* **2017**, *29* (33), 1701115. DOI: https://doi.org/10.1002/adma.201701115 (acccessed 2023/12/19).
(38) Kang, D.-Y.; Kim, S.-O.; Chae, Y. J.; Lee, J. K.; Moon, J. H. Particulate Inverse Opal Carbon Electrodes for Lithium-Ion Batteries. *Langmuir* **2013**, *29* (4), 1192-1198. DOI: 10.1021/la304556w.
(39) Lee, K. T.; Lytle, J. C.; Ergang, N. S.; Oh, S. M.; Stein, A. Synthesis and Rate Performance of Monolithic Macroporous Carbon Electrodes for Lithium-Ion Secondary Batteries. *Advanced Functional Materials* **2005**, *15* (4), 547-556. DOI: https://doi.org/10.1002/adfm.200400186 (acccessed 2023/09/15).
(40) Wang, H.; Li, X.; Hong, L.-Y.; Kim, D.-P. Preparation of phenolic resin derived 3-D ordered macroporous carbon. *Journal of Porous Materials* **2006**, *13* (2), 115-121. DOI: 10.1007/s10934-006-7006-9.
(41) Li, H.; Zhang, L.; Dai, H.; He, H. Facile Synthesis and Unique Physicochemical Properties of Three-Dimensionally Ordered Macroporous Magnesium Oxide, Gamma-Alumina, and Ceria−Zirconia Solid Solutions with Crystalline Mesoporous Walls. *Inorganic Chemistry* **2009**, *48* (10), 4421-4434. DOI: 10.1021/ic900132k.
(42) Voskanyan, A. A.; Chan, K.-Y.; Li, C.-Y. V. Colloidal Solution Combustion Synthesis: Toward Mass Production of a Crystalline Uniform Mesoporous CeO2 Catalyst with Tunable Porosity. *Chemistry of Materials* **2016**, *28* (8), 2768-2775. DOI: 10.1021/acs.chemmater.6b00505.
(43) Merlen, A.; Buijnsters, J. G.; Pardanaud, C. A guide to and review of the use of multiwavelength Raman spectroscopy for characterizing defective aromatic carbon solids: From graphene to amorphous carbons. *Coatings* **2017**, *7* (10), 153.
(44) Xiao, L.; Lu, H.; Fang, Y.; Sushko, M. L.; Cao, Y.; Ai, X.; Yang, H.; Liu, J. Low-defect and low-porosity hard carbon with high coulombic efficiency and high capacity for practical sodium ion battery anode. *Advanced Energy Materials* **2018**, *8* (20), 1703238.
(45) Xie, F.; Xu, Z.; Jensen, A. C. S.; Au, H.; Lu, Y.; Araullo-Peters, V.; Drew, A. J.; Hu, Y.-S.; Titirici, M.-M. Hard–Soft Carbon Composite Anodes with Synergistic Sodium Storage Performance. *Advanced Functional Materials* **2019**, *29* (24), 1901072. DOI: https://doi.org/10.1002/adfm.201901072 (acccessed 2023/12/02).
(46) Wang, M.; Zhu, Y.; Zhang, Y.; Yang, T.; Duan, J.; Wang, C. Cost-effective hard–soft carbon composite anodes with promising potassium ions storage performance. *Electrochimica Acta* **2021**, *368*, 137649.

(47) Xue, B.; Xu, J.; Xiao, R. Synthesis of hierarchically porous carbon with tailored porosity and electrical conductivity derived from hard–soft carbon precursors for enhanced capacitive performance. *ACS Sustainable Chemistry & Engineering* **2021**, *9* (47), 15925-15934.
(48) Yadegari, H.; Koronfel, M. A.; Wang, K.; Thornton, D. B.; Stephens, I. E.; Molteni, C.; Haynes, P. D.; Ryan, M. P. Operando measurement of layer breathing modes in lithiated graphite. *ACS Energy Letters* **2021**, *6* (4), 1633-1638.
(49) Hou, H.; Banks, C. E.; Jing, M.; Zhang, Y.; Ji, X. Carbon Quantum Dots and Their Derivative 3D Porous Carbon Frameworks for Sodium-Ion Batteries with Ultralong Cycle Life. *Advanced Materials* **2015**, *27* (47), 7861-7866. DOI: https://doi.org/10.1002/adma.201503816 (acccessed 2023/12/02).
(50) Komaba, S.; Murata, W.; Ishikawa, T.; Yabuuchi, N.; Ozeki, T.; Nakayama, T.; Ogata, A.; Gotoh, K.; Fujiwara, K. Electrochemical Na insertion and solid electrolyte interphase for hard-carbon electrodes and application to Na-Ion batteries. *Advanced Functional Materials* **2011**, *21* (20), 3859-3867.
(51) Cao, Y.; Xiao, L.; Sushko, M. L.; Wang, W.; Schwenzer, B.; Xiao, J.; Nie, Z.; Saraf, L. V.; Yang, Z.; Liu, J. Sodium ion insertion in hollow carbon nanowires for battery applications. *Nano letters* **2012**, *12* (7), 3783-3787.
(52) Wenzel, S.; Hara, T.; Janek, J.; Adelhelm, P. Room-temperature sodium-ion batteries: Improving the rate capability of carbon anode materials by templating strategies. *Energy & Environmental Science* **2011**, *4* (9), 3342-3345.
(53) Zheng, P.; Liu, T.; Guo, S. Micro-nano structure hard carbon as a high performance anode material for sodium-ion batteries. *Scientific Reports* **2016**, *6* (1), 35620. DOI: 10.1038/srep35620.
(54) Tang, K.; Fu, L.; White, R. J.; Yu, L.; Titirici, M.-M.; Antonietti, M.; Maier, J. Hollow Carbon Nanospheres with Superior Rate Capability for Sodium-Based Batteries. *Advanced Energy Materials* **2012**, *2* (7), 873-877. DOI: https://doi.org/10.1002/aenm.201100691 (acccessed 2023/12/02).
(55) Chen, Y.; Qin, L.; Lei, Y.; Li, X.; Dong, J.; Zhai, D.; Li, B.; Kang, F. Correlation between Microstructure and Potassium Storage Behavior in Reduced Graphene Oxide Materials. *ACS Applied Materials & Interfaces* **2019**, *11* (49), 45578-45585. DOI: 10.1021/acsami.9b14534.
(56) Peng, S.; Wang, L.; Zhu, Z.; Han, K. Electrochemical performance of reduced graphene oxide/carbon nanotube hybrid papers as binder-free anodes for potassium-ion batteries. *Journal of Physics and Chemistry of Solids* **2020**, *138*, 109296.
(57) Kang, H.; Chen, Q.; Ma, Q.; Zhang, L.; Yang, Q.; Li, H.; Xie, X.; Lan, S.; Zhang, C. Coaxial spiral structural polymer/reduced graphene oxide composite as a high-performance anode for potassium ion batteries. *Journal of Power Sources* **2022**, *545*, 231951.
(58) Wang, W.; Zhou, J.; Wang, Z.; Zhao, L.; Li, P.; Yang, Y.; Yang, C.; Huang, H.; Guo, S. Short-range order in mesoporous carbon boosts potassium-ion battery performance. *Advanced Energy Materials* **2018**, *8* (5), 1701648.
(59) Sun, D.; Luo, B.; Wang, H.; Tang, Y.; Ji, X.; Wang, L. Engineering the trap effect of residual oxygen atoms and defects in hard carbon anode towards high initial Coulombic efficiency. *Nano Energy* **2019**, *64*, 103937. DOI: https://doi.org/10.1016/j.nanoen.2019.103937.
(60) Wu, X.; Chen, Y.; Xing, Z.; Lam, C. W. K.; Pang, S.-S.; Zhang, W.; Ju, Z. Advanced Carbon-Based Anodes for Potassium-Ion Batteries. *Advanced Energy Materials* **2019**, *9* (21), 1900343. DOI: https://doi.org/10.1002/aenm.201900343 (acccessed 2023/12/09).

(61) Sun, N.; Liu, H.; Xu, B. Facile synthesis of high performance hard carbon anode materials for sodium ion batteries. *Journal of materials chemistry a* **2015**, *3* (41), 20560-20566.
(62) Xiao, L.; Cao, Y.; Henderson, W. A.; Sushko, M. L.; Shao, Y.; Xiao, J.; Wang, W.; Engelhard, M. H.; Nie, Z.; Liu, J. Hard carbon nanoparticles as high-capacity, high-stability anodic materials for Na-ion batteries. *Nano Energy* **2016**, *19*, 279-288.
(63) He, H.; Huang, D.; Tang, Y.; Wang, Q.; Ji, X.; Wang, H.; Guo, Z. Tuning nitrogen species in three-dimensional porous carbon via phosphorus doping for ultra-fast potassium storage. *Nano Energy* **2019**, *57*, 728-736. DOI: https://doi.org/10.1016/j.nanoen.2019.01.009.
(64) Jin, Q.; Wang, K.; Feng, P.; Zhang, Z.; Cheng, S.; Jiang, K. Surface-dominated storage of heteroatoms-doping hard carbon for sodium-ion batteries. *Energy Storage Materials* **2020**, *27*, 43-50.
(65) Komaba, S.; Hasegawa, T.; Dahbi, M.; Kubota, K. Potassium intercalation into graphite to realize high-voltage/high-power potassium-ion batteries and potassium-ion capacitors. *Electrochemistry Communications* **2015**, *60*, 172-175. DOI: https://doi.org/10.1016/j.elecom.2015.09.002.
(66) Zhao, L. F.; Hu, Z.; Lai, W. H.; Tao, Y.; Peng, J.; Miao, Z. C.; Wang, Y. X.; Chou, S. L.; Liu, H. K.; Dou, S. X. Hard carbon anodes: fundamental understanding and commercial perspectives for Na-ion batteries beyond Li-ion and K-ion counterparts. *Advanced Energy Materials* **2021**, *11* (1), 2002704.
(67) Peled, E.; Eshkenazi, V.; Rosenberg, Y. Study of lithium insertion in hard carbon made from cotton wool. *Journal of power sources* **1998**, *76* (2), 153-158.
(68) Thomas, P.; Billaud, D. Electrochemical insertion of sodium into hard carbons. *Electrochimica Acta* **2002**, *47* (20), 3303-3307.
(69) Qiu, S.; Xiao, L.; Sushko, M. L.; Han, K. S.; Shao, Y.; Yan, M.; Liang, X.; Mai, L.; Feng, J.; Cao, Y. Manipulating adsorption–insertion mechanisms in nanostructured carbon materials for high-efficiency sodium ion storage. *Advanced Energy Materials* **2017**, *7* (17), 1700403.
(70) Yuan, Z.; Si, L.; Zhu, X. Three-dimensional hard carbon matrix for sodium-ion battery anode with superior-rate performance and ultralong cycle life. *Journal of Materials Chemistry A* **2015**, *3* (46), 23403-23411.
(71) Chen, C.; Wu, M.; Wang, Y.; Zaghib, K. Insights into pseudographite-structured hard carbon with stabilized performance for high energy K-ion storage. *Journal of Power Sources* **2019**, *444*, 227310.
(72) Liu, Z.; Yuan, X.; Zhang, S.; Wang, J.; Huang, Q.; Yu, N.; Zhu, Y.; Fu, L.; Wang, F.; Chen, Y.; et al. Three-dimensional ordered porous electrode materials for electrochemical energy storage. *NPG Asia Materials* **2019**, *11* (1), 12. DOI: 10.1038/s41427-019-0112-3.
(73) Vu, A.; Qian, Y.; Stein, A. Porous Electrode Materials for Lithium-Ion Batteries – How to Prepare Them and What Makes Them Special. *Advanced Energy Materials* **2012**, *2* (9), 1056-1085, https://doi.org/10.1002/aenm.201200320. DOI: https://doi.org/10.1002/aenm.201200320 (acccessed 2023/06/22).
(74) Zhou, J.; Wang, B. Emerging crystalline porous materials as a multifunctional platform for electrochemical energy storage. *Chemical Society Reviews* **2017**, *46* (22), 6927-6945.
(75) Hu, X.; Jia, J.; Wang, G.; Chen, J.; Zhan, H.; Wen, Z. Reliable and General Route to Inverse Opal Structured Nanohybrids of Carbon-Confined Transition Metal Sulfides Quantum Dots for High-Performance Sodium Storage. *Advanced Energy*

Materials **2018**, *8* (25), 1801452. DOI: https://doi.org/10.1002/aenm.201801452 (acccessed 2023/11/12).
(76) Grant, A.; Carroll, A.; Zhang, Y.; Gulzar, U.; Ahad, S. A.; Geaney, H.; O'Dwyer, C. Comparing Cycling and Rate Response of SnO2 Macroporous Anodes in Lithium-Ion and Sodium-Ion Batteries. *Journal of The Electrochemical Society* **2023**, *170* (12), 120505. DOI: 10.1149/1945-7111/ad0ff5.
(77) Simon, P.; Gogotsi, Y.; Dunn, B. Where do batteries end and supercapacitors begin? *Science* **2014**, *343* (6176), 1210-1211.
(78) Augustyn, V.; Come, J.; Lowe, M. A.; Kim, J. W.; Taberna, P.-L.; Tolbert, S. H.; Abruña, H. D.; Simon, P.; Dunn, B. High-rate electrochemical energy storage through Li+ intercalation pseudocapacitance. *Nature materials* **2013**, *12* (6), 518-522.
(79) Fleischmann, S.; Mitchell, J. B.; Wang, R.; Zhan, C.; Jiang, D.-e.; Presser, V.; Augustyn, V. Pseudocapacitance: from fundamental understanding to high power energy storage materials. *Chemical Reviews* **2020**, *120* (14), 6738-6782.
(80) Cao, B.; Zhang, Q.; Liu, H.; Xu, B.; Zhang, S.; Zhou, T.; Mao, J.; Pang, W. K.; Guo, Z.; Li, A.; et al. Graphitic Carbon Nanocage as a Stable and High Power Anode for Potassium-Ion Batteries. *Advanced Energy Materials* **2018**, *8* (25), 1801149. DOI: https://doi.org/10.1002/aenm.201801149 (acccessed 2023/12/12).
(81) Wang, H.; Yao, T.; Li, C.; Meng, L.; Cheng, Y. Constructing three-dimensional ordered porous MoS2/C hierarchies for excellent high-rate long-life pseudocapacitive sodium storage. *Chemical Engineering Journal* **2020**, *397*, 125385.
(82) Du, Y.; Zhang, Z.; Xu, Y.; Bao, J.; Zhou, X. Metal sulfide-based potassium-ion battery anodes: storage mechanisms and synthesis strategies. *Acta Phys.-Chim. Sin* **2022**, *38* (11), 2205017.

Chapter 7

Conclusions and Outlook on Future Work

7.1 Conclusions and Future Research

The primary focus of this thesis centres on exploring the potential of inverse opal structures and three-dimensional ordered macroporous (3DOM) architectures to enhance electrochemical energy storage systems. Investigating various electrode materials, including intercalation-mode materials and conversion/alloying materials, this research highlights how combining different materials can produce synergistic results. Chapter 4 revealed how incorporating small amounts of an expensive, high-capacity material can significantly enhance storage and rate capabilities for an inexpensive, low-specific-capacity material (TiO_2). In Chapter 5, the study demonstrated that the amalgamation of structurally robust TiO_2 with electrically conductive carbon can elevate high-rate performance and specific capacity beyond the capabilities of individual materials. Chapter 6 illustrated how the benefits of the inverse opal structure, using carbon as an example, can be effectively applied in sodium-ion and potassium-ion batteries.

Chapter 4 explored highly ordered, macroporous inverse opal structures as TiO_2/GeO_2 nanocomposites with varying GeO_2 content, showcasing stable coulombic efficiencies and voltage responses influenced by the Ge content distribution. Characterisation reveals anatase TiO_2 and hexagonal GeO_2 phases at the macro-scale, with XPS depth profiling revealing graded GeO_2 incorporation. Localised atomic resolution analysis revealed that the material was largely amorphous at the nano-scale with regions of crystallinity. Small amounts of germanium enhance the specific capacity of TiO_2, with the 2:1 (Ti:Ge) ratio achieving an initial specific capacity of 1994 mAh/g and the 5:1 ratio reaching 1665 mAh/g at 150 mA/g. Both composites exhibit intriguing behavior, with an initial increase in specific capacities followed by

capacity fading attributed to pulverization and a reduction in GeO_2 content. Despite consistent and stable cycling behavior of the inverse opal electrodes, composites demonstrate capacity increases during cycling, retaining > 99% coulombic efficiency. Rate testing and fast-rate cycling show good capacity retention, with the 2:1 ratio retaining 94% capacity and the 5:1 ratio retaining 83.5%. Post-cycling SEM imaging reveals partial structure retention for the 2:1 ratio after 2000 cycles. The findings illustrate the complex behavior of interconnected macroporous Li-ion battery anode materials in composites, emphasizing the impact of spatial distribution on capacity, offering insights for tailoring materials to enhance performance and stability.

While various material characterisation techniques were used to analyse this material, there remains an opportunity for additional research focused on crystallising both oxides. Investigating the crystallisation process may unveil potential enhancements in stability and specific capacity for the electrode.[1, 2] Germanium is known for its high theoretical capacity (1384 mAh/g)[3]. Given this, the utilized current densities were optimized for TiO_2. It would be beneficial to investigate the response of these IO composites to current densities exceeding 500 mA/g, providing a more in-depth analysis of their high-rate performance and the fundamental limitation of the materials electronic conductivity at fast rates, and for electrodes with greater thickness and overall mass loading. Electrochemical testing was conducted on both inverse opal (IO) composites against pure lithium metal counter electrodes. However, it is advisable to extend the testing to a complete lithium-ion cell configuration to obtain comprehensive insights. Evaluating the capacity and energy density values in the context of a full cell setup would enable a direct comparison with commercially available cells, providing a more comprehensive understanding of the material's performance in practical applications.

Chapter 5 demonstrated carbon and TiO_2 nanocomposite IOs, denoted as C/TiO_2. Both materials were amorphous at the atomic level within a 3D macro-scale architecture, similar to Chapter 4. While both materials possess a comparable theoretical capacity of ~ 350 mAh/g, the composite IO exhibited discharge and charge capacities surpassing this value. This enhancement was attributed to the presence of additional charge compensation sites resulting from defects within the inverse opal structure. Using the individual inverse opals as baselines, the composite IO demonstrated impressive capacity retention and improved coulombic efficiency at both the 150 mA/g and 700 mA/g current density. Rate testing conducted across various current densities highlighted the superior stability and coulombic efficiency of the composite IO at elevated rates. Although it exhibited a higher capacity loss than its individual counterparts, the results were comparable to, if not better than, those reported for other C/TiO2 macroporous structures. Impressively, post-mortem analysis on this material revealed minimal expansion, with swelling recorded at 1% and 19% after 250 cycles at 150 mA/g and 700 mA/g, respectively.

To expand on this work, additional characterisation, such as XPS, could be employed to confirm the oxidation state of TiO_2. While titanium isopropoxide serves as the precursor and initial heating occurs at 100 ℃ in air, the primary heating is conducted under Ar. The flow rate of Ar during high temperature treatment was set low to allow for the formation of TiO_2. Although Raman spectroscopy reveals peaks indicative of crystallized TiO_2, the inclusion of XPS would be advantageous for examining the oxidation state of the sample without localized heating. Throughout cycling, minor fluctuations in capacity are detected, potentially attributed to factors like the retention of electrolyte decomposition byproducts within the inverse opal (IO) structure. To confirm that this phenomenon is the primary cause and not

influenced by environmental temperature variations, such as day-night cycles and overall weather changes, we propose conducting an in-depth investigation into the impact of temperature changes on the resulting capacity values during cycling. In addition, TiO_2 is a recognized semi-conducting material. The integration of this material with carbon aimed to enhance the overall conductivity of the composite.[4] In this context, impedance testing would be valuable to assess the improvements in overall resistance, both ohmic and ionic, in the composite inverse opals compared to TiO_2 inverse opals alone.

In Chapter 6, the focus shifted towards exploring the utility of inverse opal structures in 'beyond Li-ion' technologies, specifically sodium-ion and potassium-ion batteries. While sodium-ion batteries have been a subject of research for the past couple of decades[5, 6], potassium-ion batteries have gained attention more recently.[7, 8] Given the larger size of sodium and potassium ions compared to lithium ions, the implementation of macroporous structures becomes beneficial to facilitate efficient ion exchange and minimize diffusion distances. Utilizing carbon as a representative material, electrochemical tests in the sodium-ion half-cell exhibited stable and reversible reactions, maintaining capacity across 250 cycles. While the potassium-ion cell exhibited greater capacity fading compared to the sodium-ion cell, this phenomenon may be linked to the material's or the electrolyte’s compatibility with potassium rather than the integrity of the macroporous structure. This distinction is supported by post-mortem analysis, which revealed that the inverse opal structure remained intact even after 250 cycles. Electrochemical kinetics analysis highlights the role of both diffusion-controlled intercalation and surface-induced double-layer capacitance to the charge storage mechanism. When compared to the non-templated carbon, the inverse opal structure exhibited enhanced specific capacity and coulombic

efficiency in the sodium-ion cell. Additionally, in the potassium-ion cell, the inverse opal material displayed higher specific capacity and consistently improving coulombic efficiency throughout the cycle life, surpassing the performance of the thin film.

To continue this research, impedance testing would be advantageous to analyse internal resistance in sodium-ion versus potassium-ion cells. Such testing could unveil whether the 3DOM structure contributed to an overall reduction in resistance, compared to the non-templated carbon. Raman spectroscopy showed a low I_D/I_G ratio of 0.97, higher ratios have been linked to improved specific capacity in carbon electrodes.[9, 10] In this regard, temperature and ramp rate adjustments could be studied to obtain the optimal carbonisation method to ensure additional charge compensation sites for sodiation/potassiation.

In this work, carbon synthesised from sucrose is used as an example for the 3DOM structure to examine what advantages the structure brings. Future research could explore higher-capacity materials, previously dismissed due to volumetric expansion concerns, within an inverse opal structure to assess their suitability for use in both Na-ion and K-ion batteries. The realm of potassium-ion batteries is new and virtually unexplored in terms of inverse opal-like structures. While Sb and Sn based electrodes have been studied for K-ion batteries[11, 12], challenges related to volume expansion have been encountered, and the application of inverse opal structures might provide a solution to these issues. Possibly combining these materials with a structurally robust material, like TiO_2, could produce a high energy density and structurally stable nanocomposite for Na-ion and K-ion batteries.

In summary, the research on inverse opal composite structures holds significant importance in advancing the field of electrochemical energy storage. The

findings presented in this thesis showcase the potential of these structures to enhance the performance and stability of electrode materials, ranging from TiO_2/GeO_2 nanocomposites to carbon and TiO_2 combinations. The ability of inverse opals to accommodate volumetric changes, maintain structural integrity, and provide additional charge compensation sites has been highlighted. The exploration of these structures in 'beyond Li-ion' technologies, specifically sodium-ion and potassium-ion batteries, opens new avenues for diverse energy storage applications. Incorporating inverse opal composites in next-generation batteries can lead to improved specific capacity, stable cycling behavior, and enhanced high-rate performance. However, the complexity of electrochemical processes and the dynamic nature of materials necessitate continued research in battery materials. This ongoing research is essential to address challenges, improve efficiency, and pave the way for the development of advanced and sustainable battery systems that play a fundamental role in the transition to a greener and more energy-efficient future.

7.2 References

(1) Kang, K.; Meng, Y. S.; Breger, J.; Grey, C. P.; Ceder, G. Electrodes with high power and high capacity for rechargeable lithium batteries. *Science* **2006**, *311* (5763), 977-980.
(2) Rougier, A.; Gravereau, P.; Delmas, C. Optimization of the composition of the Li1− z Ni1+ z O 2 electrode materials: structural, magnetic, and electrochemical studies. *Journal of The Electrochemical Society* **1996**, *143* (4), 1168.
(3) McNulty, D.; Geaney, H.; Buckley, D.; O'Dwyer, C. High capacity binder-free nanocrystalline GeO2 inverse opal anodes for Li-ion batteries with long cycle life and stable cell voltage. *Nano Energy* **2018**, *43*, 11-21. DOI: https://doi.org/10.1016/j.nanoen.2017.11.007.
(4) Xia, T.; Zhang, W.; Wang, Z.; Zhang, Y.; Song, X.; Murowchick, J.; Battaglia, V.; Liu, G.; Chen, X. Amorphous carbon-coated TiO2 nanocrystals for improved lithium-ion battery and photocatalytic performance. *Nano Energy* **2014**, *6*, 109-118. DOI: https://doi.org/10.1016/j.nanoen.2014.03.012.
(5) Delmas, C. Sodium and sodium-ion batteries: 50 years of research. *Advanced Energy Materials* **2018**, *8* (17), 1703137.
(6) Abraham, K. Intercalation positive electrodes for rechargeable sodium cells. *Solid State Ionics* **1982**, *7* (3), 199-212.
(7) Pramudita, J. C.; Sehrawat, D.; Goonetilleke, D.; Sharma, N. An initial review of the status of electrode materials for potassium-ion batteries. *Advanced energy materials* **2017**, *7* (24), 1602911.
(8) Wessells, C. D.; Peddada, S. V.; Huggins, R. A.; Cui, Y. Nickel Hexacyanoferrate Nanoparticle Electrodes For Aqueous Sodium and Potassium Ion Batteries. *Nano Letters* **2011**, *11* (12), 5421-5425. DOI: 10.1021/nl203193q.
(9) Zhang, W.; Ming, J.; Zhao, W.; Dong, X.; Hedhili, M. N.; Costa, P. M. F. J.; Alshareef, H. N. Graphitic Nanocarbon with Engineered Defects for High-Performance Potassium-Ion Battery Anodes. *Advanced Functional Materials* **2019**, *29* (35), 1903641. DOI: https://doi.org/10.1002/adfm.201903641 (acccessed 2023/12/18).
(10) Guo, Z.; Xu, Z.; Xie, F.; Jiang, J.; Zheng, K.; Alabidun, S.; Crespo-Ribadeneyra, M.; Hu, Y.-S.; Au, H.; Titirici, M.-M. Investigating the Superior Performance of Hard Carbon Anodes in Sodium-Ion Compared With Lithium- and Potassium-Ion Batteries. *Advanced Materials* **2023**, *35* (42), 2304091. DOI: https://doi.org/10.1002/adma.202304091 (acccessed 2023/12/18).
(11) McCulloch, W. D.; Ren, X.; Yu, M.; Huang, Z.; Wu, Y. Potassium-ion oxygen battery based on a high capacity antimony anode. *ACS applied materials & interfaces* **2015**, *7* (47), 26158-26166.
(12) Sultana, I.; Ramireddy, T.; Rahman, M. M.; Chen, Y.; Glushenkov, A. M. Tin-based composite anodes for potassium-ion batteries. *Chemical communications* **2016**, *52* (59), 9279-9282.